

**Investigation of the interaction  
between Nanoparticles and I-line  
radiation for Nanolithography  
applications**

**By Scott Lewis**

UMI Number: U585240

All rights reserved

INFORMATION TO ALL USERS

The quality of this reproduction is dependent upon the quality of the copy submitted.

In the unlikely event that the author did not send a complete manuscript and there are missing pages, these will be noted. Also, if material had to be removed, a note will indicate the deletion.



UMI U585240

Published by ProQuest LLC 2013. Copyright in the Dissertation held by the Author.  
Microform Edition © ProQuest LLC.

All rights reserved. This work is protected against  
unauthorized copying under Title 17, United States Code.



ProQuest LLC  
789 East Eisenhower Parkway  
P.O. Box 1346  
Ann Arbor, MI 48106-1346

| PERIODIC TABLE OF THE ELEMENTS  |                      |                       |                              |                            |                      |                         |                        |                       |                         |                        |                        |                        |                         |                           |                       |                       |                      |                     |
|---|----------------------|-----------------------|------------------------------|----------------------------|----------------------|-------------------------|------------------------|-----------------------|-------------------------|------------------------|------------------------|------------------------|-------------------------|---------------------------|-----------------------|-----------------------|----------------------|---------------------|
| GROUP   |                      |                       |                              |                            |                      |                         |                        |                       |                         |                        |                        |                        |                         |                           |                       |                       |                      | 18 - VIIA           |
| PERIOD  | 1                    | 2                     |                              |                            |                      |                         |                        |                       |                         |                        |                        |                        | 13                      | 14                        | 15                    | 16                    | 17                   | 18                  |
| 1   | 1<br>H<br>HYDROGEN   |                       |                              |                            |                      |                         |                        |                       |                         |                        |                        |                        |                         |                           |                       |                       |                      | 2<br>He<br>HELIUM   |
| 2   | 3<br>Li<br>LITHIUM   | 4<br>Be<br>BERYLLIUM  |                              |                            |                      |                         |                        |                       |                         |                        |                        |                        | 5<br>B<br>BORON         | 6<br>C<br>CARBON          | 7<br>N<br>NITROGEN    | 8<br>O<br>OXYGEN      | 9<br>F<br>FLUORINE   | 10<br>Ne<br>NEON    |
| 3   | 11<br>Na<br>SODIUM   | 12<br>Mg<br>MAGNESIUM |                              |                            |                      |                         |                        |                       |                         |                        |                        |                        | 13<br>Al<br>ALUMINUM    | 14<br>Si<br>SILICON       | 15<br>P<br>PHOSPHORUS | 16<br>S<br>SULFUR     | 17<br>Cl<br>CHLORINE | 18<br>Ar<br>ARGON   |
| 4   | 19<br>K<br>POTASSIUM | 20<br>Ca<br>CALCIUM   | 21<br>Sc<br>SCANDIUM         | 22<br>Ti<br>TITANIUM       | 23<br>V<br>VANADIUM  | 24<br>Cr<br>CHROMIUM    | 25<br>Mn<br>MANGANESE  | 26<br>Fe<br>IRON      | 27<br>Co<br>COBALT      | 28<br>Ni<br>NICKEL     | 29<br>Cu<br>COPPER     | 30<br>Zn<br>ZINC       | 31<br>Ga<br>GALLIUM     | 32<br>Ge<br>GERMANIUM     | 33<br>As<br>ARSENIC   | 34<br>Se<br>SELENIUM  | 35<br>Br<br>BROMINE  | 36<br>Kr<br>KRYPTON |
| 5   | 37<br>Rb<br>RUBIDIUM | 38<br>Sr<br>STRONTIUM | 39<br>Y<br>YTTORIUM          | 40<br>Zr<br>ZIRCONIUM      | 41<br>Nb<br>NIOBIUM  | 42<br>Mo<br>MOLYBDENUM  | 43<br>Tc<br>TECHNETIUM | 44<br>Ru<br>RUTHENIUM | 45<br>Rh<br>RHODIUM     | 46<br>Pd<br>PALLADIUM  | 47<br>Ag<br>SILVER     | 48<br>Cd<br>CADMIUM    | 49<br>In<br>INDIUM      | 50<br>Sn<br>TIN           | 51<br>Sb<br>ANTIMONY  | 52<br>Te<br>TELLURIUM | 53<br>I<br>IODINE    | 54<br>Xe<br>XENON   |
| 6   | 55<br>Cs<br>CAESIUM  | 56<br>Ba<br>BARIUM    | 57-71<br>La-Lu<br>Lanthanide | 72<br>Hf<br>HAFNIUM        | 73<br>Ta<br>TANTALUM | 74<br>W<br>TUNGSTEN     | 75<br>Re<br>RHENIUM    | 76<br>Os<br>OSMIUM    | 77<br>Ir<br>IRIDIUM     | 78<br>Pt<br>PLATINUM   | 79<br>Au<br>GOLD       | 80<br>Hg<br>MERCURY    | 81<br>Tl<br>THALLIUM    | 82<br>Pb<br>LEAD          | 83<br>Bi<br>BISMUTH   | 84<br>Po<br>POLONIUM  | 85<br>At<br>ASTATINE | 86<br>Rn<br>RADON   |
| 7   | 87<br>Fr<br>FRANCIUM | 88<br>Ra<br>RADIUM    | 89-103<br>Ac-Lr<br>Actinide  | 104<br>Rf<br>RUTHERFORDIUM | 105<br>Db<br>DUBNIUM | 106<br>Sg<br>SEABORGIUM | 107<br>Bh<br>BOHRNIUM  | 108<br>Hs<br>HASSIUM  | 109<br>Mt<br>MEITNERIUM | 110<br>Uun<br>UNUNNIUM | 111<br>Uuh<br>UNUNBIUM | 112<br>Uub<br>UNUNBIUM | 113<br>Uut<br>UNUNTRIUM | 114<br>Uuq<br>UNUNQUADIUM |                       |                       |                      |                     |
| <div><div>RELATIVE ATOMIC MASS (A)</div><div>GROUP IUBAC</div><div>GROUP CAS</div><div>ATOMIC NUMBER (Z)</div><div>SYMBOL</div><div>ELEMENT NAME</div></div> <div><div>Metal</div><div>Semimetal</div><div>Nonmetal</div><div>Alkali metal</div><div>Alkaline earth metal</div><div>Transition metals</div><div>Lanthanide</div><div>Actinide</div><div>Chalcogens element</div><div>Halogens element</div><div>Noble gas</div></div> <div><div>STANDARD STATE (25 °C; 101 kPa)</div><div>Ne - gas</div><div>Fe - solid</div><div>Ga - liquid</div><div>Tc - synthetic</div></div>  |                      |                       |                              |                            |                      |                         |                        |                       |                         |                        |                        |                        |                         |                           |                       |                       |                      |                     |
| <div><div>LANTHANIDE</div><div>57 138.91 La LANTHANUM</div><div>58 140.12 Ce CERIUM</div><div>59 140.91 Pr PRASEODYMIUM</div><div>60 144.24 Nd NEODYMIUM</div><div>61 (145) Pm PROMETHIUM</div><div>62 150.36 Sm SAMARIUM</div><div>63 151.96 Eu EUROMIUM</div><div>64 157.25 Gd GADOLINIUM</div><div>65 158.93 Tb TERBIUM</div><div>66 162.50 Dy DYSPROSIUM</div><div>67 164.93 Ho HOLMIUM</div><div>68 167.26 Er ERBIUM</div><div>69 168.93 Tm THULIUM</div><div>70 173.04 Yb YTTERIUM</div><div>71 174.97 Lu LUTETIUM</div></div> <div><div>ACTINIDE</div><div>89 (227) Ac ACTINIUM</div><div>90 232.04 Th THORIUM</div><div>91 231.04 Pa PROTACTINIUM</div><div>92 238.03 U URANIUM</div><div>93 (237) Np NEPTUNIUM</div><div>94 (244) Pu PLUTONIUM</div><div>95 (243) Am AMERICIUM</div><div>96 (247) Cm CURIUM</div><div>97 (247) Bk BERKELIUM</div><div>98 (251) Cf CALIFORNIUM</div><div>99 (252) Es EINSTEINIUM</div><div>100 (257) Fm FERMIUM</div><div>101 (258) Md MENDELVIUM</div><div>102 (259) No NOBELIUM</div><div>103 (262) Lr LAWRENCIUM</div></div> |                      |                       |                              |                            |                      |                         |                        |                       |                         |                        |                        |                        |                         |                           |                       |                       |                      |                     |

Taken from [http://geology.isu.edu/geoscience/periodic\\_table.gi](http://geology.isu.edu/geoscience/periodic_table.gi)

## **Acknowledgements**

I would like to express my gratitude to my supervisor Dr. Richard Perks for allowing me to work on the subject of nano technology. He has bestowed me with the chance to explore and pursue paths on my own whilst advising the work presented in this thesis.

I would like to thank Rolfe Wheeler – Jones for his time and talent with operating the SEM and support throughout this thesis. I would like to thank Vic Haynes for investing hours brainstorming ideas for developing materials used in this thesis. I will always be grateful to them both for giving me their expert knowledge to complete this thesis. I would like to thank Alex Crowe who has provided me with the balance between work and life.

I would like to specifically thank Prof. Lucio Piccirillo for his guidance and support while completing this thesis. Also I would like to thank Dr. Bruno Maffei, Dr. Giampaolo Pisano and Dr. Simon Melhuish who have guided me to complete this thesis.

I would like to thank Chris Royston, Mark Brocklebank, Anthony Waldron and Craig Butler at E. M. Systems Support ltd for their input and allowing me the time to work on a high resolution electron beam lithography tool.

I would like to thank all my friends, Peter McGovern, Tudor Williams, Gareth Michell and Shahid Mian for their support throughout my time spent at Cardiff University. Most of all, I am grateful to my parents for supporting my ventures throughout my life.



## **Table of Contents**

|   |        |
|---|--------|
| Acknowledgements.....   | -iii-  |
| Table of Contents.....  | -iv-   |
| List of Figures.....  | -v-    |
| List of Tables.....   | -xiii- |
| Abstract.....   | -xiv-  |
| <br>  |        |
| Chapter 1 Introduction.....   | -1-    |
| Chapter 2 Development of a novel nanocomposite resist for high resolution e – beam lithography next generation mask production..... | -22-   |
| Chapter 3 Characterization of a PMMA based Nanocomposite Resist for Next Generation Lithography.....                                | -50-   |
| Chapter 4 Applied Monte Carlo Simulations of the proximity effects on a PMMA based Nanocomposite Resist.....                        | -80-   |
| Chapter 5 Characterization of the Nanocomposite Resist Photo Mask for I-line applications.....                                      | -105-  |
| Chapter 6 Self Assembled Nanoparticle Film for Direct I – line Nanolithography applications.....                                    | -123-  |
| Chapter 7 Conclusions.....  | -151-  |
| Appendix A.....   | -157-  |
| Appendix B.....   | -159-  |
| Appendix C.....   | -161-  |
| Appendix D.....   | -167-  |
| Appendix E.....   | -173-  |
| Appendix F.....   | -175-  |

## **List of Figures**

### Chapter 1

|   |     |
|---|-----|
| Figure 1 – 0: The relationship between the minimum feature size and the density of transistors in an integrated circuit [2].....  | -2- |
| Figure 1 – 1: Schematic of a MOSFET structure.....  | -3- |
| Figure 1 – 2: Schematic of the lithographic process.....  | -5- |
| Figure 1 – 3: Schematic presentation of the functionality of a CAR. (a) the photoresist before exposure, (b) radiation induced generation of photoacid in exposed areas, (c) acid catalyzed thermal deprotection of inhibitor during PEB and (d) chemical development of the photoresist..... | -6- |
| Figure 1 – 4: Trends of lithography technologies and exposure wavelengths [8].....  | -8- |

### Chapter 2

|   |      |
|---|------|
| Figure 2 – 1: E-beam chain scission process with PMMA e-beam resist.....  | -23- |
| Figure 2 – 2: The opaque structure of the photomask for I – line applications.....  | -27- |
| Figure 2 – 3: Optical transmission spectra of Borosilicate glass.....   | -28- |
| Figure 2 – 4: Optical transmission spectra of the various thickness of Au on Borosilicate glass.....  | -29- |
| Figure 2 – 5: Optical transmission of PMMA (thickness of 800nm) on 7nm of Au thin film.....   | -29- |
| Figure 2 – 6: a) Contact I – line exposure using PMMA e-beam resist as the optical mask, b) Resultant Photoresist after development (2401 developer) stage.....   | -30- |
| Figure 2 – 7: a) Contact I – line exposure using composite resist (PMMA and the Nanoparticles) as the optical mask, b) Resultant Photoresist after development (2401 developer) stage.....                            | -30- |
| Figure 2 – 8: XRD diffraction patterns of the polycrystalline structure of the nanoparticle species.....  | -31- |
| Figure 2 – 9: a) AFM image of 200mg of TiO <sub>2</sub> nanoparticles embedded directly into 1g of PMMA, b) AFM image of 200mg of Al <sub>2</sub> O <sub>3</sub> nanoparticles embedded directly into 1g of PMMA..... | -32- |

|  |      |
|--|------|
| Figure 2 – 10: Schematic representation of the nanoparticle /Anisole /PMMA system.....   | -33- |
| Figure 2 – 11: Contact angles of solvents. a) Toluene, b) Xylene, c) Anisole, d) IPA, e) Methanol, f) Acetic Acid, g) Water.....   | -35- |
| Figure 2 – 12: Contact angles of the solvents shown in the previous figure.....  | -36- |
| Figure 2 – 13: Hydrogen bonding mechanism between the borosilicate glass / oxide nanoparticle surface and the various solvents.....  | -38- |
| Figure 2 – 14: Zeta potential of the two test cases – $\text{Al}_2\text{O}_3$ & $\text{TiO}_2$ suspended in methanol and toluene respectively.....   | -39- |
| Figure 2 – 15: Schematic representation of the nanoparticle /Methanol /Anisole /PMMA system.....   | -40- |
| Figure 2 – 16: a) AFM image of $\text{TiO}_2$ /Methanol embedded in the PMMA matrix b) AFM image of $\text{Al}_2\text{O}_3$ /Methanol embedded in the PMMA matrix.....   | -40- |
| Figure 2 – 17: PMMA based nanocomposite resist surface when suspended by 200mg of $\text{TiO}_2$ nanoparticles that was prepared with a methanol suspension.....   | -41- |
| Figure 2 – 18: Transmission spectra of the nanoparticles embedded in PMMA matrix.....  | -42- |
| Figure 2 – 19: a) Schematic diagram of the scattered radiation process in arbitrary nanoparticle, b) Radiation intensity of the UV – IR radiation propagating through the nanocomposite thin film in the z – direction, c) Schematic diagram of the scattering process of multiple nanoparticles inside the nanocomposite thin film..... | -43- |
| Figure 2 – 20: Number of nanoparticles embedded in the nanocomposite resist.....   | -44- |
| Figure 2 – 21: (a) Optical transmission of the nanocomposite resist at I – line wavelengths, (b) Developed S1813 photoresist thickness.....  | -45- |
| Figure 2 – 22: Schematic representation of the effect of the amount of oxide nanoparticles embedded in the PMMA.....   | -46- |

## Chapter 3

|  |      |
|--|------|
| Figure 3 – 1: Schematic of a typical Monte Carlo simulation demonstrating the proximity effect.....        | -51- |
| Figure 3 – 2: E-beam lithography test patterns a) sensitivity squares, b) sub 100nm proximity crosses..... | -54- |

|  |      |
|--|------|
| Figure 3 – 3: Developed nanocomposite resist a) Unloaded P96K7%, b) loaded P96K7% with 50mg of Al <sub>2</sub> O <sub>3</sub> nanoparticles, c) loaded P96K7% with 100mg of Al <sub>2</sub> O <sub>3</sub> nanoparticles, d) loaded P96K7% with 150mg of Al <sub>2</sub> O <sub>3</sub> nanoparticles. The dimensions of all squares are 20µm..... | -55- |
| Figure 3 – 4: AFM image of the PMMA 96K7% loaded with 0mg Al <sub>2</sub> O <sub>3</sub> nanoparticales: clearing dose of 120 – 150µC/cm <sup>2</sup> .....  | -56- |
| Figure 3 – 5: AFM image of the PMMA96K7% loaded with 50mg Al <sub>2</sub> O <sub>3</sub> nanoparticales: clearing dose of 180 – 210µC/cm <sup>2</sup> .....  | -57- |
| Figure 3 – 6: AFM image of the PMMA 96K7% loaded with 100mg Al <sub>2</sub> O <sub>3</sub> nanoparticales: clearing dose of 180 – 210µC/cm <sup>2</sup> .....  | -58- |
| Figure 3 – 7: AFM image of the P96K7% loaded with 150mg Al <sub>2</sub> O <sub>3</sub> nanoparticales: clearing dose of 210 – 240µC/cm <sup>2</sup> .....  | -58- |
| Figure 3 – 8: Overall thickness's of the nanocomposite resist.....   | -59- |
| Figure 3 – 9: PMMA 950K 7% resist clearing doses based on the electron energy stopping powers of the Al <sub>2</sub> O <sub>3</sub> nanoparticles.....   | -60- |
| Figure 3 – 10: PMMA 96K 7% resist clearing doses based on the electron energy stopping powers of the Al <sub>2</sub> O <sub>3</sub> nanoparticles.....   | -61- |
| Figure 3 – 11: Electron exposure clearing doses of the PMMA 950K7% and PMMA 96K7% based nanocomposite resists.....   | -62- |
| Figure 3 – 12: SEM image of the e-beam characterization pattern in the PMMA 950K 7% nanocomposite resist.....  | -62- |
| Figure 3 – 13: SEM image of PMMA 950K 7% loaded with 150mg of Al <sub>2</sub> O <sub>3</sub> nanoparticles.....  | -63- |
| Figure 3 – 14: AFM image of the PMMA 950K 7% loaded with 150mg of Al <sub>2</sub> O <sub>3</sub> nanoparticles.....  | -64- |
| Figure 3 – 15: SEM image of PMMA 950K 7% loaded with 100mg of Al <sub>2</sub> O <sub>3</sub> nanoparticles.....  | -65- |
| Figure 3 – 16: AFM image of PMMA 950K 7% loaded with 100mg of Al <sub>2</sub> O <sub>3</sub> nanoparticles.....  | -65- |
| Figure 3 – 17: SEM image of PMMA 950K 7% loaded with 50mg of Al <sub>2</sub> O <sub>3</sub> nanoparticles.....   | -66- |
| Figure 3 – 18: AFM image of PMMA 950K 7% loaded with 50mg of Al <sub>2</sub> O <sub>3</sub> nanoparticles.....   | -66- |
| Figure 3 – 19: SEM image of unloaded PMMA 950K 7%.....   | -67- |

|  |      |
|--|------|
| Figure 3 – 20: AFM image of unloaded PMMA 950K 7%.....   | -68- |
| Figure 3 – 21: SEM image of PMMA 96K 7% loaded with 150mg of Al <sub>2</sub> O <sub>3</sub> nanoparticles.....                               | -68- |
| Figure 3 – 22: SEM image of PMMA 950K 7% loaded with 100mg of Al <sub>2</sub> O <sub>3</sub> nanoparticles.....                              | -69- |
| Figure 3 – 23: SEM image of PMMA 96K 7% 50mg sample.....   | -70- |
| Figure 3 – 24: SEM image of unloaded PMMA 96K 7%.....  | -70- |
| Figure 3 – 25: High aspect ratios of the PMMA 950K and 96K based nanocomposite resists.....  | -71- |
| Figure 3 – 26: SEM image of collapsed features in PMMA 950K 7% loaded with 150mg of Al <sub>2</sub> O <sub>3</sub> nanoparticles resist..... | -72- |
| Figure 3 – 27: SEM image of collapsed features in PMMA 950K 7% loaded with 100mg of Al <sub>2</sub> O <sub>3</sub> nanoparticles resist..... | -73- |
| Figure 3 – 28: SEM image of collapsed features in PMMA 950K 7% loaded with 50mg of Al <sub>2</sub> O <sub>3</sub> nanoparticles resist.....  | -73- |
| Figure 3 – 29: SEM image of collapsed features in unloaded PMMA 950K 7% resist.....  | -74- |
| Figure 3 – 30: SEM image of collapsed features in PMMA 96K 7% loaded with 150mg of Al <sub>2</sub> O <sub>3</sub> nanoparticles resist.....  | -75- |
| Figure 3 – 31: SEM image of collapsed features in PMMA 96K 7% loaded with 100mg of Al <sub>2</sub> O <sub>3</sub> nanoparticles resist.....  | -75- |
| Figure 3 – 32: SEM image of collapsed features in PMMA 96K 7% loaded with 50mg of Al <sub>2</sub> O <sub>3</sub> nanoparticles resist.....   | -76- |
| Figure 3 – 33: SEM image of collapsed features in unloaded PMMA 96K 7% resist.....   | -77- |

#### Chapter 4

|  |      |
|--|------|
| Figure 4 – 1: A flowchart of the simulating the nanocomposite resist using the Monte Carlo method.....   | -83- |
| Figure 4 – 2: Point electron distributions of PMMA loaded with 0, 50, 100 and 150mg of Al <sub>2</sub> O <sub>3</sub> nanoparticles exposed with dose of 150, 200, 240μC/cm <sup>2</sup> , for 25KeV incident electron energies..... | -87- |

|  |      |
|--|------|
| Figure 4 – 3: Point electron distributions of PMMA loaded with 0, 50, 100 and 150mg of $\text{Al}_2\text{O}_3$ nanoparticles exposed with dose of 150, 200, $240\mu\text{C}/\text{cm}^2$ , for 100KeV incident electron energies.....                              | -88- |
| Figure 4 – 4: Average radial distances of a 400nm thick film of PMMA and for nanocomposite films with densities of 50, 100, 150mg at incident electron energies of 25 and 100KeV and a dose of $150\mu\text{C}/\text{cm}^2$ .....                                  | -89- |
| Figure 4 – 5: Average radial distances of a 400nm thick film of PMMA and for nanocomposite films with densities of 50, 100, 150mg at incident electron energies of 25 and 100KeV and a dose of $200\mu\text{C}/\text{cm}^2$ .....                                  | -90- |
| Figure 4 – 6: Average radial distances of a 400nm thick film of PMMA and for nanocomposite films with densities of 50, 100, 150mg at incident electron energies of 25 and 100KeV and a dose of $240\mu\text{C}/\text{cm}^2$ .....                                  | -90- |
| Figure 4 – 7: Average radial distances of a 550nm thick film of PMMA and for nanocomposite films with densities of 50, 100, 150mg at incident electron energies of 25 and 100KeV and a dose of $150\mu\text{C}/\text{cm}^2$ .....                                  | -91- |
| Figure 4 – 8: Average radial distances of a 550nm thick film of PMMA and for nanocomposite films with densities of 50, 100, 150mg at incident electron energies of 25 and 100KeV and a dose of $200\mu\text{C}/\text{cm}^2$ .....                                  | -91- |
| Figure 4 – 9: Average radial distances of a 550nm thick film of PMMA and for nanocomposite films with densities of 50, 100, 150mg at incident electron energies of 25 and 100KeV and a dose of $240\mu\text{C}/\text{cm}^2$ .....                                  | -92- |
| Figure 4 – 10: Number of secondary electrons created in a 400nm film at 25KeV incident electron energy and a dose of $240\mu\text{C}/\text{cm}^2$ .....  | -93- |
| Figure 4 – 11: Total distance of the travelling secondary electrons in a 400nm film at 25KeV incident electron energy.....   | -94- |
| Figure 4 – 12: Total distance travelled by the secondary electrons in a 400nm film at 100KeV incident electron energy.....   | -95- |
| Figure 4 – 13: Total distance travelled by the secondary electrons in a 550nm film at 25KeV incident energy.....   | -96- |
| Figure 4 – 14: Total distance of the travelling secondary electrons in a 550nm film at 100KeV incident electron energy.....  | -96- |
| Figure 4 – 15: A cross section of the 90nm lines directly written into the PMMA based nanocomposite resist (a) unloaded PMMA 400nm film at 25KeV incident energy and a dose of $220\mu\text{C}/\text{cm}^2$ , (b) PMMA loaded with 50mg of $\text{Al}_2\text{O}_3$ |      |

nanoparticles in a 450nm film at 25KeV incident energy and a dose of  $250\mu\text{C}/\text{cm}^2$ , (c) PMMA loaded with 100mg of  $\text{Al}_2\text{O}_3$  nanoparticles in a 500nm film at 25KeV incident energy and a dose of  $300\mu\text{C}/\text{cm}^2$ , (d) PMMA loaded with 150mg of  $\text{Al}_2\text{O}_3$  nanoparticles in a 550nm film at 25KeV incident energy and a dose of  $300\mu\text{C}/\text{cm}^2$ .....-99-

Figure 4 – 16: A cross section of the 80nm lines directly written into the PMMA based nanocomposite resist (a) unloaded PMMA 400nm film at 25KeV incident energy and a dose of  $220\mu\text{C}/\text{cm}^2$ , (b) PMMA loaded with 50mg of  $\text{Al}_2\text{O}_3$  nanoparticles in a 450nm film at 25KeV incident energy and a dose of  $250\mu\text{C}/\text{cm}^2$ , (c) PMMA loaded with 100mg of  $\text{Al}_2\text{O}_3$  nanoparticles in a 500nm film at 25KeV incident energy and a dose of  $300\mu\text{C}/\text{cm}^2$ , (d) PMMA loaded with 150mg of  $\text{Al}_2\text{O}_3$  nanoparticles in a 550nm film at 25KeV incident energy and a dose of  $300\mu\text{C}/\text{cm}^2$ .....-101-

Figure 4 – 17: A cross section of the 70nm lines directly written into the PMMA based nanocomposite resist (a) unloaded PMMA 400nm film at 25KeV incident energy and a dose of  $220\mu\text{C}/\text{cm}^2$ , (b) PMMA loaded with 50mg of  $\text{Al}_2\text{O}_3$  nanoparticles in a 450nm film at 25KeV incident energy and a dose of  $250\mu\text{C}/\text{cm}^2$ , (c) PMMA loaded with 100mg of  $\text{Al}_2\text{O}_3$  nanoparticles in a 500nm film at 25KeV incident energy and a dose of  $300\mu\text{C}/\text{cm}^2$ , (d) PMMA loaded with 150mg of  $\text{Al}_2\text{O}_3$  nanoparticles in a 550nm film at 25KeV incident energy and a dose of  $300\mu\text{C}/\text{cm}^2$ .....-102-

## Chapter 5

Figure 5 – 1: (a), Nanocomposite resist photo mask, (b) Resultant S1813 photoresist.....-108-

Figure 5 – 2: (a) PMMA based nanocomposite resist following development, (b) developed S1813 photoresist on Silicon, which has been exposed to I – line wavelengths.....-109-

Figure 5 – 3: Schematic representation of the I-line radiation magnitude when the surface of the nanocomposite resist was in contact with the S1813 photoreist.....-110-

Figure 5 – 4: SEM image of the  $1\mu\text{m}$  trenches directly written into the nanocomposite resist.....-110-

|   |       |
|---|-------|
| Figure 5 – 5: The nanocomposite resist photomask.....   | -112- |
| Figure 5 – 6: SEM image of the nanoparticles in the nanocomposite resist.....   | -112- |
| Figure 5 – 7: Developed S1813 photoresist.....  | -113- |
| Figure 5 – 8: SEM image of the resultant S1813 photoresist.....   | -113- |
| Figure 5 – 9: A three dimensional grey scale test feature.....  | -115- |
| Figure 5 – 10: Fabrication parameters for 2D and 3D micro structures for S1813 photoresist.....   | -115- |
| Figure 5 – 11: The method for achieving the etch rates and selectivity.....   | -116- |
| Figure 5 – 12: (a) Graded S1813 photoresist steps with an angle of $0.045^\circ$ , (b) Graded silicon steps with an angle of $0.028^\circ$ .....          | -117- |
| Figure 5 – 13: (a) Thermal expansion of the features in PMMA mask. (b) Thermal expansion of $\text{Al}_2\text{O}_3$ and $\text{TiO}_2$ nanoparticles..... | -118- |
| Figure 5 – 14: Thermal expansion of the nanocomposite resist.....   | -119- |

## Chapter 6

|   |       |
|---|-------|
| Figure 6 – 1: a) Schematic drawing of the surface plasmon dispersion curve. At the same frequency, surface plasmons display a shorter modal wavelength compared to that of free space photons, therefore, allowing sub – wavelength lithography, b) Schematic of the nanolithography process using the Silver mask. Inset: The charges and the electromagnetic field of surface plasmons propagating on the grating surface in the x direction..... | -125- |
| Figure 6 – 2: Model of a metal surface when excited by SPR.....   | -126- |
| Figure 6 – 3: Experimental configuration for the detection of the SPR propagating on a metal thin film.....   | -129- |
| Figure 6 – 4: schematic illustration of the three step process for transferring a nanoparticle monolayer from the water surface to a solid substrate.....   | -131- |
| Figure 6 – 5: contact angle of the untreated silver.....  | -133- |
| Figure 6 – 6: Contact angle of the hydrophobic silver and hydrophilic borosilicate glass.....   | -133- |
| Figure 6 – 7: An alkanethiol monolayer with sulphur atoms bound to the Silver surface, creating an hydrophobic Silver surface.....  | -134- |
| Figure 6 – 8: Defects of the Langmuir film.....   | -135- |
| Figure 6 – 9: Aggregation of multiple nanoparticles forming a Langmuir film....   | -136- |



|  |      |
|--|------|
| Figure 6 – 10: Reflection of Silver films of different thickness. Detection of Surface Plasmon modes, the data represented in black were performed at the 635nm wavelengths in comparison with the data of [13] at 546nm shown in grey.....  | 137- |
| Figure 6 – 11: The perfect asymmetric lens system consisting of a thin film of silver.....   | 138- |
| Figure 6 – 12: Transmission spectrum of the 30nm spherical Silver nanoparticle with a spacing period of 20nm forming a hcp 2D array.....   | 140- |
| Figure 6 – 13: a) Silver nanoparticle hcp 2D array positioned by self assembly, b) developed S1813 photoresist exposed at I – line wavelength produced by surface plasmons.....  | 141- |
| Figure 6 – 14: Schematic of lithographic process to obtain the correct edge bead thickness to focus the plasmonic mask. a) edge beads occurring when spun at a particular speed, b & c) UV exposure to get rid of the edge beads & develop, d) UV exposure as a function of time, inset, close up showing the distance of the UV exposure penetrating the photoresist as a function of time, e) developed photoresist, inset, resultant thickness to focus the plasmonic mask..... | 144- |
| Figure 6 – 15: a) TEM micrograph of self assemblies of Ag nanowire to form a suitable plasmonic mask, b) Developed S1813 photoresist exposed at I-line wavelength produced by surface plasmon.....   | 145- |
| Figure 6 – 16: SEM image of an InP HEMT, Inset shows a 120nm gate structure fabricated using e-beam technology, images courtesy of A. Jones.....   | 146- |

## Chapter 7

|  |      |
|--|------|
| Figure 7 – 1: The nano island formation process.....   | 154- |
| Figure 7 – 2: A TEM micrograph of Silver on Carbon when the temperature was elevated to 640°C for 5 minutes..... | 155- |

## **List of Tables**

|   |       |
|---|-------|
| Table 2 – 1: nanostructural data for the nanoparticles.....                           | -32-  |
| Table 2 – 2: Solvent molecules and contact angle.....                                 | -34-  |
| Table 2 – 3: Optical transmission of the composite resist at I – line wavelength..... | -42-  |
| Table 3 – 1: Clearing doses of the PMMA based nanocomposite resists.....              | -61-  |
| Table 5 – 1: The thickness data required to calculate the selectivity.....            | -117- |

# **Abstract**

In 1965 Gordon E. Moore forecasted that the number of transistors on a chip would double every 18 months. This became known throughout the semiconductor industry as Moore's law. However, it was observed that this cannot be continued indefinitely but, it has been seen as a goal for the industry.

Since the 1960s, semiconductor manufacturers have strived to scale down device features according to Moore's law. This has been achieved by photolithography, and has unquestionably been one of the major driving forces behind the progress made in the field of semiconductor technology. It is in this miniaturization of features that photolithography has made its contribution, and where the advancement of the fabrication techniques to produce a mask has played its role.

In this thesis the focus was on investigating suitable technologies to economically maintain the trend of Moore's Law. The fabrication of next generation optical photomasks was studied that could produce the next generation ultra large scale integration (ULSI). Two methods were developed and contrasted; these were both based on 'top down' photolithography using I-line radiation. However, two different approaches were adopted to fabricate these optical masks. The first was based on electron beam lithography by fabricating a novel nanocomposite electron beam resist that incorporated nanoparticles into Polymethylmethacrylate (PMMA). The nanoparticles were used to attenuate the radiation propagating through the electron beam resist as the PMMA was found to be transparent at the wavelength of the incident radiation. When the nanocomposite resist was patterned by the electron beam, the pattern was transferred to a photoresist via contact printing using the conventional photolithography technique.

The second approach exploited a novel photolithography technique using periodic hexagonally closely packed silver nanoparticle 2D arrays. A method to precisely control the spacing between nanoparticles by temperature has been demonstrated; this was then used to transfer a nano – pattern into a photoresist. The high – density nanoparticle thin film was accomplished by self-assembling through the Langmuir – Schaefer (LS) technique on a water surface and transferring the nanoparticle monolayer to a temperature sensitive polymer membrane. A 30nm hexagonally

packed silver nanoparticle 2D array pattern with a 50nm period has been successfully transferred into photoresist. The resultant feature sizes were 34nm with a period of 16nm, due to the surface plasmon resonance where the photoresist is approximately 11 times smaller than wavelength.

This work demonstrated the suitability of these novel masks in certain applications; where the complexity of fabrications and the associated costs varied considerably. 'Top down' techniques were often expensive and slow, but provided a direct route to achieving the desired features. The 'bottom up' techniques were often achieved at low cost but were limited in terms of control over geometry.

## CHAPTER

# 1

## Introduction

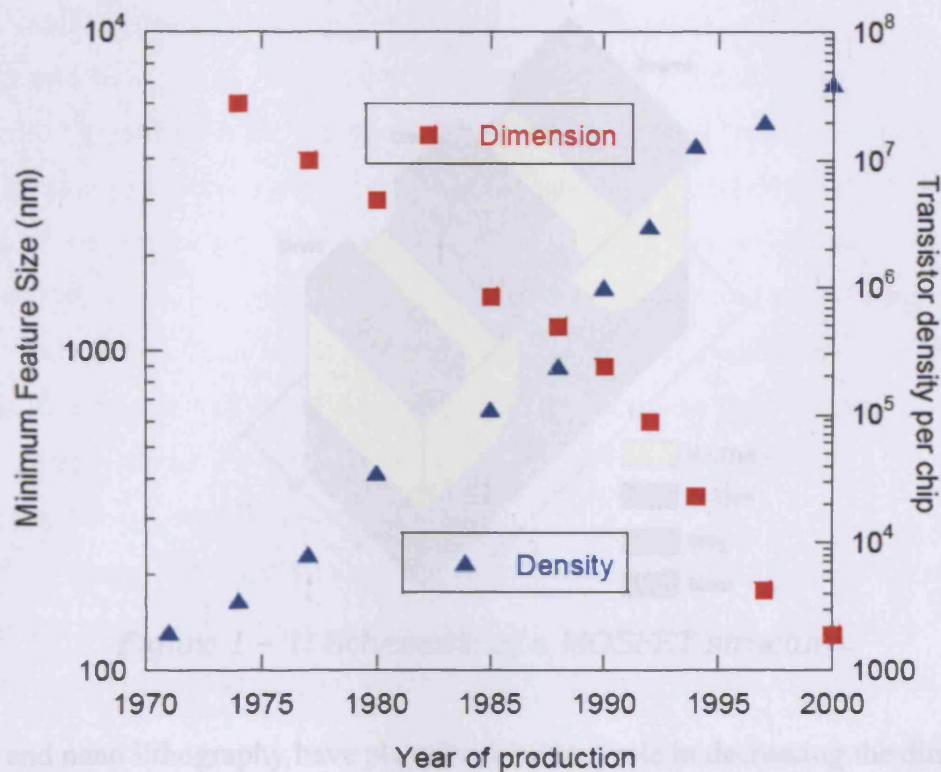
### Contents

|   |     |
|---|-----|
| 1.1 Introducing the main driving force of the semiconductor industry.....                                     | 1-  |
| 1.2 The Lithographic Process.....   | 4-  |
| 1.3 Next Generation Lithography Technologies.....   | 7-  |
| 1.3.1 Electron Beam Lithography.....  | 10- |
| 1.3.2 Electron Beam Resists.....  | 10- |
| 1.4 Motivation and Objectives.....  | 14- |
| 1.4.1 Synthesis and characterization of a PMMA based nanocomposite I-line optical photomask technologies..... | 15- |
| 1.4.2 Self assembled nanoparticle film for direct I-line nanolithography applications.....                    | 17- |
| 1.5 References.....   | 18- |

### 1.1 Introducing the main driving force of the Semiconductor Industry

In 1958, Jack Kilby and Robert Noyce invented the integrated circuit (IC). Electrical circuits could perform logical functions of great complexity by the high integration of active and passive devices such as transistors, resistors and capacitors in a semiconductor wafer. In 1965 it was observed by Gordon E. Moore that the number of integrated devices (transistors) approximately doubled every two years, which has

been known as 'Moore's Law' [1]. This law has driven the semiconductor industry to maintain this observation by the miniaturization of devices for the increased device density per unit area. Figure 1 – 0 shows the relationship of critical device dimensions and transistor density in the Intel microprocessor [2]. The transistor density has increased by approximately five orders of magnitude where as the physical dimensions of the devices have been reduced from approximately 20 $\mu\text{m}$  to the deep sub- $\mu\text{m}$  regime. Furthermore, in the past years the total manufacturing cost of an integrated circuit has essentially remained constant as the next generation devices have adopted similar production methods.



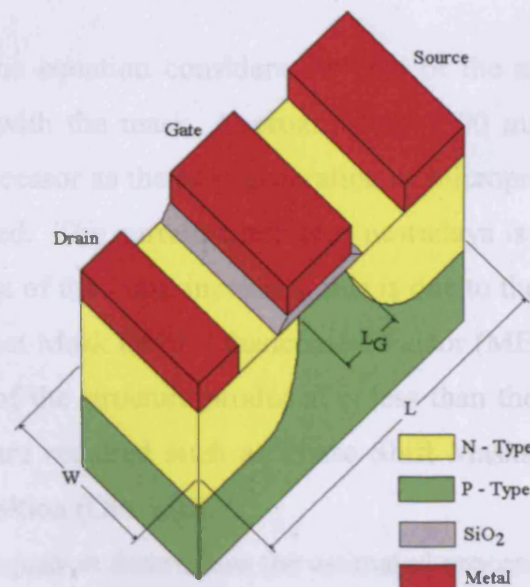
*Figure 1 – 0: The relationship between the minimum feature size and the density of transistors in an integrated circuit from [2].*

Since the early 1970's microprocessors have progressed from 4-bit integrated circuits to 64-bit integrated circuits found in computers today. Not only have microprocessors made a leap forward but memory has also advanced from a capacity of approximately 1 Kbit in the early 1970's to the 100's Gbit dynamic random access memories (DRAM) seen today.

The main component of an integrated circuit is a metal oxide semiconductor field effect transistor (MOSFET). The direct impact of the tremendous miniaturization of



MOSFETs is that their performance is enhanced. This is due to the scaling factors associated with the physical dimensions of the device, substrate doping and swing voltages. These factors directly enhance the speed, reduce power dissipation and give a reduction in the power delay product [3]. As these scaling factors enhance the overall performance of the integrated circuit, the cost per functionality is decreased as more and more MOSFET's are manufactured into a single integrated circuit. The structure of the MOSFET seen in figure 1 – 1 has not been modified but the dimensions of the MOSFET have decreased. This has been achieved by reducing the physical dimensions of the width and length.



*Figure 1 – 1: Schematic of a MOSFET structure.*

Micro and nano lithography have played a dominant role in decreasing the dimensions of MOSFET devices, this has been made possible by photolithography. Since the 1970's, lithography has progressed from the micron scale into the nanometre scale.

The economics of the semiconductor industry is the sole driving force behind the improvement in lithography and Moore's Law. This entails that the performance is improved while the costs associated to lithography must remain constant. Lithography is possibly the most critical of the processing steps as about half of the capital equipment cost for a wafer fab is in lithography.

For calculating the lithography costs many models exist. The critical issues of the lithography process can be calculated by this approximation given by equation 1 – 0 [4].

$$Cost/Level = \frac{Tool}{Throughput} + \frac{Mask}{Usage} + Process \quad (1 - 0)$$

When calculating the cost for printing a circuit level on a wafer, there are three main providers. These are the costs that are associated to the method of exposure, mask, and the processing costs.

The first term approximates the relation of the tool costs are obtained by taking the time that the exposure tool is used (labour, depreciation, space, etc.) and dividing it by the time taken to print those wafers – the throughput. This has motivated equipment manufacturers to produce tools with high throughput as this has been the main factor in lithography costs.

The second term in the equation considers the cost of the mask by the number of wafers to be printed with the mask. Approximately 1500 masks are needed, when fabricating a microprocessor as the next generation of microprocessor dimensions are decreased and improved. The current trend seen nowadays is that each mask is used less and less as the cost of the mask increases; this is due to the rapid design revisions [4]. It has been seen that Mask Error Enhancement Factor (MEEF) becomes larger, as minimum dimension of the structure produced is less than the exposure wavelength. Mask enhancements are required such as Phase Shift Masks (PSM) [5] or Optical Proximity effect Correction (OPC) [6].

The third term in the equation determines the estimated process costs this includes the cost of the resist development and its purpose. These days, the process cost is small compared to the tool and mask terms, because it is based on a single – layer resist process.

## **1.2 The Lithographic Process**

For the production of semiconductor devices, patterning is required by selecting areas so that subsequent microelectronics processing steps can be employed, such as etching, deposition, diffusion, or ion implantation for doping. This technique of producing patterns is referred to as ‘lithography’ which physically ‘masks off’ the desired and exposes undesired areas for future processing. Figure 1 – 1 depicts the fundamental steps that make up the lithography process



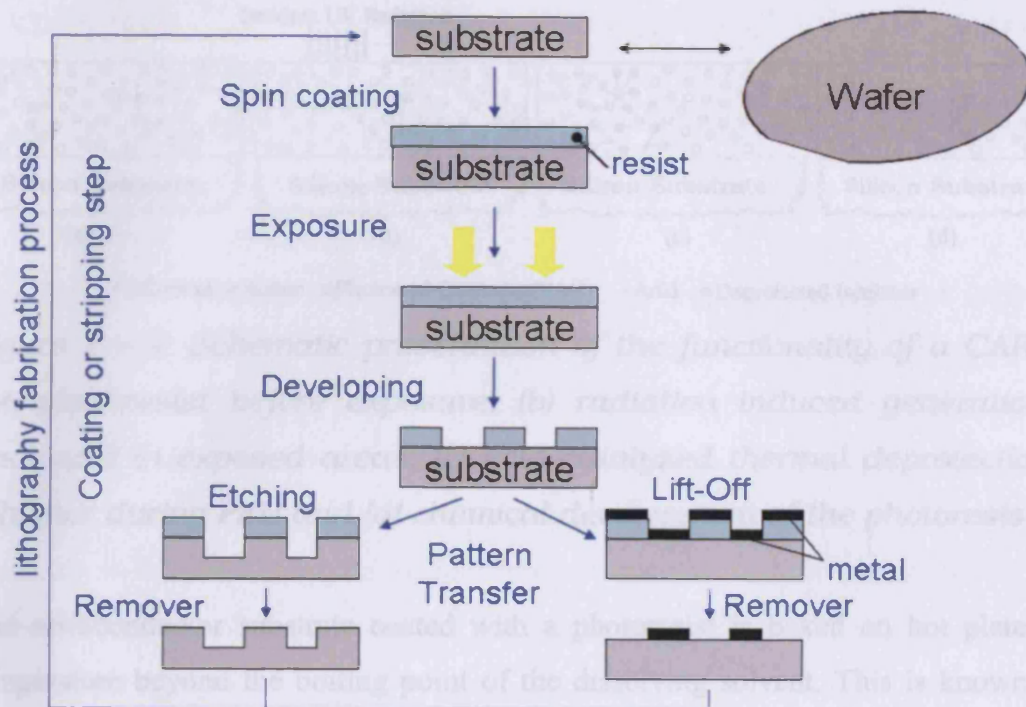
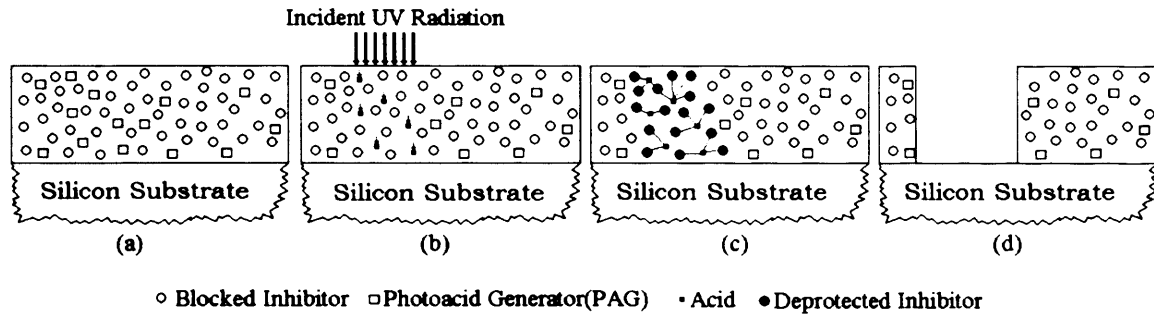


Figure 1 – 1: Schematic of the lithographic process.

The aim of the lithographic process is to protect selected areas of the device that are not to be modified during a particular processing step like an etching process, by coating that area. The criteria of the lithographic process is that it must be able to protect a selected area of a device by creating a pattern of the desired feature size by fabricating a material referred to as a 'photoresist'. The photoresist is 'photo' sensitive and it 'resists' chemical and physical attack of the underlying substrate. The photoresist material is an organic polymer that consists of dissolution inhibitors and photoacid generators. The dissolution inhibitors are extended chains of molecules that are not dissolved in a developer. When struck by a photon, the photoacid generators produce a photoacid. The photoresist during the different processing steps is illustrated by figure 1 – 2.

The first step in the lithography process is that the contaminants on the surface of Silicon must be removed by using cleaning chemicals, which may result in poor adhesion and form defects in the photoresist film. However, an adhesion promoter (such as HMDS) improves the adhesion between the photoresist and the substrate that the device will be made from. To produce a uniform coating of the photoresist on to a semiconductor substrate, it is spun from a solution that contains the polymer that is dissolved in a cast solvent.



*Figure 1 – 2: Schematic presentation of the functionality of a CAR. (a) the photoresist before exposure, (b) radiation induced generation of photoacid in exposed areas, (c) acid catalyzed thermal deprotection of inhibitor during PEB and (d) chemical development of the photoresist.*

The semiconductor substrate coated with a photoresist is baked on hot plate at a temperature beyond the boiling point of the dissolving solvent. This is known as a post bake (PB). This is done to evaporate the cast solvent from the photoresist film and to thermally anneal the residual stress that has occurred during spin coating. Figure 1 – 2a demonstrates that both the dissolution inhibitors and the photoacid generators (PAG) are uniformly distributed within the photoresist.

The pattern is produced using a Chrome mask. This contains the information that is to be transferred into a polymer in contact with the photoresist. The photoresist is irradiated with ultra violet (UV) radiation. This causes the exposed areas of the photoresist to under go a chemical transformation by altering the solubility of these areas of the photoresist in the developing stage. Figure 1 – 2b depicts the interaction of incident light on the central part of the resist and initializes the photoacid generators (PAG) to produce an acid. The acid catalyzed deprotection of inhibitor molecules is triggered from the supply of thermal energy during the PEB, which can be seen from figure 1 – 2c.

The solubility of the resist during the development process is deprotected by the long chains of the inhibitor molecules. It should be noted that in such a reaction the acid is not consumed. One acid molecule may add to the contribution to the deprotection of several inhibitor molecules.

The complexity of these processes in chemical amplified resist (CAR) systems is more complicated. To control the concentration of acid that is generated in certain parts of the resist, recent CARs also incorporate a quencher base into the fabrication of the resist. The mobility of the acid is increased when the source of thermal energy

is applied to the deprotection of inhibitor resulting in complex diffusion phenomena [7].

Figure 1 – 2d shows the concluding step in the processing sequence. This is the chemical development of the resist. The areas of the resist with a decreased concentration of inhibitor are dissolved.

The photoresist can have tone which is either positive or negative. The difference between these is that if the exposed areas are rinsed away when developed with a solvent it is said to have a positive tone or if the exposed areas remain it is negative tone. The developing step of the lithographic process transforms the image that was irradiated with ultra violet radiation into a three dimensional structure. The structures produced in the photoresist can be removed using a solvent called ‘Acetone’ or a dry etching technique that incorporates oxygen plasma without damaging the device structure underneath the photoresist.

### **1.3 Next Generation Lithography Technologies**

Figure 1 – 3 shows the historic improvements in IC lithography resolution. This has been driven by decreasing the wavelength of the illumination sources. The progression from G – line at 436nm to I – line at 365nm is illustrated by the figure. Mercury arc lamps filtered for different spectral lines were used as the illumination sources.

This was followed by a conversion to KrF at 248nm by the introduction of excimer laser sources in 2001, and in recent times, ArF at 193nm was introduced [4]. Before the establishment of KrF lithography, the minimum structures produced in practice were 250nm as this was larger than the wavelength. However, developments was made in 1999, when the 180nm technology was introduced as this was achieved when structures produced that were printed considerably below the wavelength (248nm) [4].

Production of features with geometry significantly smaller than the wavelength of the exposure radiation, where it depicts that the minimum feature size achievable becomes smaller than the exposure radiation, is known as sub wavelength lithography. This can be largely attributed to the improvements in the system optics and resist materials. With the blend of high – contrast imaging material and good process (exposure dose) control can reliably produce sub wavelength structures.

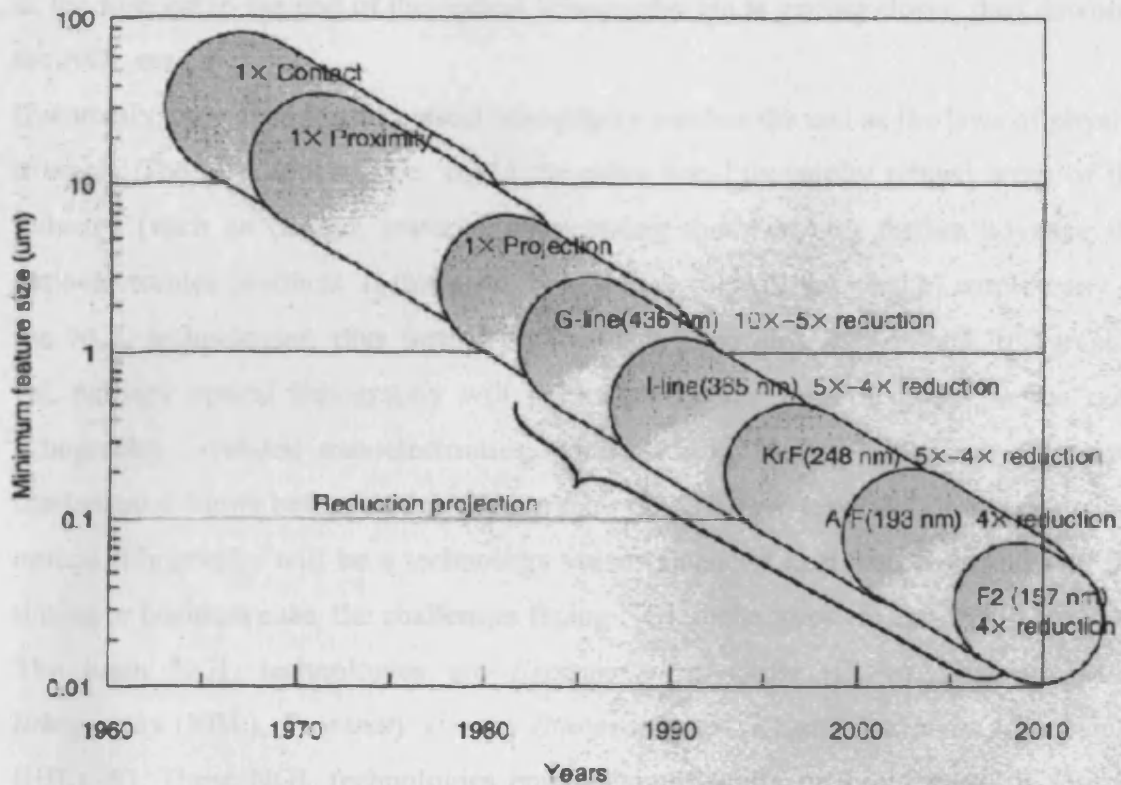


Figure 1 – 3, Trends of lithography technologies and exposure wavelengths from [8].

Even though the light intensity image has below full modulation for the nano structures, the best lithographic performance is seen at 193nm. However, unless the acid generators in the photoresist materials for the shorter wavelengths such as 157nm ( $F_2$  excimer) and beyond can be developed to a performance point equal to or better than that for 248nm materials, continued feature size shrinkage through wavelength reduction is not feasible.

Therefore, as seen in figure 1 – 3 the limits of photolithography draws nearer and nearer. New technologies must be developed to enable the transition from the dimensions of hundreds of nanometers to tens of nanometers; via 'NGL' or 'Next Generation Lithography'. The operation of any of the NGL technologies has been far later than predicted as the optical lithography techniques continue to provide the imaging needed at a justifiable cost. The operation of any of the NGL technologies has been far later than predicted as the optical lithography techniques continue to provide the imaging needed at a justifiable cost. This has surprised many and dashed the expectations of several technology ventures. However, for decades the industry's fascination with any NGL technology referring to it as 'the technology of the future',

as the forecast to the end of the optical lithography era is getting closer, thus dawning the NGL era.

Eventually, the capability of optical lithography reaches the end as the laws of physics triumph. The question will be 'could the other non-lithography related areas of the industry (such as design, materials, processing methods etc) further advance the nanoelectronics products. If this is so, then it may prevent the need to employ any of the NGL technologies, thus further extending the usefulness of optical lithography. Or, perhaps optical lithography will no longer be the limiting factor as the non-lithography – related nanoelectronics manufacturing factors will reach their own fundamental limits before optical lithography does. The assessment of the demise of optical lithography will be a technology versus financial decision. Regardless of the timing or business case, the challenges facing NGL techniques are enormous.

The main NGL technologies are *Extreme ultra violet* (EUV), *Electron beam lithography* (EBL), *Proximity x – ray lithography* (PXL) and *Ion beam lithography* (IBL) [8]. These NGL technologies employ significantly different types of sources from 13.5nm photons, 100KeV electrons, ~1nm photons and 75KeV ions respectively, for patterning wafers. The distinction between these technologies and optical technologies are the differences in mask materials and their overall architectures. New pattern transfer challenges must be faced as the exposure wavelengths are decreased. The transmission of the radiation requires equipment that is necessary to handle a vacuum for all the NGL methods. This will become more expensive and the high throughput that is seen for optical lithography will inevitably be decreased. Also new resists must be created by fabricating new photoacid generators that can be easily distributed uniformly throughout the material for the new wavelength. However, EBL and IBL, does not require the resist material to be photo sensitive as it is directly patterned by the electrons (this will be explained in the following section). The resists for the EBL technology are already developed to obtain features of sub 100nm.

### **1.3.1 Electron beam lithography**

Since the early 1970's it has been recognized that by accelerating a focused beam of electrons at the surface of a resist can produce a very high resolution pattern, where the wavelength of electrons are smaller than the photons of ultra violet radiation by more than three orders of magnitude [9]. Electrons are scanned across a resist surface. To write a pattern into the resist directly, a computer generated pattern file controls the electron beam by deflecting and turning the beam off and on according to the pixilated patterns and this directs the focused electron beam to exposure locations on the resist. By using high sensitivity resists and higher electron beam currents, the total write times can be reduced. Hence the throughput is increased.

Due to its high resolution and pattern replacement capabilities, projection based electron beam lithography is considered as a candidate for next generation lithography in semiconductor manufacturing. Moore's law can be continued by using electron beams for generating patterns in a resist for high device integration. Miniaturization of the integration circuit could be theoretically continued with electron beam lithography as the diameter of a focused electron beam is on the order of about 1nm [10]. The fabrication of critical level masks used in optical lithography has been the primary function of electron beam lithography. Production of high resolution masks is a low volume manufacturing process because the writing times are slow. Therefore, the throughput is less than optical lithography. However, this technique produces the highest pattern resolution. Due to its greater resolution, direct write electron beam technology will continue to be the method for manufacturing extremely high resolution products such as photomasks. With the development of projection electron beam lithography tools, the electron beam technology is progressing into semiconductor manufacturing laboratories. These tools may lead to the advancement for the fabrication of next generation semiconductor devices beyond the 65nm node [11].

### **1.2.2 Electron beam resists**

When the acceleration of incident electrons are driven into a solid, the energy associated with each travelling electron is transferred to the solid as the electron

collides into it. The interaction occurs by the process of elastic and inelastic collisions. During the collision and in between consecutive collision events the interaction of the energy transfer can occur. Between consecutive collisions, the electrons will become decelerated as they collide with the solid. The deceleration of the electron also known as stopping power of the solid depends upon the incident electron energy and density of atoms of the solid. During inelastic collisions with the atoms, secondary electrons can be generated when the energy is transferred to the solid. The electron trajectories produce a hidden image when the energy of the incident electrons is absorbed by the solid. This hidden image can be developed into a three dimensional structure.

The formation of the hidden image can be realized when high molecular weight polymers fragments into smaller chains this is known as the chain scission process. When the molecular weight distributions within the patterning resist are modified, a division between exposed and unexposed areas can be determined. The chain scission imaging is the classical approach for obtaining hidden images in resist, in electron beam lithography. The following section describes the mechanism of the creation of the hidden image obtained in conventional resists during electron beam exposure.

Electron beam resists that are classified as organic resists consist of carbon, oxygen, hydrogen, nitrogen and / or sulphur. These resists are typically polymeric materials that are soluble in casting solvents. Due to the casting solvents, the electron beam resist can be processed with ease. In electron beam lithography the most common polymers that are used are acrylates, sulfones, epoxies and chemically amplified resists.

Electron beam resists based on acrylates are the most widely used today due to the fact that they provide a high resolution, their ease of handling, and they have excellent film forming characteristics. A well known acrylate based resist is poly(methyl methacrylate) (PMMA), it has demonstrated very high resolution of 3nm at an accelerating voltage of 200kV [12].

To produce the high resolution seen in PMMA, high electron beam dosage is necessary due to the conversion of the polymer backbone structure. However, by combining PMMA with polymethacrylic acid (PMA) and polymethacrylic anhydride (PMAN) using a polymerization process has been verified that the sensitivity of PMMA can be improved [13]. This improvement has increased the sensitivity of the resist from 50 to  $20\mu\text{C}/\text{cm}^2$  at 20kV incident electron energy with insertion of



20mol% PMA in PMMA. In addition, the sensitivity has been increased to  $10\mu\text{C}/\text{cm}^2$  by the configuration of a terpolymer consisting of PMMA – PMA – PMAN at a molar composition of 70 – 15 – 15 [14].

By altering the development process and developer concentration, the sensitivity of the acrylate polymers can be improved. As an alternative to the standard development process, it has been shown that the use of an ultrasonic agitation improves the sensitivity from  $\sim 7.5\mu\text{C}/\text{cm}^2$  to  $\sim 6.4\mu\text{C}/\text{cm}^2$  for a  $\sim 200\text{nm}$  thick film exposed at 20kV [15]. The ultrasonic agitation process generates a dissolution front with a larger difference that can distinguish between exposed and unexposed areas. It has been shown that by optimizing the developer concentration, the sensitivity is improved. To generate patterns in the development process the solvent Methylisobutylketone (MIBK) is typically utilized for developing PMMA. But incorporating a combination of solvents such as MIBK and isopropanol (IPA) has been discovered to improve the sensitivity by  $300\mu\text{C}/\text{cm}^2$  and  $250\mu\text{C}/\text{cm}^2$  for 50kV exposures of the micron thick film with a 1:3 MIBK:IPA developers, respectively [16].

Polysulfones imaging materials have been produced as electron beam resists. Polysulfones are alternating copolymers of a small chain olefin and sulfur dioxide. Since the 1930's, these polymers have been investigated due to their low material cost [17]. These materials became popular for the purpose of the semiconductor industry after Brown and O'Donnell established that when poly(butene-1-sulfone) is exposed to electron beams they broke down with high efficiency. During the electron beam exposure the polysulfone polymers experienced the main chain scission at the carbon sulfur bond. The radical depolymerizes into smaller fragments and developed unstable species.

A novolac matrix supports the polysulfone material. The loading of solids in the novolac matrix ranges between 10 and 20 wt%. The operation of the polysulfone acts as a sensitizer in the unexposed and exposed areas and as a dissolution inhibitor. By several orders of magnitude the novolac/polysulfone mix reduces the dissolution of the polymer matrix in an aqueous base that is similar to the loading of diazonaphthoquinone (DNQ) in the classical DNQ – Novolac optical resist system. The polysulfone system offers high sensitivity when irradiated by an electron beam. This is advantageous as rapid depolymerization of the carbon sulfur bond occurs. It has been reported that the sensitivity of a 500nm polysulfone – novolac polymer film was of the order of  $5\mu\text{C}/\text{cm}^2$  at 10keV accelerating voltage.



The employment of epoxies as an organic electron beam resist has been another attempt. In the semiconductor industry these polymers were the first high performing negative tone electron beam resists [17]. Structural alteration of this polymer when induced by an electron beam was based on a ring opening event of the epoxy moiety. Upon electron beam exposure an initiating species is generated, these species can be an anion, anion radical, cation or cation radical. A ring opening event is caused by an initiator reaction with the sterically stressed epoxy moiety. Cross linking can occur between two species by the linear epoxy oxygen anion, which can also react with another epoxy moiety leading to additional ring opening events. When the oxygen anion is reduced with a radical species the chain propagation is terminated. Very high sensitivities can be obtained using epoxy based polymers as a single radiation induced initiator event that results in frequent cross linking events.

Investigations of the three primary copolymers of epoxy based resists have been implemented. The first consists of a copolymer of glycidyl ether and novolac, this is known as SU-8 [18], the second involves a copolymer of glycidyl methacrylate and ethyl acrylate, in the industry this is called COP and the third has been demonstrated using a copolymer of novolac and ethyl acrylate this is called ETPR [19]. A 700 nm thick ETPR film has been verified to have a sensitivity and contrast of  $2\mu\text{C}/\text{cm}^2$  and 3.2, respectively at 25keV accelerating voltage. High line edge roughness and resist swelling have been seen when patterning lines. The SU-8 resist can be employed as a negative tone optical resist or for achieving high aspect ratio structures greater than 20:1, the primary employment for it is producing micro-electromechanical systems (MEMS). However, it has shown to be a high resolution electron beam resist, as nanometer sized structures have been created.

Using SU-8 with a thickness of 150nm, minimum line widths of 30 nm with exposure doses of approximately  $100\mu\text{C}/\text{cm}^2$  at 40 keV accelerating voltage have been obtained [20]. Even though the epoxy based resists such as SU-8 demonstrate that they can achieve a resolution below 50nm they have a problem, the crosslinking reaction propagates into undesired areas away from the exposed areas resulting in low contrast.

As electron beam lithography is a serial process, it has been fraught by low throughput. However, throughput can be improved by employing a method to use highly sensitive resists that require short dwell times for imaging. These are known as chemically amplified resists (CAR) and contain extensions of the standard

poly(hydroxystyrene) polymer that is blocked with t-butylcarbonyl with an sulfonium acid generator. Just like the photoresist seen in §1.1, these resists have electron acid generator (EAG) molecules uniformly dispersed throughout the resist, a reaction is produced when energy is transferred from electrons instead of photons into the resist and releases an acid. After exposure and acid generation, the reaction is catalyzed between the acid molecule and the protecting group integrated in the polymer backbone when a post exposure thermal bake step is performed. The solubility of the polymer changes the deprotection reaction in an aqueous base whereas the reaction within the polymer matrix can be further amplified by the regenerating the acid.

There are several varieties of chemically amplified resists existing with different base polymers, electron acid generators, and dissolution inhibitors as key components in the polymer matrix. It has been shown that high resolution with low exposure doses below  $100\mu\text{C}/\text{cm}^2$  can be obtained by these CARs. This is a major advantage for achieving high throughput and makes them an ideal candidate as resist platforms when projection electron beam lithography tools are delivered for manufacturing.

### **1.3 Motivation and Objectives**

The motivation behind this thesis was to find a reproducible method to create photomasks to extend Moore's law using conventional equipment while maintaining a high throughput just like the semiconductor industry has done over the past decades. This method must incorporate a viable technology that is cost effective and using methods that are well known and exercised.

The aim was to produce a feasible technology that fabricates sub 100nm features that can be generated from I-line wavelength using top down and bottom up approaches. The top-down approach adopts methods that use externally controlled tools to cut, mill and shape materials into a shape that is required. In contrast, the bottom-up approach causes single-molecule components to automatically arrange themselves into useful structures by manipulation of the chemical properties of single molecules. This approach employs concepts of molecular self-assembly and should be able to produce a mask in parallel and much cheaper than top-down methods, but could potentially be overwhelmed as the size and complexity of the assembly increases.

Both of these studies and investigations are the focal theme of this thesis and are described in more detail in the following paragraphs. Furthermore, this thesis points

the way to find a unified method to produce an optical photomask to potentially extend Moore's law into the next decade.

### **1.3.1 Synthesis and characterization of a PMMA based nanocomposite I-line optical photomask technologies**

For the top-down method, electron beam resists have demonstrated superior potential for high resolution patterning below 50 nm. This ability to pattern high resolution structures provides unique opportunities in development of nanometer sized semiconductor ICs to extend Moore's law, but this method is incredibly slow. However, the throughput may be increased, if the electron beam resist can be manipulated by incorporating oxide nanoparticles into an electron beam resist to change its optical properties to absorb the optical radiation so that it behaves as an optical photomask. The benefit of this is that the pattern is directly written once and can be used again and again in a conventional mask aligner, therefore, increasing the throughput.

In the past decade, researchers have concentrated their efforts on exploiting the properties of nanoparticle materials to design new polymer nanocomposite materials [20 – 22]. The over all conclusions that have been drawn demonstrate that the mechanical and optical properties have been improved when compared to their microparticle materials [20, 21, 23 – 26]. The nanoparticles provide high energy surfaces due to their high surface to volume ratio; which is due to their size. From the nanoparticle high interfacial energy, an anticipated result is an enhanced bonding between the polymer matrix and the embedded nanoparticles [21, 26]. This has been predicted by the polymer composite theory and shows that the mechanical properties are improved [21 26, 27]. Therefore, it has been hypothesized that by loading an e-beam resist with nanoparticles enhances the mechanical properties during development process, this may lead to the reduction of collapsed features patterned in the resist. However, if the e-beam resist is over loaded with nanoparticles, then the lithographic properties of the resist may be affected by the degradation of the resolution of the written features, therefore, the quantity of nanoparticles embedded into the e-beam resist is critical. Researchers have investigated the effects of loading fullerenes and silica nanoparticles in resists [28, 29]. It has been demonstrated with

the ZEP520/Silica nanocomposite system that the features had a resolution of 50 nm while retaining the high sensitivity property of the polymer [30] while a twenty fold reduction in etch rate in an ashing oxygen plasma resulted with a 7 wt% loading of silica nanoparticles in ZEP520. As the electron beam lithography (EBL) system can produce patterns with a high resolution, it is suspected that this method of fabricating optical photomask may be adapted for EUV and x – ray lithography to create sub 100nm features in a photoresist. However, for the purpose of this thesis the objectives of chapters 2 – 5 demonstrates this technology at the I-line wavelengths producing sub 10 $\mu$ m features. Chapter 2 looks at the synthesis of the nanocomposite resist thin film by demonstrating the difficulties and techniques required when dispersing the nanoparticles into the polymer matrix. It also shows the optical effects when the nanoparticles are introduced into the PMMA e-beam resist. Chapter 3 characterizes the nanocomposite resist by directly writing a pattern into the nanocomposite resist. It characterizes the minimum feature size that can be achieved, without collapsing. It was speculated that the nanoparticles would prevent the e-beam resist from collapsing by minimizing the proximity effect. As a figure of merit, the smallest features possible with PMMA is approximately 100nm when the resist thickness is 400nm, hence the aspect ratio is 4:1. It is hypothesized that as the nanoparticles are embedded into the polymer matrix the aspect ratio would increase. This is important as the higher the aspect ratio then the more nanoparticles can be embedded in the PMMA resist thin film. Hence, more of the I-line radiation can be absorbed. Chapter 4 investigated the effects of the nanoparticles embedded in the PMMA that was seen in the previous chapter. This was achieved by modelling the nanocomposite resist using the Monte Carlo method.

Chapter 5 characterizes the nanocomposite resist as an optical photomask at I-line wavelengths for high through put. The idea here was to prove the concept by testing the nanocomposite photomask at I-line wavelength, but it could be adapted at EUV or X – ray wavelengths to achieve even smaller features.

### **1.3.2 Self assembled nanoparticle film for direct i-line nanolithography applications**

Researchers have been able to achieve the fabrication of nano features by developing a near-field optical nanolithography system [31]. This technology operates by localizing the surface plasmon waves on a periodic structured planar metallic optical photomask. Surface plasmons are surface electromagnetic waves that propagate in a direction parallel to the metal/dielectric interface. By altering the configuration of a metal's surface into a periodic structure, an EM wave can be coupled to the surface of that metal structure by oscillating at its surface. This is due to that they are sensitive to the change in structure. More detail of this phenomena, is given in chapter 6.

Conventional UV light sources can be used while the resolution of the periodic structure can be considerably increased. Results of simulations have shown that one and two dimensional periodical structures of 40 – 100nm features can be patterned using the surface plasmon technology [32]. These studies have shown that by using a silver photomask, the lithographic resolution at 34nm is achievable by using I-line wavelengths [31].

The silver photomask was fabricated by depositing a 3 nm titanium film using an *E*-beam evaporator on a quartz substrate. The silver film was deposited to a thickness of 40 nm on the titanium layer. The periodic structure that was fabricated in silver film was a hole array, this was produced by a focused ion-beam (FIB) miller. Subsequently, to act as a spacer an Omni-Coat was spun on the patterned silver film to a thickness of 15 nm. A negative near UV photoresist called SU-8 was directly spun on the top of the spacer layer and polymerized on the mask. The SU-8 was exposed using the silver photomask and the light source was a filtered mercury lamp with a radiation peak at 365 nm. From this experiment the researchers demonstrated the technique of nanolithography, as the developed features in the SU-8 photoresist had a resolution at 60nm [32]. Clearly this was far beyond the resolution limit of conventional lithography using I-line wavelength.

The objectives of chapter 6 in this thesis, was to develop a plasmonic optical photomask, which produces nano features in a photoresist called S1813 using an I – line radiative source. As the surface plasmon silver photomask was produced with a Focused Ion beam miller. This equipment is very expensive and not all laboratories

can afford it. Therefore, the plasmonic photomask will be fabricated from a bottom up technique. This technique utilizes a self assembly method that assembles silver nanoparticles into a periodic hexagonally closely packed (hcp) array structure. This allows the excitation of surface plasmons on the silver nanoparticle hcp array to enhance the optical (365nm) transmission through these structures with shorter wavelengths compared to the excitation radiation wavelength, which produces sub wavelength features (below 100nm) in the S1813 photoresist. This photomask technology does not need IBL system to perform its operation and nor does it need a vacuum system for EUV or X – ray lithography. Therefore, the costs are greatly reduced when compared to that of an IBL system.

## **1.4 References**

- 1) G. E. Moore, ‘Cramming more components onto intergrated circuits’, Electronics, 38 (80 (1965).
- 2) R. Mahajan, R. Nair, V. Wakharkar, J. Swan, G. Vandentop, ‘Emerging directions for packaging technologies’, Intel Technology Journal, 6 (2), pp. 62 – 75, (2002).
- 3) H. Bakoglu, ‘Circuit, interconnection and packaging for VLSI’, Addison – Wesley publication Company, Reading MA, (1990).
- 4) M. D. Levenson, D. S. Goodman, S. Lindsey, P. W. Bayer, H. A. E. Santini, ‘The phase – shifting mask II: imaging simulations & sub micrometer resist exposure’, IEEE. Trans. Electron. Dev, vol ED – 30 (6) pp. 753 – 763 (1984).
- 5) L. R. Harriot, ‘Limits of Lithography’, Proc. IEEE, Vol 89, issue 3 pp 366 – 374 (2001).
- 6) F. M. Schellenberg, H. Zhang, J. Morrow, ‘Sub wavelength lithography using OPC’, SEMATECH J111 project OPC validation, Proc SPIE, 3334, pp. 892 – 911 (1998).
- 7) A. Erdmann, W. Henke, S. Robertson, E. Richter, B. Tollkuhn, W. Hoppe, ‘Comparison of simulation approaches for chemically amplified resist’, Proc SPIE, 4404, 99 (2001).
- 8) S. Rizvi, ‘Handbook of photomask manufacturing technology’, CRC Taylor & Francis group pp 139 (2005).

- 9) W. R. Livesay, R. B. Fritz, 'Electron image projection systems for microcircuit lithography' IEEE Trans. Electron. Dev., ED – 19 (5), pp. 647 – 651, (1972).
- 10) C. Vieu, F. Carcenac, A. Pepin, Y. Chen, M. Mejias, A. Lebib, L. Manin – Ferlazzo, L. Couraud, H. Launois, 'Electron beam lithography: resolution limits and applications', Appl. Surf. Sci., 164 (1), pp 111 – 177 (2000).
- 11) Semiconductor Industry Association, International technology Roadmap for Semiconductors, (1999).
- 12) D. R. S. Cumming, S. Thomas, J. M. R. Weaver, S. P. Beaumont, '3nm NiCr wires made using electron beam lithography and PMMA resist', Micro. Eng., 30, pp. 423 – 425, (1996).
- 13) M. Hatzakis, 'PMMA copolymers as high sensitivity electron resists', J. Vac. Sci. Technol. B., 16 (60), pp. 1984 – 88, (1980).
- 14) W. Moreau, D. Merrit, W. Moyer, M. Hatzakis, D. Johnson, L. Pederson, 'Speed enhancement of PMMA resist', J. Vac. Sci. Technol B., 16 (6) pp. 1989 – 1981 (1980).
- 15) J. M. Ryan, A. C. F. Hoole, A. N. Broers, 'A study of the effect of ultra sonic agitation during development of poly(methylmethacrylate) for ultra high resolution electron beam lithography', J. Vac. Sci. Technol. B., 13 (6), pp. 3035 – 3039, (1995).
- 16) S. Yasin, D. G. Hasko, H. Ahmed, 'Comparison of MIBK/IPA and Water/IPA as PMMA developers for electron beam nanolithography', Micro. Eng. 61 – 62, pp. 745 – 753, (2002).
- 17) L. F. Thompson, C. G. Wilson M. J. Bowden, 'Introduction to microlithography', ACS professional reference book.
- 18) M. Aktary, M. O. Jensen, K. L. Westra, M. J. Brett, M. R. Freeman, 'High – resolution pattern generation using the epoxy novolak SU-8 2000 resist by electron beam lithography', J. Vac. Sci. Technol. B., 21 (40), pp. L5 – L7, (2003).
- 19) K. G. Chiong, S. wind, D. Seeger, 'Exposure characteristics of high resolution negative resists', J. Vac. Sci. Technol. B., 8 (6), pp. 1447 – 1483, (199).
- 20) S. Su, D. D. Jiang, C. A. Wilkie, 'Methacrylate modified clays and their polystyrene and poly(methyl methacrylate) nanocomposites', Poly. Adv. Technol., 15, pp 225 – 231 (2004).

- 21) D. Gersappe, 'Molecular mechanisms of failure in polymer nanocomposites', *Phys. Rev. Lett.*, 89 (50 pp. 058301 – 1 – 4 (2002).
- 22) J. H. Park, S. C. Jana, 'The relationship between Nano and micro structures and mechanical properties in PMMA – Epoxy – Nanoclay Composites', *Polymer*, 44, pp. 2091 – 2100 (2003).
- 23) E. Reynaud, T. Jouen, C. Gauthier, G. Vigier, J. Varlet, 'Nanofillers in polymeric matrix: A study on silica reinforced PA6', *Polymer* 42, pp. 8759 – 68, (2001).
- 24) M. Alexandre, P. Dubois, 'Polymer layered silicate nanocomposites: preparation, properties and uses of a new class of materials', *Material Sci. Eng.*, 28, pp 1 – 63, (2000).
- 25) M. Z. Rong, M. Q. Pan, S. L. Pan, B. Lehmann, K. Friedrich, 'Analysis of the interfacial interactions in polypropylene/Silica nanocomposites', *Polymer International*, 53, pp 176 – 83, (2003).
- 26) S. W. Shang, J. W. Williams, K. –J. M. Soderholm, 'How the work of adhesion affects the mechanical properties of silica – filled polymer composites', (1994).
- 27) Y. Brechet, J. –Y. Y. Cavaille, E. Chabert, L. Chazeau, R. Dendievel, L. Flandin, C. Gauthier, 'Polymer based nanocomposites: effects of filler – filler and filler – matrix interactions', *Adv. Eng. Materials*, 3 (8), pp. 571 – 77 (2001).
- 28) L. Merhari, K. E. Gonsalves, Y. Hu, W. He, W. S. Huang, M. Angelopoulos, W. H. Bruenger, C. Dzionk, M. Tokler, 'Nanocomposite resist systems for next generation lithography', *Micr. Eng.* 63 (4) pp. 391 – 403, (2002).
- 29) T. Ishii, H. Nozawa, T. Tamamura, A. Ozawa, 'C60 – incorporated nanocomposites resist system for practical nanometer pattern fabrication', *J. Vac. Sci. Technol. B.*, 15 (60), pp. 2570 – 74 (1997).
- 30) Y. Hu, H. Wu, K. Gonsalves, L. Merhari, 'Nanocomposite resists for electron beam lithography', *Micro. Eng.*, 56 (3 – 40), pp. 289 – 94, (2001).
- 31) S. Lewis, R. Wheeler – Jones, V. Haynes, R. M. Perks, 'High density self assembled nanoparticle film with temperature-controllable interparticle spacing for deep sub-wavelength nanolithography using localized surface plasmon modes on planar silver nanoparticle tunable grating', *Micro. Eng.*, 85 (2) pp. 486 – 491 (2008).



- 32) W. Srituravanich, S. Durant, H. Lee, C. Sun, X. Zhang, 'Deep subwavelength nanolithography using localized surface plasmon modes on planar silver mask', J. Vac. Sci. Technol. B 23 (6) (2005).

## CHAPTER

# 2

### **Development of a novel nanocomposite resist for high resolution e – beam lithography next generation mask production**

#### **Contents**

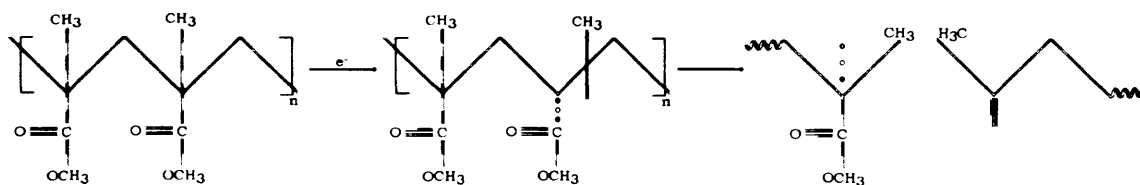
|  |      |
|--|------|
| 2.1 Introduction.....  | -23- |
| 2.2 Experimental Details.....  | -24- |
| 2.2.1 Synthesis of nanocomposite resist.....                             | -24- |
| 2.2.2 Characterisation of the oxide nanoparticle surface properties..... | -26- |
| 2.2.3 The photolithography experiment.....                               | -27- |
| 2.3 Results.....   | -27- |
| 2.3.1 Optical Properties of PMMA based Electron Beam Resist.....         | -27- |
| 2.3.2 Surface Analysis.....  | -31- |
| 2.3.3 Optical properties of the Nanocomposite Resist.....                | -42- |
| 2.4 Discussion.....  | -45- |
| 2.5 Summary.....   | -47- |
| 2.6 References.....  | -48- |

## 2.1. Introduction

In the early photomask lithography applications, non chemically amplified resists (NCA) were used. The advancement of these resist materials have provided high resolution, sensitivity, etch resistance and chemical stability for photomask fabrication.

Positive tone e-beam resists are based on polymer chain scission. Upon exposure, the molecular weight of the polymer chains, are reduced by the chain scission process. This increases the solubility of the polymer in organic solvents.

Figure 2 – 1 illustrates the chain scission process with a resist called poly(methyl methacrylate) (PMMA). The chain scission process occurs when the radiolysis of the main chain carbon to carbonyl bond is initiated.



*Figure 2 – 1: E-beam chain scission process with PMMA e-beam resist.*

When the resulting tertiary radical is rapidly rearranged, the main chain is cleaved and produces unstable products. Therefore, the dissolution rate is increased in an organic developer like Methyl – IsoButyl Ketone (MIBK) : IsoPropAnol (IPA) (1:3 ratio) as the main – chain scissions reduces molecular weight of the PMMA [1]. To increase the resist contrast, the dissolution properties of PMMA as a function of exposed energy and polymer molecule have been studied [2].

The e-beam system such as the JEOL 6300 SEM or a dedicated e-beam writer (e.g. Raith50) can produce nanometre scale structures, hence, in order to direct write a nano scale pattern, the time period is a matter of hours [3], whereas photolithography at I – line wavelengths (365nm) can be achieved in a matter of seconds. Therefore, to mass produce nano scale structures, there is a reluctance in the semiconductor industry to use these e-beam tools other than just for research. However, if the nano scale pattern was written once and then reused as a photo mask at I – line wavelengths or below, then volume production time scales would be greatly reduced.

PMMA was chosen because of its e-beam properties and that it does not change the processing method in the laboratory, this is very important as it is the most widely e-beam resist today. However, it was found (see in §2.3.1) that the PMMA polymer

possesses poor optical properties when used as an optical photomask. However, it is possible to modify the PMMA optical properties. One method of achieving this was by introducing inorganic nanoparticles into the PMMA polymer matrix; creating a hybrid material by dispersing nanoparticles such as  $\text{Al}_2\text{O}_3$  and  $\text{TiO}_2$  into a polymer matrix (15 – 25nm  $\text{Al}_2\text{O}_3$  and  $\text{TiO}_2$  nanoparticles were readily available at the start of this investigation and used throughout. Early experiments showed that their dispersal in PMMA could sufficiently attenuate I – line radiation. The addition of such nanoparticles has a considerable effect on various properties of the resist in application; characterisation of these changes is the subject of the next chapters [4–6]. The first requirement for the nanocomposite hybrid material is that the dispersion of the nanoparticles must be well defined. It has often proved difficult to form a stable dispersion of nanoparticles in polymer matrices, as the particles tend to aggregate. The strength of the inter-nanoparticle coupling in liquids typically ranges from weak van der Waals interactions to relatively strong hydrogen bonding. The geometrical form of the nanoparticle aggregates can be string, network, or globular structures. The surface nature of these oxide nanoparticle species is hydrophilic due to the existence of hydroxyl groups [7]. In order to embed the nanoparticle in a hydrophobic polymer matrix, the interfacial interaction must be improved. The modification of the nanoparticle surface with different interfacial methods has been applied. Such techniques incorporated the encapsulation of the nanoparticle by an emulsion polymerization in PMMA [8].

The physical properties like electrical, mechanical and optical properties are enhanced by these materials. The type of nanoparticle species can affect the polymer nanocomposite properties, these are determined by its nanostructure, size, shape and concentration and by interactions with the polymer matrix [9, 10]. These hybrid materials allow the designer to manipulate their physical and chemical properties, are processed with ease and have a relatively low cost [11 – 13]. The goal here was that the nanoparticles must not effect or interfere with the process of e-beam lithography in order to fabricate a nano structured photomask.

In this study, the surface of  $\text{TiO}_2$  and  $\text{Al}_2\text{O}_3$  nanoparticles was modified so that the nanoparticles could be embedded into the PMMA. The influence of the nanopaticles can affect the PMMA polymer matrix so that the optical responses can be tailored to suit the application. This chapter describes a protocol for the synthesis of a reasonably

high concentration of polymer matrix compatible homogeneous  $\text{TiO}_2/\text{PMMA}$  and  $\text{Al}_2\text{O}_3/\text{PMMA}$  thin films.

## **2.2 Experimental Details**

### **2.2.1 Synthesis**

The PMMA based nanocomposites used in this investigation were synthesized by the homogeneous dispersal of 15 – 25nm diameter  $\text{Al}_2\text{O}_3$  and  $\text{TiO}_2$  nanoparticles (obtained from MKnano.com 99.999%) in PMMA. Samples were prepared by dissolving the PMMA (obtained from Sigma – Aldrich) in the solvent Anisole (obtained from Sigma – Aldrich 97%). Anisole is used to dissolve the PMMA by unravelling the PMMA particles into molecular chains. The PMMA was used ‘as is’. The ratio of PMMA was kept at 7% to ensure the thickness of the film was approximately 400nm (when spun at 4000rpm). This was achieved by dissolving 350mg of PMMA (for each molecular weight of 950K and 96K) in 4.65g of Anisole (the samples of PMMA 96K 7% will be studied in the next chapter). The Anisole was filtered under vacuum (assisted by a rotary pump) through a 25nm millipore membrane filter (obtained from Fisher Scientific). The PMMA/Anisole samples were shaken using an IKA rotary/gyrative shaker for 96 hours, in order for the Anisole to dissolve the PMMA. This produced a PMMA based electron beam resist. This was repeated sixteen times for the molecular weight of 950K and four times for the molecular weight of 96K.

The  $\text{Al}_2\text{O}_3$  and  $\text{TiO}_2$  nanoparticles were filtered through the 25nm membrane filter, to obtain 15 – 25nm nanoparticles. This was achieved by measuring the  $\text{Al}_2\text{O}_3$  nanoparticles by weight to 550mg, which were directly dispersed into 500ml of the deionized water. This was repeated using the  $\text{TiO}_2$  nanoparticles. The deionized water / nanoparticles were filtered under vacuum. Next, both of the deionized water / nanoparticles samples were put in a desiccator to absorb the deionized water leaving behind the appropriate nanoparticles. The  $\text{Al}_2\text{O}_3$  nanoparticles were then weighed out twice to 50, 100, 150, 200mg to achieve two sets of samples. The first set was directly dispersed into PMMA / Anisole and the second set was dispersed into 0.5ml of Methanol (obtained from Sigma – Aldrich 99.9%) to produce a nanoparticle

suspension before being mixed with the PMMA / Anisole. The  $\text{Al}_2\text{O}_3$  nanoparticles that were suspended in Methanol were introduced to the PMMA / Anisole solution and were shaken for 36 hours to achieve a good nanoparticle suspension in the PMMA mix. This was repeated for the  $\text{TiO}_2$  nanoparticles.

These PMMA based nanocomposite resists were then spun onto 24mm×24mm borosilicate glass microscope slide cover slips. The cover slips were sputter coated with a 7nm layer of gold (Au) to obtain additional adhesion qualities necessary to bond the nanocomposite resist to the borosilicate substrate. The nanocomposite resist was spun using a spin cycle of 4000rpm for 45 seconds which was followed by a soft-bake at 180°C for 3 minutes, as this allows the Anisole and Methanol to evaporate. The overall thickness of the resist films after spinning was dependent on the density of  $\text{Al}_2\text{O}_3$  nanoparticles incorporated into the polymer matrix.

### **2.2.2 Characterisation of Nanoparticle surface properties**

To test the stability of the dispersion of the oxide nanoparticles when embedded in the PMMA polymer matrix, the surface of the oxide nanoparticles were characterized by encapsulating them in various solvents. In this experiment the oxide nanoparticle species was substituted by the borosilicate glass, this was done because the oxide nanoparticles are also hydrophilic. The borosilicate glass surface was treated to produce a hydrophilic surface state as this will give more of a surface contact contrast when the various solvents are dropped on the borosilicate glass surface. The surface of the borosilicate glass was arranged to be hydrophilic first, this was prepared by using  $\text{NH}_4\text{OH}:\text{H}_2\text{O}_2:\text{H}_2\text{O}$  solution in a ratio of 1:1:5. The hydrophilic solution was then brought to the boiling point condition for 15mins. This produced a hydrophilic surface state on the borosilicate glass. The various solvents were dropped on to the borosilicate glass using a pipette. The contact angle was then measured.

The optical transmission of the nanocomposite films were measured over the wavelength range of  $\lambda=200\text{nm} - 1000\text{nm}$  using a Jenway spectrophotometer. The surface measurements were achieved using an atomic force microscope (AFM) in the non contact mode, and the zeta potential measurement was performed using a zeta

sizer nanoseries which incorporated a laser Doppler velocimeter in combination with phase analysis light scattering technique called M3 – PALS.

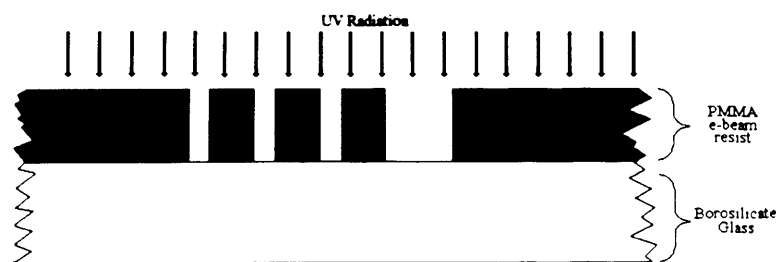
### **2.2.3 The Photolithography experiment**

The photolithography experiment consisted of Microposit S1813 positive photoresist (obtained from Shipley.com) was exposed using the nanocomposite photo – masks. This was spun onto silicon substrates at 6000rpm for 45 seconds yielding a photoresist thickness of typically 1.1 $\mu$ m. The nanocomposite masks were then placed in contact with the S1813 photoresist and a typical 6 second UV exposure using a Karl Suss mask aligner. The sample was then developed for 40 seconds at room temperature, if the temperature had increased then the S1813 photoresist will develop at a much faster rate. The developer solution was 2401 developer and water in the ratio 1:10.

## **2.3 Results and Discussion**

### **2.3.1 Optical properties of electron beam resist**

For a photolithography optical mask there must be an optical contrast between the Borosilicate glass and the patterned PMMA e-beam resist, the structure is illustrated in figure 2 – 2.

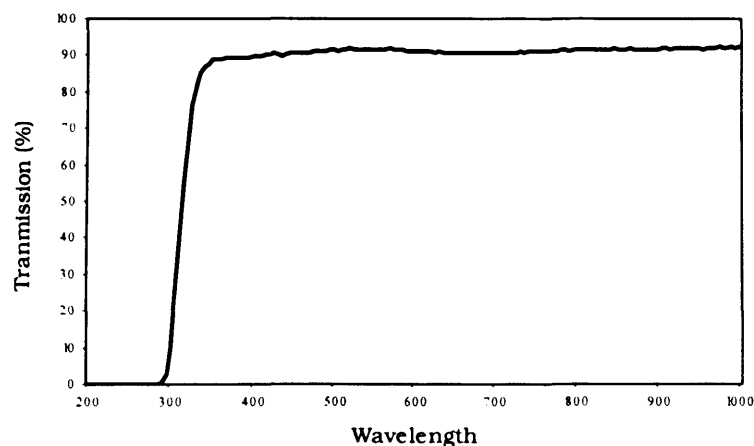


*Figure 2 – 2: The opaque structure of the photomask for I – line applications.*

The optical transmission spectra for the borosilicate glass, is shown in figure 2 – 3. The borosilicate glass is a good substrate for the photomask as it was observed that it was approximately 90% transparent in the UV – IR radiation wavelengths, as this will

provide a good optical transmission from about 300nm and above. Therefore, transmitting the features incorporated in the PMMA e-beam resist by the e-beam equipment (Raith50 and JEOL SEM system) through the borosilicate medium. As the borosilicate glass provides a good optical substrate for the photomask, the PMMA must be put directly on the surface of the glass substrate. However, as the borosilicate glass has a poor electrical conductivity ( $8.0\Omega/\text{cm}$ ) [14], a gold thin film was sputtered coated on the surface of the borosilicate glass, this served two purposes.

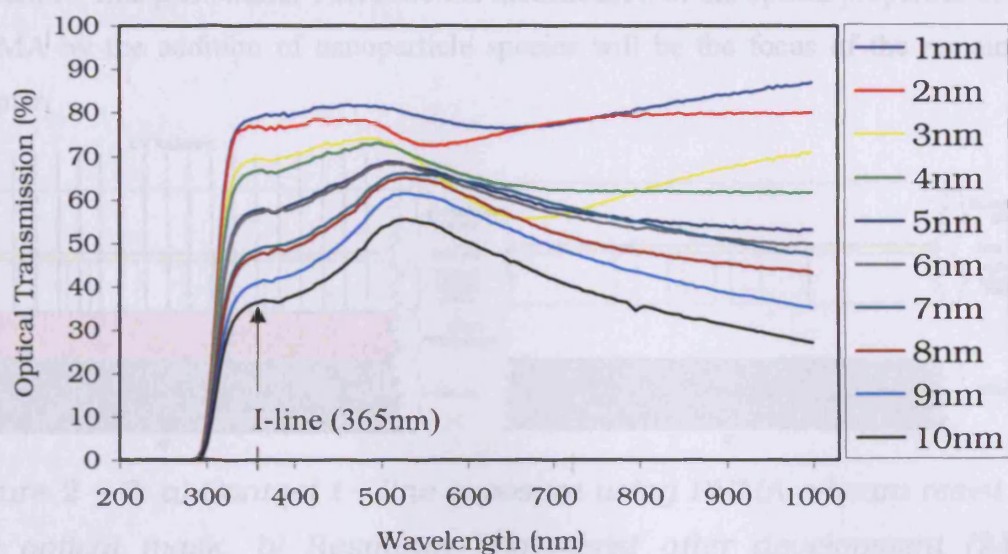
- I) The Au thin film is a good conductor ( $2.2\text{m}\Omega/\text{cm}$ ) [15], this is necessary as the PMMA needs to be patterned using an e-beam direct writer (Raith50 or JEOL SEM). If the Au thin film was not present the e-beam resist would experience charging effects and consequently would not be able to pattern the desirable features into the PMMA resist.
- II) It was found that the PMMA could not bond with the borosilicate glass. This is due to the surface chemistry of both the PMMA e-beam resist and the borosilicate glass, where the former is hydrophobic and the latter is hydrophilic. The borosilicate glass was sputter coated with an Au thin film to provide an adhesion quality so that the PMMA could bond with the cover slip.



*Figure 2 – 3: Optical transmission spectra of Borosilicate glass.*

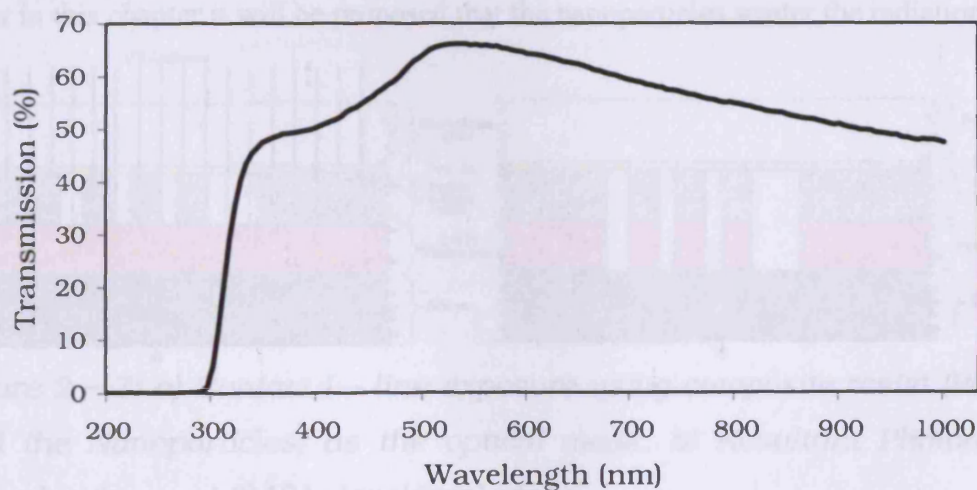
Figure 2 – 4 shows that as the Au thin film thickness increases, from 1nm to 10nm the optical transmission decreases, from approximately 80% to 37% at the I – line wavelength, this was due to the free electron absorption in the Gold film.





*Figure 2 – 4: Optical transmission spectra of the various thickness of Au on Borosilicate glass.*

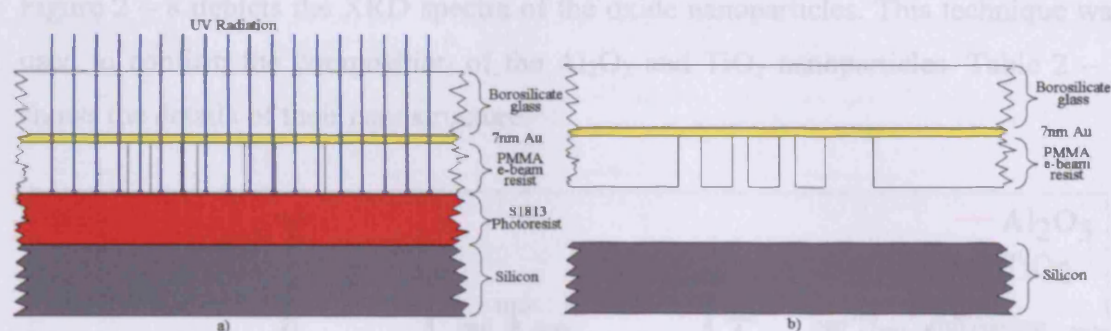
The PMMA e-beam resist was spun on the surface of the Au with a thickness of 7nm at 6000rpm and had an overall thickness of approximately 400nm. Figure 2 – 5 shows that the PMMA is 90% transparent. Clearly, PMMA alone will not provide sufficient I – line contrast for photolithography.



*Figure 2 – 5: Optical transmission of PMMA (thickness of 800nm) on 7nm of Au thin film.*

Thus, the patterned features in the e-beam resist will not be transmitted into another photoresist as demonstrated by figure 2 – 6. The pattern cannot be used as a reusable

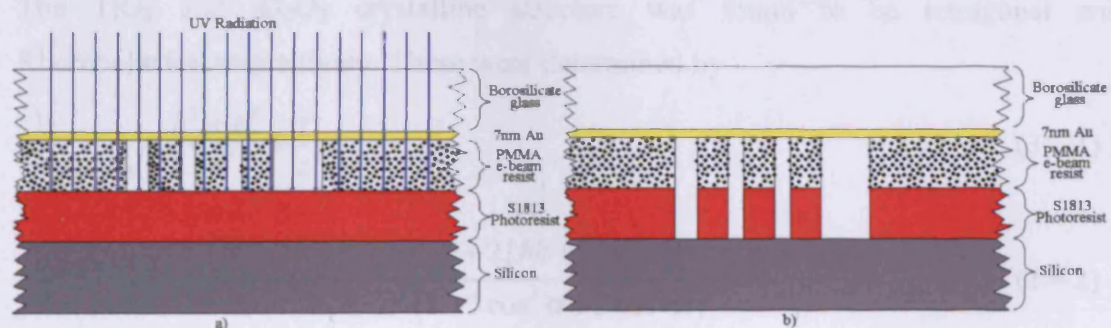
e-beam I – line photomask. Therefore the modification of the optical properties of the PMMA by the addition of nanoparticle species will be the focus of the remaining chapter.



*Figure 2 – 6: a) Contact I – line exposure using PMMA e-beam resist as the optical mask, b) Resultant Photoresist after development (2401 developer) stage.*

Hence, the optical properties of the PMMA e-beam resist must be modified to produce a contrast between the borosilicate glass substrate and the PMMA polymer itself.

One method of achieving this is to add nanoparticles in to the PMMA polymer matrix. These nanoparticles will absorb the I – line radiation as illustrated in figure 2 – 7 (later in this chapter it will be proposed that the nanoparticles scatter the radiation).



*Figure 2 – 7: a) Contact I – line exposure using composite resist (PMMA and the Nanoparticles) as the optical mask, b) Resultant Photoresist after development (2401 developer) stage.*

The inclusion of the nanoparticles should have minimal effect in the PMMA electron beam resist properties; also by increasing its opacity to I-line wavelength, there should be sufficient light/dark contrast for pattern transfer into S1813 photoresist. This is demonstrated in the subsequent sections.



### 2.3.2 Surface Analysis

Figure 2 – 8 depicts the XRD spectra of the oxide nanoparticles. This technique was used to confirm the composition of the  $\text{Al}_2\text{O}_3$  and  $\text{TiO}_2$  nanoparticles. Table 2 – 1 shows the details of their nanostructure.

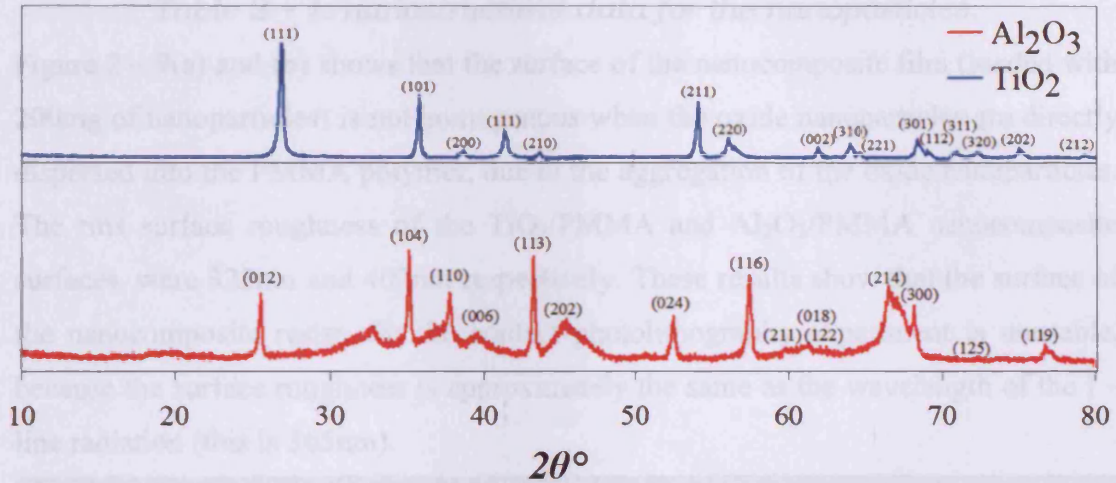


Figure 2 – 8: XRD diffraction patterns of the polycrystalline structure of the nanoparticle species (XRD patterns were obtained with the assistance of F. Pooley).

The  $\text{TiO}_2$  and  $\text{Al}_2\text{O}_3$  crystalline structure was found to be tetragonal and Rhombohedral respectively. These were determined by

$$\frac{1}{d^2_{\text{tetragonal}}} = \frac{h^2 + k^2}{a^2} + \frac{l^2}{c^2} \quad (3-1)$$

$$\frac{1}{d^2_{\text{Rhombohedral}}} = \frac{(h^2 + k^2 + l^2) \sin^2 \alpha + 2(hk + kl + hl)(\cos^2 \alpha - \cos \alpha)}{a^2(1 - 3\cos^2 \alpha + 2\cos^3 \alpha)} \quad (3-2)$$

where the interplanar angles were found by

$$\cos \phi_{\text{tetragonal}} = \frac{\frac{h_1 h_2 + k_1 k_2}{a^2} + \frac{l_1 l_2}{c^2}}{\sqrt{\left(\frac{h_1^2 + k_1^2}{a^2} + \frac{l_1^2}{c^2}\right) \left(\frac{h_2^2 + k_2^2}{a^2} + \frac{l_2^2}{c^2}\right)}} \quad (3-3)$$

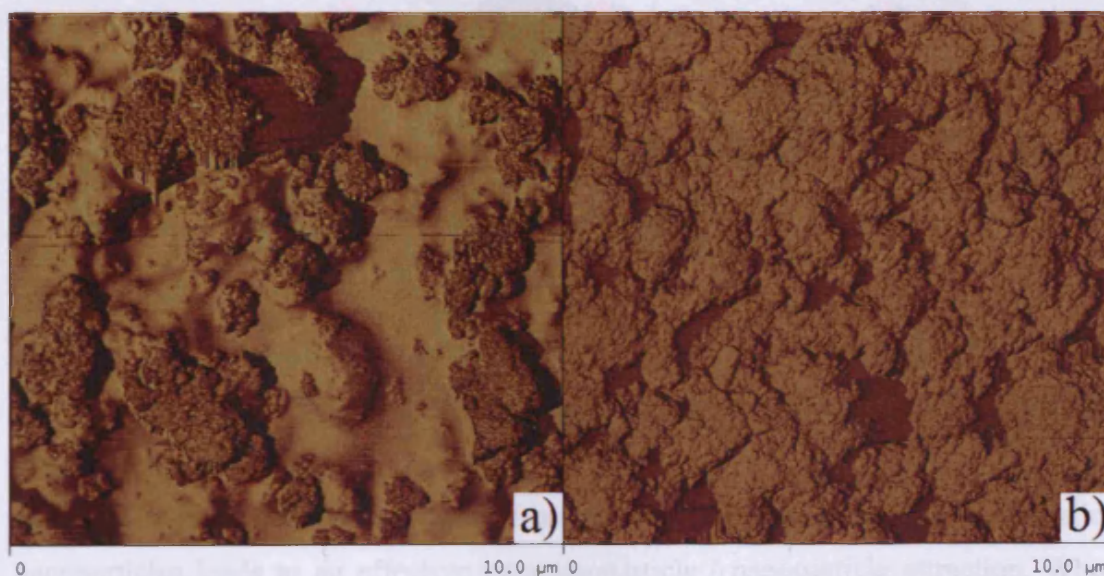
$$\cos \phi_{\text{Rhombohedral}} = \frac{a^4 d_1 d_2}{V^2} \left[ \sin^2 \alpha (h_1 h_2 + k_1 k_2 + l_1 l_2) + (\cos^2 \alpha - \cos \alpha) (k_1 l_2 + k_2 l_1 + l_1 h_2 + l_2 h_1 + h_1 k_2 + h_2 k_1) \right] \quad (3-4)$$

In order for the photolithography experiment to be preformed, the surface of the nanocomposite resist must come into contact with a photoresist that is to be patterned. Therefore, the flatness of the surface must be quantified.

| Nanoparticles                  | Nanostructure | Lattice constant (Å) |       |         |
|--------------------------------|---------------|----------------------|-------|---------|
|                                |               | a                    | b     | c       |
| Al <sub>2</sub> O <sub>3</sub> | Rhombohedral  | 4.764                | 4.764 | 13.0091 |
| TiO <sub>2</sub>               | Tetragonal    | 4.58                 | 4.85  | 2.95    |

*Table 2 – 1: nanostructural data for the nanoparticles.*

Figure 2 – 9(a) and (b) shows that the surface of the nanocomposite film (loaded with 200mg of nanoparticles) is not homogenous when the oxide nanoparticles are directly dispersed into the PMMA polymer, due to the aggregation of the oxide nanoparticles. The rms surface roughness of the TiO<sub>2</sub>/PMMA and Al<sub>2</sub>O<sub>3</sub>/PMMA nanocomposite surfaces, were 322nm and 402nm respectively. These results show that the surface of the nanocomposite resist, for the contact photolithography experiment is unusable, because the surface roughness is approximately the same as the wavelength of the I – line radiation (this is 365nm).



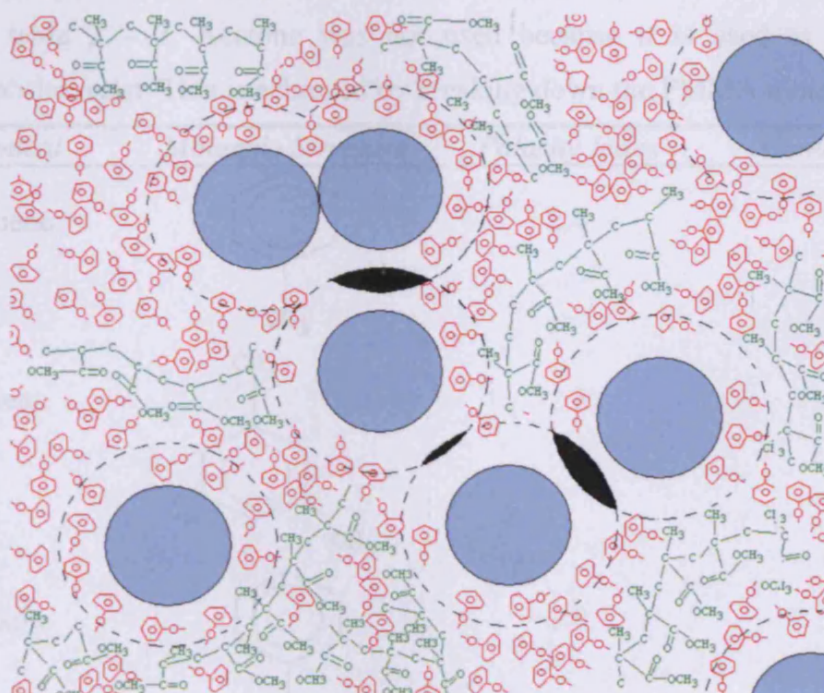
*Figure 2 – 9: a) AFM image of 200mg of TiO<sub>2</sub> nanoparticles embedded directly into 1g of PMMA, b) AFM image of 200mg of Al<sub>2</sub>O<sub>3</sub> nanoparticles embedded directly into 1g of PMMA.*

Therefore, the photolithographic pattern will not transfer correctly from the nanocomposite resist to S1813 photoresist, as the I – line radiation will escape from the pattern edges of the nanocomposite resist photomask. The pattern in the photoresist will result in poor edge definition. Therefore, the nanocomposite resist



surface must be improved, but first a good level of understanding of the mechanism of nanoparticle/nanoparticle interactions must be gained in order to achieve this goal.

Both oxide nanoparticle species are of same charge type and are suspected to unbalance the depletion effects and osmotic pressures in the PMMA. The ‘depletion’ effect is illustrated in figure 2 – 10. It depicts the three tier system consisting of the PMMA molecule chain indicated in green. To achieve its chain form, the PMMA is dissolved in a solvent called Anisole, shown in red. It can be seen from the illustration that each nanoparticle is surrounded by a depletion zone; this is the region immediately next to each nanoparticle surface (indicated by the dotted line).



*Figure 2 – 10: Schematic representation of the nanoparticle /Anisole /PMMA system.*

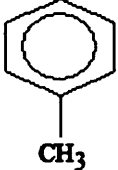
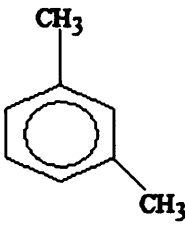

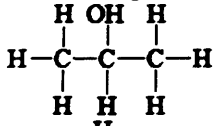
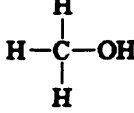
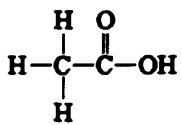
The depletion of polymer molecules from the region between closely spaced oxide nanoparticles leads to an effective internanoparticle / nanoparticle attraction. When the nanoparticles are introduced into the PMMA polymer matrix, the unbalanced osmotic pressure pushes the nanoparticles towards one another. Hence nanoparticle aggregation occurs when the depletion regions of two nanoparticles intersect, indicated by the black area in the depletion zones in figure 2 – 10.

To improve the homogenous surface quality of the nanocomposite resist, the nanoparticle surface must be encapsulated, so that they will repel each other and then be homogeneously dispersed into the PMMA. Therefore, the nanoparticles must be suspended in a solvent first. It is this parameter that governs its viscosity and overall

thickness. When the quantity of the solvent is increased, the PMMA thickness decreases as it becomes less viscous.

An experiment was preformed to determine the behaviour of the solvents used to suspend the oxide nanoparticles. This was achieved by substituting the oxide nanoparticles with borosilicate glass, as the oxide nanoparticles are also hydrophilic. The borosilicate glass surface was treated to produce a hydrophilic surface state (the method of achieving this is given in §2.2.1), as this will give more of a surface contact contrast when the various solvents are dropped on the borosilicate glass surface.

The solvents were chosen by their polarity index property, the value for these can be found in table 2 – 2. Acetone was not used because it is used to remove the nanocomposite resist. This is achieved by breaking down the PMMA molecular chain.

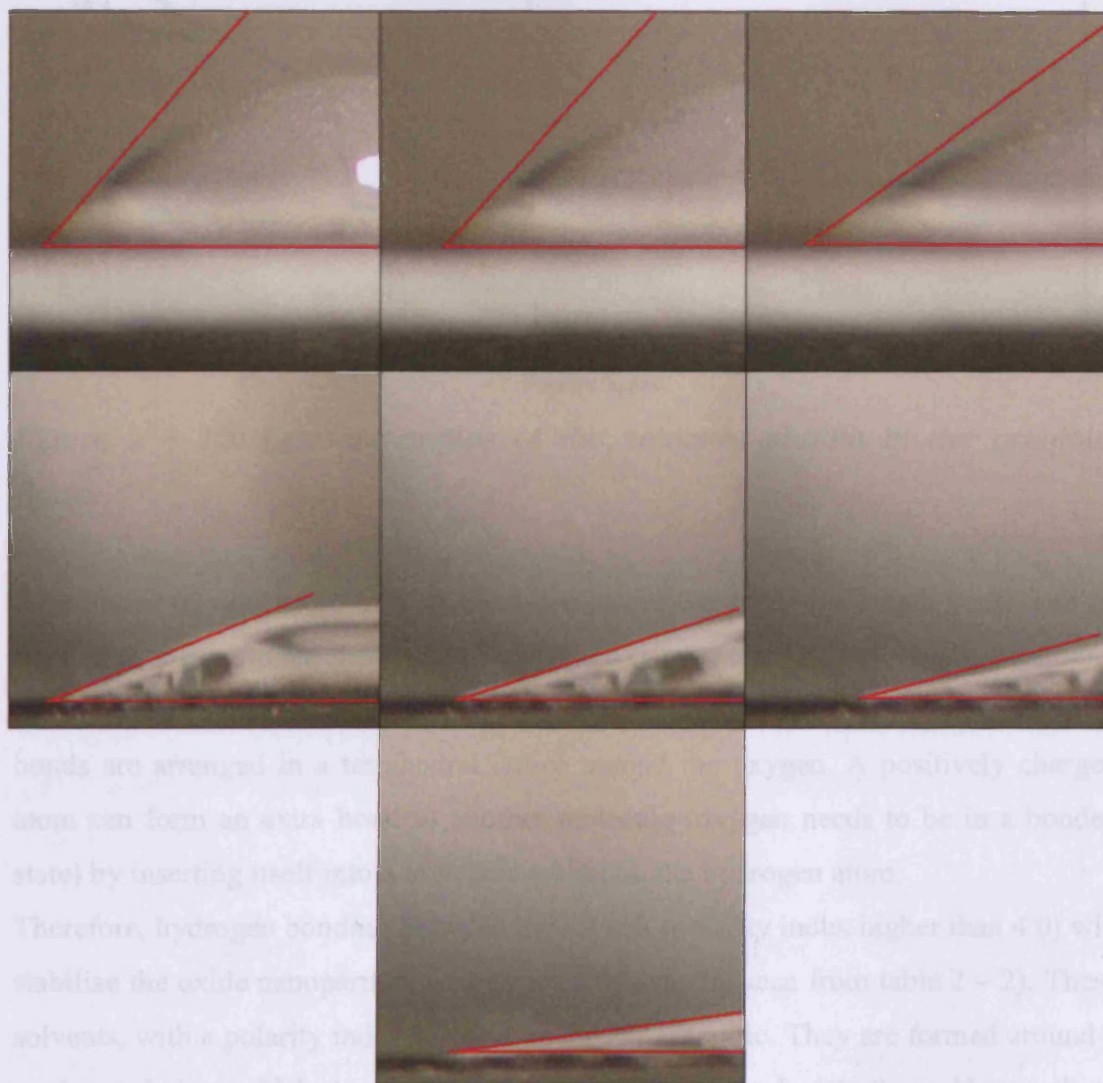
| <i>Chemical</i> | <i>Molecule Structure</i>   | <i>Polarity Index</i> | <i>Contact Angle</i> |
|-----------------|---|-----------------------|----------------------|
| Toluene         |   | 2.4                   | 52°                  |
| Xylene          |  | 2.5                   | 49°                  |
| Anisole         |  | 3.8                   | 38.5°                |
| IPA             |  | 4.0                   | 22°                  |
| Methanol        |  | 5.1                   | 18°                  |
| Acetic Acid     |  | 6.2                   | 14°                  |
| Water           | H <sub>2</sub> O  | 9                     | 7.5°                 |

*Table 2 – 2: Solvent molecules and contact angle.*

Each solvent was dropped onto the surface of the borosilicate glass and the contact angle was measured. Due to the nature of the borosilicate glass the solvents with a

relatively high polarity index should have a smaller contact angle due to the molecule having OH groups attached to them. This will lead to hydrogen bonding. The results are shown in figure 2 – 11a – g and in table 2 – 2.

Table 2 – 2 shows the molecule structure of each solvent incorporated in this experiment. It is evident that the solvents (Toluene, Xylene and Anisole) with a polarity index less than four do not have any OH groups, where as the solvents with a higher polarity index more than four have OH groups attached to the molecule, hence, hydrogen bonding can take place.



*Figure 2 – 11: Contact angles of solvents. a) Toluene, b) Xylene, c) Anisole, d) IPA, e) Methanol, f) Acetic Acid, g) Water.*

It was found from the data shown in figure 2 – 12 that in order to achieve a stable oxide nanoparticle suspension, solvent molecules with a polarity index higher than 4.0

are extremely hydrophilic. Due to the nature of these solvents, hydroxyl (OH) groups are attached to them. These OH groups have a dipole, where the hydrogen atom is bonded with oxygen atom. The electron field is directed from the hydrogen atom towards the oxygen atom pulling electrons away from the hydrogen atom on to the oxygen atom. This causes the hydrogen to have a slight positive charge and the oxygen will become negatively charged.

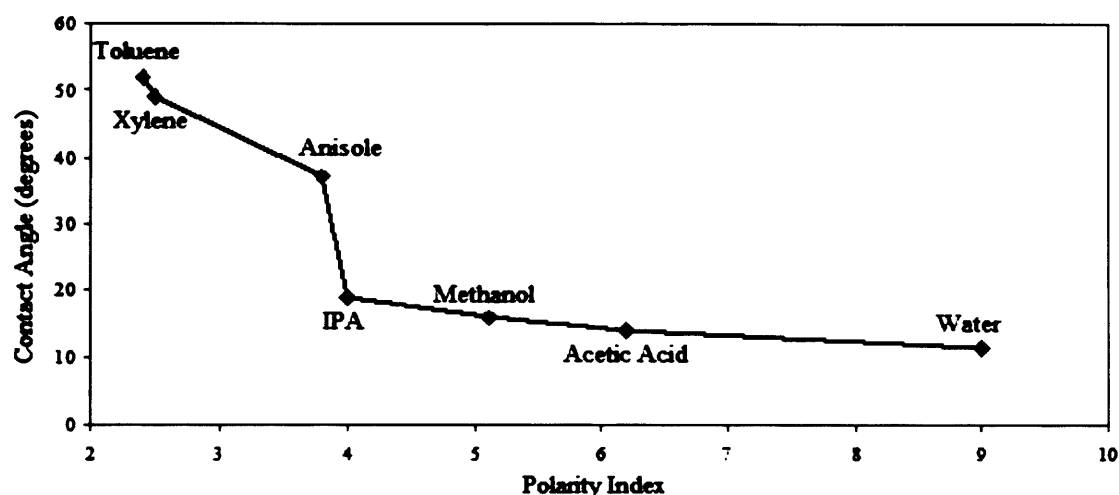


Figure 2 – 12: Contact angles of the solvents shown in the previous figure.

A saturated oxygen atom in a covalent compound can have two single bonds and be bonded to other atoms; these use two of the oxygen outer shell electrons. The other four electrons form a couple of lone pair orbitals, these lone pairs and the single two bonds are arranged in a tetrahedral lattice around the oxygen. A positively charged atom can form an extra bond to another molecule (oxygen needs to be in a bonded state) by inserting itself into a lone pair orbital on the hydrogen atom.

Therefore, hydrogen bonding between the solvent (polarity index higher than 4.0) will stabilize the oxide nanoparticle suspension, (this can be seen from table 2 – 2). These solvents, with a polarity index lower than 4.0 are aromatic. They are formed around a conjugated ring, which do not have hydroxyl groups attached to them. Hence, these substances can not bond to the oxide nanoparticle via the hydrogen bonding method, as illustrated in figure 2 – 13.

Figure 2 – 13 gives a schematic representation of the mechanism of hydrogen bonding, it can be seen clearly that the Toluene, Xylene and Anisole can not suspend the oxide nanoparticle because there is no mechanism for hydrogen bonding process



to occur. This is because the dipoles within the hydroxyl groups are not present. There is no barrier immediate to the surface of the oxide nanoparticle. This allows the depletion region around each oxide nanoparticle to intersect and therefore, the oxide nanoparticles are attracted to one another, hence, aggregation.

Aggregation of the oxide nanoparticles can be greatly reduced by using IPA, Methanol, Acetic Acid or Water. Figure 2 – 13 illustrates that these molecules have hydroxyl groups within them and are attracted to the hydroxyl groups at the surface of the oxide nanoparticles via their dipoles. Therefore, they surround the oxide nanoparticle and form a physical barrier with a thickness greater than that of the depletion region which would surround the oxide nanoparticle (see figure 2 – 10). The depletion regions of the oxide nanoparticles can never intersect. Hence, the oxide nanoparticle attraction is greatly reduced and the oxide nanoparticle suspension is stable.

Due to the fact that the PMMA polymer is dissolved in Anisole, it is evident that when the oxide nanoparticles were dispersed directly into the PMMA polymer matrix / Anisole system they would never be suspended homogeneously.

The obvious choice of solvent to start with was Methanol and Toluene, the reason for this choice was that Methanol was more hydrophilic (contact angle of 18°) than Toluene (contact angle of 52°) as they are on opposite sides of the index polarity spectrum, with 5.1 and 2.4 respectively. IPA was not used because it was too close to the less hydrophilic / more hydrophilic definition edge (see figure 2 – 12). As the homogeneous dispersal of the oxide nanoparticles could be ambiguous, the performance of the suspension was measured using the zeta potential measurement system.

The test cases were 200mg of the oxide nanoparticles directly suspended in Methanol and Toluene. Figure 2 – 14 shows, that Methanol suspends the oxide nanoparticles successfully. The zeta potential values were 31.9mV and 39.2mV with  $\text{TiO}_2$  and  $\text{Al}_2\text{O}_3$  respectively. The zeta potential peaks shows that  $\text{TiO}_2$  and  $\text{Al}_2\text{O}_3$  nanoparticles are both positive. From the data here, it can be seen that the nanoparticles suspended in Methanol have a zeta potential above the 30mV threshold, therefore the nanoparticle suspension was stable, however, both nanoparticle species suspended in

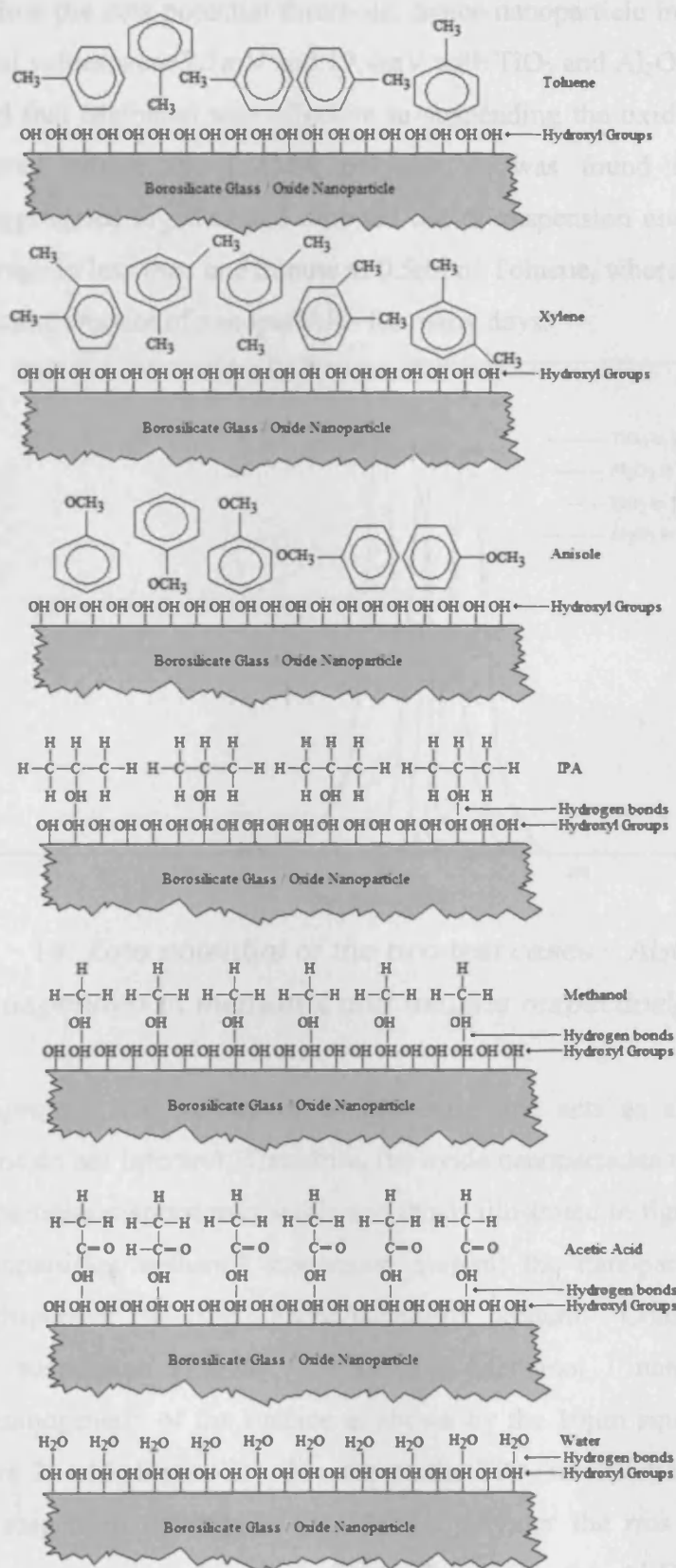
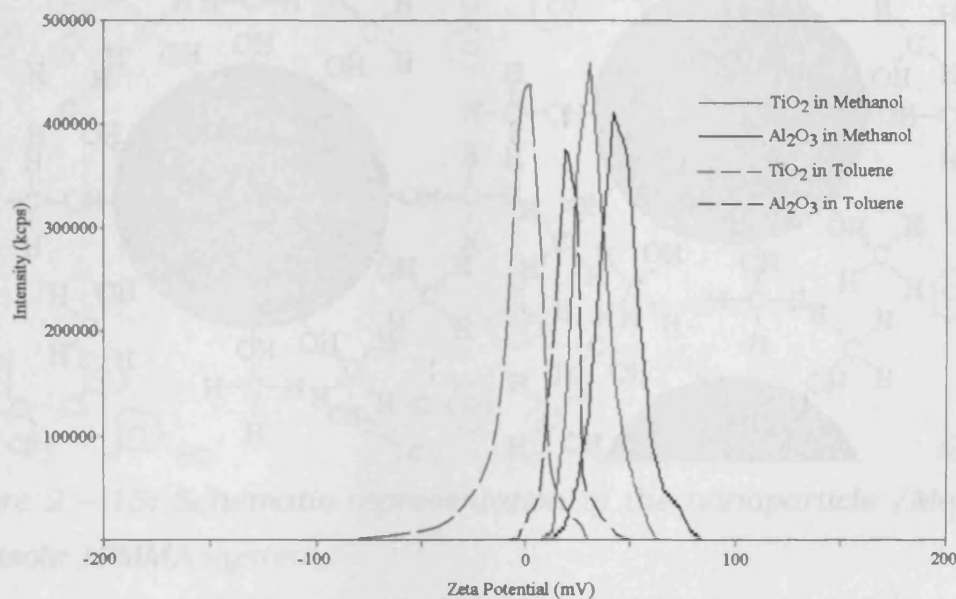


Figure 2 – 13: Hydrogen bonding mechanism between the borosilicate glass / oxide nanoparticle surface and the various solvents.

Toluene are below the zeta potential threshold, hence nanoparticle instability, where the zeta potential values were 7.7mV and 19.4mV with  $\text{TiO}_2$  and  $\text{Al}_2\text{O}_3$  respectively. It was observed that Methanol was effective in suspending the oxide nanoparticles, prior to dispersal within the PMMA polymer. It was found that 200mg of nanoparticles aggregated together and dropped out of suspension under the force of gravity, on average in less than one minute in 0.5ml of Toluene, whereas the methanol suspended the same amount of nanoparticles for many days.



*Figure 2 – 14: Zeta potential of the two test cases –  $\text{Al}_2\text{O}_3$  &  $\text{TiO}_2$  suspended in methanol and toluene respectively.*

Methanol encapsulates the surface of nanoparticles and acts as a barrier so the depletion regions do not intersect. Therefore, the oxide nanoparticles repel each other. Thus, the nanoparticles dispersion is stable and this is illustrated in figure 2 – 15.

Using the nanoparticles/methanol suspension system; the nanoparticles could be successfully dispersed in the PMMA/Anisole system. Consequently, this nanocomposite suspension (PMMA / Anisole / Methanol / nanoparticles) had improved the homogeneity of the surface as shown by the  $10\mu\text{m}$  square phase AFM images in figure 2 – 16. Figure 2 – 16a shows the  $\text{TiO}_2$  nanoparticles treated with methanol and suspended directly in the PMMA polymer the rms roughness was 50nm, however, comparing this with figure 2 – 16b, the  $\text{Al}_2\text{O}_3$  nanoparticles suspended directly in the PMMA polymer the rms roughness was 63nm. It must be noted that, the  $\text{Al}_2\text{O}_3$  is less dense ( $4000 \text{ kg m}^{-3}$ ) than  $\text{TiO}_2$  ( $4230 \text{ kg m}^{-3}$ )

nanoparticles, subsequently more  $\text{Al}_2\text{O}_3$  nanoparticles can be embedded in the PMMA.

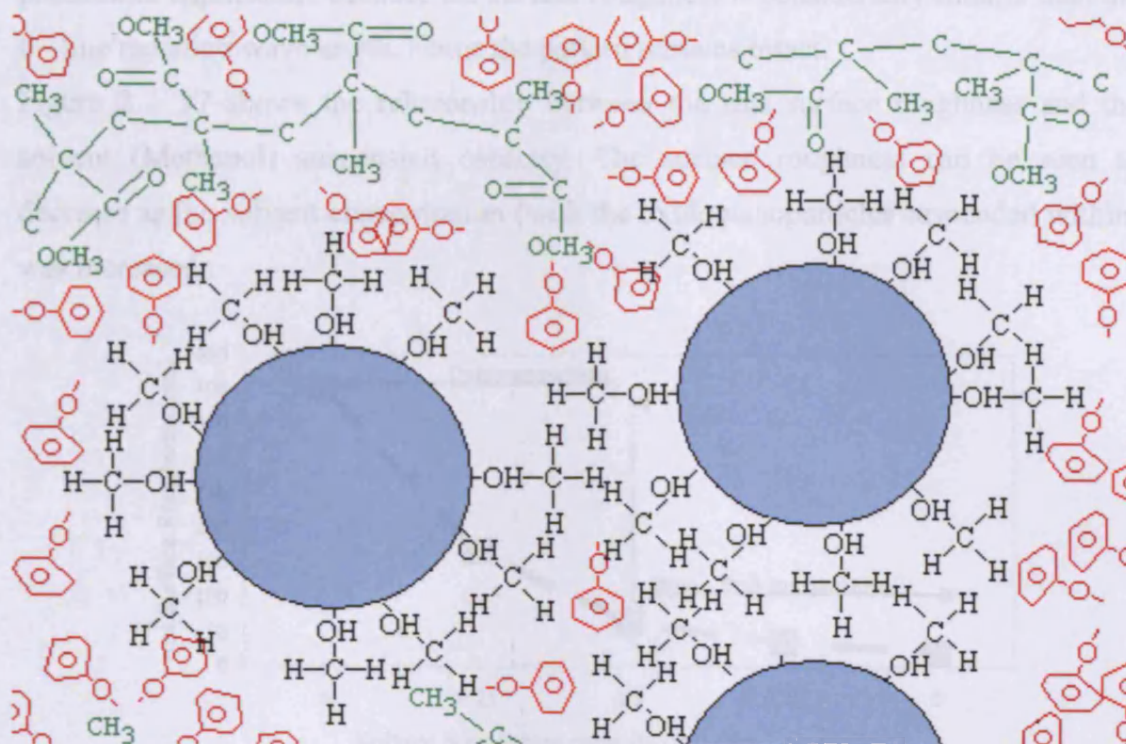


Figure 2 – 15: Schematic representation of the nanoparticle /Methanol /Anisole /PMMA system.

Thus, as more nanoparticles are embedded in the PMMA, then the surface roughness is increased. However, the surface of the nanocomposite film has been improved by a

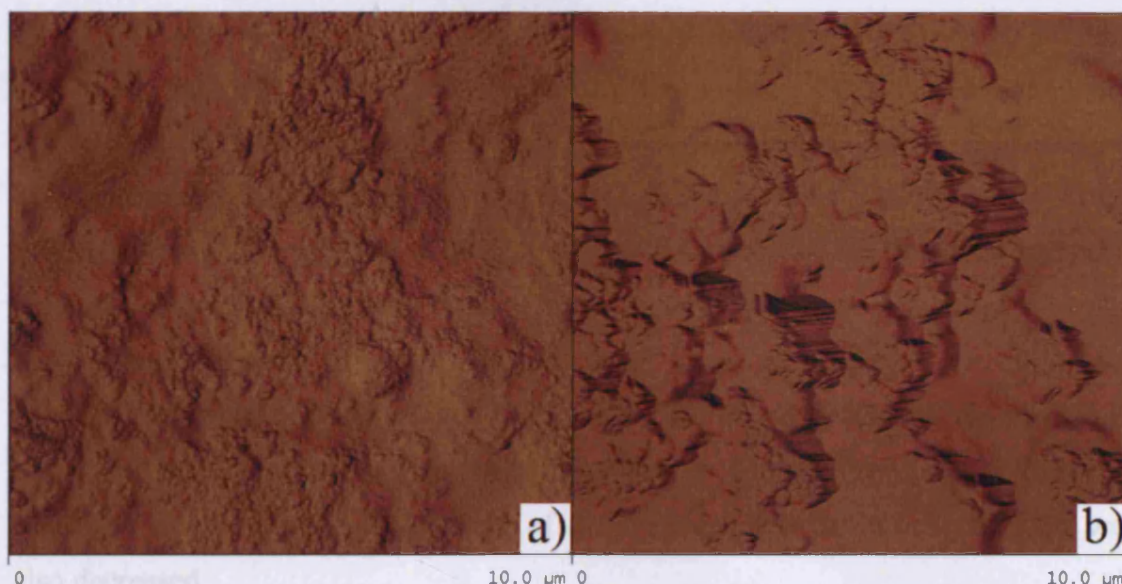
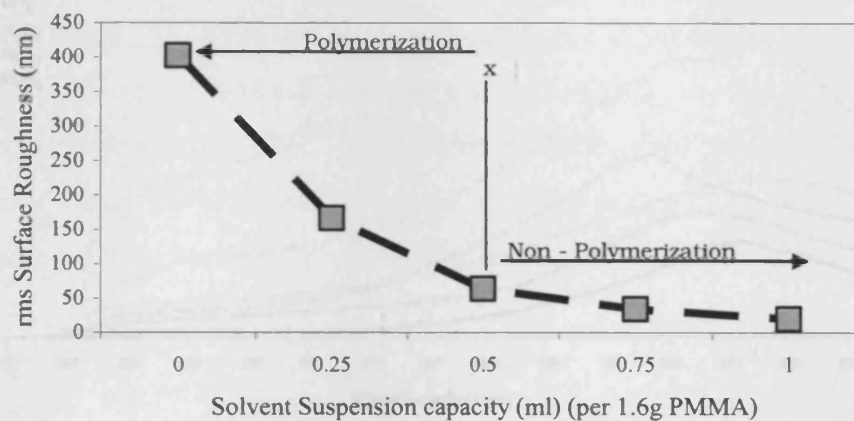


Figure 2 – 16: a) AFM image of  $\text{TiO}_2$  nanoparticles embedded in the PMMA matrix that was suspended in Methanol b) AFM image of  $\text{Al}_2\text{O}_3$  nanoparticles embedded in the PMMA that was suspended in Methanol.



factor of 6.45 times and 6.34 times respectively. This is more suitable for the photomask application, because the surface roughness is considerably smaller than the I – line radiation wavelength, hence the pattern remains intact.

Figure 2 – 17 shows the relationship between the rms surface roughness and the solvent (Methanol) suspension capacity. The surface roughness can be seen to decrease as the solvent concentration (with the oxide nanoparticles suspended within) was increased.



*Figure 2 – 17: PMMA based nanocomposite resist surface when suspended by 200mg of  $\text{TiO}_2$  nanoparticles that was prepared with a methanol suspension.*

When the solvent concentration was sufficiently high beyond the cut – off polymerization limit at  $x$ , which for this case was 0.5ml of methanol suspending 200mg of oxide nanoparticles in 1g of PMMA polymer, the PMMA polymer would not polymerize. The polymer chains would not form because the increased solvent – polymer interaction causes the osmotic pressure to increase non – linearly, allowing the polymer chains to relax toward their ideal state [16]. Therefore, the polymerization (curing) can not take place. This has a direct effect on the amount of oxide nanoparticles that can be suspended in the Methanol. As the amount of Methanol was decreased, the number of nanoparticles that could be suspended was also decreased.

### 2.3.3 Optical Properties of the NanoComposite Resist

It was observed that the optical transmission of the PMMA e-beam resist was approximately 90% in the UV – near IR wavelengths. Attenuation of the I – line radiation has been demonstrated by the nanocomposite resist. The optical extinction spectra are illustrated in figure 2 – 18.

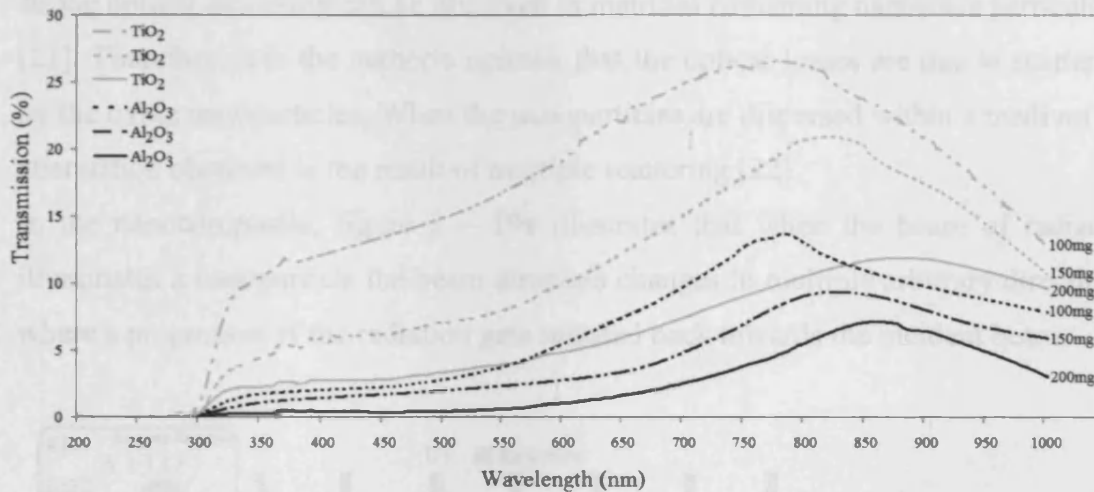


Figure 2 – 18: Transmission spectra of the nanoparticles embedded in PMMA matrix.

These graphs show that as the amount of nanoparticles increases, the optical transmission decreases. Table 2 – 3 presents the percentage of I-line transmitted through the each nanocomposite resist.

| Nanoparticle species           | Transmission (%) |       |       |       |
|--------------------------------|------------------|-------|-------|-------|
|                                | 50mg             | 100mg | 150mg | 200mg |
| Al <sub>2</sub> O <sub>3</sub> | 37.2             | 37.7  | 38    | 38.5  |
| TiO <sub>2</sub>               | 25.8             | 29.7  | 33.7  | 36.4  |

Table 2 – 3: Optical transmission of the composite resist at I – line wavelength.

Comparing the effect of the two oxide nanoparticle species, it is evident that the optical extinction is more pronounced with Al<sub>2</sub>O<sub>3</sub> than with TiO<sub>2</sub>. The optical band gaps have been reported to be 8.7eV and 3.03eV for bulk Al<sub>2</sub>O<sub>3</sub> and TiO<sub>2</sub> materials [17, 18] However, the nanoparticles are not in contact with each other, as each nanoparticle is encapsulated with Methanol [19], therefore the nanoparticle will not behave like the bulk material. This is because of the quantum sizing effects associated

with the optical band gaps as they will be much larger than the bulk values; this is caused by the defects throughout the crystal structure [20]. It should be noted, however, that defects can give rise to intra band absorption centres that absorb at much shorter wavelengths. Nevertheless, due to the fact that the average nanoparticle size is approximately 15 times smaller than the I-line wavelength, attenuation, as a result of direct absorption by the nanoparticles, is assumed to be negligible. However, strong optical scattering can be observed in matrices containing nanoscale particulates [21]. Therefore, it is the author's opinion that the optical losses are due to scattering by the oxide nanoparticles. When the nanoparticles are dispersed within a medium the attenuation observed is the result of multiple scattering [22].

In the nanocomposite, figure 2 – 19a illustrates that when the beam of radiation illuminates a nanoparticle the beam direction changes in multiple arbitrary directions, where a proportion of the radiation gets radiated back towards the incident beam.

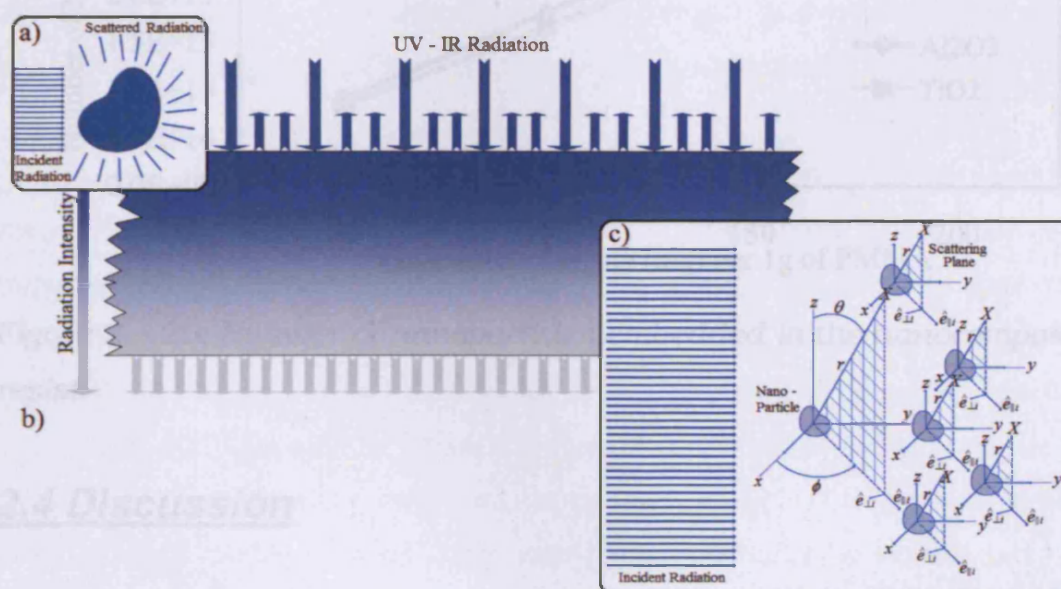


Figure 2 – 19: a) Schematic diagram of the scattered radiation process in arbitrary nanoparticle, b) Radiation intensity of the UV – IR radiation propagating through the nanocomposite thin film in the  $z$  – direction, c) Schematic diagram of the scattering process of multiple nanoparticles inside the nanocomposite thin film.

The energy of the propagating radiation beam through the nanocomposite thin film is attenuated by small amounts, as depicted by the radiation intensity arrow in figure 2 –



19b. This multiple scattering process is repeated until all the radiation propagating through the film is lost or is at a minimum, as shown in figure 2 – 19c. Evidently, if the density of the nanoparticles, is increased and the scattering cross section of the nanoparticle is increased, then the greater the multiple scattering.

As stated earlier, there are more  $\text{Al}_2\text{O}_3$  nanoparticles embedded in the nanocomposite film than  $\text{TiO}_2$  nanoparticles, resulting in more multiple scattering, therefore the effect of multiple scattering increases which will attenuate more of the UV radiation, as indicated in figure 2 – 20, where the increase in nanoparticles corresponds to an increase in the number density of nanoparticles.

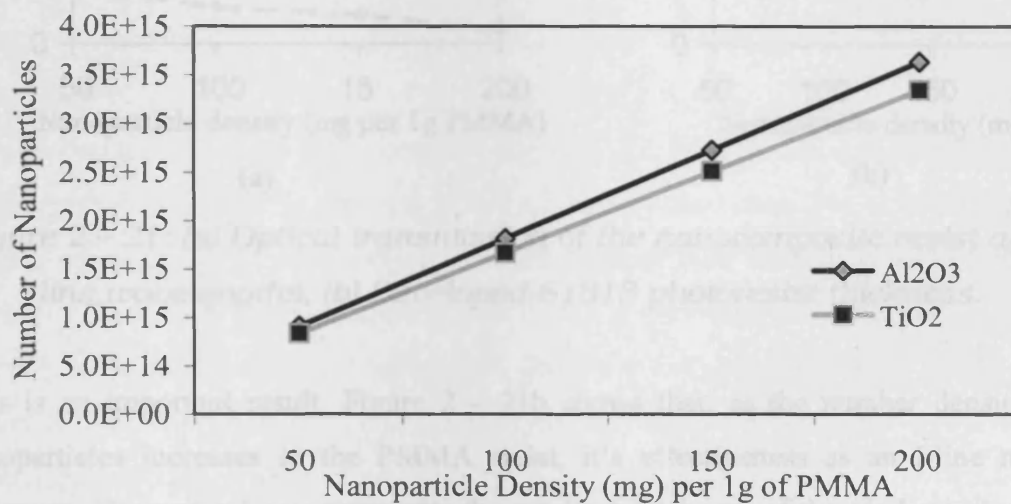


Figure 2 – 20: Number of nanoparticles embedded in the nanocomposite resist.

## 2.4 Discussion

The data shown in figure 2 – 21(a) is taken from figure 2 – 18. It highlights the important relationship between nanoparticle number density and overall attenuation at the I-line wavelength; increasing optical contrast with increasing number density of nanoparticles. It is evident that the optical transmission decreases considerably when the nanoparticle density is increased to 200mg/1g PMMA, therefore, achieving an improved light/dark contrast. It is this optical contrast that is required at I – line wavelengths for transferring a micro scale pattern from the nanocomposite resist to a photoresist. Additionally, since Photoresists are generally thicker than PMMA ‘as spun’, higher aspect ratio structures are possible.



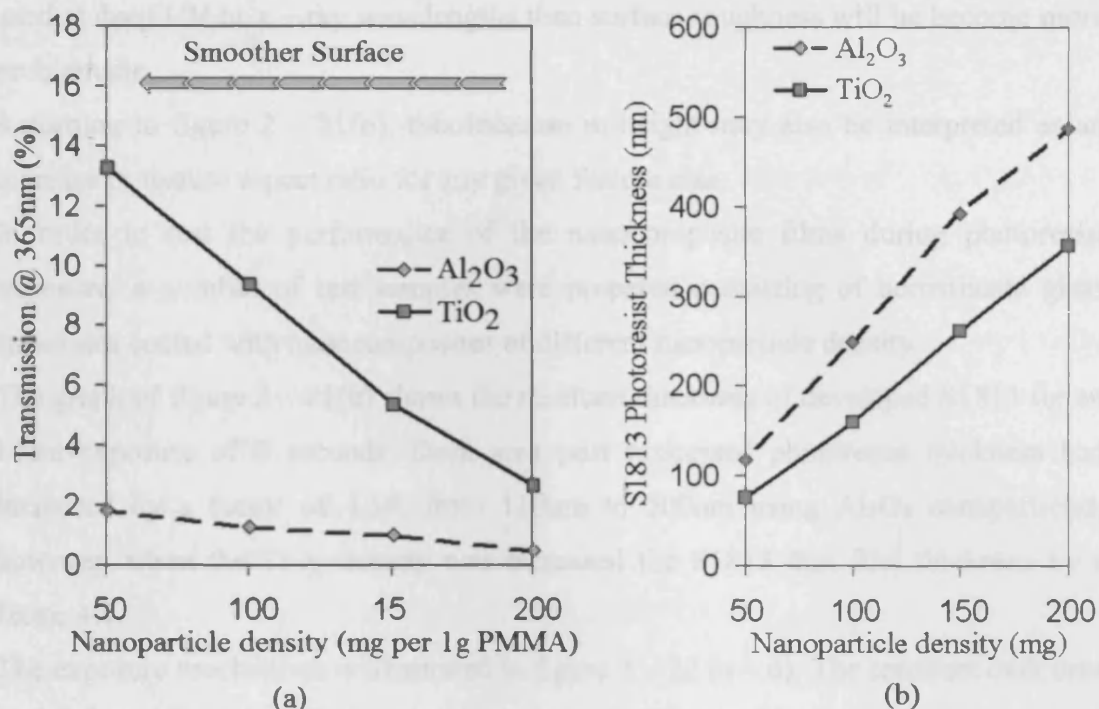


Figure 2 – 21: (a) Optical transmission of the nanocomposite resist at I – line wavelengths, (b) Developed S1813 photoresist thickness.

This is an important result. Figure 2 – 21b shows that, as the number density of nanoparticles increases in the PMMA resist, it's effectiveness as an I-line mask improves. The vertical axis represents the resultant thickness of the 'dark area' of an exposed and developed S1813 photoresist film. Specifically, the 'dark area' or opaque region defines the portion of the mask that is meant to block the exposing radiation. Conversely, the 'light area' is the region where exposure of the resist is intended. In this context, the light areas are regions of the PMMA composite that have already been exposed during e-beam lithography and subsequently etched away in development.

It is presumed at this stage that the improved contrast is due to scattering, as already mentioned. This change in contrast is highlighted in figure 2 – 21(a) where the PMMA sample loaded with 200mg of Al<sub>2</sub>O<sub>3</sub> nanoparticles results in an optical transmission of 0.3% at the I – line wavelength of 365nm. Additionally, as the density of nanoparticles increases, the surface roughness increases, therefore, an important trade off arises. As mentioned in the previous section, the oxide nanoparticles were treated so that the surface roughness was kept smaller than the I – line wavelength and thus the trade off is not a problem for I-line exposure. If the nanocomposite resist is

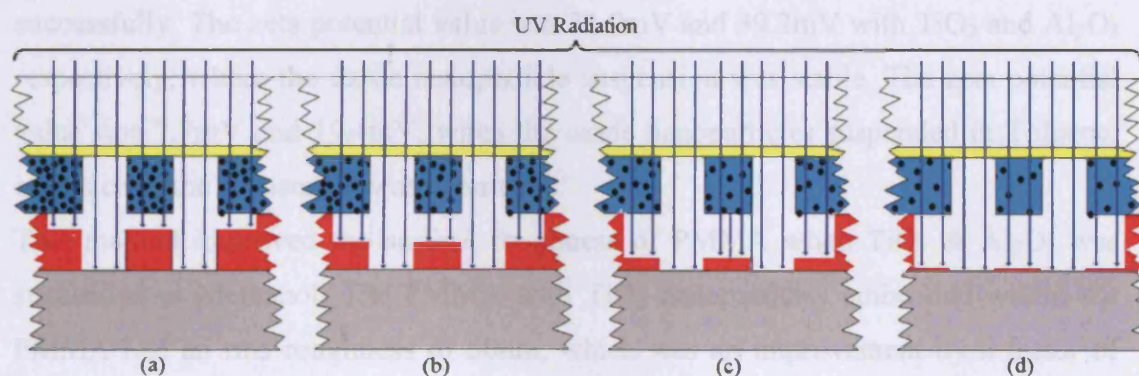
used at deep UV or x – ray wavelengths then surface roughness will be become more problematic.

Returning to figure 2 – 21(b), this increase in height may also be interpreted as an increase in feature aspect ratio for any given feature size.

In order to test the performance of the nanocomposite films during photoresist exposure, a number of test samples were prepared consisting of borosilicate glass substrates coated with nanocomposites of different nanoparticle density.

The graph of figure 2 – 21(b) shows the resultant thickness of developed S1813 for an I-line exposure of 6 seconds. Dark area post processed photoresist thickness had increased by a factor of 4.54, from 110nm to 500nm using  $\text{Al}_2\text{O}_3$  nanoparticles, however, when the  $\text{TiO}_2$  density was increased the S1813 thin film thickness by a factor 4.1.

The exposure mechanism is illustrated in figure 2 – 22 (a – d). The resultant dark area photoresist thickness, following exposure and development decreases (left to right, (a) to (d)), corresponding to a reduction in nanoparticle density illustrated by the reduced number of dots in the nanocomposite (left to right). The variation in S1813 thickness appears to be proportional to nanoparticle density over the range shown. Clearly, the presence of  $\text{Al}_2\text{O}_3$  results in a higher opacity than for  $\text{TiO}_2$  by a factor of approximately 1.42.



*Figure 2 – 22: Schematic representation of the effect of the amount of oxide nanoparticles embedded in the PMMA.*

## **2.5 Summary**

It was found that the PMMA had high optical transmission at I – line wavelengths and as a result would have poor optical contrast for an optical photomask. For PMMA to perform as a photomask, modification of its transmission would be required. Oxide nanoparticles ( $\text{TiO}_2$  and  $\text{Al}_2\text{O}_3$ ) were introduced into the polymeric matrix to improve this optical contrast at the I – line wavelength. By adding the oxide nanoparticles directly into the PMMA matrix, the PMMA became inhomogeneous. This was indicated by an increase in surface rms roughness measured (via an AFM). This was found to be 322nm and 402nm produced by  $\text{TiO}_2$  and  $\text{Al}_2\text{O}_3$  nanoparticles respectively. This was due to poor particle dispersion as a result of the inter-particle attraction between each nanoparticle caused by the depletion effect. With the surface roughness comparable to the wavelength of the I – line (365nm) the potential for standing wave artefacts became more probable. As for the transfer of the pattern from the nanocomposite resist photomask into the S1813 photoresist, the resultant pattern developed in the S1813 photoresist would have had a poor edge definition.

Therefore, to improve the homogeneous surface quality, the oxide nanoparticles were suspended in Methanol and Toluene. This was measured by using the zeta potential parameter. It was found that the Methanol suspended the oxide nanoparticles successfully. The zeta potential value was 31.9mV and 39.2mV with  $\text{TiO}_2$  and  $\text{Al}_2\text{O}_3$  respectively; where the oxide nanoparticle suspension was stable. The zeta potential value was 7.7mV and 19.4mV, when the oxide nanoparticles suspended in Toluene; in this case, the suspension was not stable.

This method improved the surface roughness of PMMA when  $\text{TiO}_2$  &  $\text{Al}_2\text{O}_3$  was suspended in Methanol. The PMMA with  $\text{TiO}_2$  nanoparticles embedded within the PMMA had an rms roughness of 50nm, which was an improvement by a factor of 6.45 and PMMA with  $\text{Al}_2\text{O}_3$  embedded within it had an rms roughness of 63nm. The improvement here was a factor of 6.34.

It was also found that as the solvent concentration increases, the surface quality increased. However, there is a limit, if too much solvent was used then the PMMA would not polymerise. This is an important but critical trade off.

It was suspected that the attenuation via optical absorption at the I-line wavelength was minimal. The argument put forward was that 365nm is lower than the wavelength associated with the band gap for both bulk  $\text{Al}_2\text{O}_3$  and  $\text{TiO}_2$  (8.7eV and 3.03eV

respectively); and that the quantum sizing effects would serve to reduce this further. As each nanoparticle is encapsulated with Methanol, the nanoparticles are not in contact with each other. Therefore, the optical losses are more likely due to scattering of the light by aggregates of inorganic nanoparticles.

By the addition of multiple nanoparticles into the e – beam resist, the I – line radiation was attenuated. It was observed that the optical transmission of the composite resist decreases as the number density of nanoparticles was increased. Comparing the effect of the two materials, the composite resist with  $\text{Al}_2\text{O}_3$  nanoparticles transmitted approximately 0.3% of the I – line radiation, whereas 2.1% of the I – line radiation was transmitted by the composite resist with  $\text{TiO}_2$ . This will provide a good optical contrast between dark and light areas of the mask as required for optical lithography. The optical properties of the e – beam resist have thus been modified to absorb the I – line radiation by the addition of nanoparticles into the polymer matrix.

## **2.6 References**

- [1] [http://www.microchem.com/products/pdf/PMMA\\_data\\_sheet.pdf](http://www.microchem.com/products/pdf/PMMA_data_sheet.pdf), (2003).
- [2] D. G. Hasko, S. Yasin, A. Mumtaz, 'Influence of developer and development conditions on the behavior of high molecular weight electron beam resists', J. Vac. Sci. Technol. B 18 (6), 3441 – 3444 (2000).
- [3] E. Knappek, C. K. Kalus, M. Madore, M. Hintermaier, U. Hofmann, H. Scherer-Winner and R. Schlager, 'Computer aided proximity correction for direct write E-beam lithography' Microelectronic Engineering, 13 (1-4), March 1991, pp181-184 (1991).
- [4] L. L. Beecroft, C. K. Ober, 'Nanocomposite materials for optical application', Chem. Mater, (9) (1997) 1302–17.
- [5] R. Gangopadhyay, A. De, 'Conducting polymer nanocomposites: a brief overview', Chem. Mater (12) pp608–22 (2000).
- [6] J. Jordan, K. I. Jacob, R. Tannenbaum, M. A. Shart, I. Jasiuk, 'Experimental trends in polymer nanocomposites – a review', Mater. Sci. Eng A (393) pp1–11 (2005).
- [7] A. Sidorenko, S. Minko, G. Gafijchuk, S. Voronov, 'Radical polymerization initiated from a solid substrate. 3. grafting from the surface of an ultrafine powder', Macromolecules (32) pp 4530 – 43 (1999).

- [8] B. Erdem, E. D. Sudol, V. L. Dimonie, M. S. El – Aasser, ‘Encapsulation of inorganic particles via miniemulsion polymerization. II. Preparation and characterization of styrene miniemulsion droplets containing TiO<sub>2</sub> particles’, *J. Polym. Sci. Part. A: Polym. Chem* (38) pp 4431 – 40 (2000).
- [9] A. H. Yuwono, B. Liu, J. Xue, J. Wang, H. I. Elim, W. Ji et al., ‘Controlling the crystallinity and nonlinear optical properties of transparent TiO<sub>2</sub> – PMMA nanohybrids’, *J. Mater. Chem* (14) pp 2978 – 87 (2005).
- [10] S. R. Lu, H. L. Zhang, C. X. Zhao, X. Y. Wang, ‘Studies on the properties of a new hybrid materials containing chain extended area and SiO<sub>2</sub> – TiO<sub>2</sub> particles’, *Polymer* (46) pp 10484 – 92 (2005).
- [11] P. Judeinstein, C. Sanchez, ‘Hybrid organic – inorganic materials: a land of multidisciplinary’, *J. Mater. Chem* (6) pp 511 – 25 (1996).
- [12] R. A. Potyrailo, ‘Polymeric sensor materials: toward an alliance of combinatorial and rational design tools?’, *Angew. Chem. Int. Edit.* (45) pp 702 – 23 (2006).
- [13] P. R. Sperry, ‘Morphology and Mechanism in Latex Flocculated by Volume Restriction’, *J. Colloid Interface Sci.* (99) (1984) 97.
- [14] [www.sylvania.com/content/display.scfx?id=003679916](http://www.sylvania.com/content/display.scfx?id=003679916), (2003).
- [15] [www.webelements/webelement/elements/text/Au/phy.html](http://www.webelements/webelement/elements/text/Au/phy.html), (2003).
- [16] M. Muthukumar, S. F. Edwards, ‘Extrapolation formulas for polymers solution properties’, *J. chem. Phys.* 76, pp 2720 – 30 (1982).
- [17] D. W. Fischer, ‘X – ray band spectra and molecular – orbital structure of Rutile TiO<sub>2</sub>’, *J. phys. Chem. Solids* (5) 11, pp 4219 (1972).
- [18] W. Y. Ching, Y. –N Xu, ‘First principles calculation of electronic, optical and structural properties of  $\alpha$ - Al<sub>2</sub>O<sub>3</sub>’, *J. Am. Ceram. Soc.* 77 (2) 404 – 11 (1994).
- [19] W. P. Halperin, ‘Quantum size effects in metal particles’, *Rev. Mod. Phys.* Vol 58 (3) (1986).
- [20] A. Convertino, G. Leo, M. Tamborra, C. Sciancalepore, M. Striccoli, M. L. Curri, A. Agostiano, ‘TiO<sub>2</sub> colloidal nanocrystals functionalized of PMMA: A tailoring of optical properties and chemical adsorption’, *Sensors and actuators B* 126 138 – 43 (2007).
- [21] H. C. van der Hulst, ‘Light scattering by small particles’, Published by Courier Dover Publications, (1981)
- [22] A. L. Aden, M. Kerker, ‘Scattering of Electromagnetic Waves from Two Concentric Spheres’, *J. Appl. Phys.* 22, 1242 (1951).



# **Characterization of a PMMA based Nanocomposite Resist for Next Generation Lithography**

## **Contents**

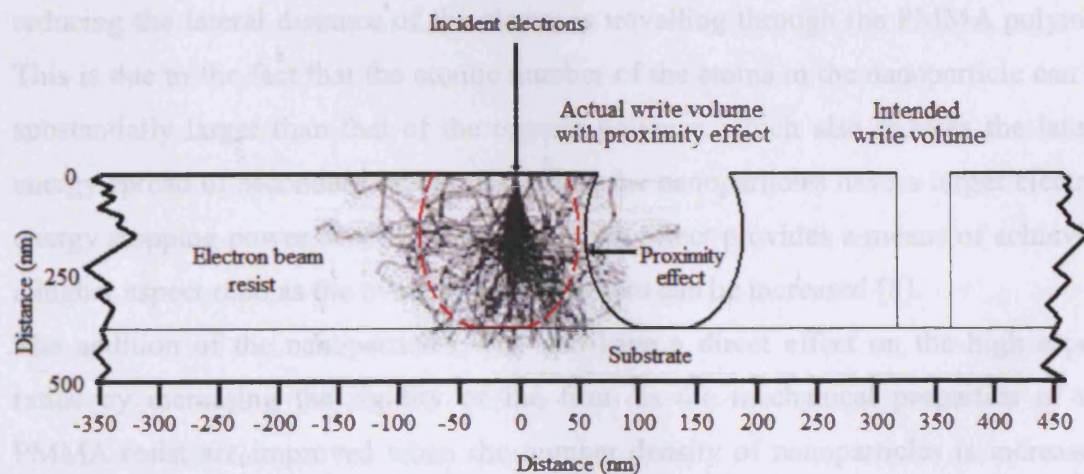
|  |      |
|--|------|
| 3.1 Introduction.....  | -50- |
| 3.2 Experimental details.....  | -53- |
| 3.2.1 Characterisation of the nanocomposite resists performance in situ..... | -53- |
| 3.3 Results and discussion.....  | -54- |
| 3.3.1 Clearing doses of the nanocomposite resist.....                        | -54- |
| 3.3.2 Characterization of the nanocomposite resist.....                      | -62- |
| 3.4 Summary.....   | -77- |
| 3.5 References.....  | -78- |

## **3.1 Introduction**

The trend of Moore's law has been maintained using the current technology of the ultra large scale integration which produces circuits of sub 100 nm [1]. This has been made possible by sub 100nm lithography, by the design of next generation resists operating at extreme ultra violet wavelengths. However, it is well known that electron

beam lithography can achieve similar dimensions using conventional chain scission resists such as PolyMethylMethAcrylate (PMMA), Polybutene – 1 – Sulfone (PBS) and ZEP520 [2, 3]. Unfortunately, there is a limit to the negative scaling factor, called the proximity effect [4]. Therefore, it is essential to optimize these resists to perform with a higher sensitivity for high throughput and a higher contrast to achieve sub 100nm resolution.

As a figure of merit, the smallest feature size possible with PMMA is approximately 100nm when the resist thickness is approximately 400nm. Hence, the aspect ratio is 4:1. This is due to the fact that a minority of the incident electrons when penetrating the surface of the PMMA resist undergo small angle forward scattering while the majority of them participate in large angle scattering events that contribute to backscattering. Therefore, this leads to additional exposure in the bulk resist (the proximity effect), outside of the intended 'write volume'. The bulk of the resist is exposed by primary electrons. As their range in the resist is a few nanometers their contributions to the proximity effect are negligible. However, secondary electrons may be generated from the primary electrons and a minority of these secondary electrons may have energies of the order of 1 to 5KeV. This is significant, because these fast electrons can have a range of a few tenths of a micron, contributing to the proximity effect. This has been illustrated by the Monte Carlo simulations of electron trajectories in figure 3 – 1.



*Figure 3 – 1: Schematic of a typical Monte Carlo simulation demonstrating the proximity effect.*

Figure 3 – 1 illustrates the proximity effect which is indicated by the red line, it can be

seen that the trajectories of the secondary electrons can interfere with the structure adjacent to it, thus to achieve ever decreasing features the overall resist thickness must be decreased to compensate for this.

The limit of the smallest feature size that can be produced in PMMA is about 10nm, when the resist thickness is approximately 40nm. At these geometries, the resist cannot be used for lift off, because, if the user wanted to produce gate structures for transistors for example, then the power applied to the gate must be extremely low to avoid burning out the structure and cause an open circuit. However, for VLSI this can be advantageous, as low power transistors are required for logic circuits. In contrast, high power devices such as GaN HEMTs for the next generation mobile phone handsets, lithography via this method is not suitable.

In order to address these lithographic challenges, the current trend is toward the use of nanocomposite resists [5 – 7]. These materials can have a large impact on current integrated circuit (IC) fabrication technologies thanks to the properties of maintaining high throughput while increasing the aspect ratio of the resist. As seen in the previous chapter, nanoparticles can have an enormous effect on important properties of the resist. This has been extensively studied using carbon fullerenes and silica nanoparticles [7, 10].

It is expected that proximity effects can be greatly reduced by nanocomposite resists. This is achieved through the addition of nanoparticles throughout the PMMA polymer reducing the lateral distance of the electrons travelling through the PMMA polymer. This is due to the fact that the atomic number of the atoms in the nanoparticle can be substantially larger than that of the organic polymer, which also reduces the lateral energy spread of secondary electrons. Hence, the nanoparticles have a larger electron energy stopping power. Reducing the proximity effect provides a means of achieving a higher aspect ratio as the overall resist thickness can be increased [8].

The addition of the nanoparticles will also have a direct effect on the high aspect ratios by increasing the rigidity of the film, as the mechanical properties of the PMMA resist are improved when the number density of nanoparticles is increased. The nanoparticles will prevent the nanometer features from collapsing, giving rise to a higher achievable aspect ratio. Subsequently, this can lead to a reduction of line broadening and improve the critical dimension of feature sizes. Achieving these improvements will be the subject of the subsequent sections in this chapter.

Here the focus was on two different polymer resists, PMMA 950K 7% and PMMA



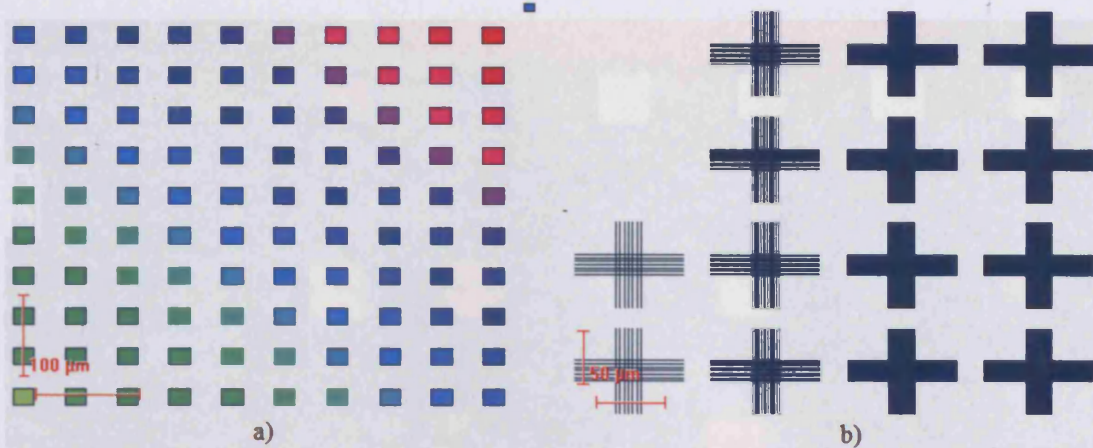
96K 7% that will serve as host matrices for Al<sub>2</sub>O<sub>3</sub> nanoparticle incorporation. Both of the nanocomposite resists are PMMA based but the molecular weights are vastly different. The reduced molecular weight of PMMA 96K as compared to 950K means that the chain size of the molecule is also greatly reduced. Therefore, the electron beam direct write times are greatly reduced as the sensitivity is improved. Thus, a higher throughput can be achieved. The two objectives were to investigate the exposure clearing doses of each nanocomposite resist species and to achieve the highest possible aspect ratio.

Here, for the purpose of producing optical masks for I-line wavelengths, it is not necessary to fabricate sub-100nm features, as the wavelength is approximately 3.65 larger, thus the interaction will be minimal. However, these sub-100nm structures may have the possibility of being used with EUV or even x-ray lithography, where the wavelengths are considerably smaller [11].

## **3.2 Experimental Details**

### **3.2.1 Characterisation of nanoparticle resist performance in situ**

The synthesis of the samples used throughout the proceeding chapters was explained in chapter 2, section 2.1. The Samples were exposed on a converted SEM, JEOL JSM 840A, driven by Elphy quantum software. The samples were exposed with an acceleration voltage of 25kV and beam current of 40pA at a working distance of 7mm. Development was carried out in solutions of MIBK (Methyl IsoButyl Ketone) and IPA (Isopropyl alcohol), in the ratio of 1:3, for 30s followed by a 40s rinse in IPA. Two test patterns were exposed on each sample. The first test pattern shown in figure 3 – 2a was used to obtain the exposure clearing doses of each resist. This was determined from a matrix of a hundred 20µm squares that were exposed with a dose scale in incremental steps of 30µC/cm<sup>2</sup>. The dose was increased in both directions with the square in the lower left having a dose of 30µC/cm<sup>2</sup>, and that of the upper right having a dose of 600µC/cm<sup>2</sup>. The size of the squares allowed for accurate AFM non contact measurements of the remaining resist thickness for each dose, and hence the clearing dose could be determined of each resist.



*Figure 3 – 2: E-beam lithography test patterns a) sensitivity squares, b) sub 100nm proximity crosses.*

To investigate proximity effects and the aspect ratio of developed features, a series of 25μm sized crosses (illustrated in figure 3 – 2b) formed from 100nm lines with various spacing and dose was exposed, this test pattern is an industrial standard and is part of the Elphy quantum software. In the first column (on the left), the crosses were with a line spacing of 1.5μm and 1.0μm, the second column, the crosses were with a line spacing of 0.7μm, 0.6μm, 0.5μm and 0.4μm, the third column, the crosses were with a line spacing of 0.3μm, 0.2μm, 0.1μm and 0.09μm and the fourth column, the crosses were with a line spacing of 0.08μm, 0.07μm, 0.06μm and 0.05μm. At the top row, the crosses were exposed with a dose of 150μC/cm<sup>2</sup>, the second row was exposed with a dose of 300μC/cm<sup>2</sup>, the third row was exposed with a dose of 600μC/cm<sup>2</sup> and the fourth row was exposed with a dose of 1200μC/cm<sup>2</sup>. SEM images of feature size together with AFM measurements of resist thickness were used to determine the aspect ratio achieved in each resist. SEM scans also determined where features had collapsed due to the proximity effect.

### **3.3 Results and Discussion**

#### **3.3.1 Clearing doses of the nanocomposite resist**

Figure 3 – 3 shows a SEM micrograph of developed 20μm squares directly written into PMMA 96K7%. This had a typical grey scale profile with a varied electron beam exposure dose as explained in §3.2.2.



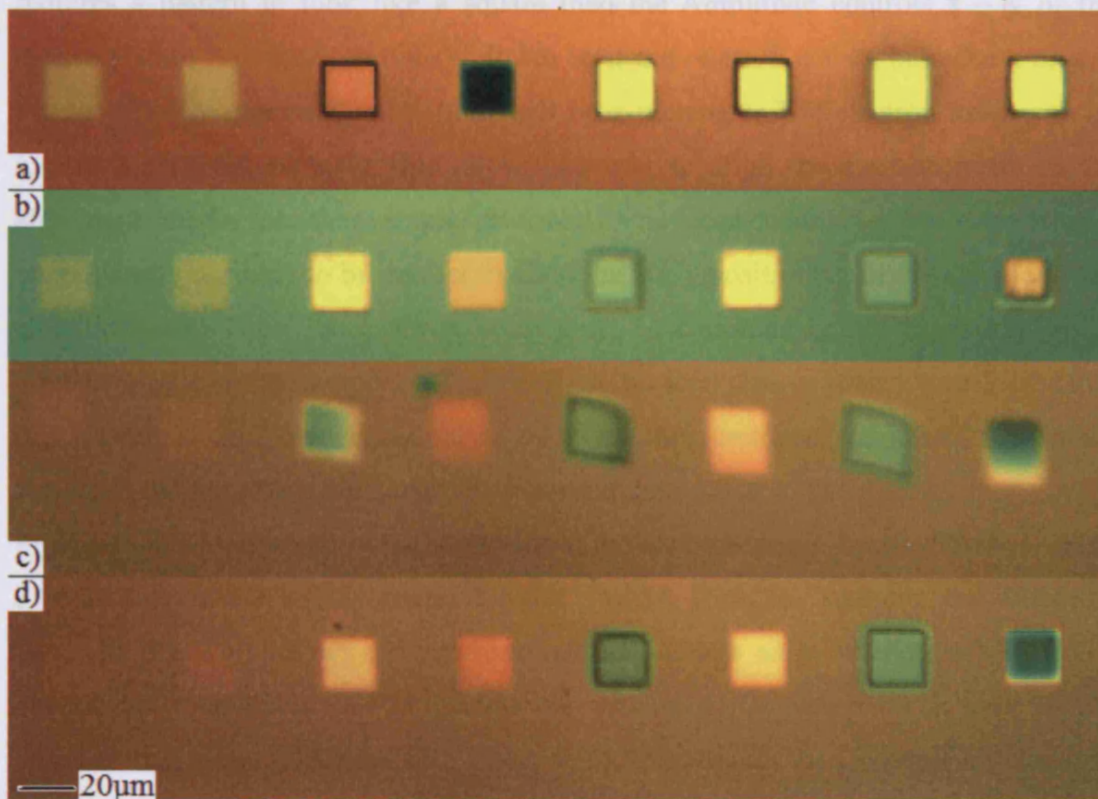


Figure 3 – 3: Developed nanocomposite resist a) Unloaded P96K7%, b) loaded P96K7% with 50mg of  $\text{Al}_2\text{O}_3$  nanoparticles, c) loaded P96K7% with 100mg of  $\text{Al}_2\text{O}_3$  nanoparticles, d) loaded P96K7% with 150mg of  $\text{Al}_2\text{O}_3$  nanoparticles. The dimensions of all squares are  $20\mu\text{m}$ .

Figure 3 – 3a depicts the PMMA 96K7% without  $\text{Al}_2\text{O}_3$  nanoparticles embedded within it, whereas figure 3 – 3b, c and d has 50mg, 100mg and 150mg of  $\text{Al}_2\text{O}_3$  nanoparticles embedded within it respectively.

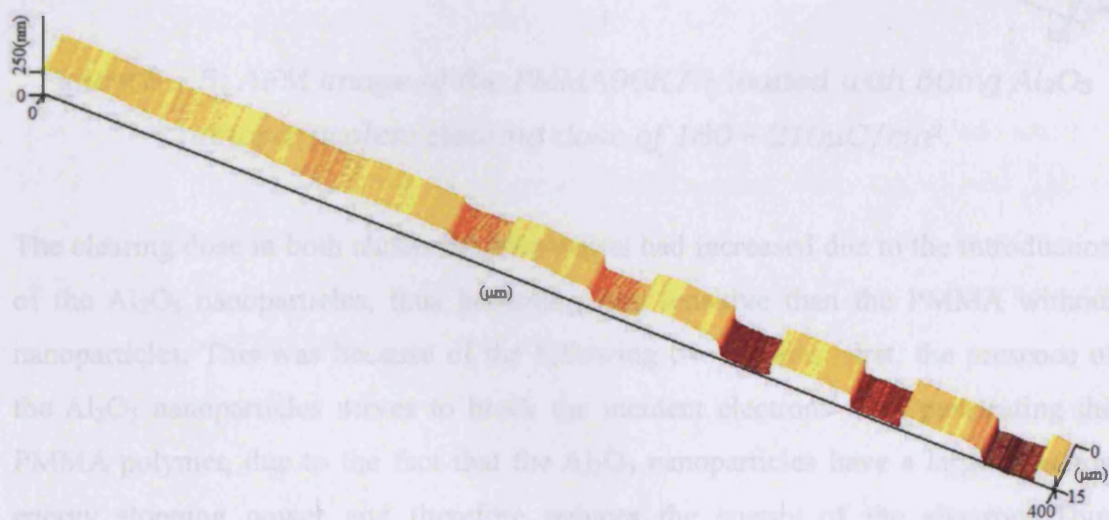
Comparing the PMMA 96K7% without any  $\text{Al}_2\text{O}_3$  nanoparticles with that of PMMA 96K7% loaded with 150mg  $\text{Al}_2\text{O}_3$  nanoparticles, it was evident that the unloaded PMMA needed an exposure dose lower than the PMMA with 150mg  $\text{Al}_2\text{O}_3$  nanoparticles. The higher exposure dose was in the range of  $210 - 240\mu\text{C}/\text{cm}^2$  (PMMA with 150mg of  $\text{Al}_2\text{O}_3$  nanoparticles), whereas the lower exposure was between the dose range of  $120 - 150\mu\text{C}/\text{cm}^2$  (PMMA without  $\text{Al}_2\text{O}_3$  nanoparticles).

It can be seen in figure 3 – 3c that the  $20\mu\text{m}$  squares are not perfectly square, this is due to the fact that the electron beam is manipulated by the scan coils. The scan coils are controlled by three multiplying DACs (digital to Analogue converters), these control the amplitude and rotation of the beam to the sample. For example, if the user



requires a pattern to look like a square then the Amplitude controls x – y of the electron beam (via the scan coils). However, if the relative scaling between x or y is out by 5% then the resultant pattern will be a rectangle. The electron beam can be rotated 360° by the DACs, this allows the user to align the electron beam to the alignment marks on the sample. Normally the scan coils are hand made and consequently unlikely to be perfect to align the x – y positioning of the sample to the electron beam. Thus, the electron beam must be corrected before exposure, this is done using the elphy quantum software. It can be seen clearly from figure 3 – 3c that this was not done, however, as only a thickness measurement is required, the pattern produced did not affect the sensitivity measurement.

Figure 3 – 4 shows an AFM measurement of the nanocomposite resist shown in figure 3 – 3a (all of the AFM images for the PMMA 950K7% samples are shown in appendix A). This shows the resultant resist thickness as a function of dose. The overall resist thickness of PMMA 96K7% without Al<sub>2</sub>O<sub>3</sub> nanoparticles was 254nm whereas the resist thickness of PMMA 950K7% without Al<sub>2</sub>O<sub>3</sub> nanoparticles was 407nm.



**Figure 3 – 4: AFM image of the PMMA 96K7% loaded with 0mg Al<sub>2</sub>O<sub>3</sub> nanoparticles: clearing dose of 120 – 150μC/cm<sup>2</sup>.**

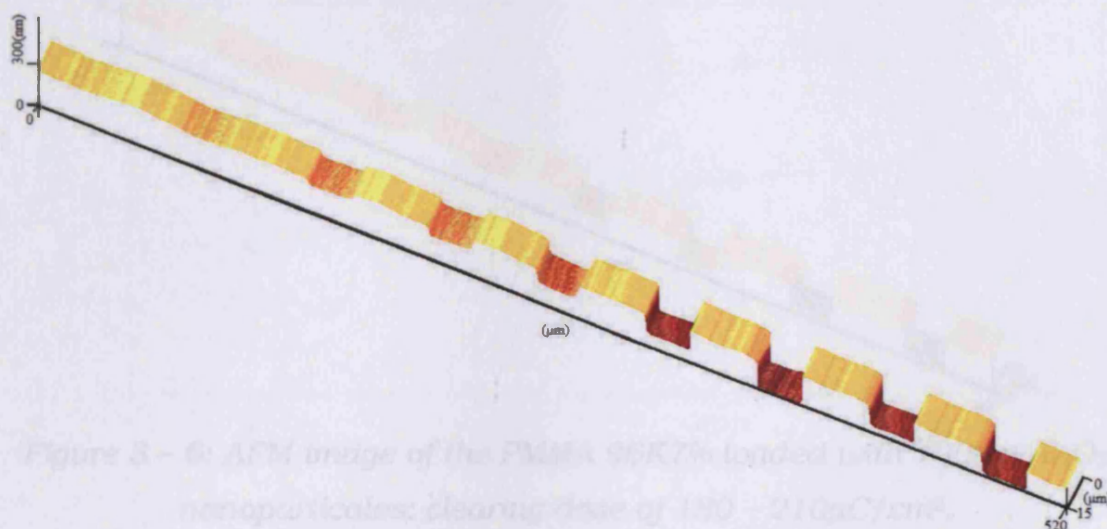
From figure 3 – 4 the clearing dose of the PMMA 96K7% was in the range of 120 – 150μC/cm<sup>2</sup>, while PMMA 950K 7% was in the range of 180 – 210μC/cm<sup>2</sup>. This is evident due to the fact that the PMMA 950K 7% resist thickness was larger when compared with that of the PMMA 96K 7% resist.

From the AFM image in figure 3 – 5, the overall thickness of the PMMA 96K7%



nanocomposite resist when loaded with 50mg  $\text{Al}_2\text{O}_3$  nanoparticles was 276nm whereas the resist thickness of PMMA 950K7% loaded with 50mg  $\text{Al}_2\text{O}_3$  nanoparticles was 455nm.

It was found from figure 3 – 5 that the clearing doses of the PMMA 96K 7% based nanocomposite resist was in the range of  $180 - 210\mu\text{C}/\text{cm}^2$  and this can be compared to the clearing dose of  $210 - 240\mu\text{C}/\text{cm}^2$  for PMMA 950K 7% with a nanoparticle density of 50mg.

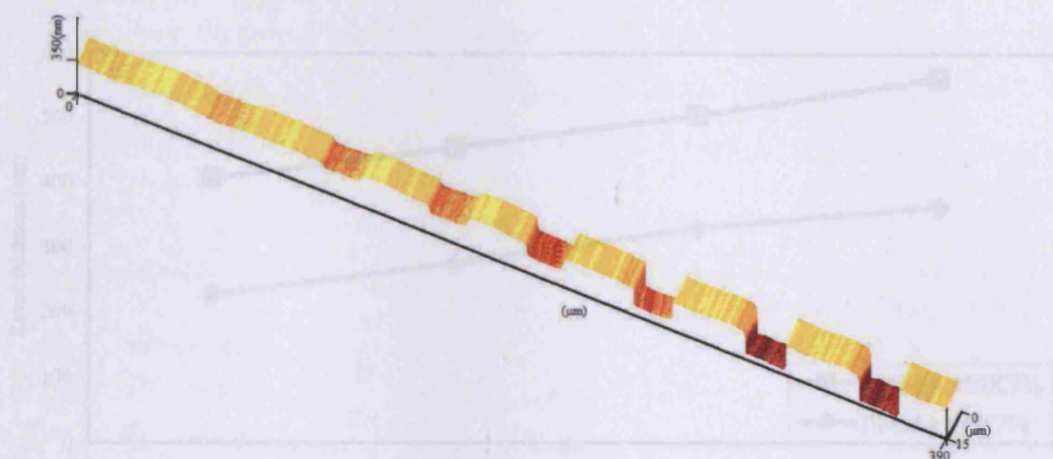


*Figure 3 – 5: AFM image of the PMMA96K7% loaded with 50mg  $\text{Al}_2\text{O}_3$  nanoparticlaes: clearing dose of  $180 - 210\mu\text{C}/\text{cm}^2$ .*

The clearing dose in both nanocomposite resists had increased due to the introduction of the  $\text{Al}_2\text{O}_3$  nanoparticles, thus becoming less sensitive than the PMMA without nanoparticles. This was because of the following two reasons: first, the presence of the  $\text{Al}_2\text{O}_3$  nanoparticles serves to block the incident electrons from penetrating the PMMA polymer, due to the fact that the  $\text{Al}_2\text{O}_3$  nanoparticles have a larger electron energy stopping power and therefore reduces the energy of the electron. Thus affecting the total distance travelled through the PMMA polymer. Second, the PMMA 950K 7% resist thickness is larger when compared with that of the PMMA 96K 7% resist, hence, the resist is less sensitive than PMMA without nanoparticles. The consequence of this is that the electrons must be transmitted at a higher exposure dose; in order for the chain scission process to occur through the nanocomposite resist write volume and also they must overcome the apparent quenching effect of the  $\text{Al}_2\text{O}_3$  nanoparticles (this will be covered in more detail in the next chapter).

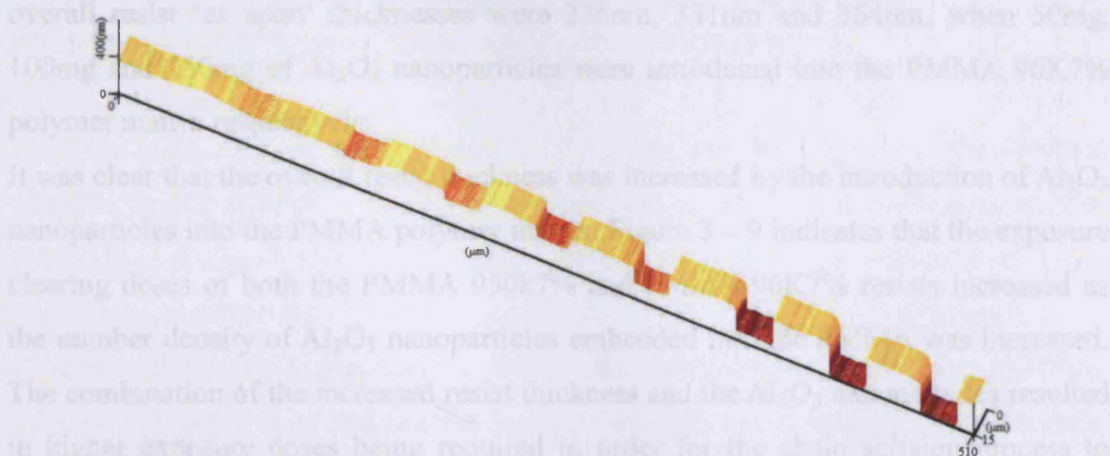
Figure 3 – 6 shows an AFM image of the PMMA 96K7% nanocomposite resist when

loaded with 100mg  $\text{Al}_2\text{O}_3$  nanoparticles; in this case the overall thickness was 331nm. The thickness of PMMA 950K with 100mg  $\text{Al}_2\text{O}_3$  nanoparticles was 505nm by comparison. The clearing dose of the PMMA 96K 7% when loaded with 100mg of  $\text{Al}_2\text{O}_3$  nanoparticles was in the range of  $180 - 210\mu\text{C}/\text{cm}^2$  as shown in figure 3 – 6. Again a clearing dose of  $240 - 270\mu\text{C}/\text{cm}^2$  for PMMA 950K 7% with a nanoparticle density of 100mg, by comparison.



*Figure 3 – 6: AFM image of the PMMA 96K7% loaded with 100mg  $\text{Al}_2\text{O}_3$  nanoparticles: clearing dose of  $180 - 210\mu\text{C}/\text{cm}^2$ .*

It was found from the AFM image in figure 3 – 7 that the overall thicknesses of PMMA 96K7% and 950K 7% based nanocomposite resist when loaded with 150mg  $\text{Al}_2\text{O}_3$  nanoparticles were 364 and 562nm respectively. The clearing doses of the PMMA 96K 7% and 950K7% when loaded with 150mg of  $\text{Al}_2\text{O}_3$  nanoparticles were in the ranges of  $210 - 240\mu\text{C}/\text{cm}^2$  and  $240 - 270\mu\text{C}/\text{cm}^2$ , respectively.



*Figure 3 – 7: AFM image of the P96K7% loaded with 150mg  $\text{Al}_2\text{O}_3$  nanoparticles: clearing dose of  $210 - 240\mu\text{C}/\text{cm}^2$ .*



As shown in figure 3 – 8, it was found that by decreasing the molecular weight of the PMMA polymer from 950K7% to 96K7%. The overall resist thickness was decreased. The molecule chain sizes of 950K7% and 96K7% were approximately 5108 and 520 respectively. Therefore, the clearing dose required for the exposure of the PMMA 96K7% was lower than that of the PMMA 950K7% samples because the PMMA 96K7% has fewer molecule chains to be cleaved by the incident electron beam.

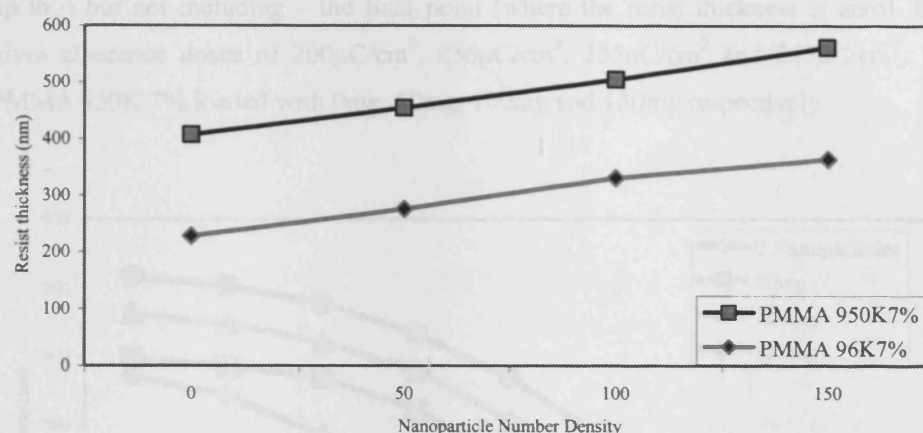


Figure 3 – 8: Overall thickness's of the nanocomposite resist.

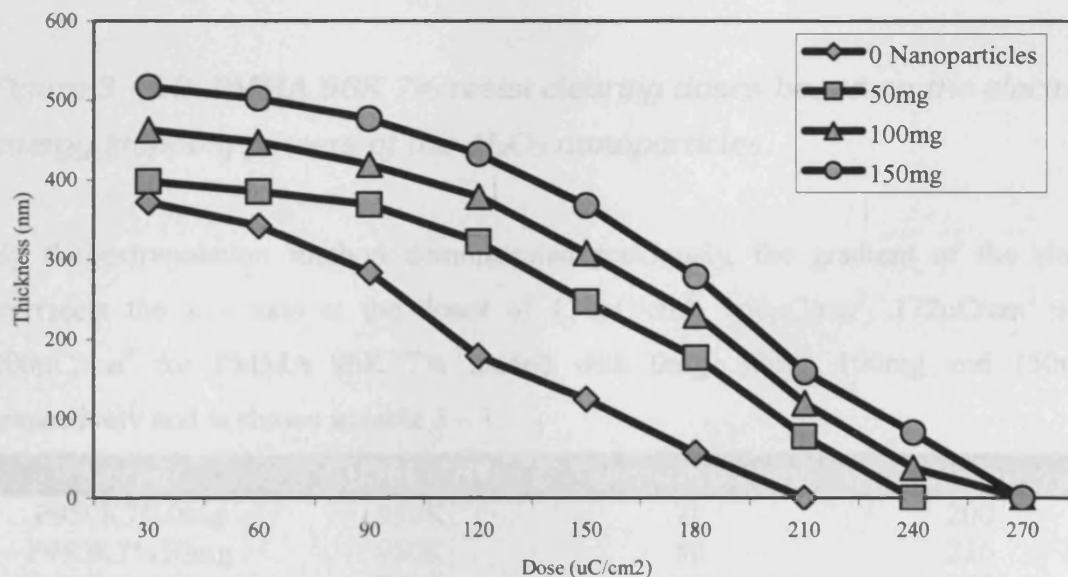
Comparing just PMMA 950K7% with PMMA 96K7% the 'as span' thicknesses were 407nm and 228nm respectively. However, when 50mg, 100mg and 150mg of  $\text{Al}_2\text{O}_3$  nanoparticles were introduced into the PMMA 950K7% polymer matrix, the overall resist thicknesses were increased to 455nm, 505nm and 562nm respectively. The overall resist 'as spun' thicknesses were 276nm, 331nm and 364nm, when 50mg, 100mg and 150mg of  $\text{Al}_2\text{O}_3$  nanoparticles were introduced into the PMMA 96K7% polymer matrix respectively.

It was clear that the overall resist thickness was increased by the introduction of  $\text{Al}_2\text{O}_3$  nanoparticles into the PMMA polymer matrix. Figure 3 – 9 indicates that the exposure clearing doses of both the PMMA 950k7% and PMMA 96K7% resists increased as the number density of  $\text{Al}_2\text{O}_3$  nanoparticles embedded into the PMMA was increased. The combination of the increased resist thickness and the  $\text{Al}_2\text{O}_3$  nanoparticles resulted in higher exposure doses being required in order for the chain scission process to occur throughout the nanocomposite resist.

As seen in figure 3 – 9, after the resist was developed, the exposure clearing doses of

the PMMA 950K7% loaded with 0mg, 50mg, 100mg and 150mg of  $\text{Al}_2\text{O}_3$  nanoparticles were in the range of  $180 - 210\mu\text{C}/\text{cm}^2$ ,  $210 - 240\mu\text{C}/\text{cm}^2$ ,  $240 - 270\mu\text{C}/\text{cm}^2$  and  $240 - 270\mu\text{C}/\text{cm}^2$  respectively, as determined from the dose scale.

It should be noted that this exposure matrix method only gives a dosage range (e.g  $240 - 270\mu\text{C}/\text{cm}^2$ ) within which complete resist exposure occurs. However, an estimate of the exact clearance dose can be obtained by extrapolation from the data set up to – but not including – the final point (where the resist thickness is zero). this gives clearance doses of  $200\mu\text{C}/\text{cm}^2$ ,  $236\mu\text{C}/\text{cm}^2$ ,  $255\mu\text{C}/\text{cm}^2$  and  $265\mu\text{C}/\text{cm}^2$ , for PMMA 950K 7% loaded with 0mg, 50mg, 100mg and 150mg respectively.



*Figure 3 – 9: PMMA 950K 7% resist clearing doses based on the electron energy stopping powers of the  $\text{Al}_2\text{O}_3$  nanoparticles.*

After the resist was developed, figure 3 – 10 shows the clearing doses of the PMMA 96K 7% loaded with 0mg, 50mg, 100mg and 150mg of  $\text{Al}_2\text{O}_3$  nanoparticles were in the ranges of  $120 - 150\mu\text{C}/\text{cm}^2$ ,  $180 - 210\mu\text{C}/\text{cm}^2$ ,  $180 - 210\mu\text{C}/\text{cm}^2$  and  $210 - 240\mu\text{C}/\text{cm}^2$  respectively.

Even though the  $\text{Al}_2\text{O}_3$  nanoparticle density has been increased from 50mg to 100mg the clearing dose range had not decreased. However, it can be seen from the AFM images that the clearing dose required would be increased, when the PMMA 96K7% was loaded with 100mg of  $\text{Al}_2\text{O}_3$  nanoparticles.



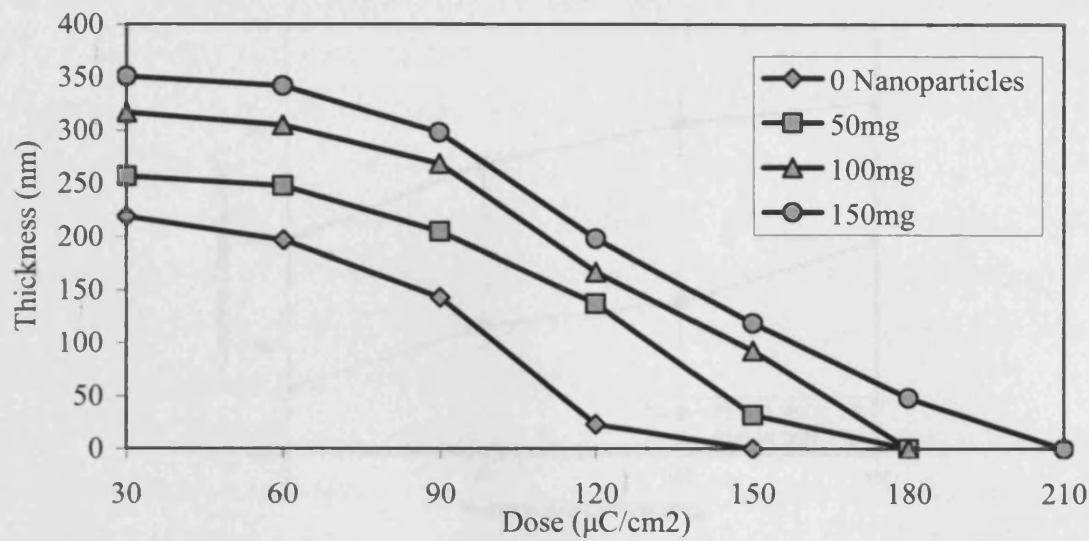


Figure 3 – 10: PMMA 96K 7% resist clearing doses based on the electron energy stopping powers of the  $Al_2O_3$  nanoparticles.

By the extrapolation method demonstrated previously, the gradient of the slope intersects the  $x$  – axis at the doses of  $131\mu C/cm^2$ ,  $160\mu C/cm^2$ ,  $172\mu C/cm^2$  and  $200\mu C/cm^2$  for PMMA 96K 7% loaded with 0mg, 50mg, 100mg and 150mg respectively and is shown in table 3 – 1.

| Sample       | PMMA (MW) | Nanoparticles (mg) | Sensitivity ( $\mu C/cm^2$ ) |
|--------------|-----------|--------------------|------------------------------|
| P950K7%0mg   | 950K      | 0                  | 200                          |
| P950K7%50mg  | 950K      | 50                 | 236                          |
| P950K7%100mg | 950K      | 100                | 255                          |
| P950K7%150mg | 950K      | 150                | 265                          |
| P96K7%0mg    | 96K       | 0                  | 131                          |
| P96K7%50mg   | 96K       | 50                 | 160                          |
| P96K7%100mg  | 96K       | 100                | 172                          |
| P96K7%150mg  | 96K       | 150                | 200                          |

Table 3 – 1: Clearing doses of the PMMA based nanocomposite resists.

Figure 3 – 11 shows the electron beam clearing dose trend that was taken from the data shown in figure 3 – 9 and 10. In both PMMA 950K7% and PMMA 96K7% based nanocomposite resists, it was found that as the number density of  $Al_2O_3$  nanoparticles was increased the clearing dose increased also. This was because of the increased resist thickness and the electrons must be transmitted at a higher exposure dose to overcome the  $Al_2O_3$  nanoparticles as the nanoparticles act as electron scattering centers and consequently decrease the electron momentum [9, 10].

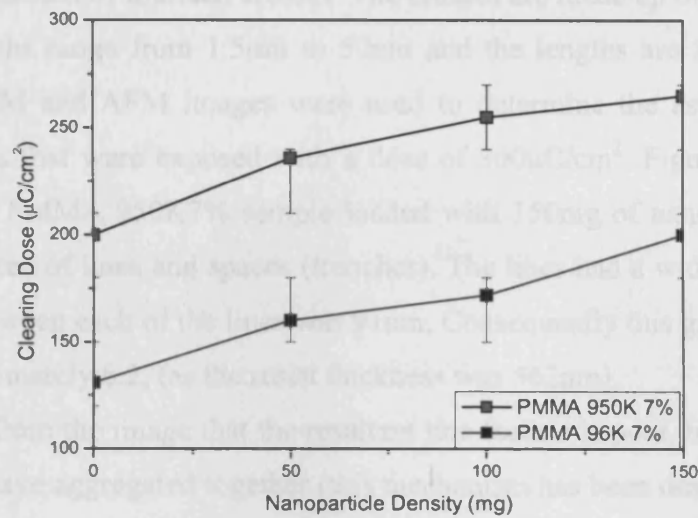


Figure 3 – 11: Electron exposure clearing doses of the PMMA 950K7% and PMMA 96K7% based nanocomposite resists.

### **3.3.2 Characterization of the nanocomposite resists**

Figure 3 – 12 shows an SEM image of the resultant test pattern that was directly written to characterize the performance of the nanocomposite resist.

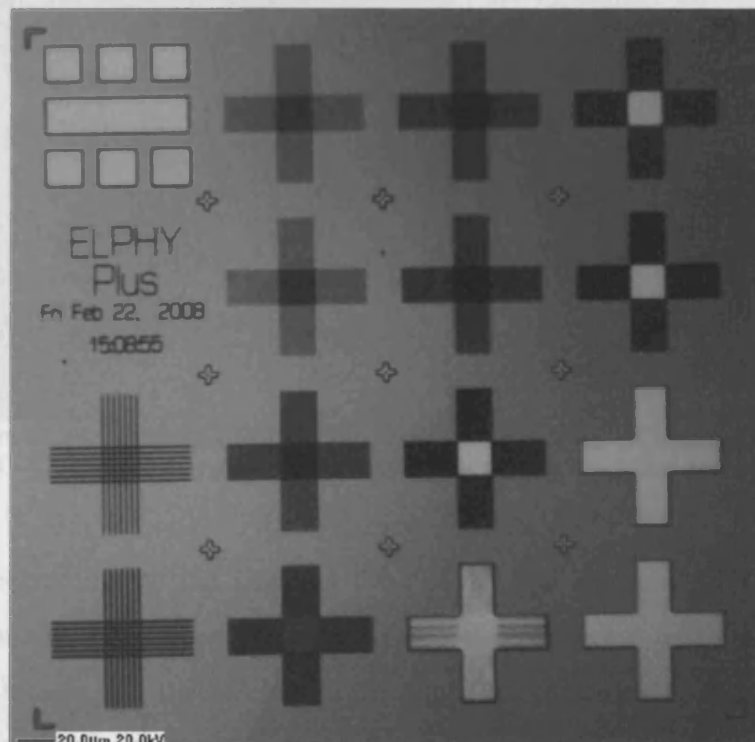
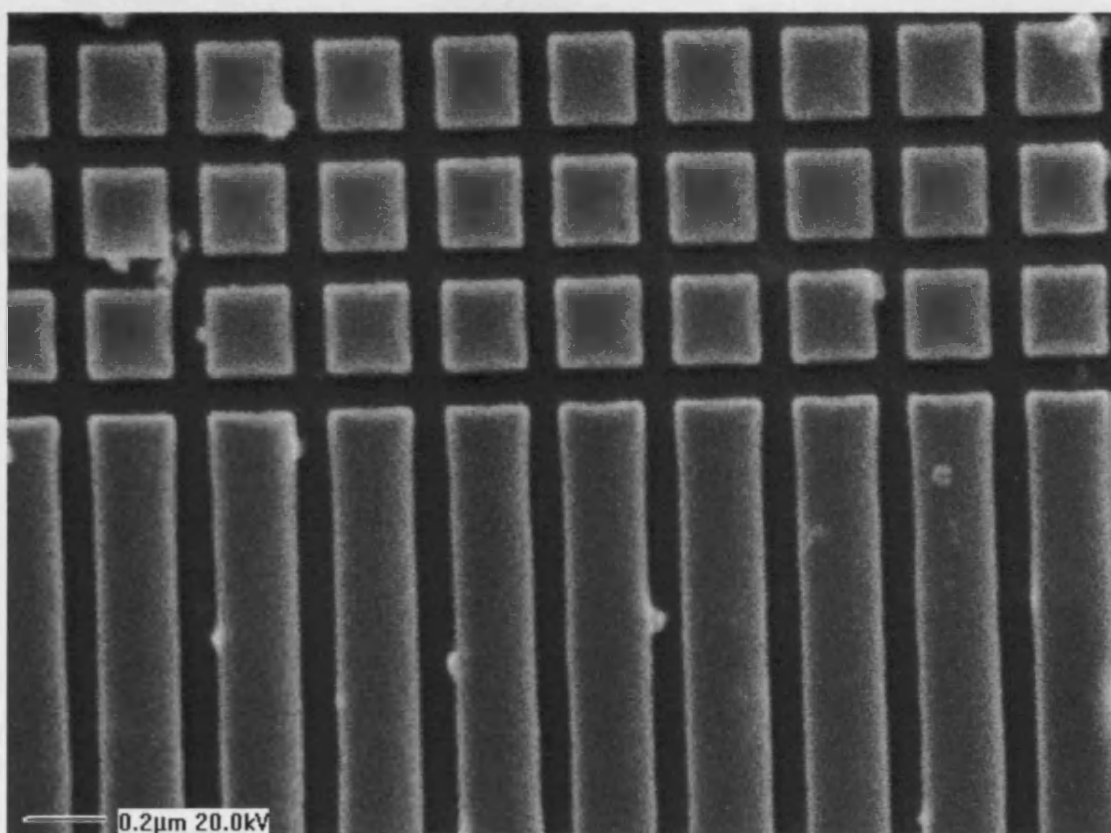


Figure 3 – 12: SEM image of the e-beam characterization pattern in the PMMA 950K 7% nanocomposite resist.

The pattern consisted of fourteen crosses. The crosses are made up of a series of lines, where the widths range from  $1.5\mu\text{m}$  to  $50\text{nm}$  and the lengths are  $25\mu\text{m}$ . All of the subsequent SEM and AFM images were used to determine the aspect ratio of the developed lines that were exposed with a dose of  $300\mu\text{C}/\text{cm}^2$ . Figure 3 – 13 shows features in the PMMA 950K7% sample loaded with 150mg of nanoparticles. These features consisted of lines and spaces (trenches). The lines had a width of  $185\text{nm}$  and the spacing between each of the lines was  $91\text{nm}$ . Consequently this gave a high aspect ratio of approximately 6.2, (as the resist thickness was  $562\text{nm}$ ).

It can be seen from the image that the resultant line feature is poor, because the  $\text{Al}_2\text{O}_3$  nanoparticles have aggregated together (this mechanism has been described in chapter two) and they have penetrated the surface of the feature.



*Figure 3 – 13: SEM image of PMMA 950K 7% loaded with 150mg of  $\text{Al}_2\text{O}_3$  nanoparticles.*

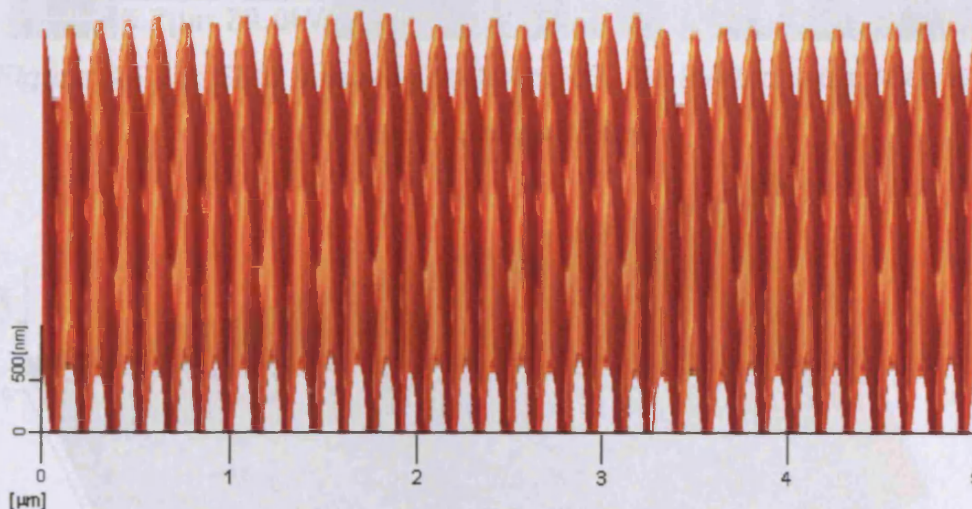
This has occurred due to the fact that the PMMA that surrounds the aggregation of  $\text{Al}_2\text{O}_3$  nanoparticles has been exposed, by the electron beam and the chain scission process has broken the PMMA molecule chain that surrounds the aggregation. By dissolution in the developing stage of the process, the PMMA has been removed. Therefore, the nanoparticles have not only affected the sensitivity of the



nanocomposite resist have also affected the overall shape of the feature. However, it can be seen that the interaction of the electron beam does not modify the shape of the nanoparticle aggregation.

Even though this resist achieves a high aspect ratio of 6.3, this resist can not be used for lift – off because the features created in this nanocomposite resist are poor. For example, if the user employed this resist to fabricate structures such as gates for transistors (such as MOSFETs, HEMTs, etc), then the current that is applied to the gate may destroy the structure because the geometry of the gate length has decreased where the nanoparticle aggregation has affected the pattern. Therefore, the electric fields will be increased at these points.

Figure 3 – 14 shows an AFM image of the nanocomposite resist. The finite radius of the AFM tip gave these ridges their rounded profile (all of the AFM images for the PMMA 950K7% samples are shown in appendix B).



*Figure 3 – 14: AFM image of the PMMA 950K 7% loaded with 150mg of  $\text{Al}_2\text{O}_3$  nanoparticles.*

The SEM image of PMMA 950K7% loaded with 100mg of  $\text{Al}_2\text{O}_3$  nanoparticles is shown in figure 3 – 15. The image confirmed that the feature size of each line was 185nm with a spacing of 92nm. This gave rise to an aspect ratio of 5.6. It can be seen that this area of the nanocomposite resist shows fewer nanoparticle aggregations than the previous sample of figure 3 – 14. However, the PMMA 950K 7% resist is still over loaded with  $\text{Al}_2\text{O}_3$  nanoparticles. Figure 3 – 16 shows an AFM of the nanocomposite resist. It is evident that the ridges of the resist have been improved with the reduction of  $\text{Al}_2\text{O}_3$  nanoparticles. It shows improved quality of the lines, where the ridges are straight and have fewer nanoparticle aggregations.



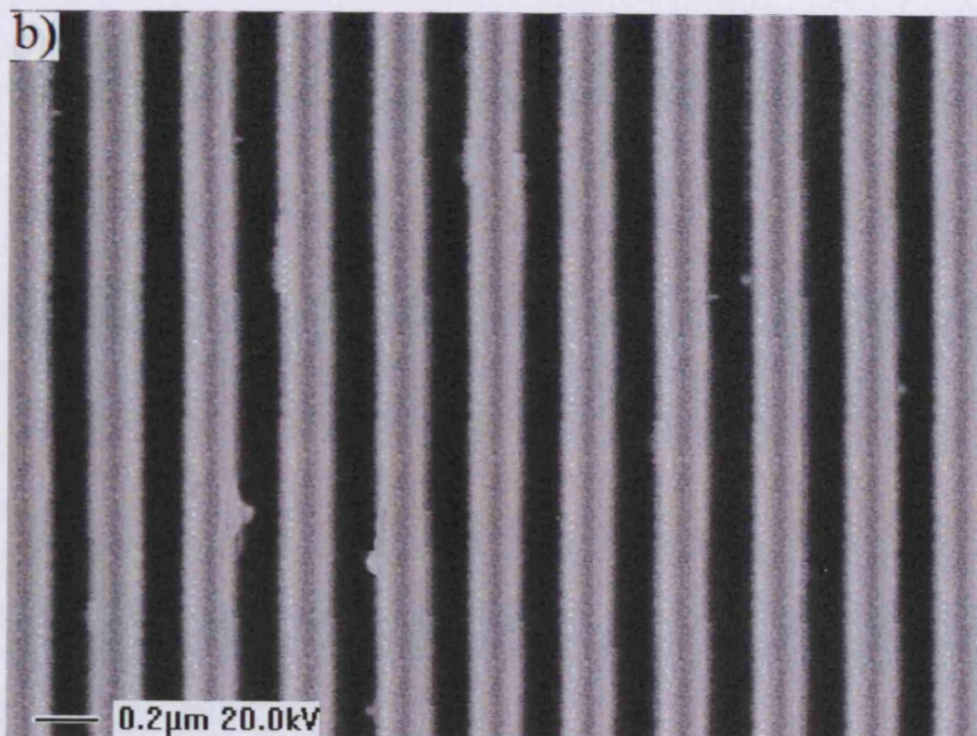


Figure 3 – 15: SEM image of PMMA 950K 7% loaded with 100mg of  $\text{Al}_2\text{O}_3$  nanoparticles.

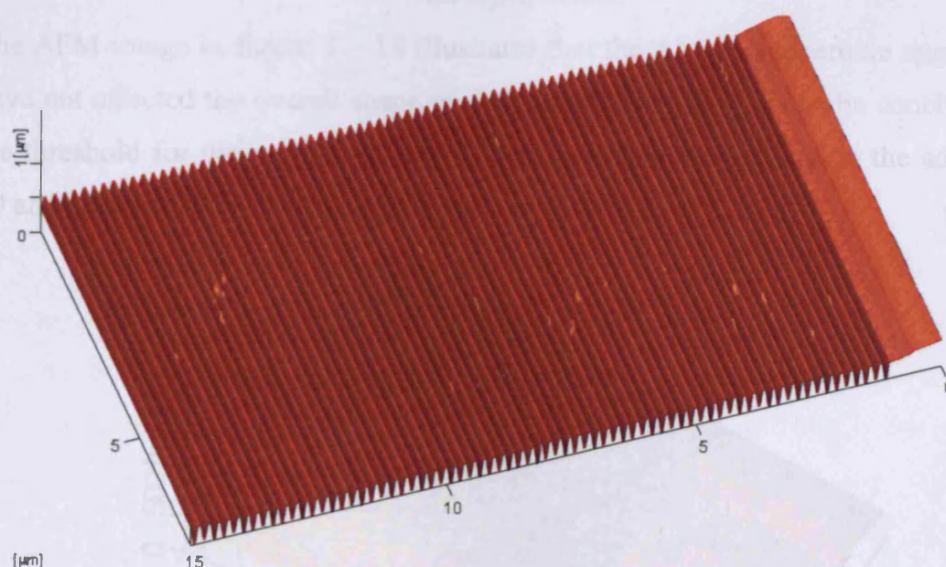


Figure 3 – 16: AFM image of PMMA 950K 7% loaded with 100mg of  $\text{Al}_2\text{O}_3$  nanoparticles.

Figure 3 – 17 shows an SEM image of the PMMA 950K 7% loaded with 50mg of  $\text{Al}_2\text{O}_3$  nanoparticles. Here the aspect ratio was 5.05 and the corresponding feature size of each line width was 180nm with spacings of 90nm. The SEM image shows that the nanoparticle aggregations are eliminated, achieved by further reducing the nanoparticle number density.

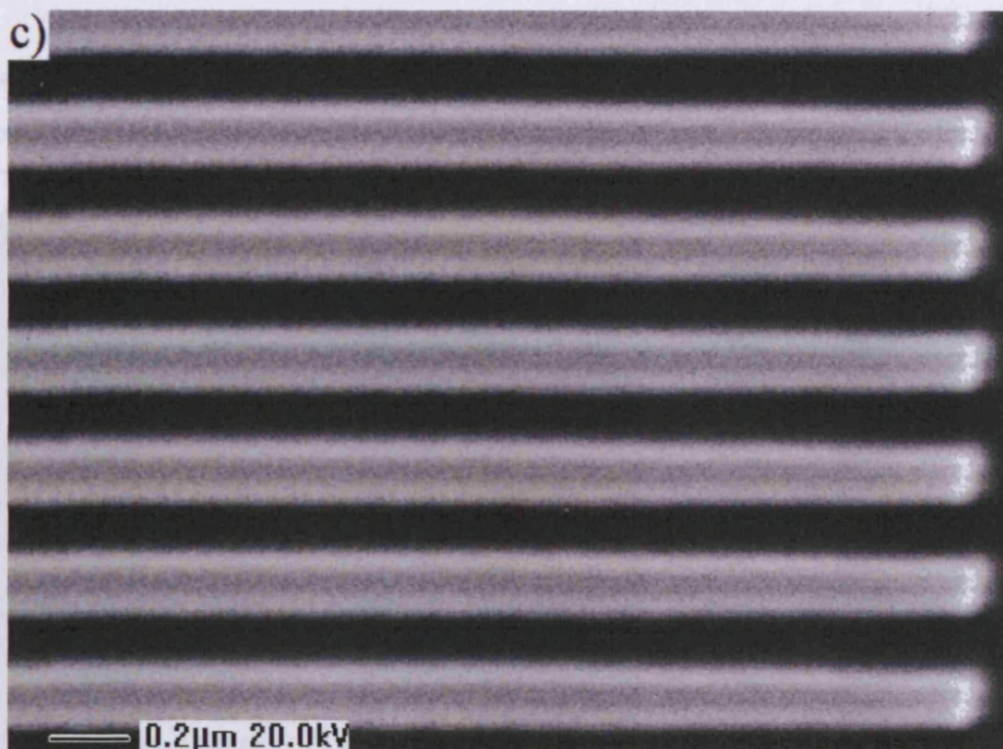


Figure 3 – 17: SEM image of PMMA 950K 7% loaded with 50mg of  $\text{Al}_2\text{O}_3$  nanoparticles.

The AFM image in figure 3 – 18 illustrates that the  $\text{Al}_2\text{O}_3$  nanoparticle aggregations have not affected the overall shape of the feature. Therefore, it can be concluded that the threshold for the number density of nanoparticles corresponds to the addition of 50 and 100mg of  $\text{Al}_2\text{O}_3$  nanoparticle per 1g of PMMA.

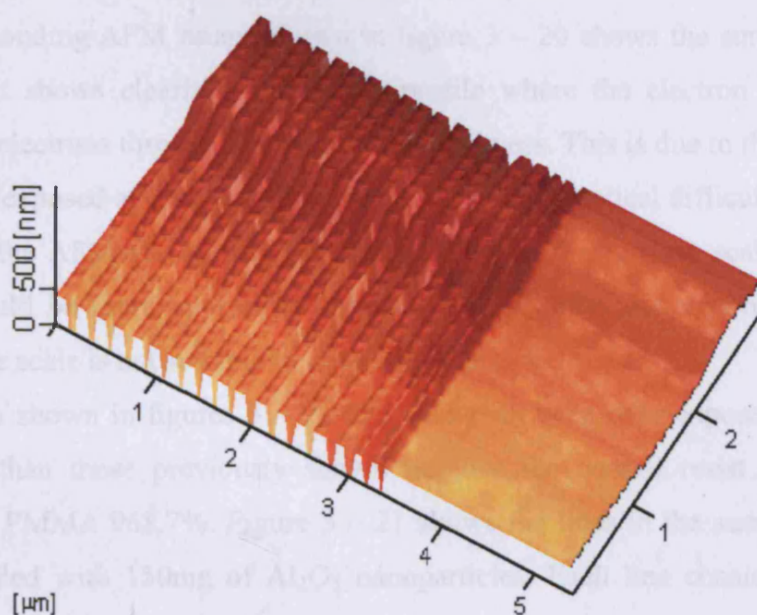
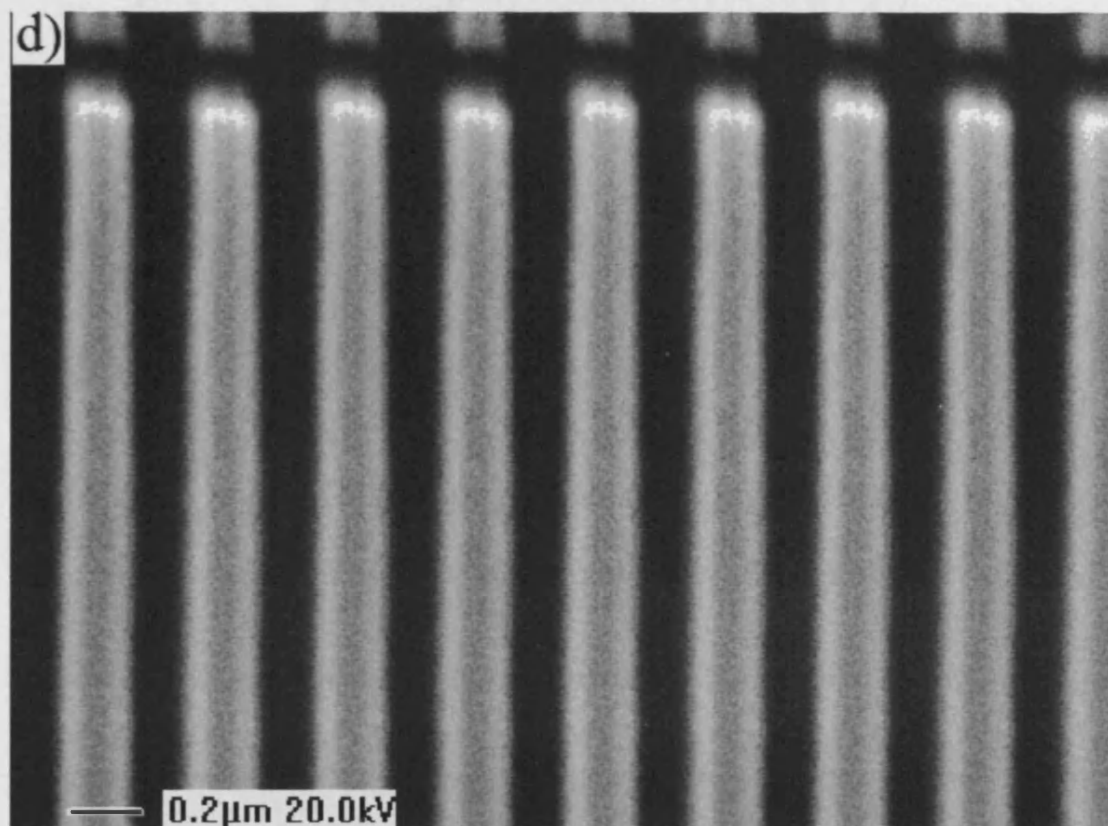


Figure 3 – 18: AFM image of PMMA 950K 7% loaded with 50mg of  $\text{Al}_2\text{O}_3$  nanoparticles.



The SEM image in figure 3 – 19 shows the unloaded PMMA 950K 7% resist. The aspect ratio is 4.4 and the width of the lines was 185nm with spacings of 91nm.



*Figure 3 – 19: SEM image of unloaded PMMA 950K 7%.*

The corresponding AFM image shown in figure 3 – 20 shows the surface profile of the resist. It shows clearly a grey scale profile where the electron beam has not transmitted electrons through the entire resist thickness. This is due to the fact that this sample was exposed at a varying dose scale. There are practical difficulties associated with using the AFM and it was felt that directly writing a dose scale using 20µm squares would be more appropriate as shown in the previous section. However, a varying dose scale is not suitable to determine the aspect ratio.

The features shown in figures 3 – 21 to 24 have all been over exposed by a greater percentage than those previously shown because the overall resist thickness was reduced for PMMA 96K7%. Figure 3 – 21 shows the lines in the sample of PMMA 96K7% loaded with 150mg of Al<sub>2</sub>O<sub>3</sub> nanoparticles. Each line consisted of feature sizes of 180nm and the trench between the lines was 91nm. This gave an aspect ratio was 4, with the resist thickness of 364nm.



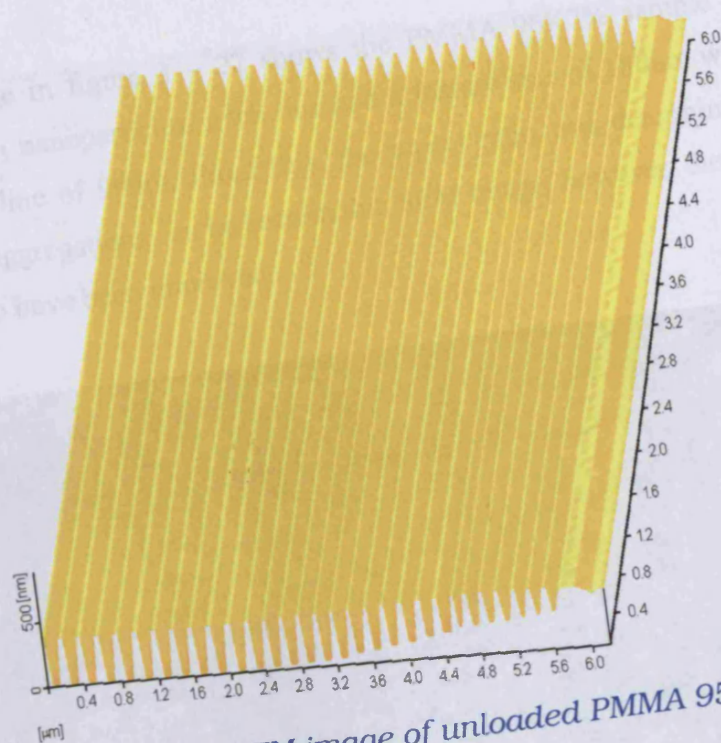


Figure 3 – 20: AFM image of unloaded PMMA 950K 7%.

However, like the sample of PMMA 950K7% loaded with 150mg of  $\text{Al}_2\text{O}_3$  nanoparticles the quality of the lines is poor for similar reasons given for that sample.

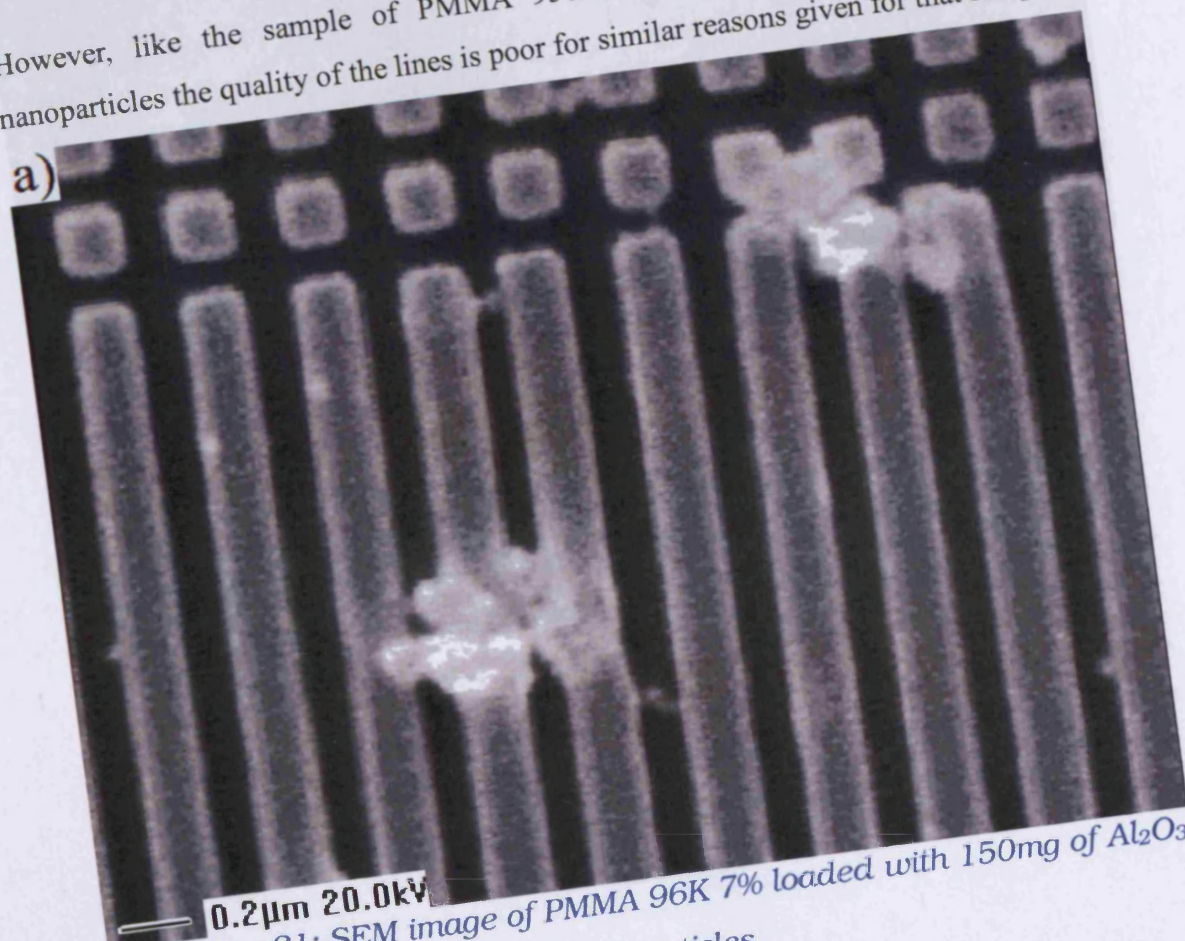
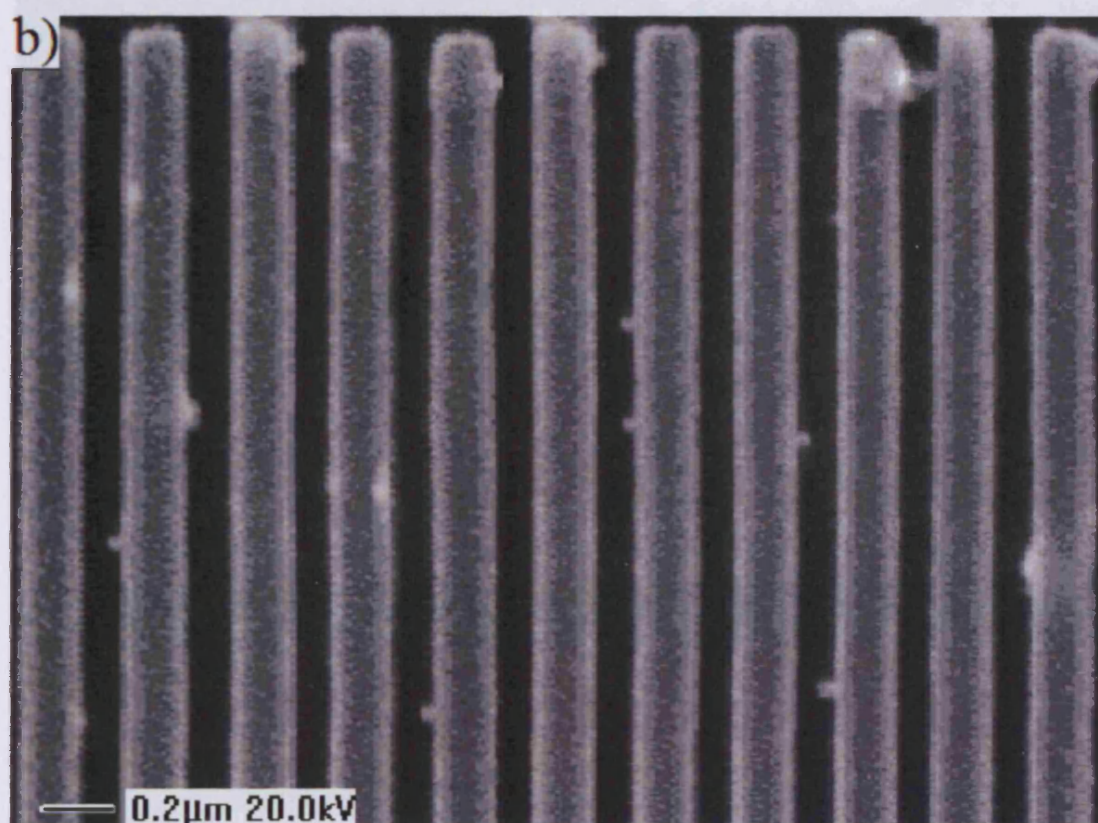


Figure 3 – 21: SEM image of PMMA 96K 7% loaded with 150mg of  $\text{Al}_2\text{O}_3$  nanoparticles.

The SEM image in figure 3 – 22 shows the PMMA 96K7% sample loaded with 100mg of  $\text{Al}_2\text{O}_3$  nanoparticles. Each line had a feature size of 180nm with a spacing between each line of 90nm. From this, the aspect ratio was determined to be 3.6. Nanoparticle aggregations can be seen in this SEM image, however, the quality of the lines appear to have been improved.



*Figure 3 – 22: SEM image of PMMA 950K 7% loaded with 100mg of  $\text{Al}_2\text{O}_3$  nanoparticles.*

Figure 3 – 23 shows a similar image of the PMMA 96K 7% loaded with 50mg of  $\text{Al}_2\text{O}_3$  nanoparticles. In this case the aspect ratio was 3 and the feature sizes of each line was 188nm with a spacing of 92nm. The corresponding image of figure 3 – 24 shows the unloaded PMMA 96K 7% e-beam resist. Here the aspect ratio was 2.8. The feature size of each line width was 187nm with a spacing of 90nm. This image shows that the nanoparticle aggregations at the surface are greatly reduced, when the concentration of the  $\text{Al}_2\text{O}_3$  nanoparticles are decreased.

*Figure 3 – 24: SEM image of unloaded PMMA 96K 7%.*



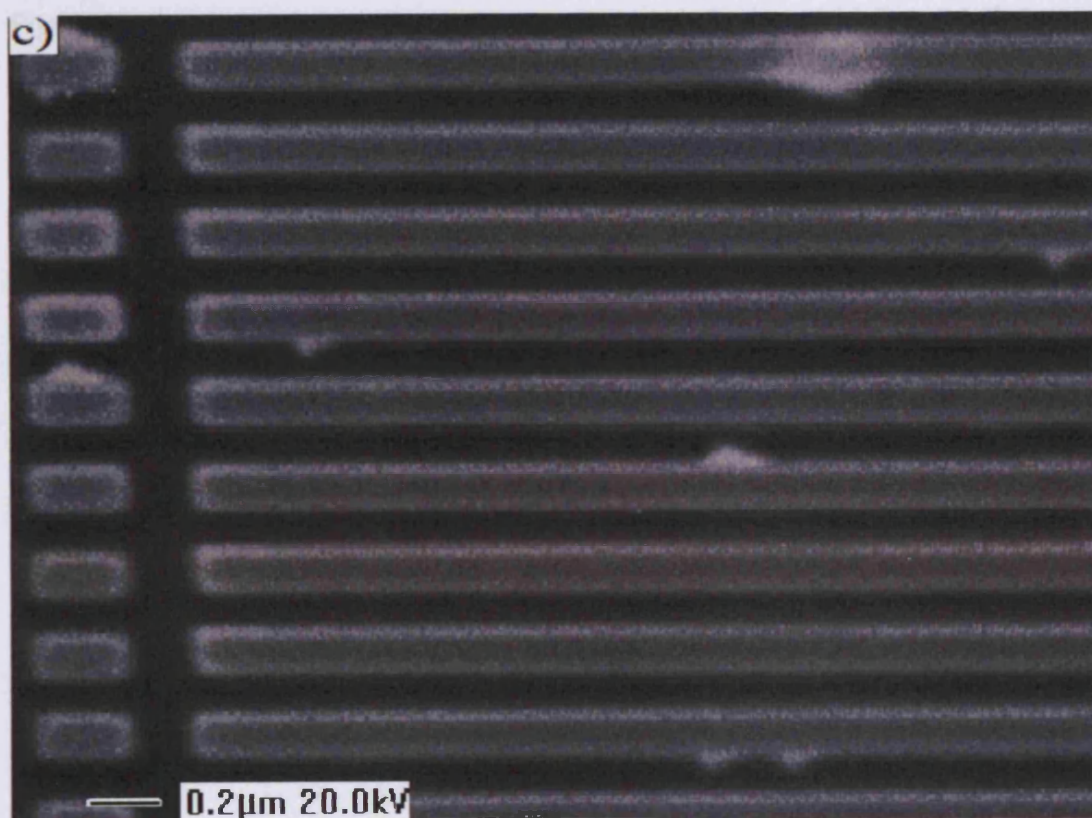


Figure 3 - 23: SEM image of PMMA 96K 7% 50mg sample.

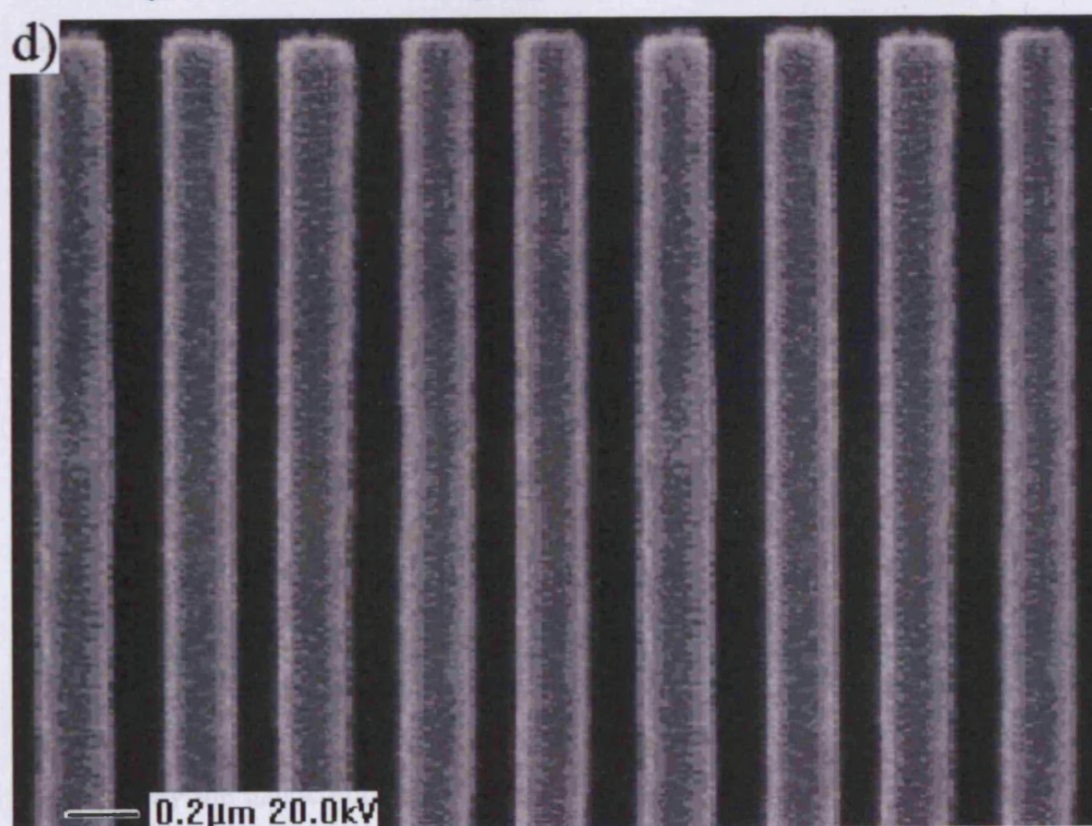
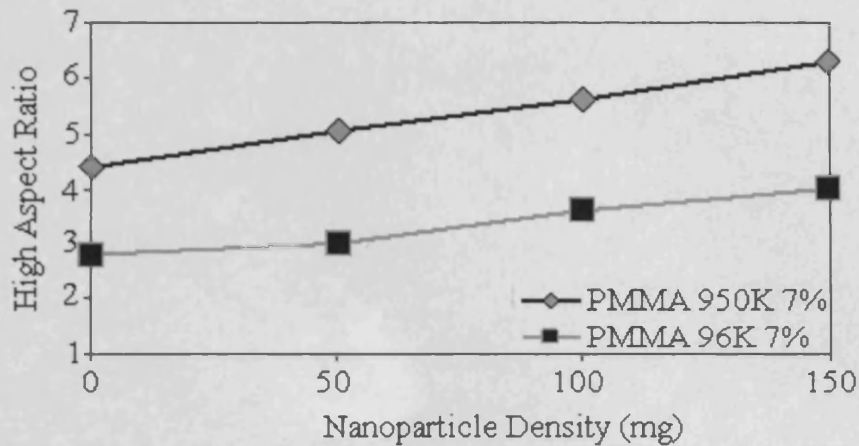


Figure 3 - 24: SEM image of unloaded PMMA 96K 7%.

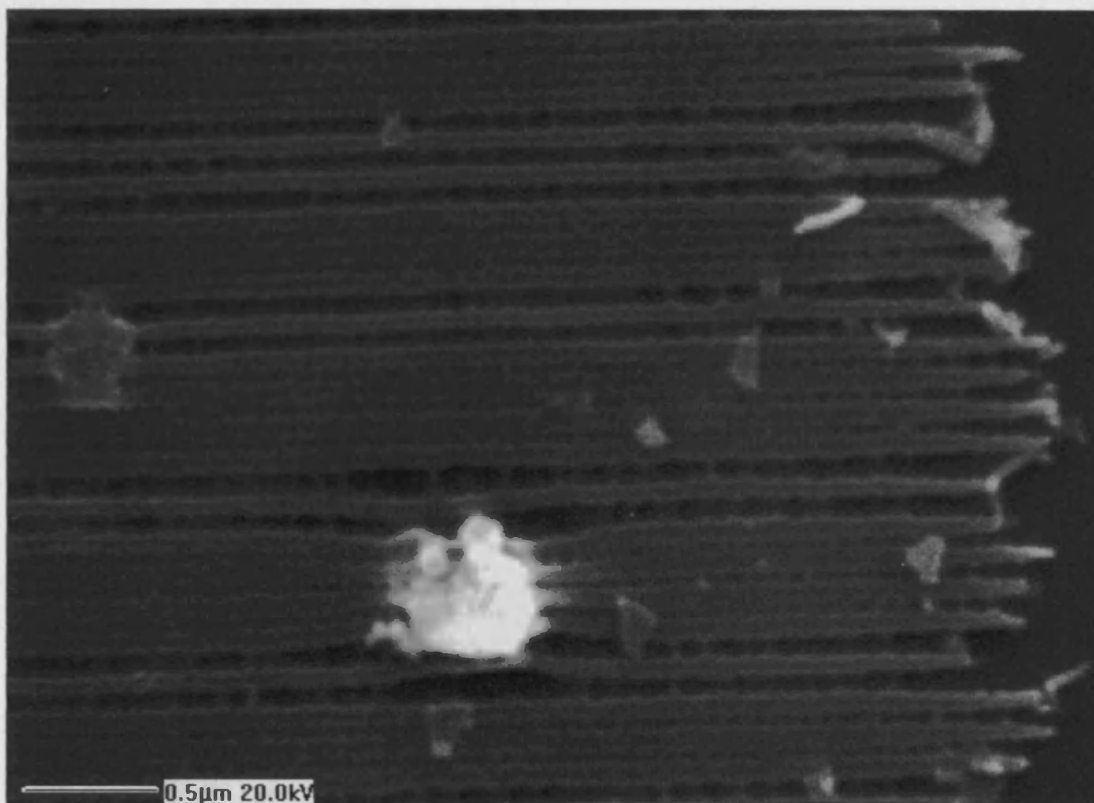
Figure 3 – 25 shows the relationship between the  $\text{Al}_2\text{O}_3$  nanoparticle number density and the corresponding aspect ratio. The PMMA 950K samples have the higher aspect ratio due to the fact that the PMMA molecule is considerably larger than that of PMMA 96K, thus producing a thicker resist.



*Figure 3 – 25: High aspect ratios of the PMMA 950K and 96K based nanocomposite resists.*

It is clear that the addition of the  $\text{Al}_2\text{O}_3$  nanoparticles has increased the overall resist thickness. Therefore, smaller resultant features with a thicker resist can be achieved as a result of the interaction of the incident electron beam with the  $\text{Al}_2\text{O}_3$  nanoparticles. This in turn has the effect of decreasing the momentum of the secondary electrons penetrating the nanocomposite resist. In all of the samples shown so far, the features on the developed resist have remained intact. The next images highlight the problems associated with developed samples that have suffered significantly from the proximity effect.

Figure 3 – 26 shows the lines fabricated in PMMA 950K7% loaded with 150mg of  $\text{Al}_2\text{O}_3$  nanoparticles. Each line consists of feature sizes of 70nm. However, most of the periodic spacing between each line has completely diminished, suggesting that the resist has collapsed. It can be seen clearly that the  $\text{Al}_2\text{O}_3$  nanoparticles have bound the PMMA polymer together, which have appeared to make the molecule more ridged. Therefore, the resist was compromised by the proximity effect. The secondary electrons have under cut the nanocomposite resist from the Au surface and consequently the nanocomposite resist has toppled over. The SEM image shows the quality of the features is at its poorest, as the edge profiles are exceptionally rough.



*Figure 3 – 26: SEM image of collapsed features in PMMA 950K 7% loaded with 150mg of Al<sub>2</sub>O<sub>3</sub> nanoparticles resist.*

The SEM images of figure 3 – 27 and 28 show that the lines in the sample of PMMA 950K7% loaded with 100mg and 50mg of Al<sub>2</sub>O<sub>3</sub> nanoparticles were not periodically spaced, hence, the nanocomposite resist has collapsed. However, the PMMA 950K 7% loaded with 100mg of Al<sub>2</sub>O<sub>3</sub> nanoparticles has not collapsed completely, but it is suspected that the lines have delaminated from the Au surface and acted like a spring and curved back to where they are anchored. It can be seen more clearly that the 50mg sample has done this as well.

The delamination is probably due to the immersion angle of the sample when being developed. Both samples have line widths of 70nm. Again, nanoparticle aggregations can be seen in the sample of PMMA 950K7% loaded with 100mg of Al<sub>2</sub>O<sub>3</sub> nanoparticles, which at the 50 – 100mg threshold. However, there are no nanoparticle aggregations in the PMMA 950K7% loaded 50mg of Al<sub>2</sub>O<sub>3</sub> nanoparticles. The bulk of the lines in each sample, show that the side of the walls are relatively smooth when compared to the PMMA 950K7% loaded with 150mg of Al<sub>2</sub>O<sub>3</sub> nanoparticles.

*Figure 3 – 28: SEM image of collapsed features in PMMA 950K 7% loaded with 50mg of Al<sub>2</sub>O<sub>3</sub> nanoparticles resist.*



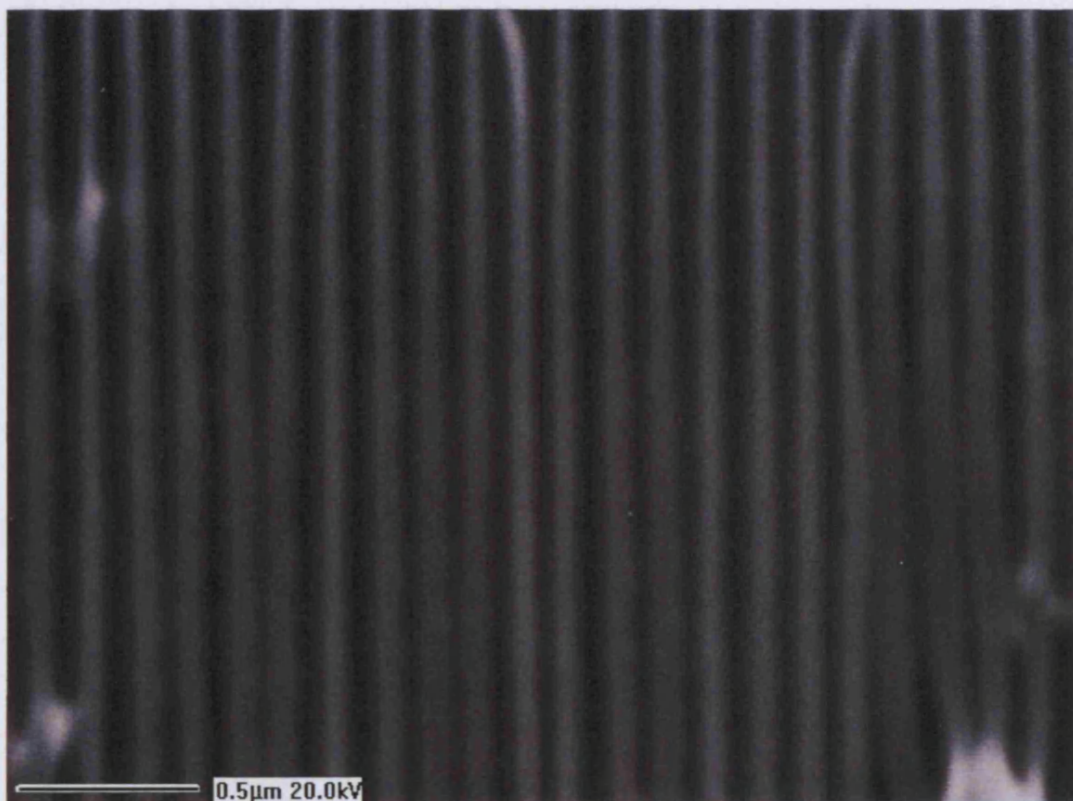


Figure 3 – 27: SEM image of collapsed features in PMMA 950K 7% loaded with 100mg of  $\text{Al}_2\text{O}_3$  nanoparticles resist.

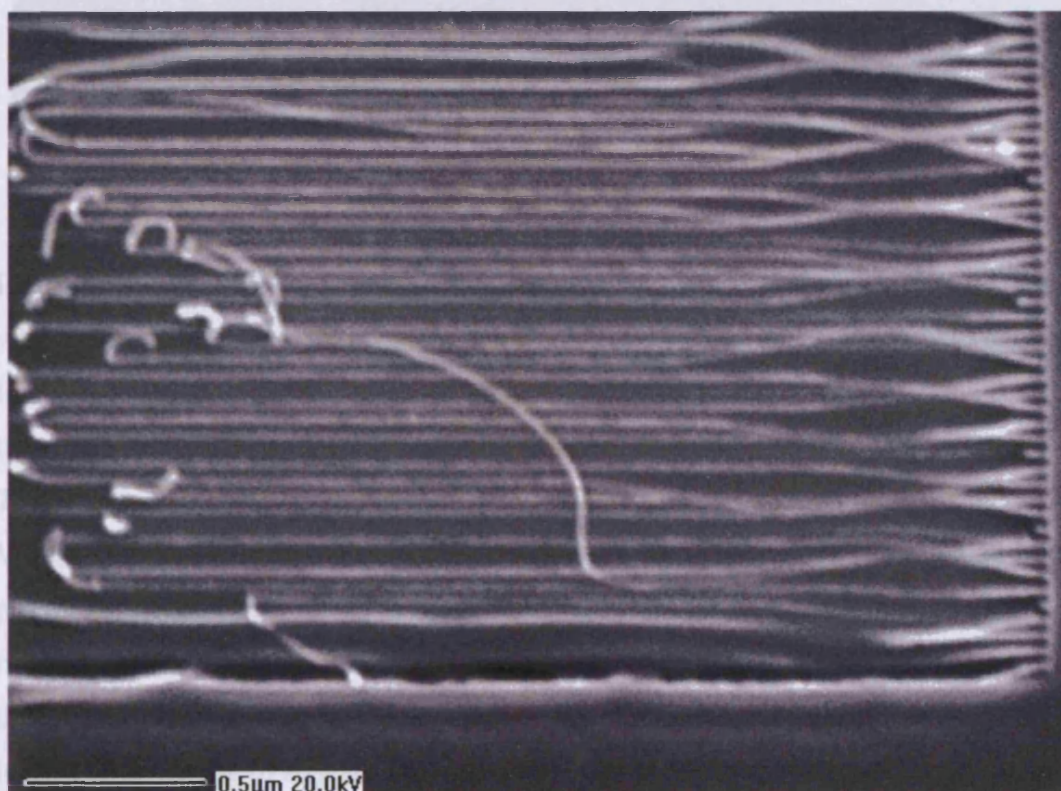
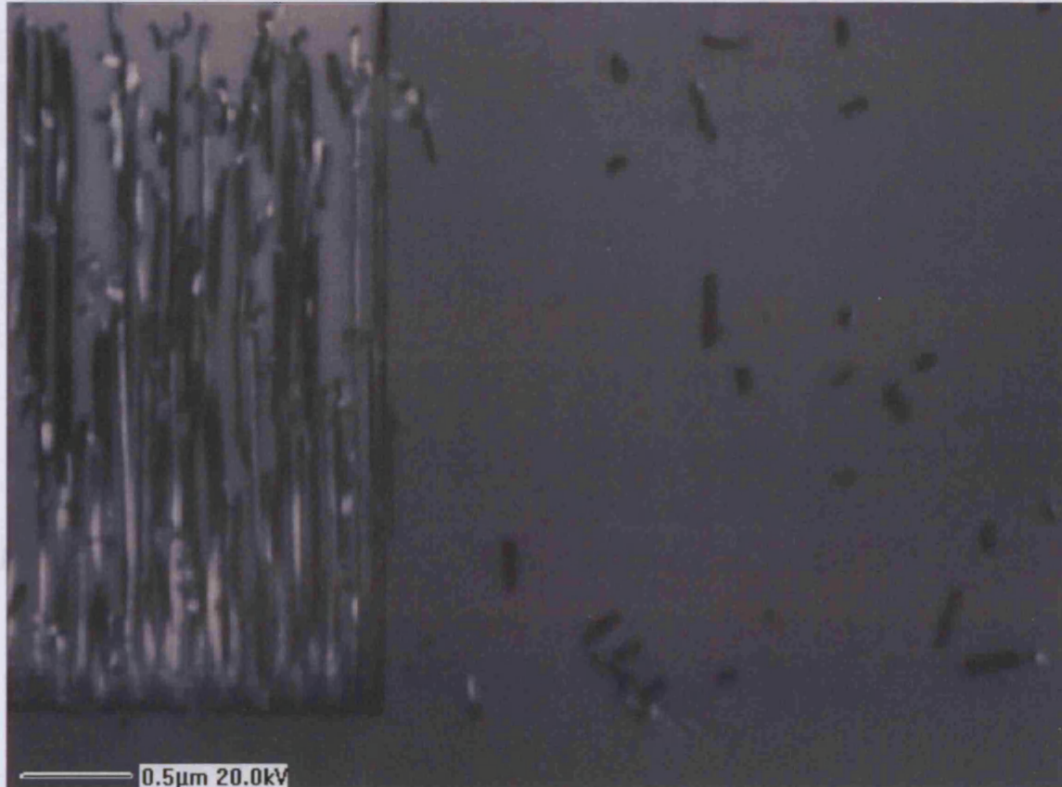


Figure 3 – 28: SEM image of collapsed features in PMMA 950K 7% loaded with 50mg of  $\text{Al}_2\text{O}_3$  nanoparticles resist.

In the sample with the unloaded PMMA 950k7%, there are no lines, as they have completely collapsed. This can be seen in figure 3 – 29. This is due to the fact that the nanocomposite resist is too thick to control the secondary electrons from transmitting laterally as seen in figure 3 – 1. Clearly, the presence of the nanoparticles is impacting on the proximity effect.



*Figure 3 – 29: SEM image of collapsed features in unloaded PMMA 950K 7% resist.*

Figure 3 – 30 shows that most of the lines in the sample of PMMA 96K7% loaded with 150mg of  $\text{Al}_2\text{O}_3$  nanoparticles have collapsed, where the spacing between each line is not periodic. In some instances, the lines appear to have snapped. This is due to the fact that the  $\text{Al}_2\text{O}_3$  nanoparticles have been dispersed into the PMMA randomly. Therefore, it is suspected that they have aggregated in random parts of the resist. Where there are no nanoparticles, the PMMA is at its weakest and is affected by the proximity effect. Each line consists of line widths of 70nm. The edge roughness of the lines was due to the fact that the nanoparticles have aggregated out of the surface of the resist. The SEM image of figure 3 – 31 shows the sample of PMMA 96K7% loaded with 100mg of  $\text{Al}_2\text{O}_3$  nanoparticles. The lines are relatively uniform. However, the spacing between them is not periodic, suggesting that they have toppled over because the sample was over exposed.



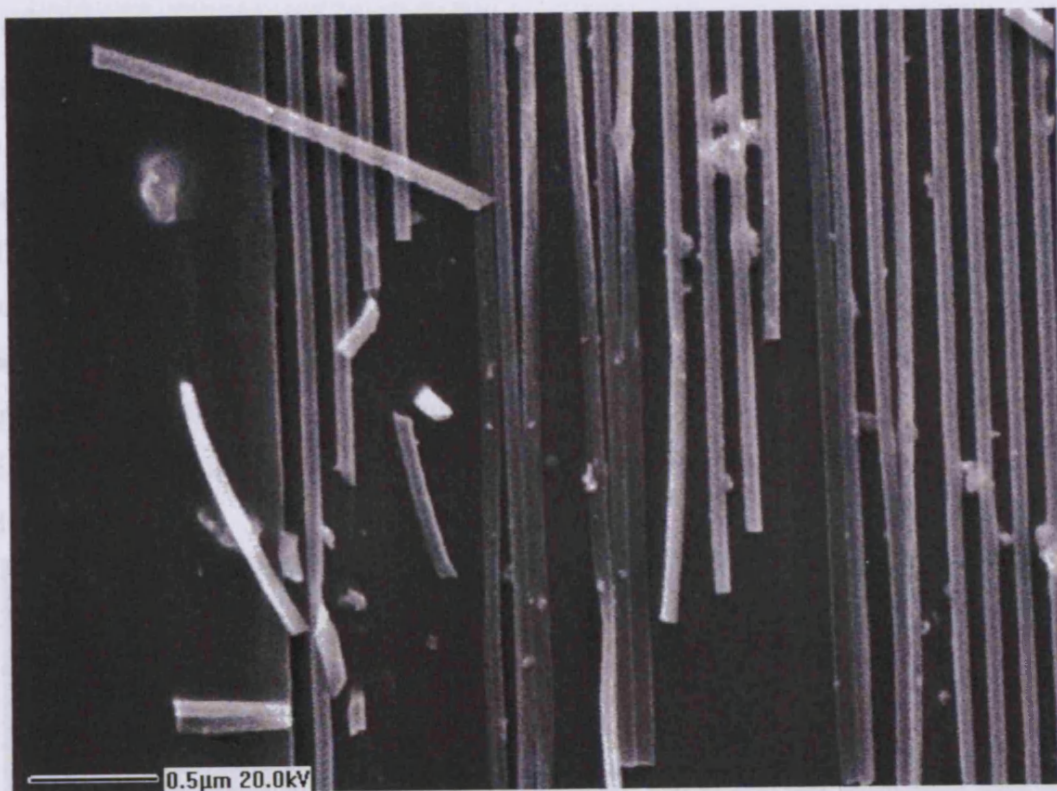


Figure 3 – 30: SEM image of collapsed features in PMMA 96K 7% loaded with 150mg of  $\text{Al}_2\text{O}_3$  nanoparticles resist.

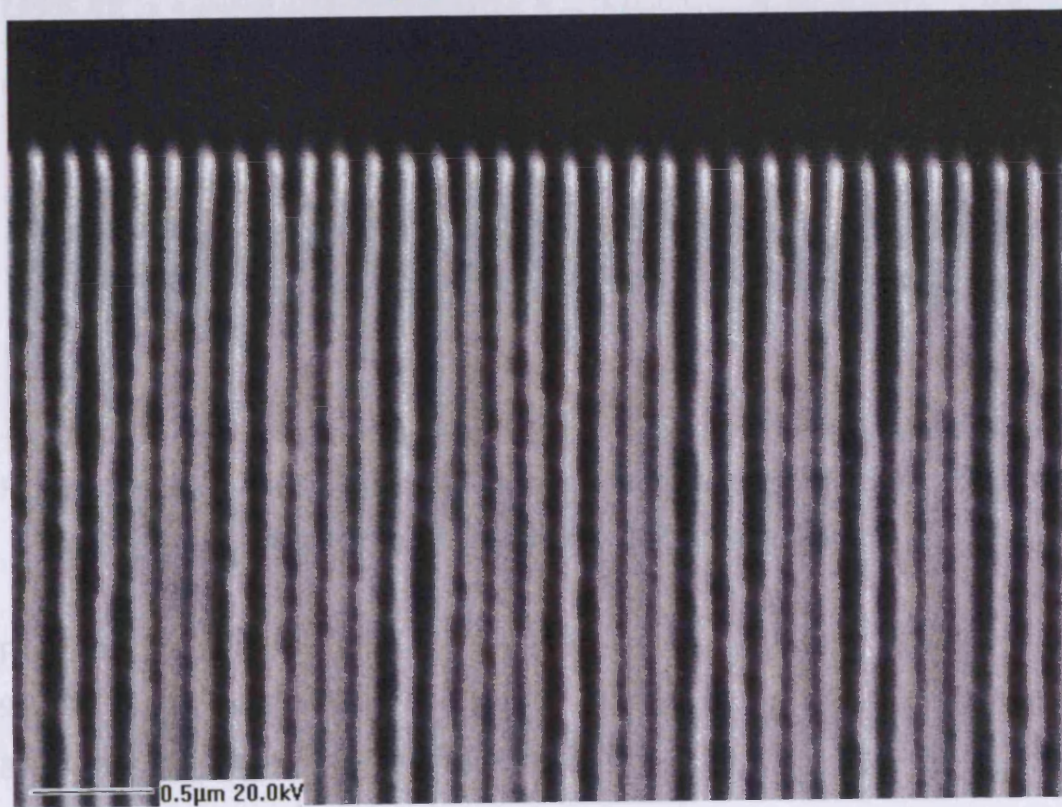
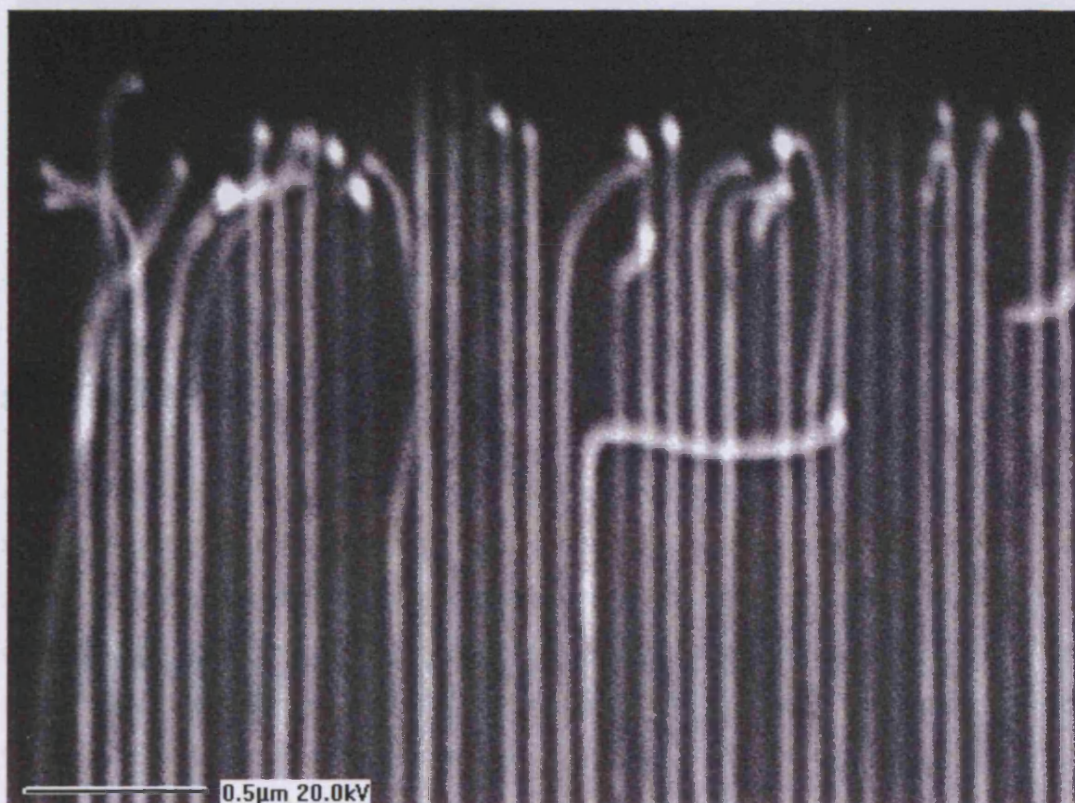


Figure 3 – 31: SEM image of collapsed features in PMMA 96K 7% loaded with 100mg of  $\text{Al}_2\text{O}_3$  nanoparticles resist.



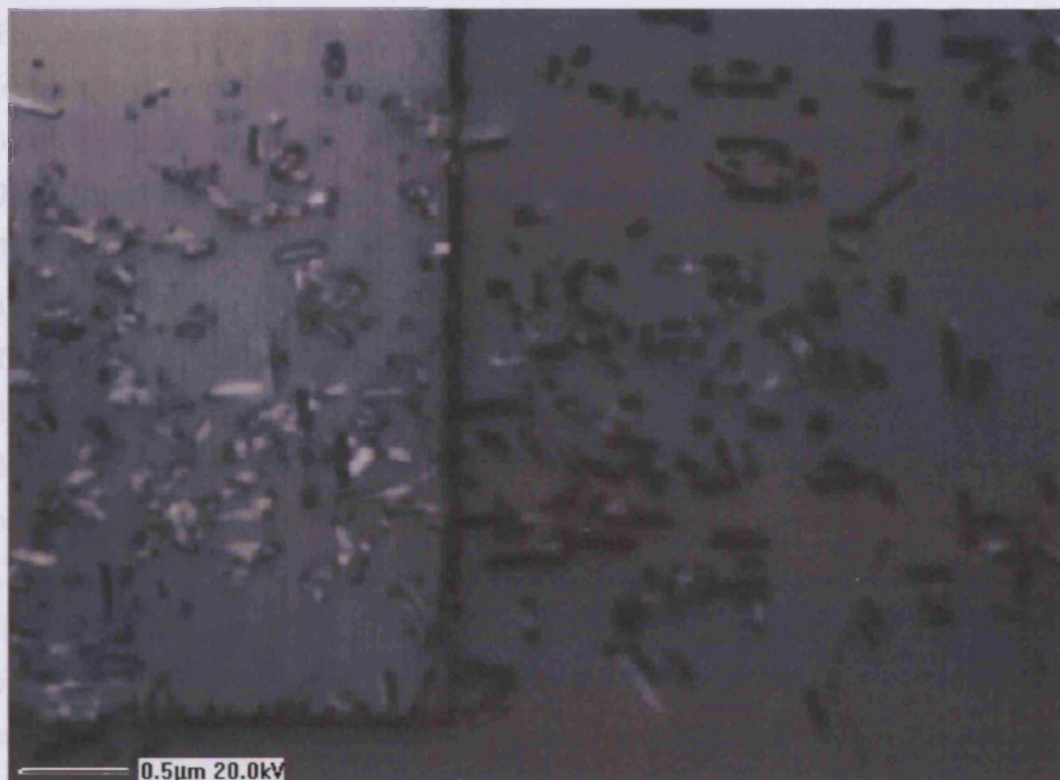
The line widths of each line is 65nm, but the side of the walls appear to be curved, since the image is out of focus, it is difficult to determine whether this is due to the nanoparticle aggregation or that the lines are becoming delaminated from the Au surface.

The tip of each line in sample of PMMA 96K7% loaded with 50mg of  $\text{Al}_2\text{O}_3$  nanoparticles have delaminated from the Au surface; hence the lines have not completely collapsed. This can be seen in figure 3 – 32. However, they appear to be uniform with periodic spacing between each line. Each line consisted of line widths of 65nm. The lines are straight and the aggregations of the  $\text{Al}_2\text{O}_3$  nanoparticles were not detected.



*Figure 3 – 32: SEM image of collapsed features in PMMA 96K 7% loaded with 50mg of  $\text{Al}_2\text{O}_3$  nanoparticles resist.*

Figure 3 – 33 shows that there are no lines in the sample of the unloaded PMMA 96k7%, as they have completely collapsed. This has occurred for the same reasons given for sample of the unloaded PMMA 950K7%.



*Figure 3 – 33: SEM image of collapsed features in unloaded PMMA 96K 7% resist.*

### **3.4 Summary**

A novel electron beam resist has been demonstrated by incorporating  $\text{Al}_2\text{O}_3$  nanoparticles with a diameter of 15 – 25nm into the PMMA polymer matrix. By introducing these additives the structural properties of the resist was improved and consequently improved the aspect ratio of the resultant features. In order to achieve faster write times, the molecular weight of the PMMA polymer was decreased from 950K7% to 96K7%. Comparing the case of PMMA 950K 7% with PMMA 96K 7% the thicknesses were 407nm and 228nm respectively. The resist clearing doses were 200 and  $131\mu\text{C}/\text{cm}^2$  respectively. Therefore, the clearing dose of the PMMA polymer was increased at the cost of the higher aspect ratio.

The resist clearing doses were 265, 255 and  $236\mu\text{C}/\text{cm}^2$  for when 150mg, 100mg and 50mg of  $\text{Al}_2\text{O}_3$  nanoparticles were introduced into the PMMA 950K7% polymer matrix respectively. However, when 150mg, 100mg and 50mg of  $\text{Al}_2\text{O}_3$  nanoparticles were introduced into the PMMA 96K7% polymer matrix, the resist clearing doses were 200, 172 and  $160\mu\text{C}/\text{cm}^2$  respectively.

The increased number density of  $\text{Al}_2\text{O}_3$  nanoparticles in the PMMA required an increase in the clearing dose. The presence of the nanoparticles had a quenching effect on the electrons within the resist responsible for 'exposing' the resist. Consequently, this affected the outcome of the developed features, to the extent that in some cases, the features produced were completely deformed. In some instances, nanoparticle aggregations affected the quality of the feature obtained.

The amount of deformation was dependent on the nanoparticle density. When the density was at its highest (150mg of  $\text{Al}_2\text{O}_3$  nanoparticles) the lines had the most deformations whereas the deformation was at its lowest when the density was 50mg of  $\text{Al}_2\text{O}_3$  nanoparticles.

Comparing the PMMA 950K7% samples to the PMMA 96K7% samples, it was found that the aspect ratio of the P950K7% nanocomposite resist from 150mg to 0mg was 6.3, 5.6, 5.05 and 4.4 respectively, whereas it was 4, 3.6, 3 and 2.8 for the P96K7% samples respectively. It was found that the  $\text{Al}_2\text{O}_3$  nanoparticles had prevented the lines from collapsing by blocking the arbitrary scattering secondary electrons from transmitting laterally throughout the nanocomposite resist. Thus, the proximity effect was reduced.

It was found that as the quantity of the nanoparticles was increased, the line edge roughness (LER) also increased. LER needs to be as small as possible as to not compromise the pattern. Therefore, 50mg of  $\text{Al}_2\text{O}_3$  nanoparticles would be the optimum nanocomposite resist scheme.

It was found in all samples that, when the line widths were reduced beyond 70nm they had collapsed. However, the lines in the nanocomposite resist had toppled over and thus not completely destroyed. It is suspected that the  $\text{Al}_2\text{O}_3$  nanoparticles have affected the mechanical properties of the PMMA by causing the molecular chain of the polymer to bond with the  $\text{Al}_2\text{O}_3$  nanoparticles [12]. All the lines are completely destroyed in both of the unloaded samples of PMMA 950 and 96K 7%.

### **3.5 References**

- [1] K. E. Gonsalves, L. Merhari, H. Wu, Y. Hu, 'Organic – inorganic nanocomposite: unique resists for nanolithography', Advanced Materials, Vol 13, No 13, (2001).
- [2] R. L. Dean, H. Y. Lem, C. A. Sauer, H. Chang, 'PBS resist profile studies for sub



- micron mask lithography', Proc. SPIE, vol. 2322, 102 (1994).
- [3] Zeonrex electron chemicals, 'ZEP520, high resolution positive electron beam resist', Technical report, ZEP520. Ver 1. 02, March 2001.
- [4] T. Ishii, H. Nozawa, T. Tamamura, 'A nano – composite resist system: a new approach to nanometer patterb fabrication', Microelectronic Engineering, vol 35, no 1 pp 113 – 116 (1997).
- [5] T. Ishii, T. Tamamura, K. Shigehara, 'Fullerene – derivative nanocomposite resist for nanometer pattern fabrication', Jpn. J. Appl. Phys. 39 pp L1068 – L1070 (2000).
- [6] T. Ishii, H. Nozawa, T. Tamamura, 'C60 incorporated nanocomposite resist system', J. Photopolymer. Sci. Technol, vol 10, no 4 pp 651 – 656 (1997).
- [7] T. Ishii, Y. Murate, K. Shigehara, 'Contrast enhancement of ZEP520 resist by fullerene – derivate incorporation', Jpn. J. Appl. Phys 40 pp L478 – L480 (2001).
- [8] K. E. Gonsalves, L. Merhari, H. Wu, y, Hu, 'Organic – Inorganic nanocomposite: unique resists for nanolithography', Advanced Materials, vol 13, no 10 (2001).
- [9] Y. Hu, H. wu, K. Gonsalves. L. Merhari, 'Nanocomposite resist for electron beam nanolithography', Microelectronic Engineering 56 pp 289 – 294 (2001).
- [10] L. Merhari, K. E. Gonsalves, Y. Hu, W. He, W. –S. Huang, m. Angelopoulos, W. H. Bruenger, C. Dzionk, M. Torker, 'Nanocomposite resist systems for next generation lithography', Microelectronic Engineering 63 (2002) pp 391 – 403.
- [11] M. A. Ali, K. E. Gonsalves, V. Golovkina, F. Cerrina, 'High sensitivity nanocomposite resists for EUV lithography', Microelectron Engineering 65 (2003) pp 454 – 462.
- [12] D. Gersappe, 'Molecular mechanisms of failure in polymer nanocomposites', Phys. Rev. lett, 89 (50 pp. 058301 – 1 – 4 (2002).

## CHAPTER

# 4

### **Applied Monte Carlo Simulations of the proximity effects on a PMMA based Nanocomposite Resist**

#### **Contents**

|  |       |
|--|-------|
| 4.1 Introduction.....                            | -80-  |
| 4.2 Monte Carlo procedure.....                   | -81-  |
| 4.3 Results.....                                 | -85-  |
| 4.3.1 The effect of the Primary Electrons.....   | -86-  |
| 4.3.2 The effect of the Secondary Electrons..... | -93-  |
| 4.3.3 The proximity effect.....                  | -97-  |
| 4.4 Limitations of the Monte Carlo model.....    | -100- |
| 4.5 Summary.....                                 | -103- |
| 4.6 References.....                              | -104- |

#### **4.1 Introduction**

From the results of the previous chapter it is obvious that the introduction of  $\text{Al}_2\text{O}_3$  nanoparticles in an electron beam resist modifies the interaction between the impinging electrons and the atoms in the resist film. The  $\text{Al}_2\text{O}_3$  nanoparticles exhibit different



scattering behaviour than the traditional atoms contained in the PMMA electron beam resist, such as Carbon, Oxygen and Hydrogen. Here, the influence of the Al<sub>2</sub>O<sub>3</sub> nanoparticles in the PMMA electron beam resist was studied through Monte Carlo simulations. The simulations for several incident electron energies with varying Al<sub>2</sub>O<sub>3</sub> nanoparticle loadings in PMMA were performed to find the effect of nanoparticles in an electron beam resist. This was determined by characterizing the scattering behaviour of the point electron distributions of the PMMA based nanocomposite resist.

The effect of the Al<sub>2</sub>O<sub>3</sub> nanoparticle density was studied by increasing or decreasing the concentration of nanoparticles in a constant unit volume of PMMA. Therefore, the effects of nanoparticle density on the interaction with incident electrons can be fully examined. The proximity effects seen in the previous chapter were investigated by predicting the critical dimensions required for preventing the nano structure from collapsing upon development. This was achieved using different thin film thicknesses that were seen in the previous chapter. This was investigated to obtain an understanding of the results found in the previous chapter.

## **4.2 Monte Carlo Procedure**

The Monte Carlo simulation that is presented here calculates electron scattering trajectories in materials, in this case PMMA based nanocomposite resist. The physical properties of the resist were calculated using the weighted percent of nanoparticles to PMMA. PMMA has a density of 1.19 g/cm<sup>3</sup> and Al<sub>2</sub>O<sub>3</sub> has a density of 4 g/cm<sup>3</sup> [1]. The total density of the nanocomposite resist was calculated using,

$$\rho_{resist} = \omega \rho_{Al_2O_3} + (1 - \omega) \rho_{PMMA} \quad (4 - 1)$$

Where  $\rho$  is the density of each material and  $\omega$  was the weighted percent of Al<sub>2</sub>O<sub>3</sub> to PMMA. The atomic weight of PMMA here was 950 000 g/mol and the atomic weight of Al<sub>2</sub>O<sub>3</sub> is 101.96 g/mol [2, 3].

The nanocomposite resist was considered to have a homogeneous dispersion of Al<sub>2</sub>O<sub>3</sub> nanoparticles throughout. As the electron travels through the resist it collides either elastically or inelastically with a molecule of PMMA or with a nanoparticle. When the electron collides with an atom, it was decided using the weighted percent of Al<sub>2</sub>O<sub>3</sub> to

PMMA and comparing it with a randomly generated number between 0 and 1. Whether it is an elastic or inelastic collision was decided by comparing a randomly generated number with the probability of getting an inelastic collision, the ratio between the inelastic cross section and the total cross section. Depending on the type of collision, the scattering cross sections and the mean free path are calculated.

For both elastic and inelastic scattering, the total scattering cross section is calculated again using the weighted percent of  $\text{Al}_2\text{O}_3$  to PMMA,

$$\sigma_{total} = \omega\sigma_{\text{Al}_2\text{O}_3} + (1 - \omega)\sigma_{\text{PMMA}} \quad (4 - 2)$$

The electron beam scattering model was written in a programming language called Interactive Data Language (IDL). IDL was chosen because of the ease in outputting data in a graphical format. Figure 4 – 1 shows the flowchart for the Monte Carlo simulation procedure for the two component system. To decide the outcome of the collisions as either elastic or inelastic a random number was generated. This was dependent upon the ratio of the elastic and inelastic scattering cross sections to the total scattering cross section.

The next random number decides if the electron has collided with an  $\text{Al}_2\text{O}_3$  nanoparticle or an atom in the PMMA molecule and compares this event to the nanoparticle loading in the polymer film. When this has been achieved, the Monte Carlo procedure calculated energy losses are calculated, and the scattering angles for the collision event.

The elastic scattering cross section is calculated using the screened Rutherford elastic cross section,

$$\sigma_{elastic} = \frac{Z^2}{E^2} \frac{4\pi}{\alpha(1 + \alpha)} \left( \frac{E + 511}{E + 1024} \right)^2 \text{ cm}^2 / \text{atom} \quad (4 - 3)$$

Where  $E$  is the electron energy in KeV,  $Z$  is the atomic number of the material and  $\alpha$  is the screening factor, this compensates for the fact that the electron does not see the all of the atom's charge as it is surrounded by a cloud of electrons.

For the case of inelastic scattering from the nanoparticles, the scattering cross section is calculated by considering only the coulomb interaction between the electron and the atom. In this case the inelastic scattering cross section per electron is,

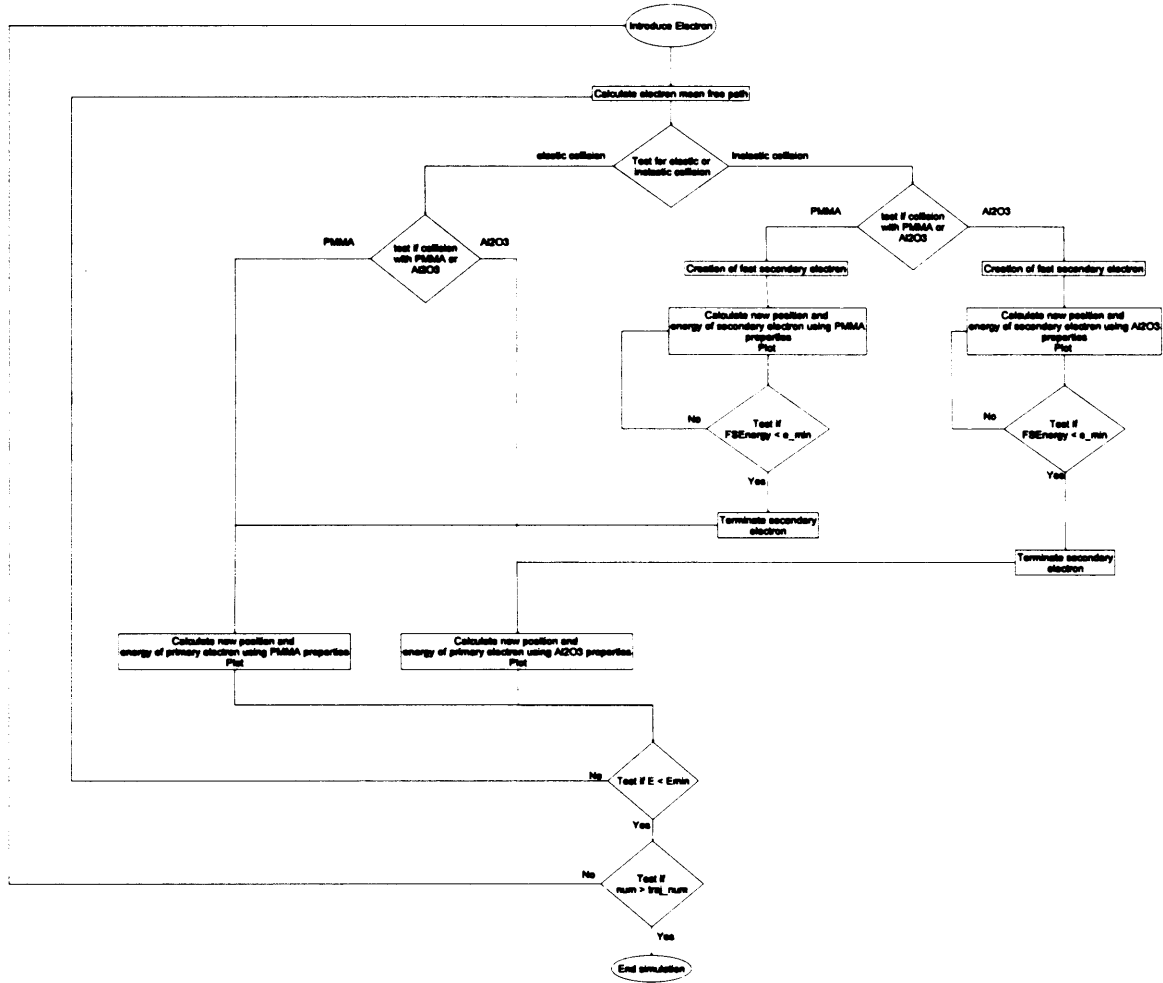


Figure 4 – 1: A flowchart of the simulating the nanocomposite resist using the Monte Carlo method.

$$\frac{d\sigma_{inelastic}}{d\Omega} = \frac{\pi e^4}{E^2} \left( \frac{1}{\Omega^2 + (1 - \Omega)^2} \right) \quad (4 - 4)$$

Where  $\Omega E$  is the energy of the secondary electron produced. The inelastic scattering event causes the primary electron to be deflected by an angle  $\alpha$  given by,

$$\sin^2 \alpha = \frac{2\Omega}{2 + t - t\Omega} \quad (4 - 5)$$

Where  $t$  is the kinetic energy of the electron in units of its rest mass. However the secondary electron created exits the collision at an angle  $\gamma$  given by,

$$\sin^2 \gamma = \frac{2(1-\Omega)}{2+t\Omega} \quad (4-6)$$

For an impact that transfers approximately 500eV to the secondary electron, the primary scatters at an angle of about 1° and the secondary electron exits at an angle of about 80°. This is why the secondary electrons play a major role in producing the so called ‘proximity effect’.

Once the scattering cross sections are calculated, the mean free path of the electron must be calculated. This is the sum of the inelastic mean free path and elastic mean free path of the electron.

$$\frac{1}{\lambda_{total}} = \frac{1}{\lambda_{elastic}} + \frac{1}{\lambda_{inelastic}} \quad (4-7)$$

The elastic and inelastic mean free paths are calculated from the scattering cross sections,

$$\lambda_{elastic} = \frac{A}{N_a \rho \sigma_{elastic}} \quad (4-8)$$

$$\lambda_{inelastic} = \frac{A}{N_a Z \rho \sigma_{inelastic}} \quad (4-9)$$

where  $A$  is the atomic weight of the material,  $N_a$  is Avogadro's number,  $\rho$  is the density of the resist and  $\sigma$  is the respective scattering cross section. The total elastic and inelastic mean free path is calculated using weighted percentages,

$$\frac{1}{\lambda} = \frac{\omega}{\lambda_{Al_2O_3}} + \frac{1-\omega}{\lambda_{PMMA}} \quad (4-10)$$

From the value of the mean free path, the distance the electron will travel before it collides again can be calculated. This is done using the step size equation given by,



$$s = -\lambda \ln(RND) \quad (4 - 11)$$

where  $\lambda$  is the total mean free path and RND is a random number between 0 and 1. This gives a distribution of step sizes with an average step size of  $\lambda$ . Therefore, the probability of obtaining a step size near the mean free path is larger than obtaining a step size much larger or smaller than the mean free path.

The final step of the Monte Carlo simulation was to calculate the energy lost by the electron during the scattering event. This was done using the Bethe equation for the stopping power of a material and is given by [4, 5],

$$\frac{dE}{dS} = 78500 \frac{Z}{AE} \ln \left( \frac{1.166(E + 0.85J)}{J} \right) \quad (4 - 12)$$

where  $J$  is the mean ionization potential of the material, which was 145 and 74eV for  $Al_2O_3$  and PMMA respectively [6]. Every time the electron scatters, this value is calculated and was subtracted from the current energy of the electron. Once the electron's energy falls below 0.5 keV, the electron was no longer tracked as the distance it travels in the material is very small.

### **4.3 Results**

To model the results found in the previous chapter, the thicknesses of the nanocomposite resist were used for the worst and best aspect ratio ascertained, which were unloaded PMMA (407nm) and PMMA loaded with 150mg of  $Al_2O_3$  nanoparticles (562nm). In this investigation, all of the resist films were free standing and had thicknesses of 400 and 550nm and the accelerating voltages were 25, 50, 75 and 100keV with clearing doses of  $150\mu C/cm^2$ ,  $200\mu C/cm^2$ , and  $240\mu C/cm^2$  respectively. These were studied to gain an understanding of the effects of primary and secondary electrons.

To validate the model here, industry standard modelling software called SRIM was used as a comparison. However, using the SRIM software it is not possible to incorporate the

Al<sub>2</sub>O<sub>3</sub> nanoparticles in to the PMMA (which was why the nanocomposite resist model was written). Therefore, it was shown (using the model written in IDL) that the results of the PMMA without the dispersal of nanoparticles agreed with that of SRIM.

#### **4.3.1 The effect of the Primary Electrons**

The model was used to determine the influence of the Al<sub>2</sub>O<sub>3</sub> nanoparticles when a primary beam of electrons was incident upon it. The average radial distances were plotted to ascertain the scattering mechanism of the primary beam in order to gain an understanding of the proximity effect relationship. This was achieved by plotting the trajectories of the incident electrons at each 50nm intervals into the depth of the resist films for 0, 50, 100 and 150mg of Al<sub>2</sub>O<sub>3</sub> nanoparticles (diameter 25nm) loadings in PMMA for incident electron energies of 25, 50, 75 and 100KeV. Figures 4 – 2 and 4 – 3 show the point electron distributions in the nanocomposite resist films with a thickness of 400nm for an accelerating voltage of 25 and 100KeV respectively. Appendix C shows the point electron distributions for the nanocomposite resist films for incident electron energies of 25 and 100KeV for thickness of 550nm and shows the point electron distributions for the nanocomposite resist films for incident electron energies of 50 and 75KeV for thickness of 400 and 550nm. The trajectories indicated in blue are secondary electrons. It can be seen from figures 4 – 2 and 4 – 3 that as the nanoparticle concentration increases, the electrons incident on the nanocomposite resist experience a greater number of collisions with the atoms in its flight through the nanocomposite resist, hence, the mean free path was decreased. Therefore, the presence of the Al<sub>2</sub>O<sub>3</sub> nanoparticles in the PMMA dramatically affects the mean free path and thus controlled the number of collisions that an incident electron encounters in its trajectory. This was due to the fact that the density of the Al<sub>2</sub>O<sub>3</sub> nanoparticle was larger than the PMMA molecule. To represent the results shown in the previous chapter, figures 4 – 4 to 4 – 9 shows a comparison of the average radial distances that the incident electron can travel between collisions in it's trajectory through a 400 and 550nm resist film. This data was taken from figures 4 – 2 and 4 – 3. The radial distance characteristics for the accelerating voltages of 50 and 75keV are shown in Appendix D.

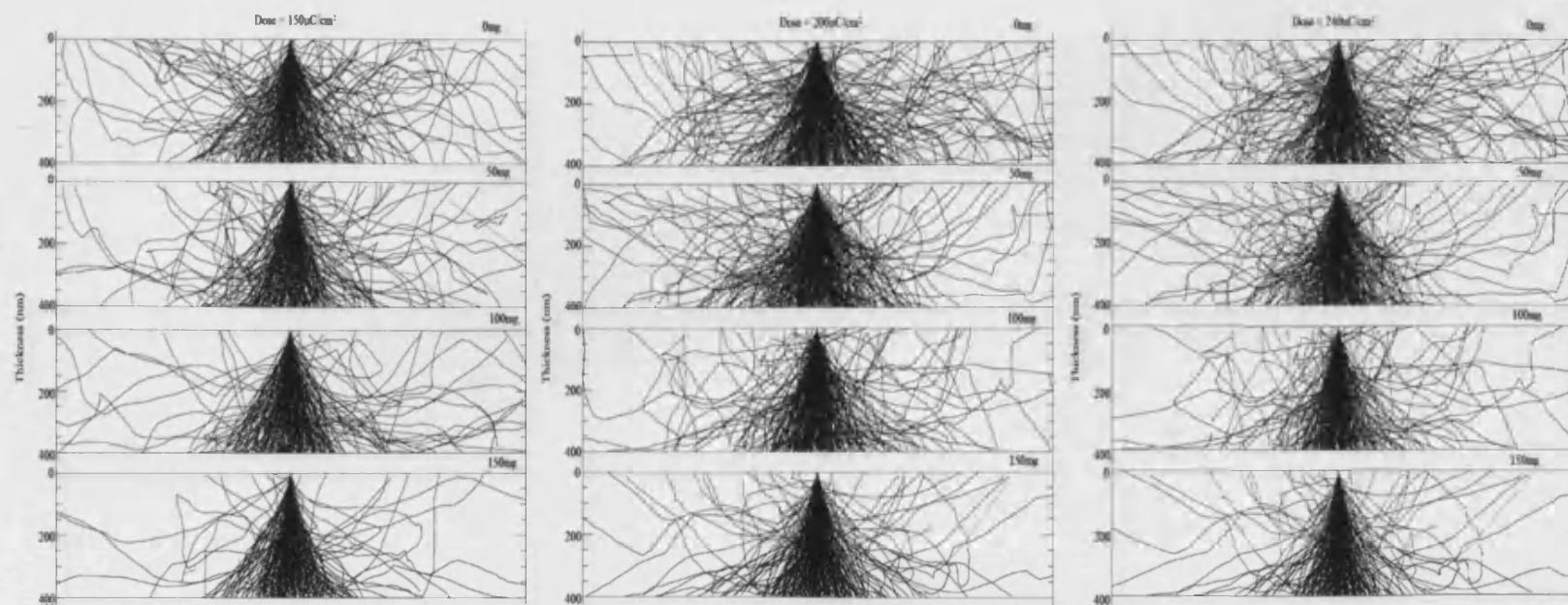


Figure 4 – 2: Point electron distributions of PMMA loaded with 0, 50, 100 and 150mg of  $\text{Al}_2\text{O}_3$  nanoparticles exposed with dose of 150, 200, 240  $\mu\text{C}/\text{cm}^2$ , for 25KeV incident electron energies.

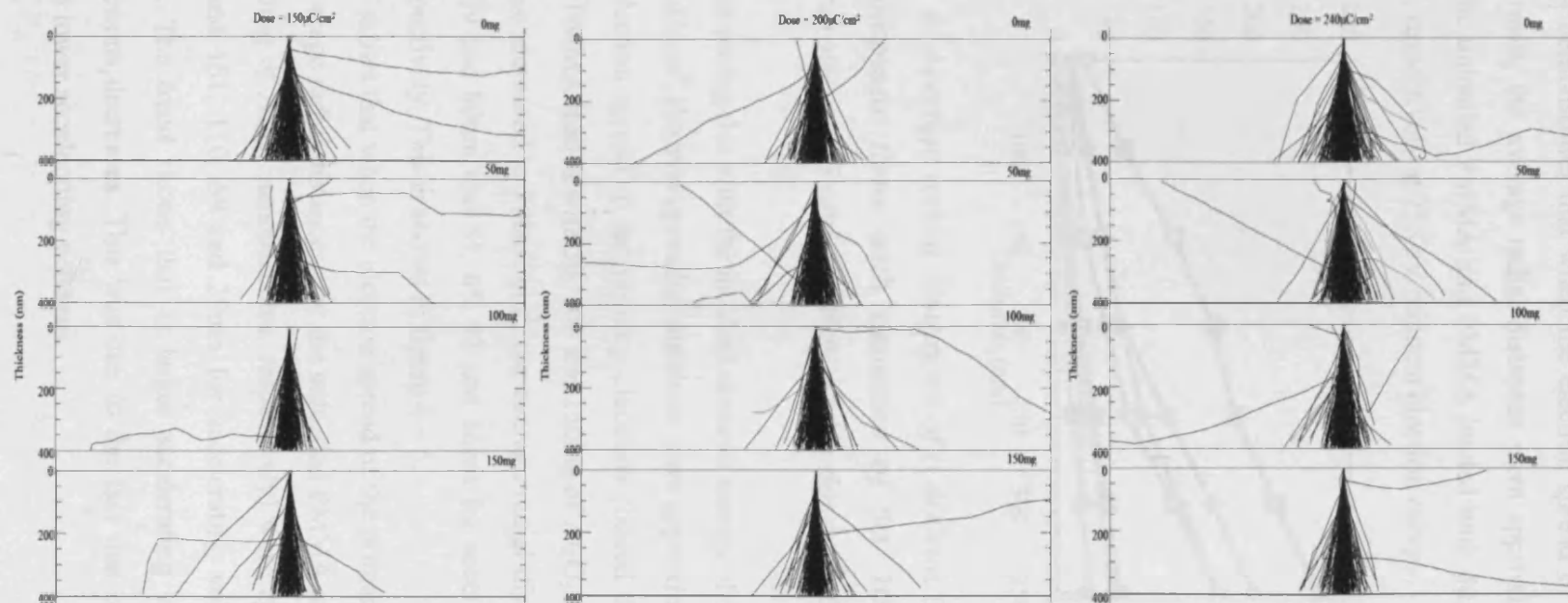


Figure 4 – 3: Point electron distributions of PMMA loaded with 0, 50, 100 and 150mg of  $\text{Al}_2\text{O}_3$  nanoparticles exposed with dose of 150, 200, 240  $\mu\text{C}/\text{cm}^2$ , for 100KeV incident electron energies.



Figure 4 – 4 demonstrates that when the electron spread of the primary electrons had cleared the resist, the average radial distances were approximately 270, 200, 171 and 165nm for the unloaded PMMA and PMMA loaded with 50, 100 and 150mg of  $\text{Al}_2\text{O}_3$  nanoparticle, respectively at 25KeV incident electron energy.

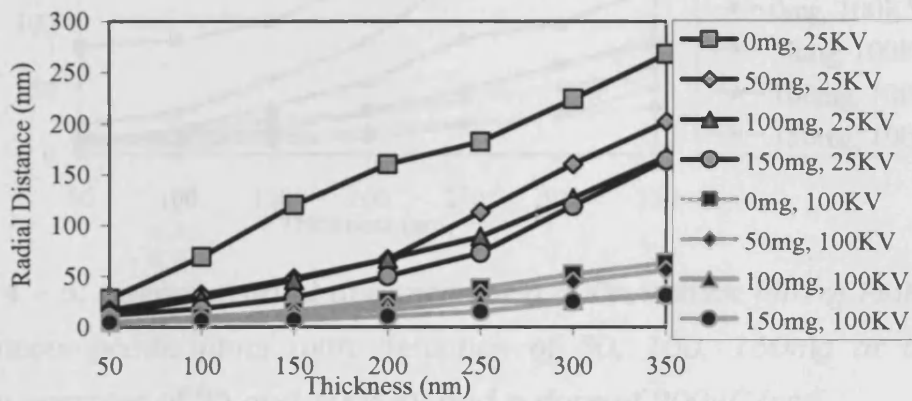


Figure 4 – 4: Average radial distances of a 400nm thick film of PMMA and for nanocomposite films with densities of 50, 100, 150mg at incident electron energies of 25 and 100KeV and a dose of  $150\mu\text{C}/\text{cm}^2$ .

However, comparing this with the incident electron energy of 100KeV with an associated dose of  $150\mu\text{C}/\text{cm}^2$ , the average radial distances were approximately 70, 56, 34 and 30nm (when the electron spread of the primary electrons cleared the resist) for the unloaded PMMA and PMMA loaded with 50, 100 and 150mg of  $\text{Al}_2\text{O}_3$  nanoparticle, respectively. With the dose increased to  $200\mu\text{C}/\text{cm}^2$ , the average radial distances were approximately 200, 177, 129 and 80nm and 81, 65, 52 and 36nm for accelerating voltages of 25 and 100KeV respectively. This is shown in figure 4 – 5.

Figure 4 – 6 shows that when the electron spread of the primary electrons had cleared the resist, the average radial distances (for the unloaded PMMA and PMMA loaded with 50, 100 and 150mg of  $\text{Al}_2\text{O}_3$  nanoparticles, respectively) were approximately 200, 128, 95 and 74nm and 161, 110, 69 and 29nm for accelerating voltages of 25 and 100KeV respectively. The trend shows that at larger accelerating voltages the spread of the primary electrons decreases. This was due to the fact that considerably less collisions occur than at lower accelerating voltages.

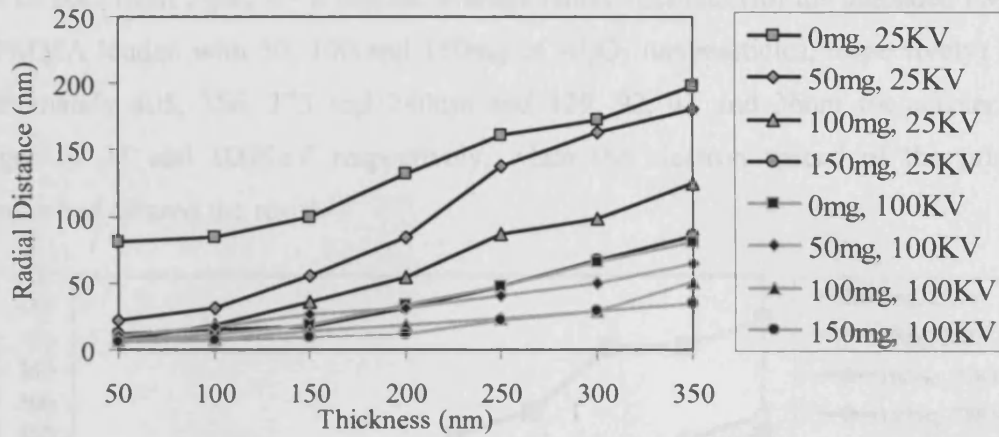


Figure 4 – 5: Average radial distances of a 400nm thick film of PMMA and for nanocomposite films with densities of 50, 100, 150mg at incident electron energies of 25 and 100KeV and a dose of  $200\mu\text{C}/\text{cm}^2$ .

When the thickness was increased to 550nm, it was evident that when the electron spread of the primary electrons had cleared the resist, the average radial distances (for the unloaded PMMA and PMMA loaded with 50, 100 and 150mg of  $\text{Al}_2\text{O}_3$  nanoparticles, respectively) were approximately 432, 282, 213 and 195nm and 235, 114, 74 and 52nm for accelerating voltages of 25 and 100KeV respectively. This can be seen in figure 4 – 7.

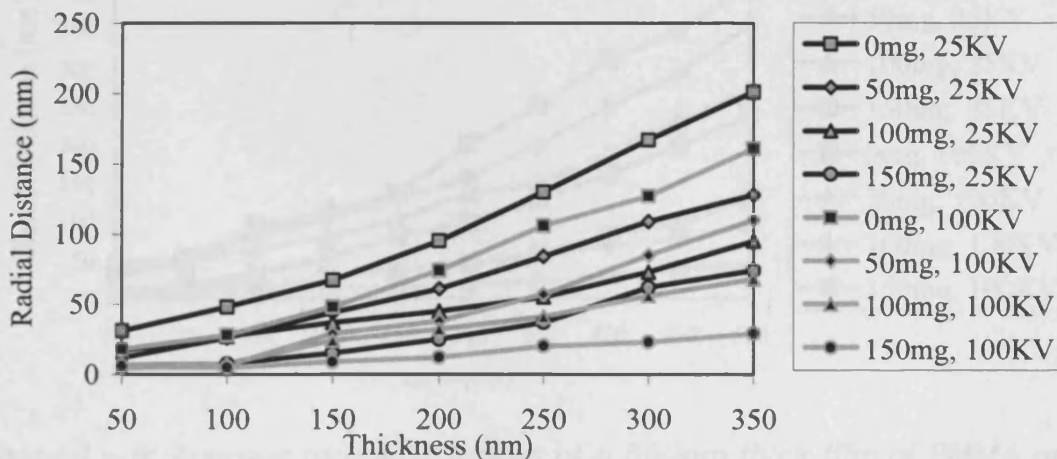


Figure 4 – 6: Average radial distances of a 400nm thick film of PMMA and for nanocomposite films with densities of 50, 100, 150mg at incident electron energies of 25 and 100KeV and a dose of  $240\mu\text{C}/\text{cm}^2$ .

It can be seen from figure 4 – 8 that the average radial distances (for the unloaded PMMA and PMMA loaded with 50, 100 and 150mg of  $\text{Al}_2\text{O}_3$  nanoparticles, respectively) were approximately 405, 356, 273 and 240nm and 129, 92, 47 and 36nm for accelerating voltages of 25 and 100KeV respectively, when the electron spread of the primary electrons had cleared the resist.

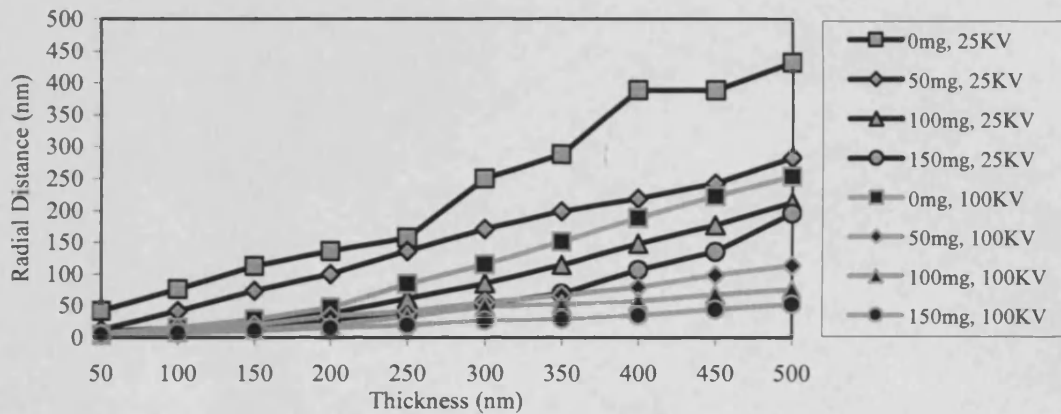


Figure 4 – 7: Average radial distances of a 550nm thick film of PMMA and for nanocomposite films with densities of 50, 100, 150mg at incident electron energies of 25 and 100KeV and a dose of  $150\mu\text{C}/\text{cm}^2$ .

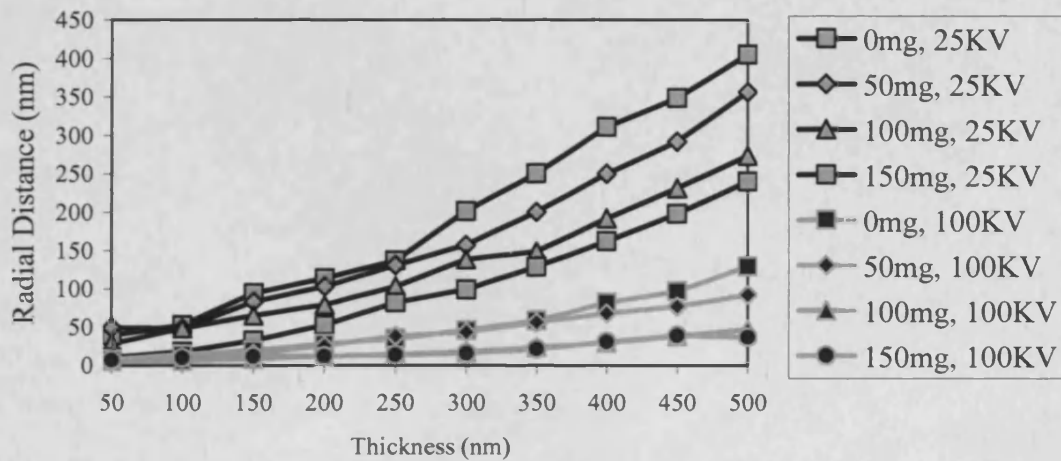


Figure 4 – 8: Average radial distances of a 550nm thick film of PMMA and for nanocomposite films with densities of 50, 100, 150mg at incident electron energies of 25 and 100KeV and a dose of  $200\mu\text{C}/\text{cm}^2$ .

From figure 4 – 9, shows similar results for the unloaded PMMA and PMMA loaded with 50, 100 and 150mg of  $\text{Al}_2\text{O}_3$  nanoparticles, respectively.

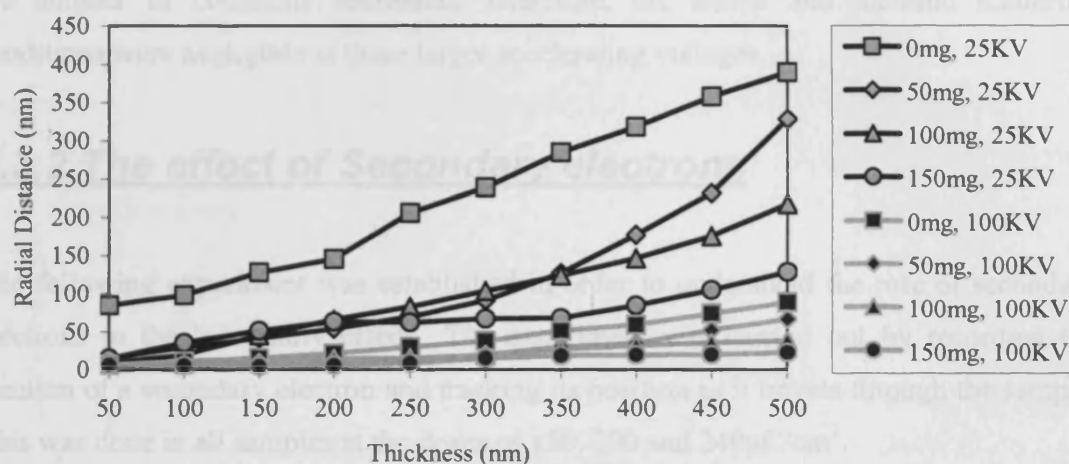


Figure 4 – 9: Average radial distances of a 550nm thick film of PMMA and for nanocomposite films with densities of 50, 100, 150mg at incident electron energies of 25 and 100KeV and a dose of  $240\mu\text{C}/\text{cm}^2$ .

When the PMMA was loaded with the  $\text{Al}_2\text{O}_3$  nanoparticles they were able to confine the incident electrons as the beam at the top half of the film was at its narrowest. This was because the  $\text{Al}_2\text{O}_3$  nanoparticles had a larger density than the PMMA molecule. This resulted in a stronger shielding of the atom which was provided by a larger charge. Therefore, an increased number of collisions took place due to an increasing density of the  $\text{Al}_2\text{O}_3$  nanoparticles. Therefore, a higher aspect ratio can be achieved by loading the PMMA with a high density material and obtains a better resolution than resists like PMMA. These results agree with the work by A. Jeyakumar on Silica nanoparticles [7].

From the results shown, it was found at the lower accelerating voltages, the radial distances of the primary electrons increases as all the nanocomposite samples demonstrated larger point electron spreads. The incident electrons had less energy, due to the increasing number of collisions with the  $\text{Al}_2\text{O}_3$  nanoparticles. From this, the probability of the electrons scattering increases, this contributed to the proximity effect highlighted in chapter three. However, at larger accelerating voltages, all of the nanocomposite samples demonstrated smaller point electron spreads because the elastic

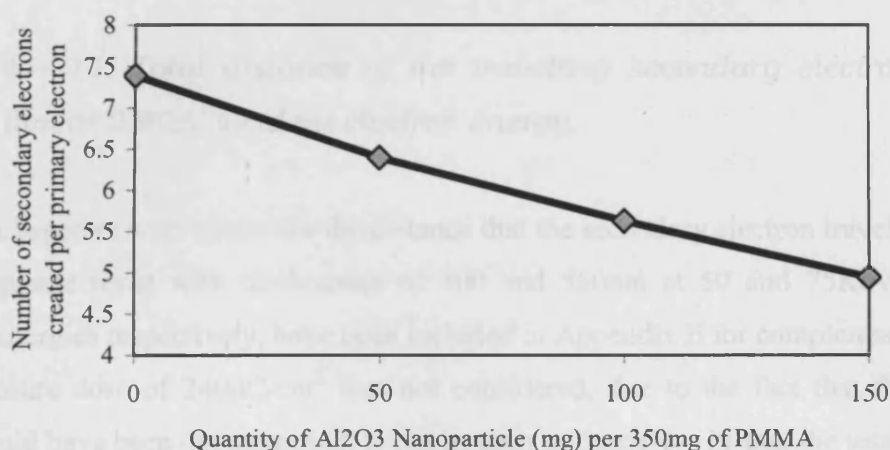


and inelastic scattering was kept at a minimum as the energy associated with it was so large they were able to travel further through the nanocomposite resist this was because the number of collisions decreased. Therefore, the elastic and inelastic scattering conditions were negligible at these larger accelerating voltages.

### **4.3.2 The effect of Secondary electrons**

The following experiment was established in order to understand the role of secondary electrons in the 'proximity effect'. The experiment was carried out by recording the creation of a secondary electron and tracking its position as it travels through the sample. This was done in all samples at the doses of 150, 200 and 240 $\mu\text{C}/\text{cm}^2$ .

The number of secondary electrons created in a 400nm film at 25KeV incident electron energy is shown in figure 4 – 10. From this characteristic, it was found that the number of secondary electrons created were considerably more than the number of the primary electrons incident on the nanocomposite resist surface.

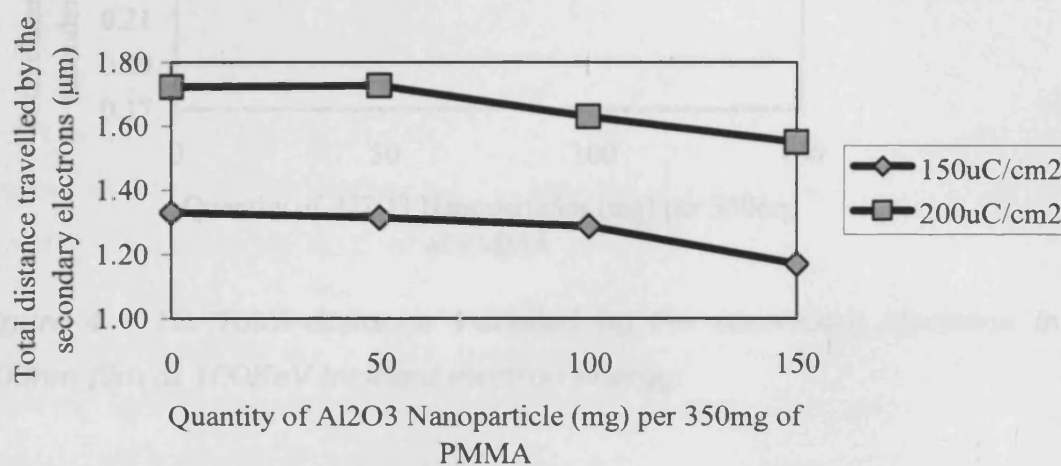


*Figure 4 – 10: Number of secondary electrons created in a 400nm film at 25KeV incident electron energy and a dose of 240 $\mu\text{C}/\text{cm}^2$ .*

It can be seen that number of secondary electrons that were created was 7.4 (per primary electron) when the PMMA was unloaded. Comparing this to the PMMA that was loaded with 150mg of Al<sub>2</sub>O<sub>3</sub> nanoparticles, the quantity of secondary electrons that were created

was 4.9 (per primary electron). Therefore, the number of secondary electrons created decreases as the density of the  $\text{Al}_2\text{O}_3$  nanoparticles increases. Thus, the presence of the  $\text{Al}_2\text{O}_3$  nanoparticles in the nanocomposite resist film had the effect of quenching the secondary electrons.

Figures 4 – 11 and 12 shows the total distance that the secondary electrons travel in the nanocomposite resist with a thicknesses of 400nm at 25 and 100KeV incident electron energies respectively.



*Figure 4 – 11: Total distance of the travelling secondary electrons in a 400nm film at 25KeV incident electron energy.*

This data, together with results for the distance that the secondary electron travelled in the nanocomposite resist with thicknesses of 400 and 550nm at 50 and 75KeV incident electron energies respectively, have been included in Appendix E for completeness.

The exposure dose of  $240\mu\text{C}/\text{cm}^2$  was not considered, due to the fact that the 400nm resist would have been over exposed. It can be seen in figure 4 – 11 that the total distance travelled by the secondary electrons in the PMMA loaded with 150mg of  $\text{Al}_2\text{O}_3$  nanoparticles was approximately 1.16 and  $1.55\mu\text{m}$  for doses of 150 and  $200\mu\text{C}/\text{cm}^2$  respectively. Comparing the secondary electrons with the primary electrons, it is evident that they travel further because the energy associated with them is much smaller (about 1 – 5KeV), thus, more collisions occur. This can be seen when the electron beam exposure dose was increased from 150 to  $200\mu\text{C}/\text{cm}^2$ . The total distance travelled by the secondary

electrons increases because the incident electrons have more energy. As a result more secondary electrons were created.

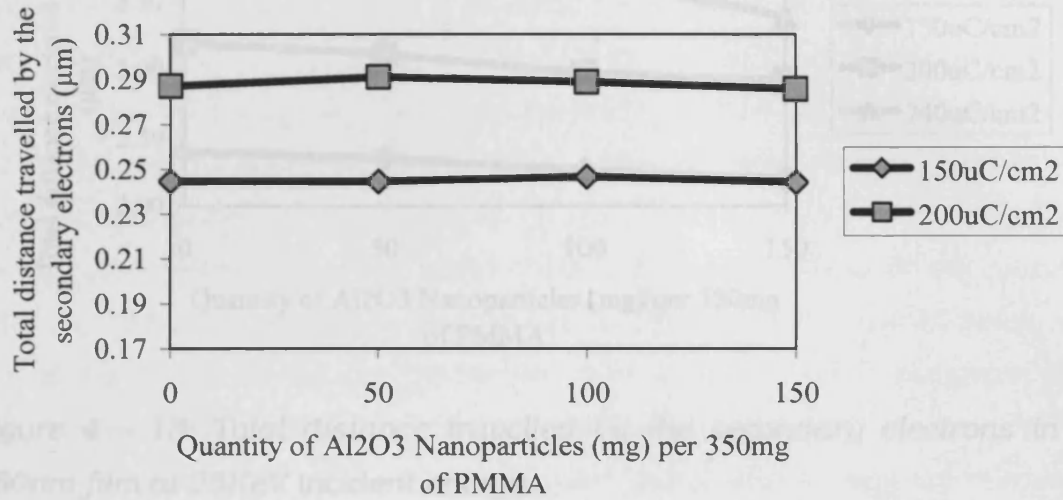


Figure 4 – 12: Total distance travelled by the secondary electrons in a 400nm film at 100KeV incident electron energy.

However, from figure 4 – 12, the total distance travelled by the secondary electrons remained relatively constant as the accelerating voltage was increased to 100KeV. The incident electron energy that generates the secondary electrons was negligible because, as previously mentioned, the elastic and inelastic scattering was kept at a minimum. Since the incident energy associated with these secondary electrons was so large, they were able to travel further through the nanocomposite resist, hence, the number of collisions decreased. It can be seen that the total distance travelled by these secondary electron was comparable to the distances travelled by the primary electrons of the unloaded PMMA (shown in figures 4 – 4 to 4 – 6) of the same thickness.

Figure 4 – 13 shows that the total distance travelled by the secondary electrons had decreased by approximately 600, 400 and 200nm when the exposure doses were 240, 200 and 150  $\mu\text{C}/\text{cm}^2$  respectively. Therefore, the distance that secondary electrons can travel, are regulated by the density of Al<sub>2</sub>O<sub>3</sub> nanoparticles and the accelerating voltage. This is significant as these are the electrons that damage the structure that is to be fabricated in the resist by contributing to the so called proximity effect.

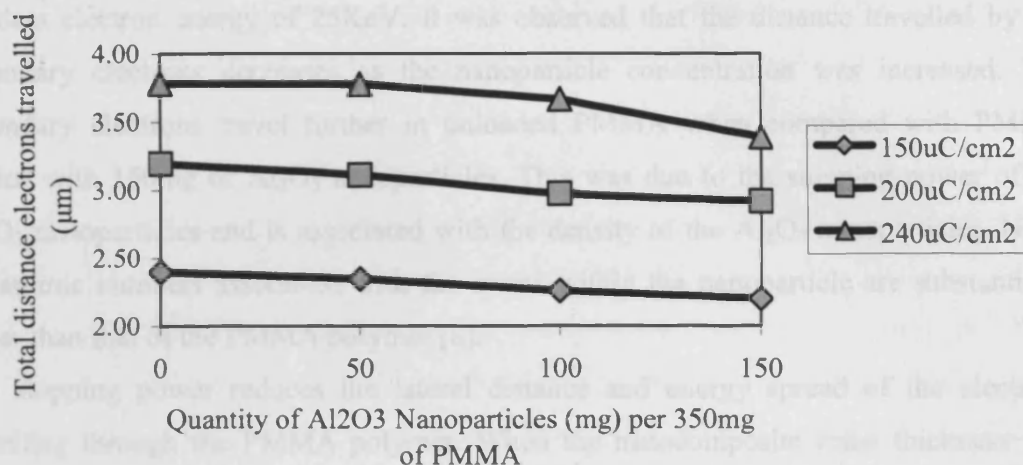


Figure 4 – 13: Total distance travelled by the secondary electrons in a 550nm film at 25KeV incident energy.

Figure 4 – 14 shows the distance travelled by the secondary electron through the unloaded PMMA and the nanocomposite resist samples. As before this remained constant, and occurs for the same reason given above.

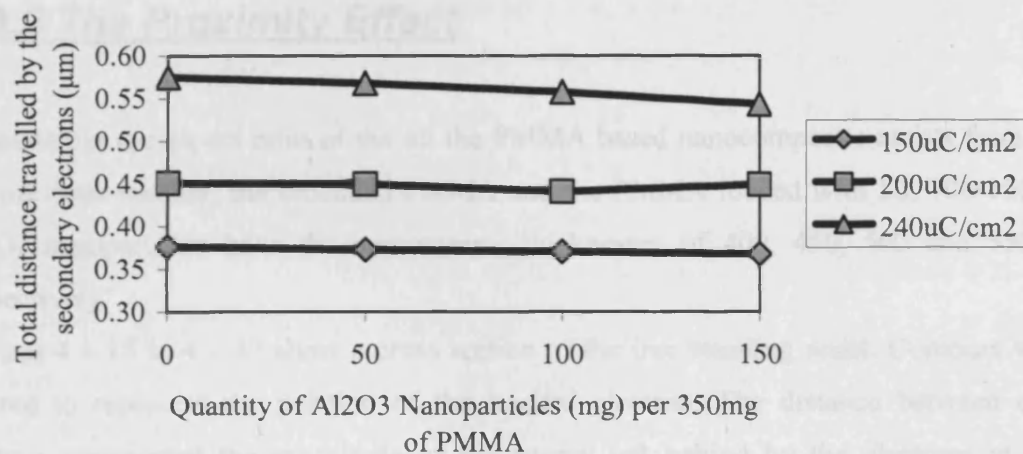


Figure 4 – 14: Total distance of the travelling secondary electrons in a 550nm film at 100KeV incident electron energy.

Comparing the distances travelled by the primary (given by the point electron distribution) and secondary electrons, the primary electrons travel approximately 200nm where the secondary electrons travel distances of approximately 1.4 and 3.75μm at lower

incident electron energy of 25KeV. It was observed that the distance travelled by the secondary electrons decreases as the nanoparticle concentration was increased. The secondary electrons travel further in unloaded PMMA when compared with PMMA loaded with 150mg of  $\text{Al}_2\text{O}_3$  nanoparticles. This was due to the stopping power of the  $\text{Al}_2\text{O}_3$  nanoparticles and is associated with the density of the  $\text{Al}_2\text{O}_3$  nanoparticles. Note: the atomic numbers associated with the atoms within the nanoparticle are substantially larger than that of the PMMA polymer [8].

The stopping power reduces the lateral distance and energy spread of the electrons travelling through the PMMA polymer. When the nanocomposite resist thickness was increased to 550nm, the distance that the secondary electrons travelled was greater than that travelled in the nanocomposite resist with a thickness of 400nm.

This was because of the increased resist thickness and as such, a larger exposure dose was needed so that the primary electrons could overcome the  $\text{Al}_2\text{O}_3$  nanoparticles and clear the resist. However, more secondary electrons were generated and scattered in an arbitrary direction and travel further.

### **4.3.3 The Proximity Effect**

To maintain the aspect ratio of the all the PMMA based nanocomposite resists found in the previous chapter, the unloaded PMMA and the PMMA loaded with 50, 100 150mg  $\text{Al}_2\text{O}_3$  nanoparticles have the approximate thicknesses of 400, 450, 500 and 550nm respectively.

Figures 4 – 15 to 4 – 17 show a cross section of the free standing resist. Contours were plotted to represent the position of the tracked electron. The distance between each contour represented the magnitude of the energy left behind by the electrons at that position, which in turn can be regarded as the probability of exposure of that region of resist. Each sample was modelled at an accelerating voltage of 25KeV and the exposure dose that was found from the previous chapter. The modelled structures consisted of lines and trenches this represents the structures discussed in chapter three. Figures 4 – 15 to 4 – 17 explores the limit of the smallest nano structure that can be fabricated with the nanocomposite resist. The feature size of the modelled structures were 90, 80, 70nm.



Figure 4 – 15 shows the features in the unloaded PMMA (a) and the PMMA loaded with 50, 100, 150mg (b – d) of  $\text{Al}_2\text{O}_3$  nanoparticles with their appropriate thicknesses. The features consisted of two lines and three spaces (trenches). The lines were of 90nm and the trenches between each of the lines were 90nm. This is defined as the feature size. As expected, in each of the samples, all of the trenches were resolved, as the appropriate exposure clearing doses were used (as obtained in chapter three).

It can be seen from the shape of each of the trenches that they were narrowest at the top and generally got thicker through the sample. This was due to the proximity effect. Comparing the aspect ratios of the worst and best of the samples (which were figures 4 – 15a and 4 – 15d), the shape of the trench that would be etched into each resist was different. Figure 4 – 15a shows that the width of the trench towards the bottom was substantially larger than that of figure 4 – 14d. From this it can be ascertained that the proximity effect is more prominent in unloaded PMMA compared with the loaded PMMA. This has been suggested in the sections of 4.3.1 and 4.3.2. Therefore, a higher aspect ratio can be achieved when the concentration of the  $\text{Al}_2\text{O}_3$  nanoparticles was 150mg (as seen in the previous chapter).

Therefore, the proximity effect was reduced by decreasing the lateral distance of the electrons travelling through the resist and this is in agreement with the results shown in [9]. This is due to the fact that the  $\text{Al}_2\text{O}_3$  nanoparticles have a larger electron energy stopping power; in effect, quenching the lateral exposure of the resist.

From figure 4 – 15, it is evident that the density of the contour lines was increased towards the surface of the resist. This signifies that the energy associated with the electrons is large and the elastic and inelastic trajectories do not occur until the energy decreases past a threshold point. By inspection, this point seems to be at a depth of 200nm. However, it should be noted that the thickness and exposure doses are not the same in all of the samples. When the electrons exceed the threshold point, the elastic and inelastic scattering of electrons occur in arbitrary directions thus enhancing the proximity effect.

Figure 4 – 16 shows three trenches of 80nm separated by 80nm. It can be seen from figures 4 – 16c and d that the trenches are resolved to the full depth of the resist in the samples loaded with 100 and 150mg of  $\text{Al}_2\text{O}_3$  nanoparticles.

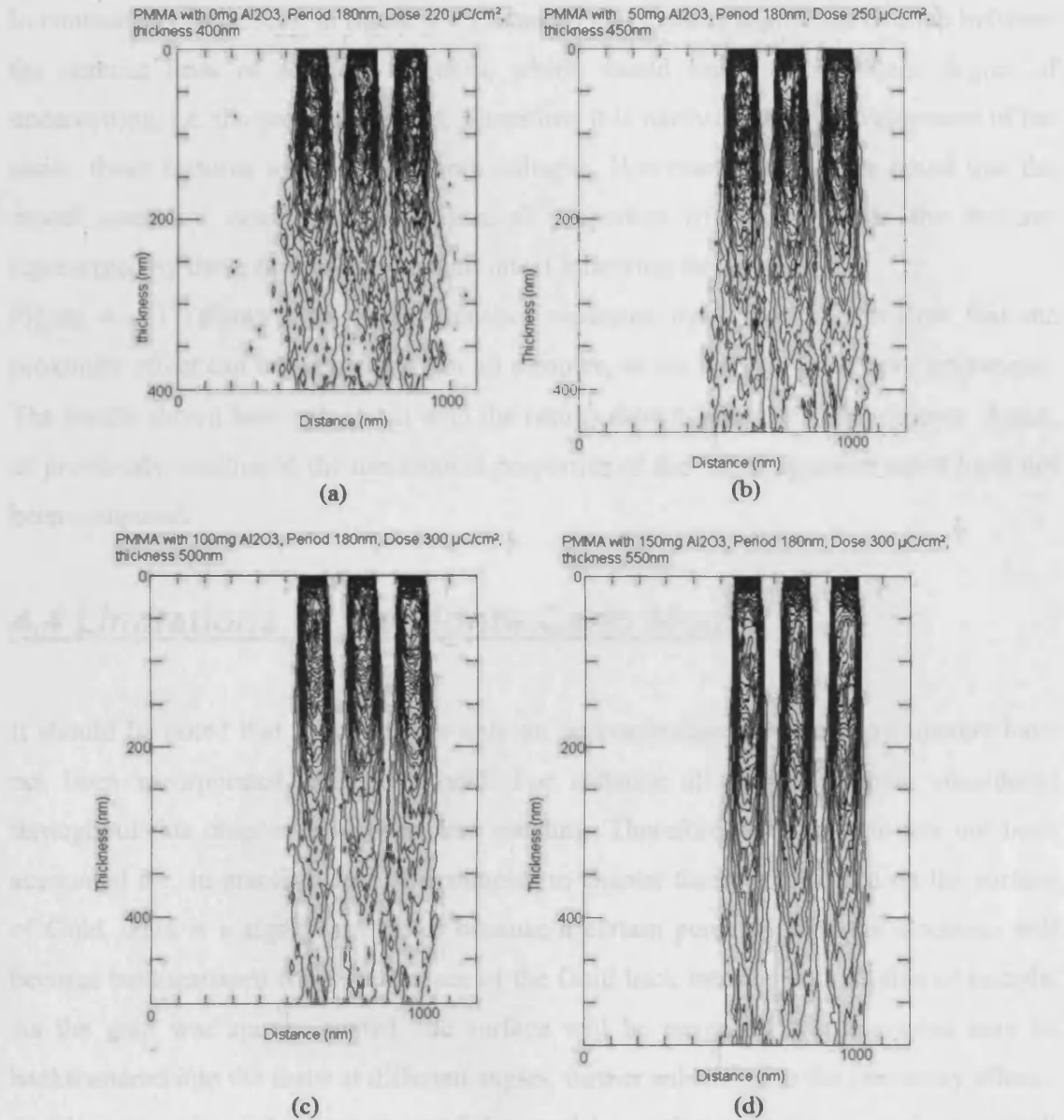


Figure 4 – 15: A cross section of the 90nm lines directly written into the PMMA based nanocomposite resist (a) unloaded PMMA 400nm film at 25KeV incident energy and a dose of 220 $\mu\text{C}/\text{cm}^2$ , (b) PMMA loaded with 50mg of Al<sub>2</sub>O<sub>3</sub> nanoparticles in a 450nm film at 25KeV incident energy and a dose of 250 $\mu\text{C}/\text{cm}^2$ , (c) PMMA loaded with 100mg of Al<sub>2</sub>O<sub>3</sub> nanoparticles in a 500nm film at 25KeV incident energy and a dose of 300 $\mu\text{C}/\text{cm}^2$ , (d) PMMA loaded with 150mg of Al<sub>2</sub>O<sub>3</sub> nanoparticles in a 550nm film at 25KeV incident energy and a dose of 300 $\mu\text{C}/\text{cm}^2$ .

In contrast, it can be seen in figure 4 – 16a and b that there is significant overlap between the contour lines of adjacent trenches, which would imply a significant degree of undercutting, i.e. the proximity effect. Therefore, it is likely that upon development of the resist, these features would suffer from collapse. However, it should be noted that the model does not compute the mechanical properties of the resist, as the features represented by these figures may remain intact following development.

Figure 4 – 17 shows three 70nm trenches separated by 70nm. It is evident that the proximity effect can be seen clearly in all samples, as the contour lines have intersected. The results shown here agree well with the results shown in the previous chapter. Again, as previously mentioned the mechanical properties of the nanocomposite resist have not been computed.

#### **4.4 Limitations of the Monte Carlo Model**

It should be noted that this model is only an approximation as several parameters have not been incorporated into the model. For instance all of the samples considered throughout this chapter have been free standing. Therefore, the substrate has not been accounted for. In practice, all of the samples in chapter three were in situ on the surface of Gold. This is a significant factor because a certain percentage of the electrons will become backscattered from the surface of the Gold back into the bottom side of sample. As the gold was sputter coated, the surface will be rough and the electrons may be backscattered into the resist at different angles, further enhancing to the proximity effect. Another example of the limitations of this model was that only the outer electron shell was considered in our model, the inner electron shell was ignored for simplicity. However, it was felt that the results shown here sufficiently demonstrate the  $\text{Al}_2\text{O}_3$  nanoparticles ability to quench the primary and secondary electrons. Furthermore, the crystalline structure and impurities in the  $\text{Al}_2\text{O}_3$  nanoparticles were not considered. The presence of the impurities, such as Phosphorus, Carbon or Silicon will affect the distribution of scattered electrons in a different way to pure  $\text{Al}_2\text{O}_3$ .

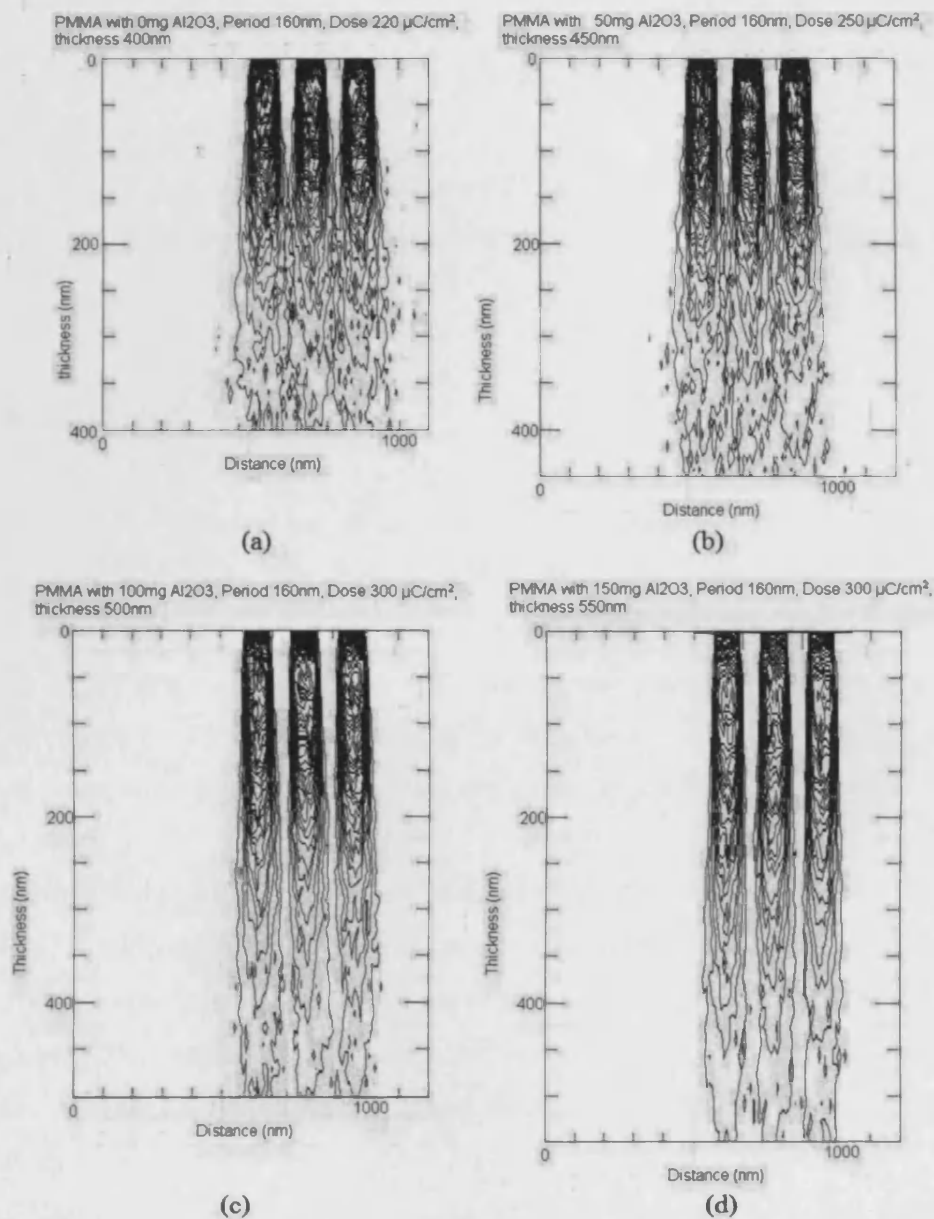


Figure 4 – 16: A cross section of the 80nm lines directly written into the PMMA based nanocomposite resist (a) unloaded PMMA 400nm film at 25KeV incident energy and a dose of 220 $\mu\text{C}/\text{cm}^2$ , (b) PMMA loaded with 50mg of Al<sub>2</sub>O<sub>3</sub> nanoparticles in a 450nm film at 25KeV incident energy and a dose of 250 $\mu\text{C}/\text{cm}^2$ , (c) PMMA loaded with 100mg of Al<sub>2</sub>O<sub>3</sub> nanoparticles in a 500nm film at 25KeV incident energy and a dose of 300 $\mu\text{C}/\text{cm}^2$ , (d) PMMA loaded with 150mg of Al<sub>2</sub>O<sub>3</sub> nanoparticles in a 550nm film at 25KeV incident energy and a dose of 300 $\mu\text{C}/\text{cm}^2$ .

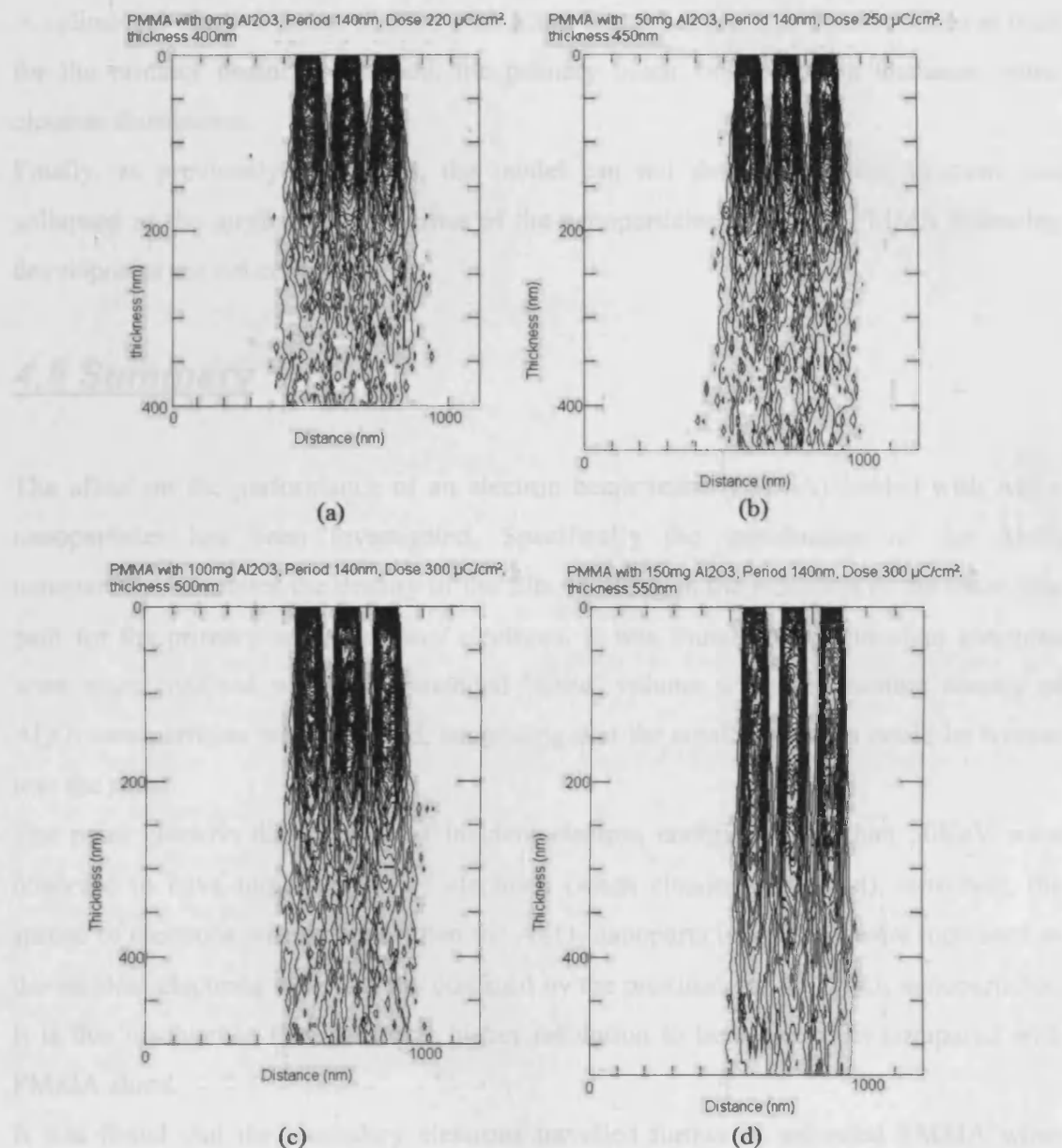


Figure 4 – 17: A cross section of the 70nm lines directly written into the PMMA based nanocomposite resist (a) unloaded PMMA 400nm film at 25KeV incident energy and a dose of 220 $\mu\text{C}/\text{cm}^2$ , (b) PMMA loaded with 50mg of Al<sub>2</sub>O<sub>3</sub> nanoparticles in a 450nm film at 25KeV incident energy and a dose of 250 $\mu\text{C}/\text{cm}^2$ , (c) PMMA loaded with 100mg of Al<sub>2</sub>O<sub>3</sub> nanoparticles in a 500nm film at 25KeV incident energy and a dose of 300 $\mu\text{C}/\text{cm}^2$ , (d) PMMA loaded with 150mg of Al<sub>2</sub>O<sub>3</sub> nanoparticles in a 550nm film at 25KeV incident energy and a dose of 300 $\mu\text{C}/\text{cm}^2$ .



A cylindrical electron beam of 3nm with a top hat radial electron distribution was used for the primary beam. In practice, the primary beam would have a Gaussian radial electron distribution.

Finally, as previously mentioned, the model can not determine if the structure has collapsed as the mechanical properties of the nanoparticles inside the PMMA following development are not computed.

## **4.5 Summary**

The affect on the performance of an electron beam resist (PMMA) loaded with  $\text{Al}_2\text{O}_3$  nanoparticles has been investigated. Specifically the introduction of the  $\text{Al}_2\text{O}_3$  nanoparticles increases the density of the film resulting in the reduction of the mean free path for the primary and secondary electrons. It was found that the incident electrons were more confined within the intended 'write' volume when the number density of  $\text{Al}_2\text{O}_3$  nanoparticles was increased, suggesting that the smaller features could be written into the resist.

The point electron distributions at incident electron energies lower than 50KeV were observed to have larger spread of electrons (when clearing the resist). However, the spread of electrons was reduced when the  $\text{Al}_2\text{O}_3$  nanoparticle loadings were increased as the incident electrons were radially confined by the proximity of the  $\text{Al}_2\text{O}_3$  nanoparticles. It is this mechanism that enables a higher resolution to be achieved as compared with PMMA alone.

It was found that the secondary electrons travelled further in unloaded PMMA when compared with PMMA loaded with 150mg of  $\text{Al}_2\text{O}_3$  nanoparticles. The total distance travelled by the secondary electrons decreases as the nanoparticle number density increases. A larger random walk of secondary electrons contributes to the proximity effect.

Of the three feature sizes studied, namely 70, 80, 90nm, a trend was observed that was consistent with the results obtained from chapter three. Specifically, that the presence of nanoparticles within the resist served to reduce the overall proximity effect resulting in 80nm structures that would probably not collapse on development. By representing point

electron distributions from the Monte Carlo model as contour plots, the relative confinement of ‘exposure’ electrons within the ‘write field volume’ highlights the quenching effect of the nanoparticles.

## **4.6 References**

- [1] [http://en.wikipedia.org/wiki/Acrylic\\_glas](http://en.wikipedia.org/wiki/Acrylic_glas) (2007).
- [2] [www.webelements.com/oxygen](http://www.webelements.com/oxygen) , (2007).
- [3] [www.webelements.com/Aluminium](http://www.webelements.com/Aluminium) (2007).
- [4] D. E. Newbury and R. L. Myklebust, ‘A Monte Carlo electron trajectory simulation for Analytical Electron Microscopy’, Analytical Electron Microscopy July 1981 (Ed. R. H. Geiss), San Francisco Press: San Francisco, p.91, (1981).
- [5] S. Luo and D. C. Joy, ‘Scanning Microscopy Suppl.’, vol. 4, p.125 (1989).
- [6] D.C. Joy, ‘Monte Carlo Modeling for Electron Microscopy and Microanalysis’, pp. 33, Oxford University Press, (1995).
- [7] A. Jeyakumar, ‘Development of inorganic resists for electron beam lithography: novel materials and simulations’, Thesis, pp 151 – 189 (2004).
- [8] K. E. Gonsalves, L. Merhari, H. Wu, Y. Hu, ‘Organic – Inorganic nanocomposite: unique resists for nanolithography’, Advanced Materials, vol 13, no 10 (2001).
- [9] L. Merhari, K. E. Gonsalves, Y. Hu, W. He, W. –S. Huang, m. Angelopoulos, W. H. Bruenger, C. Dzionk, M. Torker, ‘Nanocomposite resist systems for next generation lithography’, Microelectronic Engineering 63 (2002) pp 391 – 403.

# **Characterization of the Nanocomposite Resist Photo Mask for I-line applications**

## **Contents**

|   |       |
|---|-------|
| 5.1 Introduction.....   | -105- |
| 5.2 Experimental Details.....                                   | -106- |
| 5.2.1 Photolithography using the Nanocomposite Photo Mask.....  | -106- |
| 5.2.2 Dry Etching the photoresist using an ICP Plasma.....      | -107- |
| 5.3 Photolithography using the Nanocomposite Photo Mask.....    | -108- |
| 5.4 Pattern transfer into the substrate via plasma etching..... | -114- |
| 5.5 Limitations of the Nanocomposite Photo Mask Technology..... | -118- |
| 5.6 Summary.....  | -119- |
| 5.7 References.....   | -120- |

## **5.2 Experimental Details**

### **5.2.1 Photolithography using the Nanocomposite**

## **5.1 Introduction**

Both the semiconductor industry and research organisations rely heavily on photolithography technology to produce semiconductor, optical, Micro Electrical

Mechanical System (MEMS), superconducting and RF devices [1 - 6], as this is a well established and reliable technique. This technology is desirable as it leads to a very high throughput [7]. Advancement of photolithography has been the semiconductor industry's main focus and has produced ever decreasing features sizes [8 - 11].

As seen from chapter two the nanocomposite resist was designed as a reusable optical photo mask [12]. From the previous chapters, it was determined that sub 100nm structures could be successfully written into nanocomposite resist. The pattern that was directly written into the nanocomposite resist could be transmitted to produce an image of the same pattern on a receiving substrate, in this case a photoresist. As seen in chapter 2 section 3.3 there was an optical contrast required between the substrate material and the nanocomposite resist in order for the pattern to be transmitted successfully, by contact printing directly to the receiving photoresist.

Once the pattern in the receiving photoresist had been achieved, it must be used to transfer its pattern into the surface of substrate; this can be achieved by etching. However, in the fabrication of ULSI devices, dry etching was preferable to wet etching methods in many applications. As device dimensions are scaled down considerably, direct manipulation of the profile of the structure can be achieved by dry etching in one direction (hence, vertical profiles are possible).

The aim of this chapter was to characterise a low cost re-useable optical mask for high throughput using the nanocomposite resist and transfer the pattern to S1318 photoresist. It focuses on the characterisation of the performance of contact photolithography of the nanocomposite photo mask and demonstrates the parameters of the dry etch process with an Inductivity Coupled Plasma (ICP) dry etch system by driving the profile of the developed photoresist into a Silicon substrate using a gas mixture of  $\text{BCl}_3\text{Cl}_2$ .

## **5.2 Experimental Details**

### **5.2.1 Photolithography using the Nanocomposite Photo Mask**

The contact photolithography experiment consisted of two test cases. These test cases were designed to show the impact of the surface roughness that was shown in chapter

two in the application of contact photolithography. The first test case was the sample containing 200mg of  $\text{Al}_2\text{O}_3$  nanoparticles, dispersed directly into the PMMA / Anisole solution. When spun and soft baked, this had an overall thickness of approximately 800nm and an rms surface roughness of approximately 400nm. The nanocomposite resist that was loaded with 200mg of  $\text{Al}_2\text{O}_3$  nanoparticles using the Methanol dispersal method was the second test case. This achieved a thickness of 627nm and rms surface roughness of approximately 60nm. The RMS roughness was determined using an AFM.

The nanocomposite resist photo mask was patterned by the electron beam lithography system described earlier. Two test patterns were written, consisting of twelve  $50\mu\text{m}$  squares and twelve  $1\mu\text{m}$  lines. The samples were exposed at clearing doses of  $500\mu\text{C}/\text{cm}^2$  and  $300\mu\text{C}/\text{cm}^2$  respectively, due to their thickness. The contact photolithography was carried out as described in chapter 2 §2.3.

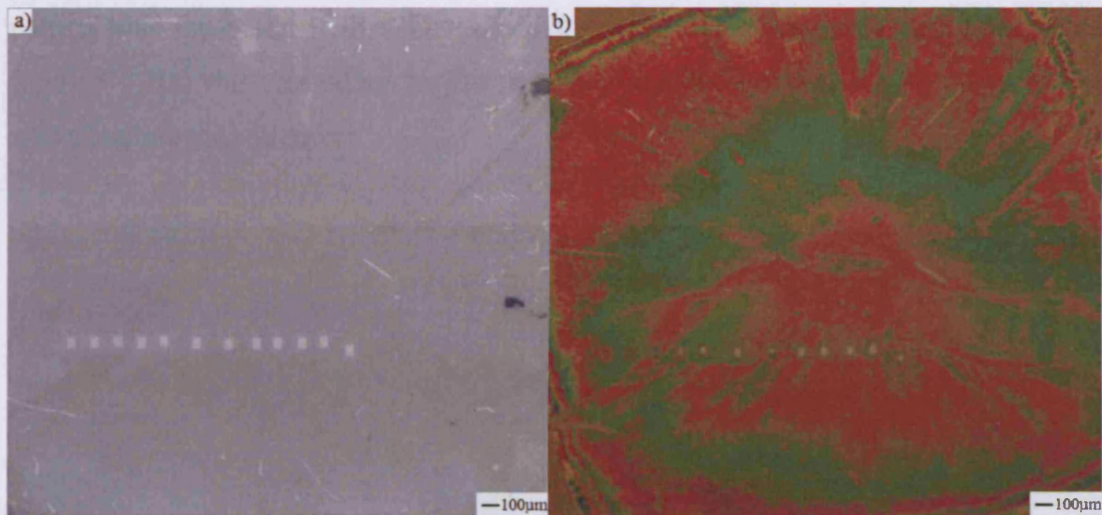
### **5.2.2 Dry Etching using an ICP Plasma**

The photoresist used in this experiment was shipley S1813 spun on a Silicon substrate at a spin speed of 6000rpm for 45 seconds to give a resist thickness of  $1.12\mu\text{m}$ . The I-line exposure time was 6 seconds and the develop time was 20 seconds using the 2401 developer. The sample was patterned using a chrome photomask which consisted of  $50\mu\text{m}$  stripes. The feature thickness was measured using the dektak profileometer before etching. The sample was etched for 4 minutes using the etch chemistry of two gases that was set up in the ICP. The first gas that was used was  $\text{BCl}_3$ , this had a flow rate of 25/sccm and the second gas was  $\text{Cl}_2$  which had a flow rate of 15/sccm at room temperature, the rf power was 80W. When the sample was etched for 4 minutes the thickness of the features were measured. Then the S1813 photoresist was removed using Acetone. The depth of the etched Silicon was measured and both the etch rates could be determined from this data. Once both of the etch rates were ascertained the etch selectivity could be determined between the two materials.



### 5.3 Photolithography using the Nanocomposite Photo Mask

The first test case was the nanocomposite resist that had directly dispersed the  $\text{Al}_2\text{O}_3$  nanoparticles within it. Figure 5 – 1(a) shows the nanocomposite photo mask that was used in this experiment with the horizontal line of twelve  $50\mu\text{m}$  squares. On inspection, the photograph in figure 5 – 1(a) shows the surface of the nanocomposite photo mask appeared to be relatively homogenous, whereas the surface of the developed S1813 photoresist in figure 5 – 1(b) shows the smear patterns due to the inhomogenous dispersion of the  $\text{Al}_2\text{O}_3$  nanoparticles. In chapter 2 §3.2 it was determined by the AFM, that the surface roughness of the nanocomposite mask was approximately  $402\text{nm}$ .



*Figure 5 – 1: (a), Nanocomposite resist photo mask, (b) Resultant S1813 photoresist.*

As 2% of the UV radiation was transmitted through the nanocomposite resist (as discussed in chapter 2 §3.3) the roughness of the surface had resulted in uneven exposure, indicated by the interference colours (indicated by the red & green colours in figure 5 – 1b).

Figure 5 – 2a & b shows a zoomed in view of figure 5 – 1. It can be seen from the SEM micrographs in figure 5 – 2(a) that the definition of the pattern appears to be good. However, as seen in chapter three, the lines of sample PMMA 950K7% loaded with  $150\text{mg}$  of  $\text{Al}_2\text{O}_3$  nanoparticles showed that nanoparticle aggregations interfered with the overall shape of the pattern, as the size of these aggregations were in the

range of just a few nanometers to approximately 50nm. However, as the nanocomposite resist shown here had the worst case of rms surface roughness, these nanoparticle aggregations may be large enough to interfere with the definition of the pattern (from the application of photolithography point of view). The aggregations can not be seen here due to the low magnification of the SEM micrograph of figure 5 – 2. Based on the data discovered in chapter three, it is suspected that the size of nanoparticle aggregations may be in the range of 100nm to 300nm. However, this may not affect the function of the optical mask as the size of the nanoparticle aggregations are below the I-line wavelength.

The pattern that was written consisted of twelve squares that had dimensions of 50 $\mu$ m. However, the pattern does not appear to be square due to the fact that the sample was tilted to an angle of approximately 20° to obtain a light/dark electron contrast. The pattern was measured with a Detak profileometer. The horizontal line featured in figure 5 – 2(a) was created by the Detak profileometer scratching the Au surface, as it was a contact measurement.

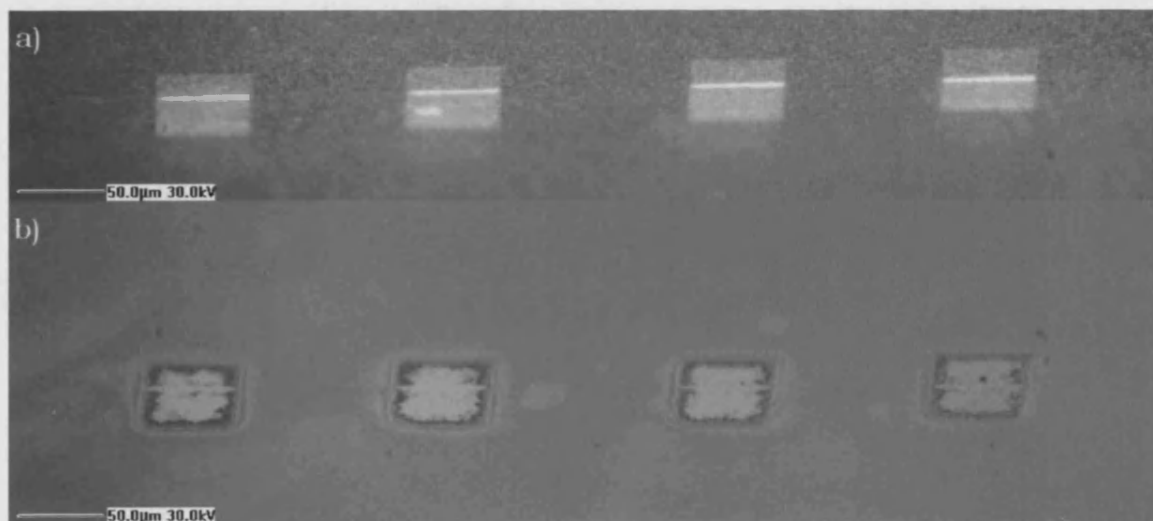


Figure 5 – 2: (a) PMMA based nanocomposite resist following development, (b) developed S1813 photoresist on Silicon, which has been exposed to I – line wavelengths.

The pattern was transferred from the PMMA based nanocomposite resist into the S1813 photoresist, through contact printing. It can be seen from figure 5 – 2(b) that the pattern has been poorly transferred into the S1813 photoresist. The surface roughness is clearly affecting the quality of transfer as illustrated in figure 5 – 3.



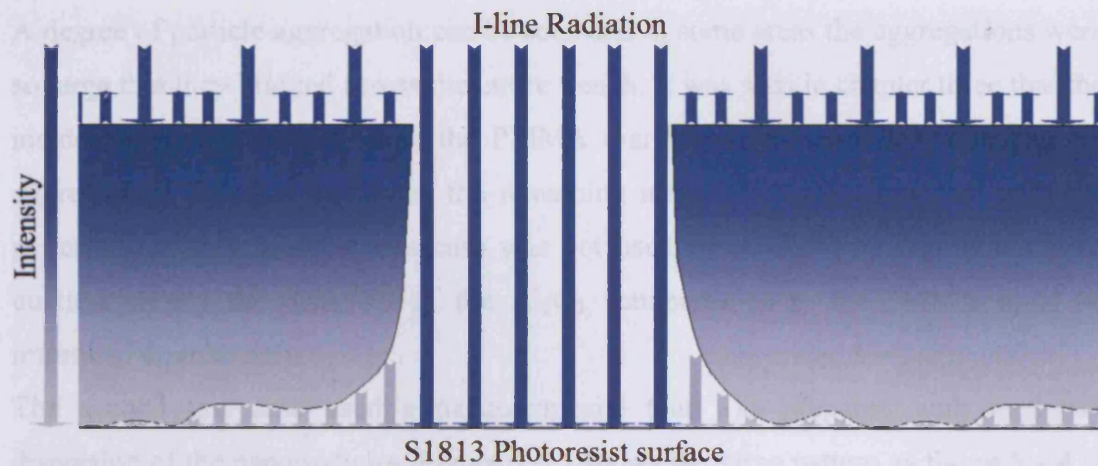


Figure 5 – 3: Schematic representation of the I-line radiation magnitude when the surface of the nanocomposite resist was in contact with the S1813 photoreist.

The overall thickness of the exposed and developed photoresist was reduced from  $1.12\mu\text{m}$  to  $500\text{nm}$  due to the fact that the nanocomposite resist has a residual transparency and an imperfect contrast between transparent and opaque regions.

Figure 5 – 4 shows an SEM image of the surface of the nanocomposite resist photomask; the pattern that was directly written in the photo mask consisted of twelve  $2\mu\text{m}$  microwires isolated by a  $1\mu\text{m}$  trench.

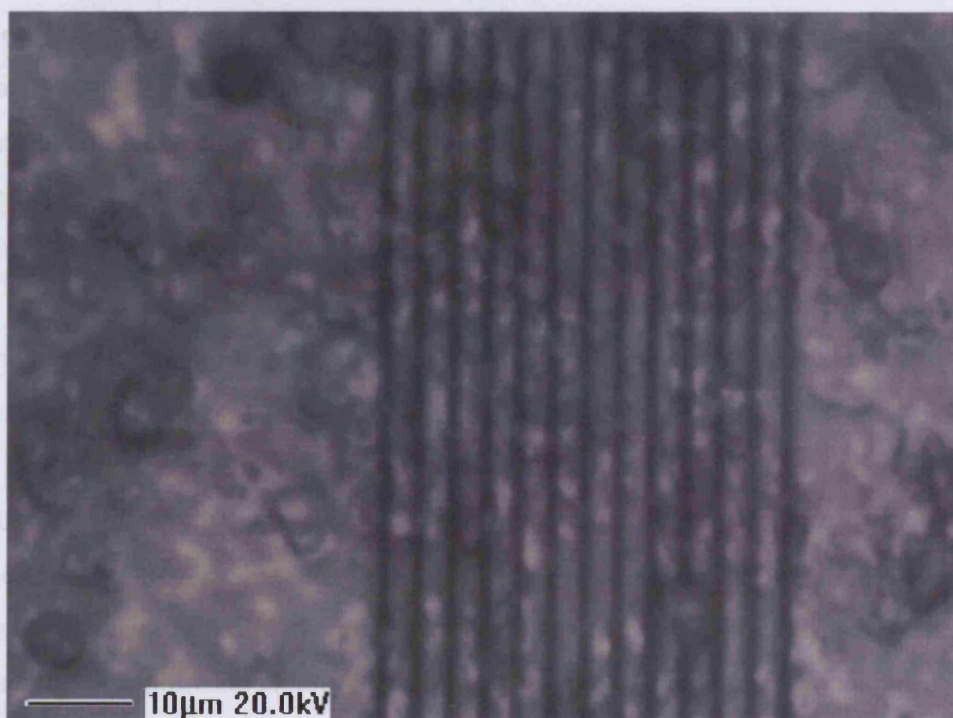


Figure 5 – 4: SEM image of the  $1\mu\text{m}$  trenches directly written into the nanocomposite resist.

A degree of particle aggregation can be seen and in some areas the aggregations were so large that they bridged across the entire trench. It was seen in chapter three that the incident electron beam cleaved the PMMA that surrounds the  $\text{Al}_2\text{O}_3$  nanoparticle aggregations, in some instances, the remaining nanoparticles can interfere with the pattern. The photomask in this case was not used in an exposure due to its poor quality; clearly the dispersal of the  $\text{Al}_2\text{O}_3$  nanoparticles in the PMMA must be improved dramatically.

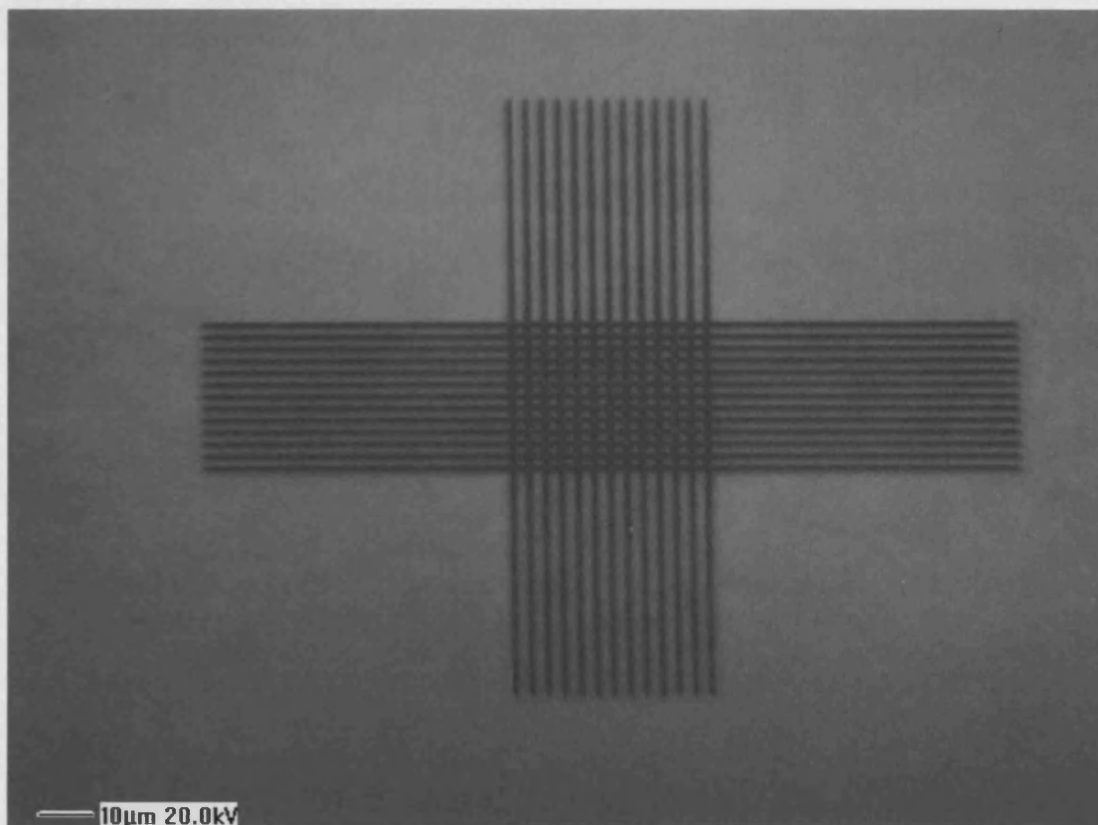
The second test case used a nanocomposite that was prepared with methanol dispersion of the nanoparticles. Figure 5 – 5 shows the same pattern as figure 5 – 4 in this nanocomposite resist photomask. It can be seen from figure 5 – 6 that the microwires had nanoparticle aggregations. These aggregations are considerably reduced when compared to the aggregations seen in figure 5 – 4. The pattern fabricated in the nanocomposite resist photo mask (see figure 5 – 5) was transferred to the S1813 photoresist.

Good pattern transfer was achieved with this mask as shown in the optical photograph of figure 5 – 7. On closer SEM inspection (figure 5 – 8), the presence of the aggregations has had minimal effect. This is because the homogeneity of the surface of the nanocomposite resist photo mask had improved.

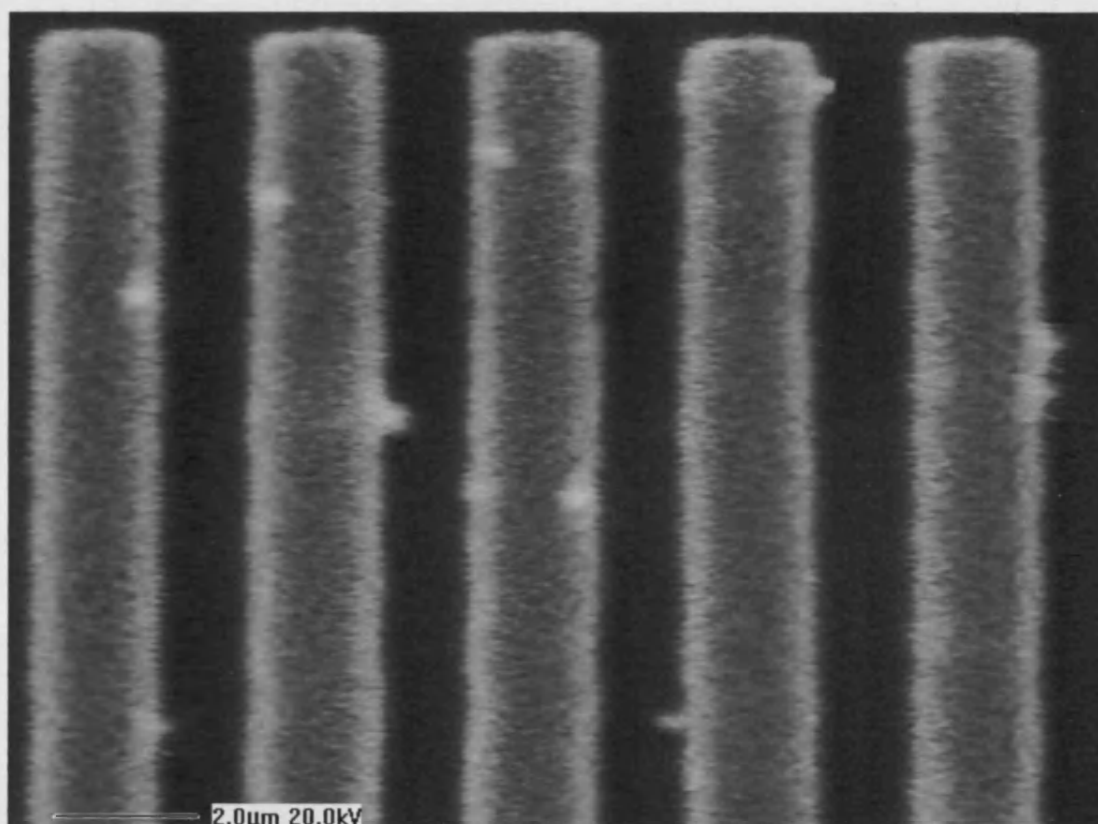
The optical properties could have been improved by fabricating a thicker resist. By achieving this, more  $\text{Al}_2\text{O}_3$  nanoparticles could be embedded into the PMMA medium. This reduces the radiation propagating through the film. However, as seen in the previous chapter using a thicker nanocomposite resist compromises the minimum achievable feature size, but for I-line wavelength this is negligible.

It is possible to produce grey-scale photomask using the nanocomposite resist technology [12] and in appendix F. This is a useful technique for fabricating three dimensional structures in a polymeric thin film. Utilizing structured photoresist as an etch mask for example can enable a three dimensional structure to be transferred to a substrate material such as silicon; anisotropic dry etching is one method. However, fabricating the grey-scale mask in the first instance is technically challenging.

Transferring the three dimensional grey-scale structure from the electron beam resist to a standard photoresist enables multiple structures to be made from a single mask is significant in that all etch masks of this type are single use. From figure 3 – 10 it is



*Figure 5 – 5: The nanocomposite resist photomask.*



*Figure 5 – 6: SEM image of the nanoparticles in the nanocomposite resist.*



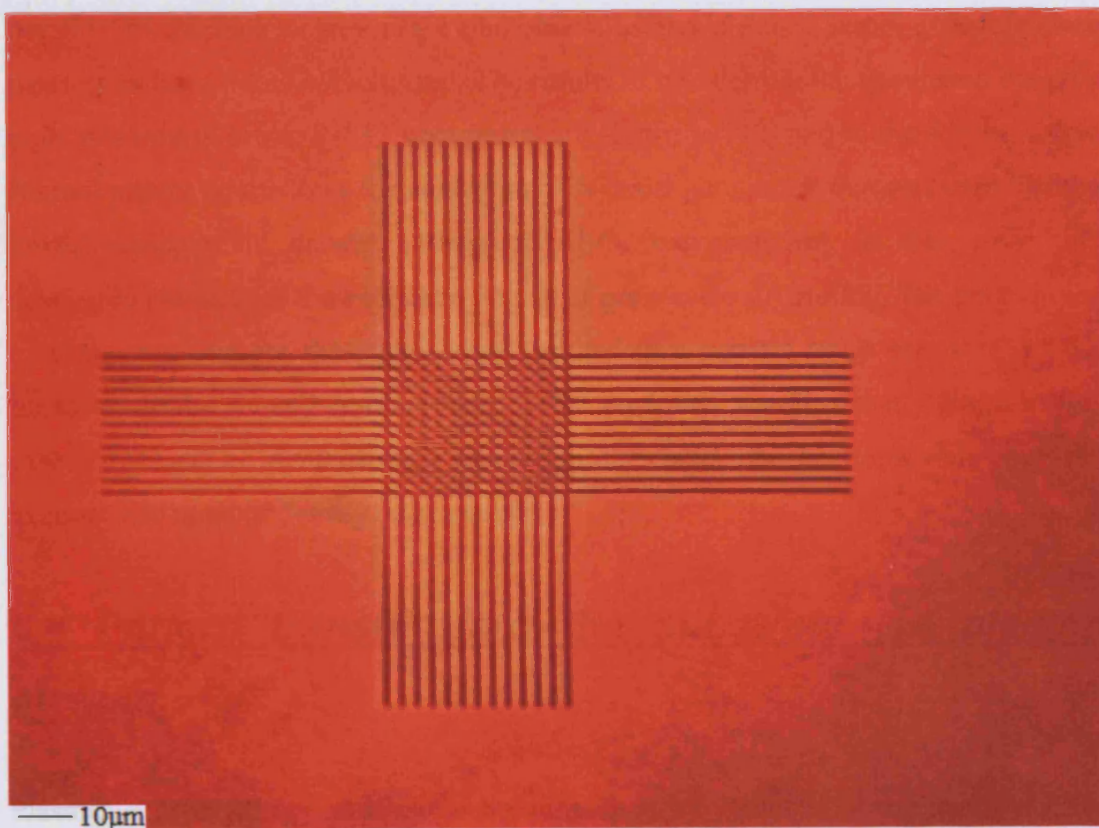


Figure 5 - 7: Developed S1813 photoresist.

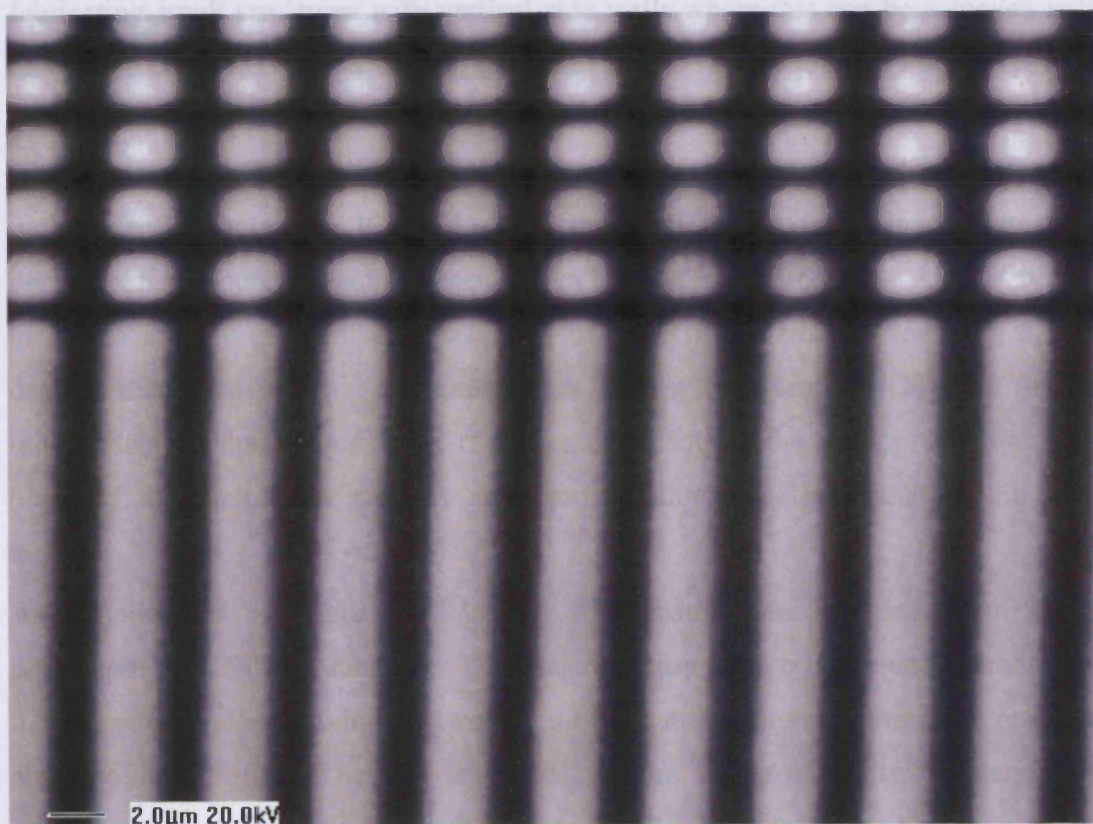


Figure 5 - 8: SEM image of the resultant S1813 photoresist.

possible to produce a grey scale photomask as the electron beam exposure dose parameters have been characterized. The results of transferring the features in the grey scale photomask to the S1813 photoresist are shown in [12] and in the section called Journal papers. In this case the nanocomposite resist photomask that was used had the lowest nanoparticle density (10mg of Al<sub>2</sub>O<sub>3</sub> nanoparticles). It was clear that developed photoresist showed some degree of grey-scale structuring. The poor choice of nanocomposite for the photo-mask resulted in a general 'over exposure' of the photoresist. The overall resultant photoresist thickness was less than 100nm in this case. However, as demonstrated earlier, these results can be improved when the nanoparticle number density is increased.

#### **5.4 Pattern transfer into the substrate via plasma etching.**

Plasma – assisted dry etching techniques such as Reactive Ion Etching (RIE), Inductively Coupled Plasma (ICP) and ECR have been the preferred methods of fabricating small structures with vertical side walls where this can be achieved with ease when compared to wet etching techniques. Inductively Coupled Plasma (ICP) is the preferred choice because in conventional RIE, the shape of the etch profile is compromised as the physical and chemical components of etch cannot be independently controlled. ICP [14 – 17] and ECR [18] systems incorporate high density plasma sources that have been shown to have larger etch rates. An ICP system generates a more efficient etch than that of the RIE system by producing a high density discharge at low pressures. Also this system provides biasing that is independent of the sample, with rf power that controls the energy at which ions bombard the sample, as well as an improved uniformity compared to the ECR method.

As demonstrated by figure 5 – 9 a grey scale feature was fabricated with S1813 photoresist on a Silicon substrate. This was done to obtain a better understanding of the impact of the selectivities between the two materials by measuring the resultant angles of the profiles. The aim was to match the angles of the two materials by achieving a 1:1 ratio, this is difficult because the S1813 photoresist is a softer material than Silicon and consequently will etch at a faster rate.

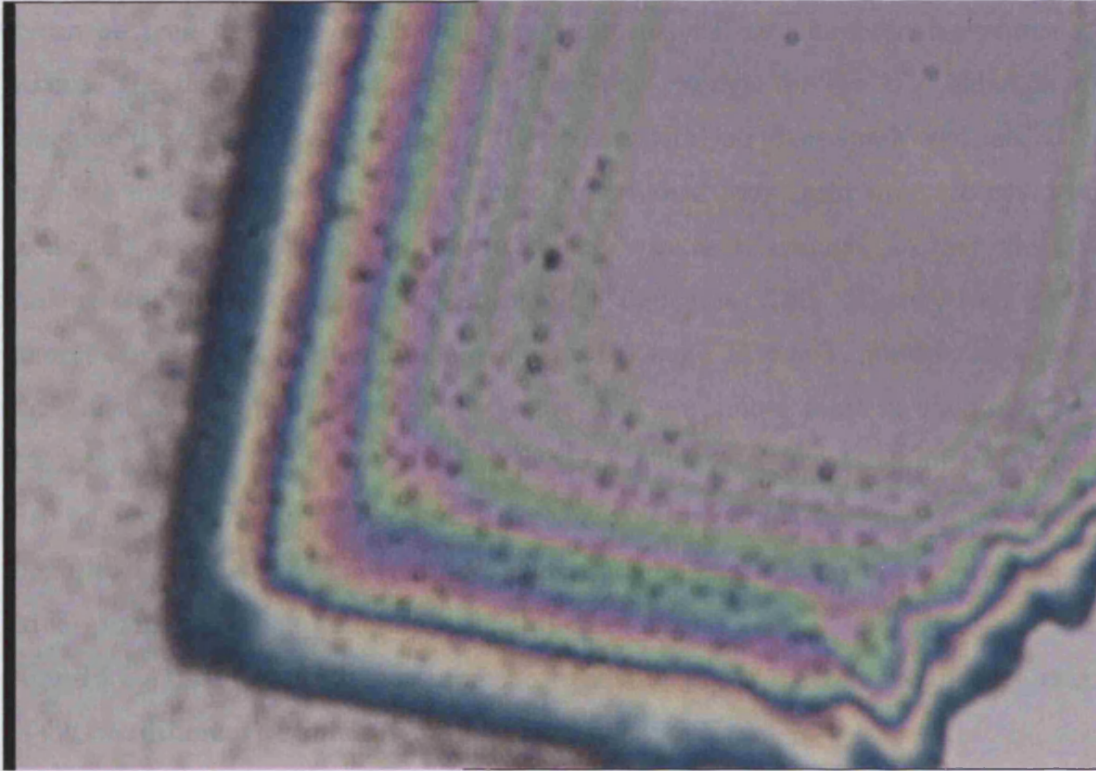


Figure 5 – 9: A three dimensional grey scale test feature.

The developed grey scale feature was fabricated using the method described below; the results of which are in figure 5 – 10. This showed the resultant thickness of exposed and developed resist as a function of a series of short one second exposures.

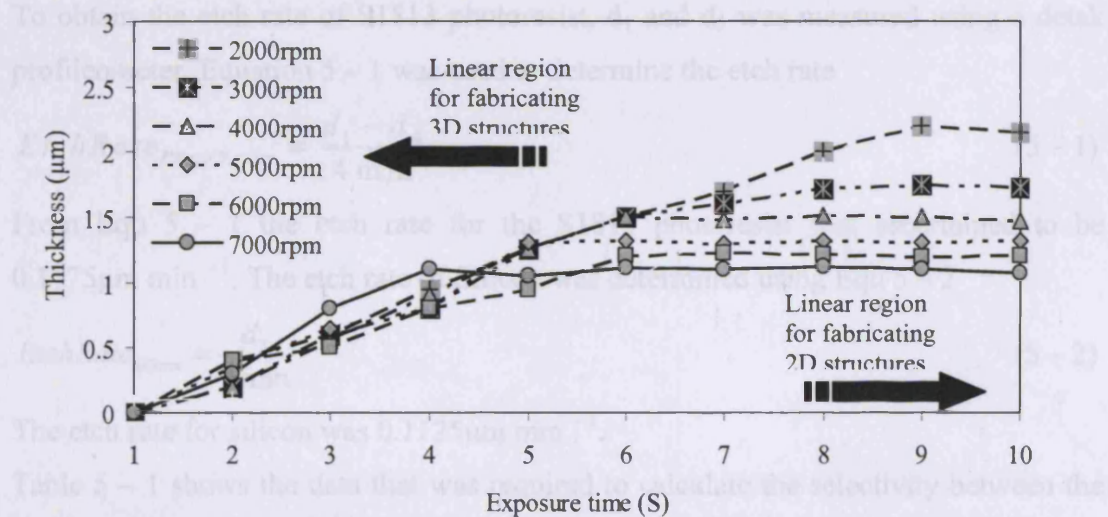


Figure 5 – 10: Fabrication parameters for 2D and 3D micro structures for S1813 photoresist.



It can be seen from the graph that a two dimensional structure can be fabricated because the duration of the exposure was long enough for the UV radiation to penetrate the total thickness of the S1813 photoresist. One photo mask was needed to fabricate this structure. However, a three dimensional grey scale structure could be fabricated, as the duration for this exposure was short enough, so that the UV radiation did not penetrate the entire resist thickness. This structure was more complex to produce, but the principle remains the same. However, multiple exposures were needed and this can mean that more than one photo mask is required. The feature in figure 5 – 9 incorporates five steps; each had a length of 250µm. This could also be verified by the change in interference colours, which was due to the S1813 thin film thickness. For convenience, this structure was used as a test structure to drive – in the grey scale structure in to a Silicon substrate.

Figure 5 – 11 depicts depth measurements needed in order to determine the etch rates of the two different materials (S1813 photoresist and silicon).

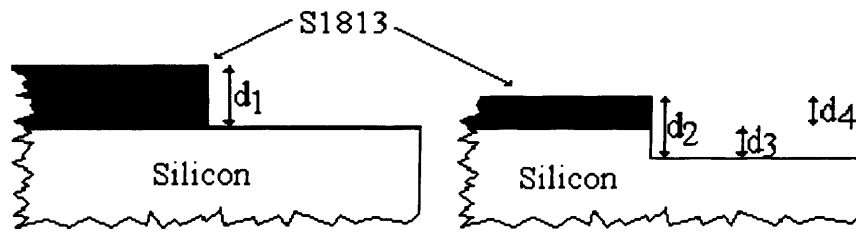


Figure 5 – 11: The method for achieving the etch rates and selectivity.

To obtain the etch rate of S1813 photoresist,  $d_1$  and  $d_3$  was measured using a detak profileometer. Equation 5 – 1 was used to determine the etch rate

$$EtchRate_{Photo\ Resist} = \frac{d_1 - d_4}{4\ min} \quad (5 - 1)$$

From Equ 5 – 1 the etch rate for the S1813 photoresist was ascertained to be  $0.1775\mu m\ min^{-1}$ . The etch rate of Silicon was determined using Equ 5 – 2

$$EtchRate_{Silicon} = \frac{d_3}{4\ min} \quad (5 - 2)$$

The etch rate for silicon was  $0.1125\mu m\ min^{-1}$ .

Table 5 – 1 shows the data that was required to calculate the selectivity between the S1813 photoresist and the Silicon substrate. This was obtained using the method described in the experimental.

It was important that the integrity of the surface profile of the S1813 photoresist remained intact as it was etched away, to maintain the angle of the grey scale structure

| <i>Etch Rate Number</i> | <i>Depth (<math>\mu\text{m}</math>)</i> |
|-------------------------|---|
| $d_1$                   | 1.1                                     |
| $d_2$                   | 0.81                                    |
| $d_3$                   | 0.45                                    |
| $d_4$                   | 0.39                                    |

*Table 5 – 1: The thickness data required to calculate the selectivity.*

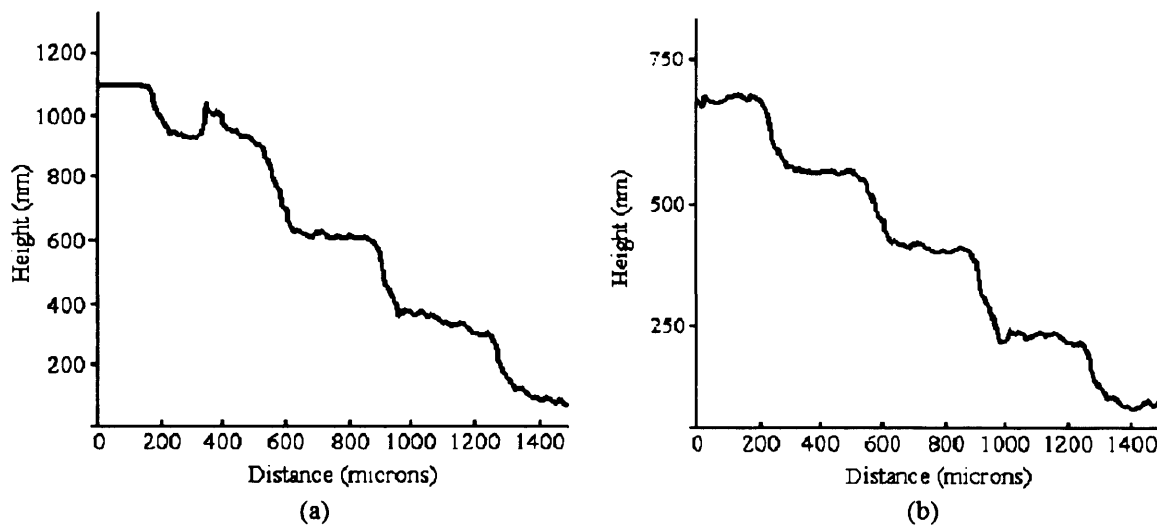
and the aspect ratio of the S1813 photoresist while transferring the photoresist profile in the substrate. It was found that Equ 4 – 3 determined the selectivity.

$$S_{\text{Etch}} = \frac{d_3}{d_4} = \frac{d_3}{d_1 - d_3}, \quad (5 - 3)$$

$$S = \frac{1}{S_{\text{Etch}}}$$

By running an etch, using the parameters stated in section 2.2, it was found that the selectivity was 1.6. Therefore, the photoresist S1813 etches 1.6 times faster than silicon.

Following this experiment, it was found that the grey scale photo masks fabricated in S1813 photoresist could be transferred into silicon via a dry etching process using  $\text{BCl}_3\text{Cl}_2$ . The figures below (5 – 12) clearly show that this staircase greyscale profile, originally in the S1813 photoresist, has been successfully transferred into the silicon.



*Figure 5 – 12: (a) Graded S1813 photoresist steps with an angle of  $0.045^\circ$ , (b) Graded silicon steps with an angle of  $0.028^\circ$ .*



## 5.5 Limitations of the Nanocomposite Photo Mask Technology

To meet the criteria of a semiconductor foundry, the throughput of Silicon Intergrated Circuits (ICs) must be exceptionally high in order to obtain high yield. Therefore, to achieve a high throughput, a photoresist on a Silicon substrate must be exposed for the shortest time possible, in our case it was a six second exposure. This was due to the intensity of the Hg vapour bulb. However, the same mask would remain in the mask aligner for a period of a working day which is eight hours. As the nanocomposite photo mask is exposed for this amount of time the temperature of the photomask may exceed the acceptable thermal expansion feature tolerances. As the temperature was elevated through out this time, the features may change shape by increasing in size. The expansion of the features patterned in the nanocomposite resist can be determined by the following equation.

$$L_T = L_{RoomTemp}(1 + \alpha T) \quad (5 - 4)$$

where the length of the feature was indicated by  $L_{RoomTemp}$  at room temperature. The thermal expansion co-efficient of the material was given by  $\alpha$  and  $T$  was the temperature. The thermal expansion co-efficient of the PMMA,  $Al_2O_3$  and the  $TiO_2$  was  $70 \times 10^{-6}$ ,  $8.1 \times 10^{-6}$  and  $7.14 \times 10^{-6} MK^{-1}$  respectively [19 – 21]. All thermal expansion models incorporate  $50\mu m$  features patterned in the nanocomposite resist. Figure 5 – 13a shows the thermal expansion of the PMMA polymer, the model clearly shows that as the temperature increases the PMMA will expand. Figure 5 – 13b shows the thermal expansion of the nanoparticle species.

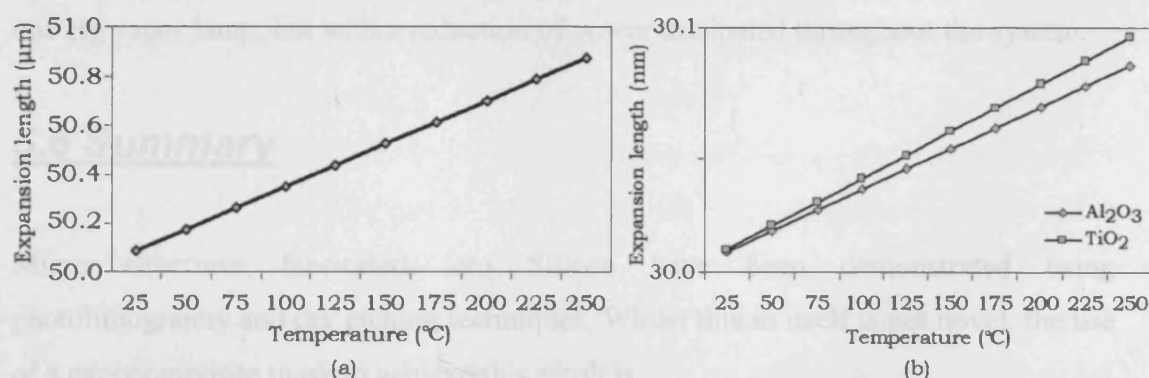


Figure 5 – 13: (a) Thermal expansion of the features in PMMA mask. (b) Thermal expansion of  $Al_2O_3$  and  $TiO_2$  nanoparticles.

Figure 5 – 14 shows the limitations of the nanocomposite photomask technology, the total thermal expansion of the nanocomposite resist was determined by combining the PMMA and the nanoparticle species. It can be seen that the oxide nanoparticles have negligible effects in the overall expansion of the nanocomposite resist as both nanocomposite resists are superposed on one another.

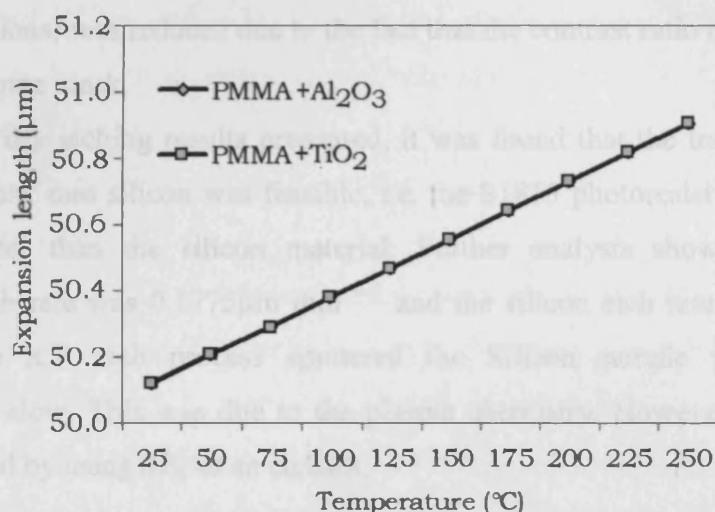


Figure 5 – 14: Thermal expansion of the nanocomposite resist.

However, at the 1µm dimension, the impact of the thermal expansion of the feature is not as critical. The nanocomposite resist would expand in the range of 10 – 20nm. However, the exposure method could be modified, by replacing the Hg vapour lamp with I-line Light Emitting Diodes (LEDs). The LEDs would not expand the features patterned in the nanocomposite resist because there is relatively little thermal radiation emitted from LEDs. Multiple LEDs could produce the same illumination as one Hg vapor lamp, but with a reduction of power dissipated throughout the system.

## **5.6 Summary**

Micro structures fabricated into Silicon have been demonstrated using photolithography and dry etching techniques. Whilst this in itself is not novel, the use of a nanocomposite mask to achieve this result is.

The first test case described at the start of this chapter consisted of an e-beam patterned nanocomposite thin film with poorly dispersed nanoparticles. Surface roughness of this film proved detrimental in contact photolithography. The resultant

features in a standard photoresist were of poor quality. A refined mask, utilising a solvent to improve the particulate dispersal was also patterned. The pattern, consisting of 50 $\mu\text{m}$  squares and 1 $\mu\text{m}$  lines showed good edge definition under SEM inspection (nanoparticle aggregates were visible, however, were few in number). More importantly, the surface roughness was minimised as compared with the first sample, resulting in good pattern transfer to photo resist. The overall thickness (dark area, or unexposed regions) was reduced due to the fact that the contrast ratio is not as good as a standard chrome mask.

From the ICP dry etching results presented, it was found that the transfer of a grey scale photo mask into silicon was feasible, i.e. the S1813 photoresist material etches 1.6 times faster than the silicon material. Further analysis showed that S1813 photoresist etch rate was 0.1775 $\mu\text{m min}^{-1}$  and the silicon etch rate was 0.1125 $\mu\text{m min}^{-1}$ . The ICP etch process sputtered the Silicon sample which made it predominately slow. This was due to the plasma chemistry. However, better results can be achieved by using  $\text{SF}_6$  as an etchant.

## **5.7 References**

- 1) K. Keem, J. Kang, C. Yoon, D. -Y. Jeong, B. -M. Moon, S. Kim, 'A fabrication technique for top gate ZnO nanowire field effect transistor by a photolithography process', Microelectronic engineering 84, 1622 – 26 (2007).
- 2) C. Y. Liu, Y. Qu, S. Yuan, S. Z. Wang, S. F. Yoon, 'InGaAs – GaAs 980nm stripe geometry and circular ring ridge waveguide lasers fabricated with pulsed anodic oxidation', IEEE photonics technology letters, vol 17, no 2, (2005)
- 3) H. -C. Yu, S. -J. Chang, Y. -K. Su, C. -P. Sung, Y. -W. Lin, H. -P. Yang, C. -Y. Huang, J. -M. Wang, 'A simple method for fabrication of high speed vertical cavity surface emitting lasers', Materials Science and Engineering, B106 101 – 104 (2004).
- 4) C. L. Goldsmith, Z. Yao, S. Eshelman, D. Denniston, 'Performance of low loss RF MEMS capacitive switches', IEEE Microwave and guided wave letters, vol 8, no 8 (1998).

- 5) Z. W. Dong, S. P. Pai, R. Ranesh, T. Venkatesan, M. Johnson, Z. Y. chen, A. Cavanaugh, Y. G. Zhao, X. L. Jiang, R. P. Sharma, s. Ogale, R. L. Greene, 'Novel high Tc temperature with manganite oxides', J. Appl. Phys. Vol 83, no 11, (1998).
- 6) G. N. Gol'tsman, A. Karneev, I. Rubtsova, I. Milostnaya, G. Chulkova, O. Minaeva, K. Smirnov, B. Voronov, W. Slysz, A. Pearlman, A. Verevkin, R. Sobolewski, 'Ultra fast superconducting single photon detectors for near infrared wavelength quantum communications', Phys. Stat. Sol. (c) 2, no 5, 1480 – 88 (2005).
- 7) K. Ronse, Optical lithography – a historical perspective', C. R. Physique 7 (2006) 844 – 57.
- 8) G. Marsh, 'Moore's law at the extremes', Materials Today, 'May (2003).
- 9) K. Deguchi, T. Haga, 'Proximity x – ray and extreme ultra violet lithography', C. R. Acad. Sci. Paris, t.1, series IV, pp 829 – 42, (2000).
- 10) H. I. Smith, D. J. D. Carter, M. Meinhold, E. E. Moon, M. H. Lim, J. Ferrera, M. Walsh, D. Gil, R. Menon, 'Soft x – rays for deep sub 100nm lithography with and with out masks', Microelectronic Engineering 53 (2000) 77 – 84.
- 11) R. S. Mackay, 'The future of lithography after 193nm optics', SEMATECH, Microelectronic Engineering 41/42 (1998) 71 – 74.
- 12) S. Lewis, R. Wheeler – Jones, R. Perks, V. Haynes, 'Low cost PMMA based photo – masks for 3D grey scale micro – structuring applications', Technical Proceeding of the 2006 Nanotechnology Conference and Trade Show, Vol 3 Chapter 2 : Nanoscale Fabrication, pp214 – 217, (May 2006).
- 13) F. A. Khan, L. Zhou, V. Kumar, I. Adesida, R. Okojie, 'High rate etching of AlN using BCl<sub>3</sub>/Cl<sub>2</sub>/Ar inductively coupled plasma', Mat. Sci. Eng. B95 (2002) 51 – 54.
- 14) J. L. Young, R. H. Hye, Y. Y. Geun, 'characteristics of magnetized inductively coupled plasma source for flat panel display applications', Surface and coatings technology 133 – 134 (2000) 612 – 616.
- 15) S. G. Park, C. Kim, B. O, 'An array of inductively coupled plasma for large area plasma', Thin solid films 355 – 356 (1999) 252 – 255.
- 16) R. J. Shul, L. Zhang, C. G. Willison, J. Han, S. J. Pearton, J. Hong, C. R. Abernathy, L. F. Lester, 'Group – III Nitride etch selectivity in BCl<sub>3</sub>/Cl<sub>2</sub> ICP plasmas', MRS Internet J. Nitride Semicond. Res. 4S1, G8.1 (1999).

- 17) S. J. Pearton, 'High ion density dry etching of compound semiconductors', materials science and engineering B40 (1996) 101 – 118.
- 18) <http://www.goodfellow.com/csp/active/static/A/polymethylmethacrylate.html> (2005).
- 19) <http://www.accuaratus.com/alumox.html> (2006).
- 20) M. E. Straumanis, T. E. Jima, W. J. James, 'The  $\text{TiO}_2$  phase expolored by the lattice constant and density method', Acta Cryst, 14, pp 493 – 97 (1961).



# **Self Assembled Nanoparticle Film for Direct 1 – line Nanolithography applications**

## **Contents**

|   |      |
|---|------|
| 6.1 Introduction.....   | 124- |
| 6.2 Experimental Details.....   | 127- |
| 6.2.1 Fabrication of the Plasmonic Mask.....  | 127- |
| 6.2.2 Detection of SPR.....   | 128- |
| 6.2.3 SPR Nanolithography Technique.....  | 130- |
| 6.3 Nano Fabrication of the Hexagonally Closely Packed Ag Nanoparticle Array.....   | 130- |
| 6.4 Detection of Surface Plasmons on Ag thin film.....                              | 136- |
| 6.5 Optical Properties of the Hexagonally Closely Packed Ag Nanoparticle Array..... | 139- |
| 6.6 Direct Nano Patterning a Two and Three Dimensional Structures.....              | 141- |
| 6.7 Discussion.....   | 143- |
| 6.8 Summary.....  | 147- |
| 6.9 References.....   | 149- |

## **6.1 Introduction**

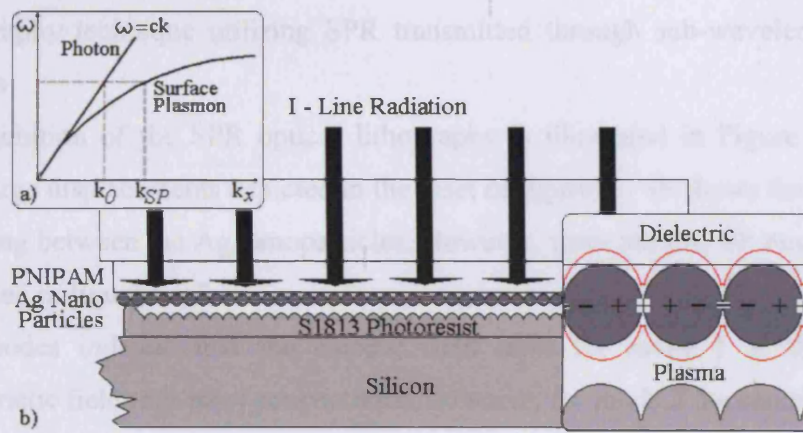
Photolithography is a well known technique for producing micrometre dimensional structures as seen by previous chapters and has been a major fabrication method for producing integrated circuits (IC) in the semiconductor industry over the past several decades. However, with an ever increasing demand on Moore's law for faster integrated circuits there is a need for transistors to have gate lengths on a nanometer scale. The advancement of fabricated nanometer structures is a difficult challenge with existing photolithography technology. As seen in chapter 3, nanometer features can be achieved with the use of e-beam technologies but the time taken to produce these structures takes longer. Therefore, the semiconductor industry such as Intel, AMD, IBM etc are not interested in this technology for mass production. Preferably, photolithography using the I-line wavelength is desirable for economic reasons, it drives the associated costs down, which includes exposure times and relative equipment costs.

Therefore, photolithography in the optical near field has been developed as a promising parallel route to the fabrication of nano features beyond the diffraction limit. To perform near-field photolithography several methods have been demonstrated which include the probe of a near-field scanning optical microscope, contact imaging through a transmission mask or a binary phase-shift mask [1,2], evanescent near-field lithography with an embedded-amplitude mask [3], light coupling masks [4], plasmon printing and evanescent interferometric methods [5, 6] have been successfully demonstrated for performing near – field photolithography.

Surface plasmon resonance (SPR) has the potential to influence light by enhancing sub-wavelength structures. The scientific community has become interested in the phenomenon of the transmission of opaque metal films when light is enhanced through sub-wavelength hole arrays. [7, 8]. The excitation of SPRs on the metal surface dramatically enhances the optical throughput via the sub-wavelength apertures. The surface plasmon dispersion relation,  $k_{sp}$  which incorporates the frequency-dependent SP wave vector, describes the interaction of light and SPR [9], this is shown here

$$k_{SP} = k_0 \sqrt{\frac{\epsilon_d \epsilon_m}{\epsilon_d + \epsilon_m}} \quad (6 - 1)$$

where  $k_0$  is the wave vector of light in vacuum,  $\epsilon_m$  and  $\epsilon_d$  are relative dielectric constants of a metal and the surrounding dielectric material. The SPR dispersion curve, shown in Figure 6 – 1a, indicates that smaller features are expected in the lithographic pattern. The wavelength of the excited SPs is shorter than the wavelength of the excitation light at the same frequency. Due to the momentum mismatch between the light waves and the SP waves, light cannot excite SPs in the metal directly. However, by using a rough surface, a grating coupler, or an attenuated total reflection (ATR) coupler, light can be converted into SPs and vice versa.



*Figure 6 – 1: a) Schematic drawing of the surface plasmon dispersion curve. At the same frequency, surface plasmons display a shorter modal wavelength compared to that of free space photons, therefore, allowing sub – wavelength lithography, b) Schematic of the nanolithography process using the Silver mask. Inset: The charges and the electromagnetic field of surface plasmons propagating on the grating surface in the x direction.*

For example, a 2D grating coupler can act as a 2D square array of holes. Light can excite SP waves on the incident side, by selecting a proper periodicity for the hole array and a proper dielectric constant for the medium surrounding the metal substrate, the SP waves can be resonantly coupled through the periodic hole array to the other side of the metal [7]. The SP waves on the exit plane are scattered on the hole array and will be converted back into light waves, if the dielectric constant of the dielectric layers match on both

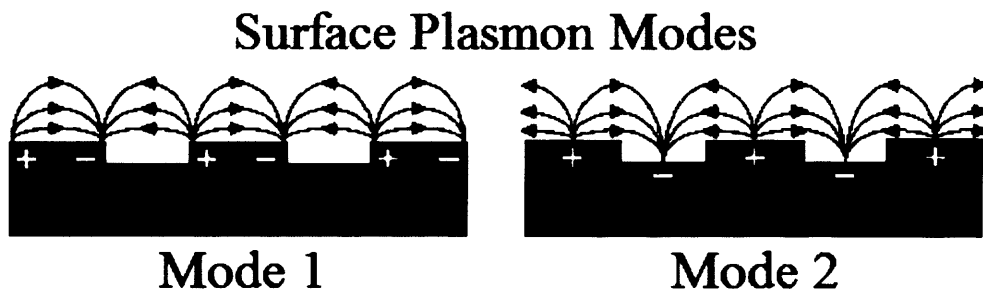
sides of the metal layer. The light wavelength that excite the SP resonance mode (when the incident light is normal to the 2D hole array) is given by [7],

$$\lambda_{(i,j)} = \frac{a}{\sqrt{i^2 + j^2}} \sqrt{\frac{\epsilon_d \epsilon_m}{\epsilon_d + \epsilon_m}} \quad (6 - 2)$$

where  $\lambda$  is the light wavelength in vacuum,  $a$  is the hole array period,  $i$  and  $j$  are lattice mode indices. The transmission of SP waves through the sub-wavelength plasmonic masks at the I-line wavelength has potential to pattern nanoscale features using conventional near UV light sources. In this paper, we demonstrate a novel UV nanolithography technique utilizing SPR transmitted through sub-wavelength 2D hole array masks.

The configuration of the SPR optical lithography is illustrated in Figure 6 – 1b. The surface charge displacements depicted in the inset of figure 6 – 1b shows the electric field lines hopping between the Ag nanoparticles. However, there are two SP modes and these are illustrated in figure 6 – 2.

The SP modes indicate that the electric field lines for mode 1 at the edges the electromagnetic fields are most concentrated, however, for mode 2 the centers of the both the ridges and the grooves the fields are at maximal. A stronger coupling between the front and back sides of the metal is expected for mode 2. The oscillating current is not dependent of the depth of the grooves, for mode 1 as it is longitudinal (with respect to the wave vector) by hopping over the grooves. It can be seen clearly for mode 2 it is not longitudinal, due to the charge displacement in and out of the grooves and the coupling to the incident light is diminished, when the depth of the grooves is increased, no charge will flow into them.



*Figure 6 – 2: Model of a metal surface when excited by SPR.*

The transmission of SP waves through the sub-wavelength plasmonic masks at the I - line wavelength has a potential to pattern nanoscale features using conventional near UV light sources. In this chapter, we demonstrate a novel UV nanolithography by utilizing SPR transmitted through sub – wavelength 2D array masks. The configuration of the SPR optical lithography is illustrated in figure 1b. A plasmonic mask designed for the UV range is composed of self assembled silver 30nm diameter nanoparticle hexagonally close packed (hcp) 2D array.

## **6.2 Experimental Details**

### **6.2.1 Fabrication of the Plasmonic Mask**

The plasmonic mask was prepared by fabricating a 30 nm diameter hexagonal close packed silver nanoparticle arrays with a period of 50 nm via a self assembly technique. This will be extensively described in section 5.3. However, a brief outline of the process will be described here. To achieve this goal of fabricating the hexagonal close packed 2D array, a hydrophobic surface chemistry was applied to the silver nanoparticles (Sigma Aldrich), in order to nucleate them to the surface of the water. Once this is achieved, the Langmuir – Schaefer (LS) method described in section 5.3 can be used. However a brief outline of LS method is described here. Silver was chosen because in order for the surface plasmon phenomena to occur, it is a pre requisite that a collection of free electrons oscillates at its surface. Hence, a highly conducting metal was chosen. Silver also has the appropriate optical properties at 365nm (I-line), which is the wavelength that is of most interest.

Converting the silver nanoparticles from a hydrophilic surface state to a hydrophobic surface state using an alkanethiol coating chemistry as described in section 5.3. Take 0.1ml of the hydrophobic suspension of silver nanoparticles and place them inside a PTFE cylinder using a pipette, fill the PTFE cylinder with deionised water to top. Top up the PTFE cylinder with more deionised water so that the surface of the water is convex. This will bring the silver nanoparticles to the surface, due to the nature of the



hydrophilic/hydrophobic interface. Place a Foamvar coated transmission electron microscope (TEM) grid on to the surface of a 2.4cm x 2.4cm borosilicate glass cover slip and cover the whole cover slip (including the TEM grid) with Poly(N-isopropylacrylamide) PNIPAM polymer (see section 5.3 for details) using a pipette. The verification of the formation of the plasmonic mask will be preformed using a TEM. However, in order for the electron beam to penetrate the sample; the sample thickness must be of the order of tens of nanometers, (here approximately 70nm). This is only a guide because the accelerating voltage can be increased to compensate for the increased sample thickness. The PNIPAM polymer thickness was approximately a 100 $\mu$ m, therefore, the PNIPAM polymer was etched to a thickness of approximately 40nm (hence, the silver nanoparticle diameter is 30nm) using an oxygen plasma. The pressure on the vacuum was  $1.6 \times 10^{-1}$  mbar, as this was adjusted by flowing Oxygen gas into the vacuum chamber. A current of 80mA was induced to cascade the plasma, the film was etched for a duration of 12min 10 seconds to achieve an approximately 40nm film, this was measured with the TECNAI TEM.

Using the Langumir-Schaefer technique the silver nanoparticles were extracted on to the surface of the PNIPAM polymer via a hydrogen bonding mechanism. The silver nanoparticles / PNIPAM sample was placed in an oven at 56°C for 24 hours in order to bring the nanoparticles closer together. The TEM grid was cut away (with the silver nanoparticles / PNIPAM on its surface) from the borosilicate glass cover slip using a scalpel and the topography of the plasmonic mask was characterized by using the TEM, operating at 60 KeV.

### **6.2.2 Detection of SPR**

In order to detect the plasmons, the following set up was used. A Silver (Ag) thin film was deposited on the surface of 2.4cm x 2.4cm borosilicate glass by the sputter coating process. The pressure in the chamber was adjusted by flowing Argon gas into the vacuum chamber, this was  $1.6 \times 10^{-1}$  mbar and the induced current was 30mA, the film was sputtered coated for a duration of 120 seconds to achieve a 30nm film, whereas by increasing the time the Ag thin film thickness was also increased. Sputtering times of

160s, 200 s and 240s gave Ag thin films thickness of 40nm, 50nm and 60nm respectively. A prism was put in contact with the Borosilicate glass surface via index matching fluid (Edmund Optics). A Helium Neon (HeNe) laser ( $\lambda=635\text{nm}$ ) was used as a light source. This was pointed at the Ag thin film through the prism / Borosilicate glass. A Silicon photodiode detector was used to detect the reflection that is directed back through the prism at a particular angle as shown in figure 6 – 3.

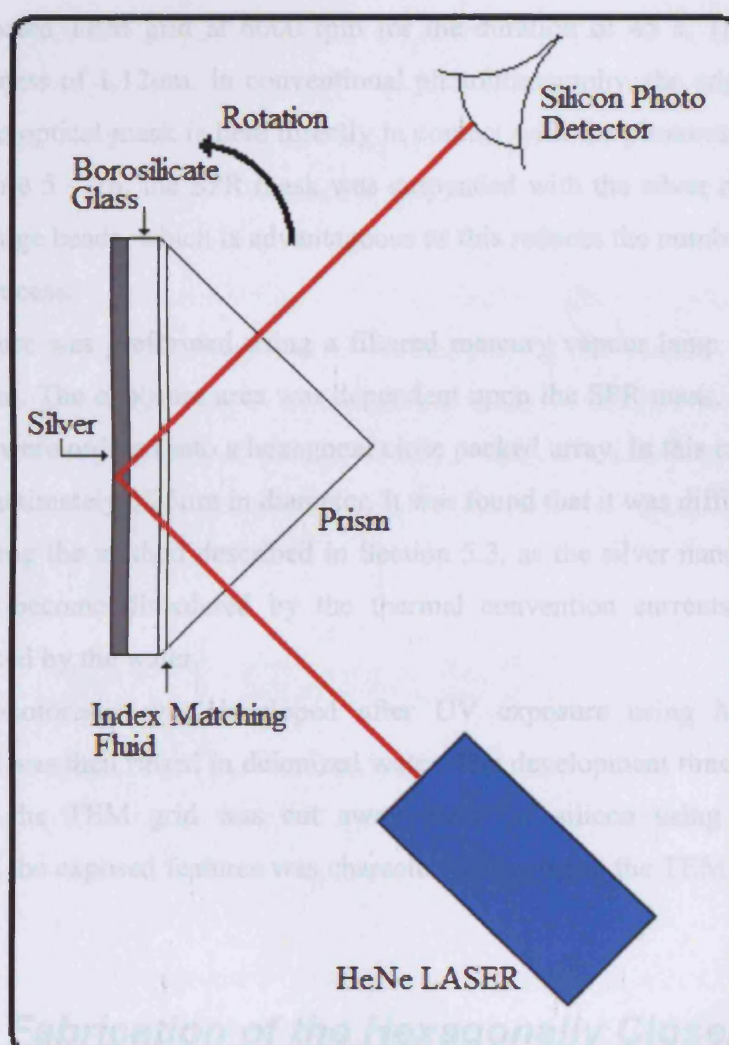


Figure 6 – 3: Experimental configuration for the detection of the SPR propagating on a metal thin film.

The sample (Ag thin film & the prism) was rotated from an angle of  $0^\circ$  to  $180^\circ$ . The reflectivity was measured by rotating the detector along with the sample, when the

detected radiation intensity decreased the surface plasmon resonance was detected. This was achieved in a dark room.

### **6.2.3 SPR Nanolithography Technique**

In the Photo–Nanolithography process, Shipley S1813 photoresist was spun directly on to a Foamvar coated TEM grid at 6000 rpm for the duration of 45 s. This resulted in a uniform thickness of 1.12 $\mu$ m. In conventional photolithography, the edge beads are not required as the optical mask is held directly in contact with the photoresist. However, as shown in Figure 5 – 1b, the SPR mask was suspended with the silver nanoparticle side down on the edge beads, which is advantageous as this reduces the number of steps in the lithography process.

An 8 s exposure was preformed using a filtered mercury vapour lamp with a radiation peak at 365 nm. The exposure area was dependent upon the SPR mask, where the silver nanoparticles were ordered into a hexagonal close packed array. In this case the exposure area was approximately 3.25 $\mu$ m in diameter. It was found that it was difficult to achieve a larger area using the method described in Section 5.3, as the silver nanoparticles would dislocate and become disordered by the thermal convection currents and Brownian motion produced by the water.

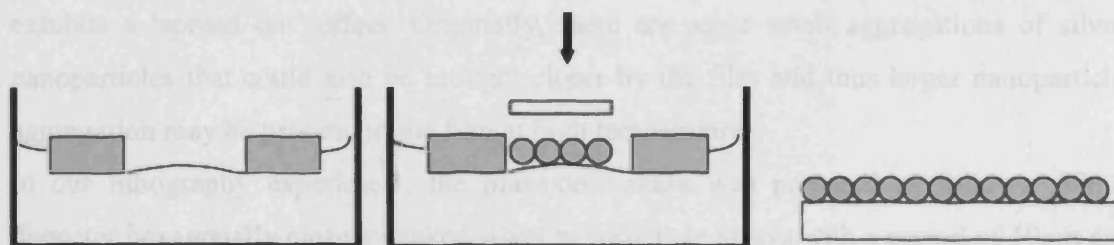
The S1813 photoresist was developed after UV exposure using Microposit 2401 developer and was then rinsed in deionized water. The development time was 15 s. After development, the TEM grid was cut away from the silicon using a scalpel. The topography of the exposed features was characterized by using the TEM, operating at 60 kV.

### **6.3 Nano Fabrication of the Hexagonally Closely Packed Ag Nanoparticle Array**

To assemble a large-scale monolayer of hydrophobic silver nanoparticles on a water surface [10] is a Langmuir– Schaefer (LS) technique [11]. This technique consists of using a colloidal dispersion of silver nanoparticles in an organic liquid, which has a

controlled convex curvature on a water surface. A monolayer of silver nanoparticles nucleates at the raised center of the water surface and grows smoothly outward, as the liquid evaporates. By bringing a smooth substrate down (from above) to the nanoparticle film, the monolayer can be transferred to it. By repeating this process, multiple layers of silver nanoparticles can be achieved. In a typical LS process, the formation of a close packed particle film is achieved, when the film is laterally pressurized. The particle array period is determined by the particle diameter and the length of the surfactant molecules. To produce an organized, high density nanoparticle film where the formation of microscopic holes (at low pressure) and multilayer aggregations (at high pressure) must be avoided. To achieve this, the pressure applied to the monolayer should be precisely controlled.

However, when the film is transferred from the water surface to solid substrates, the perfect nanoparticle film could be broken, as this process is illustrated in figure 6 – 4. Therefore, to obtain a large area of closely-packed nanoparticle film on a solid substrate by directly transferring the LS film is not trivial. A thermal sensitive polymer layer was used as a shrinkable substrate in order to further compress the nanoparticle monolayer.



*Figure 6 – 4: schematic illustration of the three step process for transferring a nanoparticle monolayer from the water surface to a solid substrate.*

A low critical solution temperature (LCST) transition in the region of 30–40 °C is demonstrated by a polymer called poly(N-isopropylacrylamide) (PNIPAM) [12]. This response is based on the fact that the network polymer chains are fully solvated and the polymer has good compatibility with the solvent. When the temperature increases further than the LCST, the polymer–solvent interaction is disrupted and the polymer–polymer interactions then dominate, resulting in the aggregation of polymer chains.

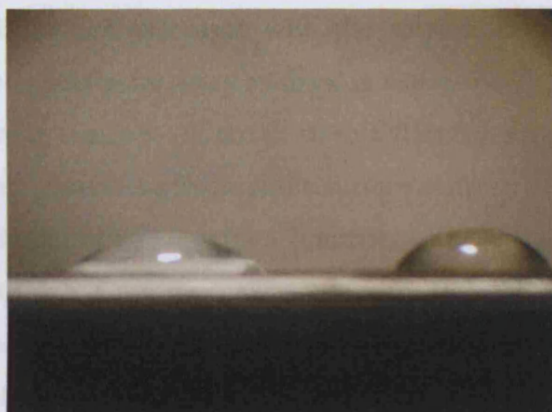
The PNIPAM thin film is prepared by photopolymerization of PNIPAM monomers, with a small amount of N,N-methylenebisacrylamide (bis-AMD) as crosslinker and 2,2'-diethoxyacetophenone (DEAP) as photoinitiator. A typical procedure consisted of 30  $\mu\text{mol}$  of (bis-AMD) and 1.6 mmol of N-isopropylacrylamide (NIPAM) being mixed with 2 ml of de-ionised water. Then 0.4  $\mu\text{mol}$  of the photoinitiator 'DEAP' is added into the solution. The resulting solution is dropped onto a borosilicate glass substrate with a pipette and is spread out over the whole surface. To prevent oxidation, it is covered with a thin glass slide. Using attenuated UV light, the samples were polymerized over a 30 min period at room temperature. When the polymer has cured, the top glass (cover slip) is removed and the polymer film can be used as the substrate to 'pick-up' the silver nanoparticle film. The PNIPAM film has a thickness of 100  $\mu\text{m}$ .

To control nanoparticle spacing this polymer film was an ideal substrate due to its ability to reorder the temperature. Most nanoparticles positioned far away from each other can be brought together as the polymer shrinks at temperatures higher than the transition temperature. The polymer film has about 10% or more shrinkage. Therefore, the interparticle distance can be reduced. The interparticle distance becomes smaller and exhibits a 'spread out' effect. Originally, there are some small aggregations of silver nanoparticles that could also be brought closer by the film and thus larger nanoparticle aggregation may be present on the film at high temperature.

In our lithography experiment, the plasmonic mask was prepared as follows: 30nm diameter hexagonally closely packed silver nanoparticle arrays with a period of 50nm are fabricated by a self assembly technique described above, in order to achieve this goal, hydrophobic surface chemistry must be applied to the silver nanoparticles, so they can nucleate on the surface of the water in order to use the LS technique.

To test the hydrophobic surface chemistry, a silver 30nm film was sputter coated on a borosilicate glass microscope slide using r.f plasma, half of the silver thin film was etched away using a diluted nitric acid solution. Figure 6 – 5 shows the results of the hydrophobic chemistry test, carried out by a water droplet to measure the contact angle. From the photograph, the water droplet on the surface of the silver thin film has a contact angle of approximately 60° whereas the contact angle of the borosilicate surface is approximately 40°. Thus, the silver film has a hydrophilic surface state.





*Figure 6 – 5: contact angle of the untreated silver.*

Figure 6 – 6 shows the contact angle of silver thin film and the borosilicate glass was  $107^\circ$  and  $11.5^\circ$  respectively. The surface of the borosilicate glass was prepared to be hydrophilic first, this was prepared by using  $\text{NH}_4\text{OH}:\text{H}_2\text{O}_2:\text{H}_2\text{O}$  solution in a ratio of 1:1:5. The hydrophilic solution was then brought to the boiling point condition for 15mins. This produced a hydrophilic surface state to the borosilicate glass. Again, a silver 30nm film was sputter coated on a borosilicate glass microscope slide using r.f plasma, half of the silver thin film was etched away using a diluted nitric acid solution.



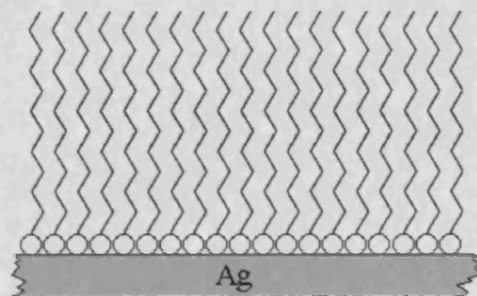
*Figure 6 – 6: Contact angle of the hydrophobic silver and hydrophilic borosilicate glass*

Firstly a hydrophobic alkanethiol coating was added to the silver thin film. This was possible by applying 2ml of an ethanol solution of 0.2ml of Octadecandiol in Hexane in a suspension, covering the entire silver surface. Allowing the ethanol solvent to evaporate,

leaving behind an alkanethiol monolayer with the sulphur atoms bound to the silver surface and hydrocarbon tails point away as show in figure 6 – 7.

From the results shown in figure 6 – 6, the silver thin film has a hydrophobic surface state, whereas the borosilicate glass has a hydrophilic surface state.

A 5cm in diameter cylinder of PTFE, with a 2cm circular hole machined in its center was used as a Langmuir trough. Care was taken to ensure that the PTFE cylinder is level. Deionized water is added to the hole in the PTFE cylinder. At this point, the water surface inside the hole assumes a convex meniscus. Control of the water level in the reservoir provides excellent control of the shape of the air–water interface within the hole. For experiments in this chapter, the water level in the reservoir was adjusted to produce a water surface with only slight convex upward curvature.



*Figure 6 – 7: An alkanethiol monolayer with sulphur atoms bound to the Silver surface, creating an hydrophobic Silver surface.*

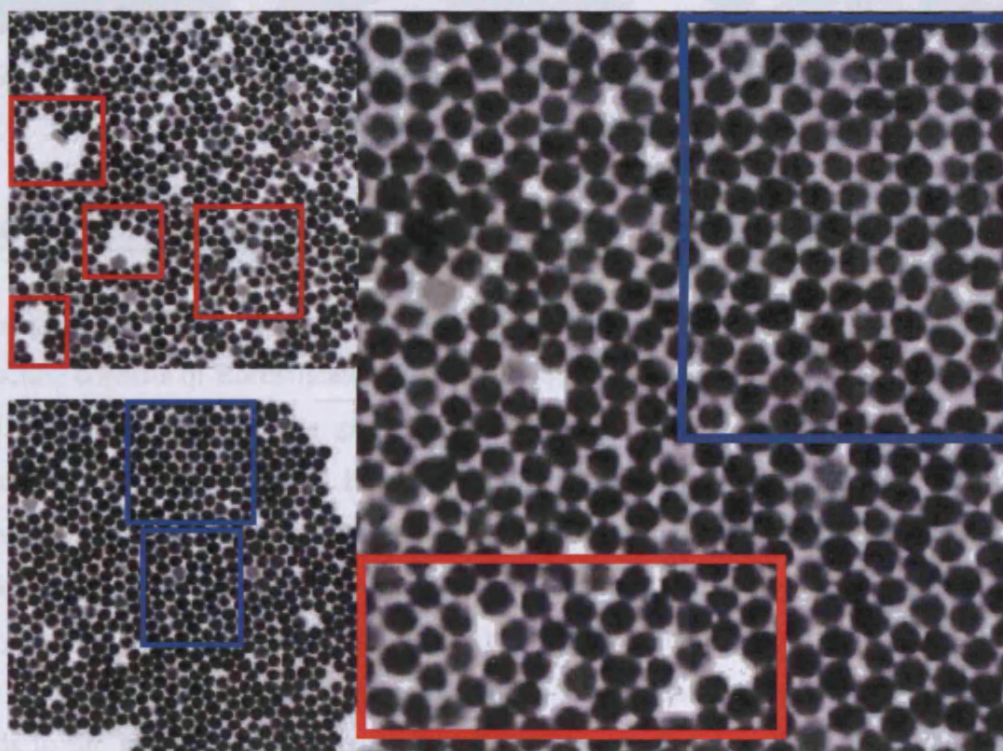
Control of the water level in the reservoir provides excellent control of the shape of the air – water interface within the hole. For experiments in this chapter, the water level in the reservoir was adjusted to produce a water surface with only slight convex upward curvature.

The nanoparticle array is formed by preparing the silver nanoparticles by creating a colloid suspension using 2ml of an ethanol solution of 0.2ml of Octadecandiol in Hexane, a 0.12ml of Oleic acid (as a surfactant) is then introduced in the solution. Dropping ~0.5ml of the colloid solution on the water surface and allowing the Ethanol solvent to evaporate (forming a monolayer of silver nanoparticles at the center) inside a fume cupboard. Care is taken to minimize air currents that might disturb the water surface.



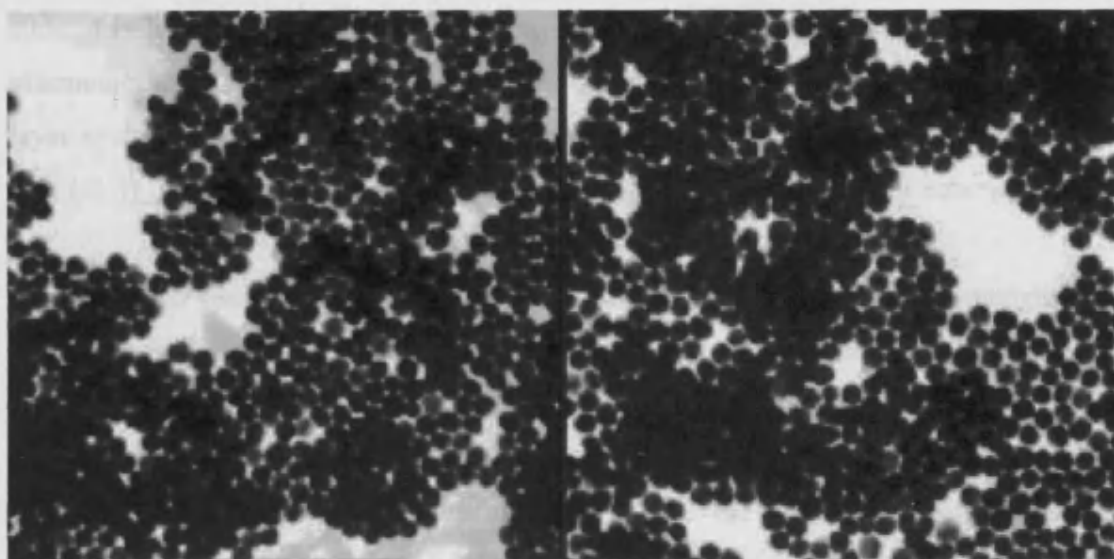
Figure 6 – 8 shows a typical example of a LS thin film consisting of a monolayer of 30nm spherical nanoparticles. It is evident that the nanoparticles are positioned in a hexagonal closely packed array, as pointed out by the blue boxes. However, defects are indicated by the red boxes the nanoparticles are not positioned correctly, these are called dislocations. When a dislocation occurs the remaining nanoparticles will never be positioned correctly, this can be caused by pressure, temperature or the amount of nanoparticles.

If the pressure of the nanoparticle film is not balanced then by the convection currents and Brownian motion in the de – ionized water causes the nanoparticles to drift apart from each other.



*Figure 6 – 8: TEM image showing the defects of the Langmuir film.*

If the temperature is not right then the PNIPAM polymer will not respond correctly as the nanoparticles will not self assemble correctly. If there are too many nanoparticles then multiple layers can build up as shown in figure 6 – 9.



*Figure 6 – 9: TEM image showing the aggregation of multiple nanoparticles forming a Langmuir film.*

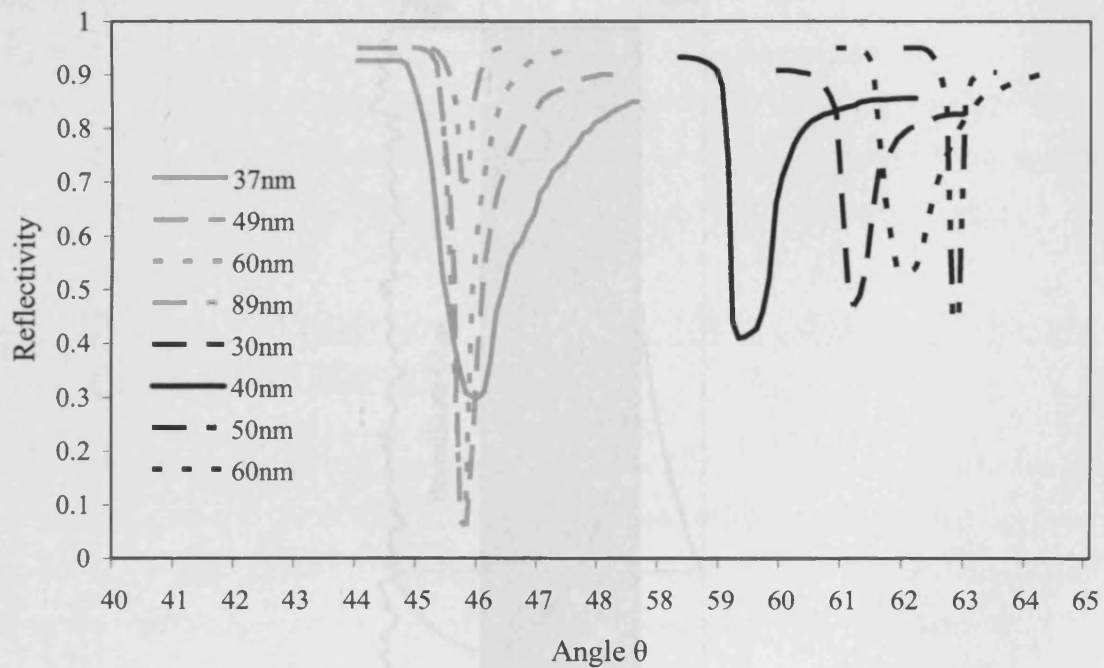
#### **6.4 Detection of Surface Plasmons on Ag thin Film**

This plasmonic mask behaves as a perfect asymmetric lens due to the fact that its structure consists of Borosilicate glass, PNIPAM polymer and Ag (which is interfaced to air). The condition of the perfect lens operates, when the permittivity and the permeability are negative [13]. However, at optical frequencies, it is clear that to fabricate a material with both negative  $\epsilon$  and  $\mu$  at the same frequency is quite difficult, due to the lack of magnetic materials. However, it is not necessary to satisfy the condition of  $-\mu$ , as only  $-\epsilon$  of the conditions may be negative because this component of the electromagnetic wave enables the amplification of evanescent waves at both interfaces of the Ag as this leads to the interaction of surface plasmons that is essential to the achievement of the sub-wavelength Photolithography.

The surface plasmon resonances are excited on each Ag interface, this forces the fields of the surface plasmon to interact destructively, therefore this cancels out the incident fields. Hence, zero reflectivity. It is this relation that governs the surface plasmons that is responsible for the perfect lens action. Therefore it is necessary to detect SPR phenomena. To detect the SPR phenomena in the silver nanoparticles hcp 2D array, Silver thin films of various thickness, were sputter coated on the surface on borosilicate glass microscope

slide, details are given in section 6.2.2, to simulate the role of surface plasmons in the plasmonic mask. Figure 6 – 3 illustrates the set up of this experiment by having a three layer system; Borosilicate glass ( $\epsilon_0$ ) which is the dielectric medium (1.536), the silver film (-2.3) [9] ( $\epsilon_1$ ) of thickness  $d$ ; and a second dielectric, which in our case was air (1) ( $\epsilon_2$ ).

Figure 6 – 10 shows the effect of variation of thickness at a constant wavelength ( $\lambda = 635\text{nm}$ ) on the position of the attenuated total reflection (ATR) minimum. The radiation wave is partially reflected at the borosilicate glass / silver film interface, having passed the prism ( $\epsilon_0$ ). It passes through the silver film of thickness  $d$  as an exponentially decaying wave as depicted in figure 6 – 11 [13]. At the Silver film / air interface it induces excitations which radiate light back into the silver film.



*Figure 6 – 10: Reflection of Silver films of different thickness. Detection of Surface Plasmon modes, the data represented in black were performed at the 635nm wavelengths in comparison with the data of [13] at 546nm shown in grey.*



If the thickness  $d$  increases, the backscattered field disappears due to the decreasing transmission. Therefore the reflectivity interaction becomes more dominant.

However, for a decreasing thickness  $d$  the back scattered field increases, where the optical transmission increases and the reflectivity has a minimal interaction. The incoming wave is in antiphase with the back scattered field, therefore, the reflection is reduced as the two interfere destructively. The antiphase radiation field, captured in the Ag film, is converted into heat.

For the surface plasmon resonance case, the decrease in radiation reflected, amounts to absorption, when there are no reflections. This is due to the radiation emitted from the SP's at the silver film / air interface back into the borosilicate glass in the direction of the reflected beam.

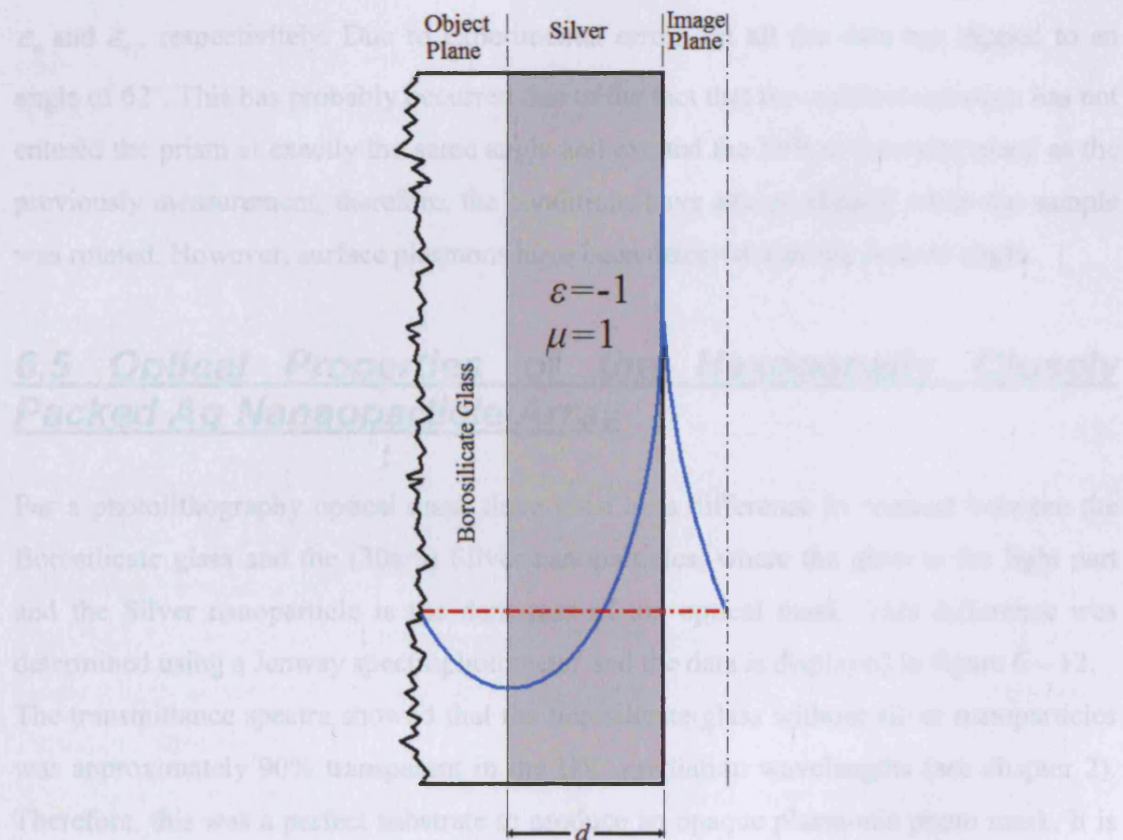


Figure 6 – 11: The perfect asymmetric lens system consisting of a thin film of silver.

If the silver film thickness  $d$  is decreased further this leads to increasing optical transmission and this has a direct effect on the reflectivity, where it's increasing role become more dominant.

A quantitative explanation of the minimum of the reflected intensity was proved by Raether [13]. It was calculated from the surface plasmon dispersion equation (see figure 6 – 1a) that the reflections would come to a minimum at an angle of 62°. The surface plasmon dispersion equation can be expressed as [9]

$$k_{sp} = \frac{2\pi}{\lambda} \sqrt{\frac{\epsilon_m \epsilon_d}{\epsilon_m + \epsilon_d}} \quad (6 - 3)$$

where  $\lambda$  is the wavelength of the incident radiation, which in this case was 635nm. The dielectric constant of a metal and a surrounding dielectric material are represented by  $\epsilon_m$  and  $\epsilon_d$ , respectively. Due to experimental error, not all the data has dipped to an angle of 62°. This has probably occurred due to the fact that the incident radiation has not entered the prism at exactly the same angle and excited the SPR at the same place as the previously measurement, therefore, the conditions have altered slightly when the sample was rotated. However, surface plasmons have been detected near the desired angle.

## **6.5 Optical Properties of the Hexagonally Closely Packed Ag Nanoparticle Array**

For a photolithography optical mask there must be a difference in contrast between the Borosilicate glass and the (30nm) Silver nanoparticles, where the glass is the light part and the Silver nanoparticle is the dark part of the optical mask. This difference was determined using a Jenway spectrophotometer and the data is displayed in figure 6 – 12.

The transmittance spectra showed that the borosilicate glass without silver nanoparticles was approximately 90% transparent in the UV – radiation wavelengths (see chapter 2). Therefore, this was a perfect substrate to produce an opaque plasmonic photo mask. It is observed that the PNIPAM polymer attenuated approximately 75% of the UV radiation at the I-line wavelength this is due to the DEAP photoinitiator. The DEAP cures at lower wavelengths but is still effective at the I-line wavelength.

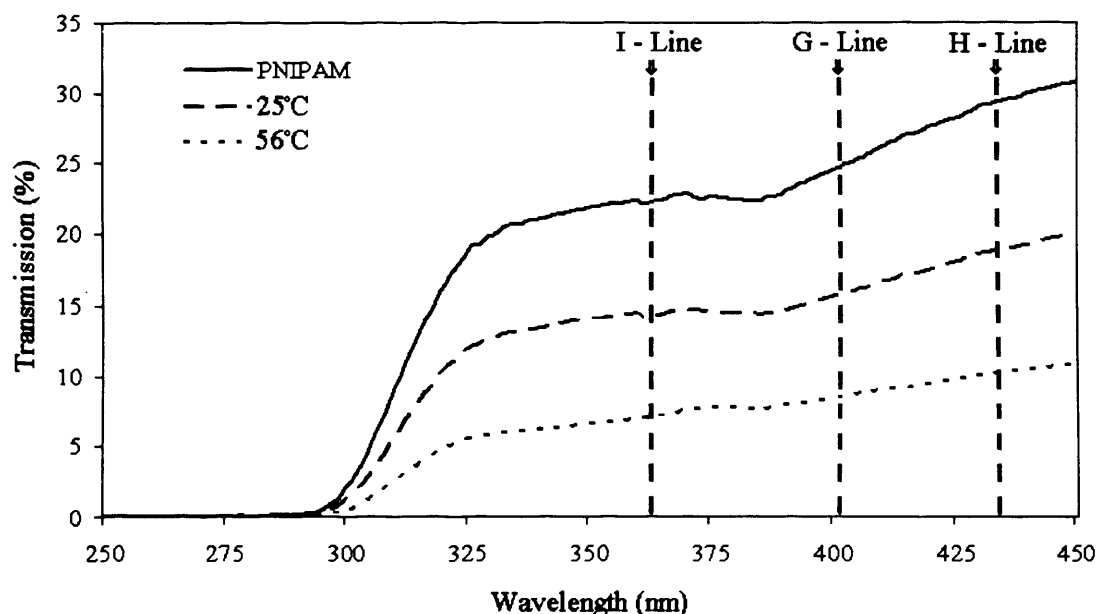


Figure 6 – 12: Transmission spectrum of the 30nm spherical Silver nanoparticle with a spacing period of 20nm forming a hcp 2D array.

As the distance between the silver nanoparticles decreases the optical transmission decreased, this is due to the SPR which the optical properties of silver nanoparticles are determined by a collective oscillation of free electrons in the nanoparticles which is mostly described by the term plasma – resonance absorption. The plasma – resonance absorption depends on the nanoparticle material and on nanoparticle structure, size and shape, in this case the Ag nanoparticles were 30nm diameter and spherical. The observed transmission, spectra strongly depends on the wavelength and the period of the hcp 2D array, which confirms the role of SPs.

The PNIPAM was heated at a temperature of 56°C for 24 hours the PNIPAM shrank in all directions as the Silver nanoparticles on the surface were brought closer together as shown in figure 6 – 13a.

From the data shown, it is evident that the silver mask is more opaque as a function of temperature. It is clear that the silver nanoparticle hcp 2D array does not absorb all of the UV radiation, 7.13% at the I – line wavelength, 8.78% at the G – line wavelength and 10.32% at the H – line wavelength. However, it is evident that from figure 6 – 13b, the absorption mechanism (SPR at the surface of each silver nanoparticle) is present as the

features remain. This will affect the resultant thickness of the exposed photoresist, as the transmission of the UV radiation increases then the resultant photoresist thickness will decrease. Therefore, G and H – line wavelengths will result with a thinner photoresist thickness.

## **6.6 Direct Nano Patterning a Two dimensional Structure**

In order for the Plasmonic mask to function as an asymmetric perfect lens to achieve sub – wavelength photolithography, the surface of the thin film must be manipulated to obtain a periodic structure so that a collection of free charge oscillations can be excited at the surface, enhancing the SPR. Figure 6 – 13a shows a highly ordered high density silver nanoparticle hexagonally closely packed 2D grating that was fabricated in section 6.3. This shows suitable periodic structure that can support the phenomena of SPR.

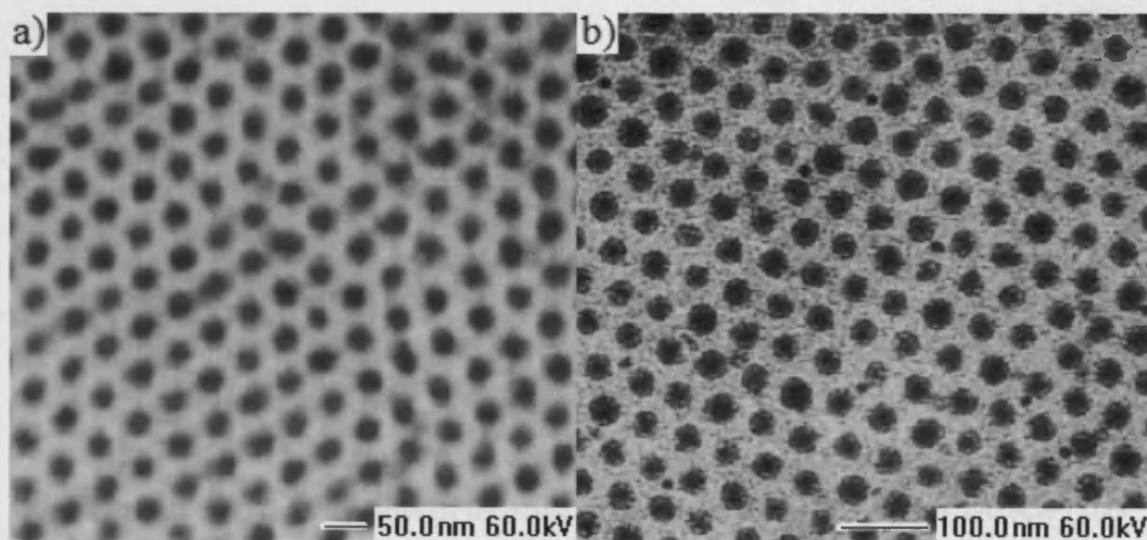


Figure 6 – 13: a) Silver nanoparticle hcp 2D array positioned by self assembly, b) developed S1813 photoresist exposed at 1 – line wavelength produced by surface plasmons.

The TEM image shows feature sizes of 30 nm with a period of 50 nm is uniform. The TEM image shown here does not look crisp as this is down to experimental error as the TEM was not focused correctly. However, it can be seen clearly that the resolution of

silver nanoparticle SPR mask is approximately 12 times smaller than the I-line wavelength ( $\lambda/12$ ).

The results shown in the TEM micrograph of figure 6 – 13b, the developed photoresist features are on average 34 nm in diameter with a smaller period of 46 nm than the features produced by the plasmonic mask, therefore, the S1813 photoresist features are 11 times smaller than the wavelength of the I-line photons ( $\lambda/11$ ). This pattern period is far beyond the diffraction limit of far-field lithography [14, 15].

From this it is evident that the evanescent electromagnetic field of the surface plasmon at the silver nanoparticle / borosilicate glass interface propagates across the silver nanoparticle and is superimposed on the field of the surface plasmon oscillating at the same frequency at the silver nanoparticle / air interface. The field is leaked into the air gap as depicted in the inset of figure 6 – 1b [15, 16]. The transmitted leaked field (in this case the radiation  $\lambda = 365\text{nm}$ ) interacts with the S1813 photoresist and produces the features shown in figure 6 – 13b.

Due to the quantity of leaked UV radiation the developed S1813 photoresist thickness was approximately 33 nm (G and H-Line would result in thinner photoresist, as the difference between light and dark areas (Ag nanoparticles) has become less, see Figure 6 – 12).

The optimal exposure time is only 8 s, this is comparable to a typical exposure dose used in conventional lithography with larger features, which implies a strong near-field transmission enhancement due to SPs.

The S1813 photoresist features are 34nm and not 30nm because the plasmonic mask lens was out of focus as the thickness of the edge beads, were either too high or too low. This can be rectified by the edge beads either being higher or lower either by spinning the photoresist at a faster / slower spin speed or by optimizing the timing of the UV exposure so that the S1813 photoresist has a resultant lip so that the plasmonic mask lens can sit directly upon on it as illustrated in figure 6 – 14.



## **6.7 Discussion**

Whilst the result of exposure and development of S1813 resist, as shown in figure 6 – 13 suggests that such nanoscale plasmonic photolithography is feasible, it's usefulness in a real, high throughput application is questionable. Self assembled arrays of nanoparticles are easily achieved; however, forming specific features is more difficult.

It was found that at the air / water interface, the Ag nanoparticles could be self assembled to form maze like structures, which consisted of continuous Ag nanowires of approximately tens of microns in length and widths of 70nm – 10 $\mu$ m. By adjusting the parameters that govern the self assembly process, the morphology of the nanostructures could be controlled.

The maze like structure was prepared by using a similar method adopted for the fabrication of the plasmonic mask shown in figure 6 – 15a. The hydrophobic Ag nanoparticle / ethanol solution was applied to the water surface inside the PTFE cylinder. By reducing the pressure applied to the Ag nanoparticle monolayer by the trough barriers, the nanowire structures were produced. A low surface pressure was applied to the compression of the Ag nanoparticle nanowire monolayer. The work of Chung et al [17] demonstrates a very good example of these nanowire like structures.

Due to the orientation of the trough barriers, the lines would align in one direction. The nanowires were aligned over the range of approximately 15 – 40 $\mu$ m, when the films were uncompressed. Observations showed that the alignment of the lines demonstrated that the separation between the inter-nanowires decreased, when the trough barriers were compressed, thus increasing the pressure.

However, as the lines were compressed further, they tend to bend, distort and the Ag nanoparticle nanowires broke up into smaller chains as they align. The average size of the line width ranged between approximately 70nm – 10 $\mu$ m. This is dependent on the pressure applied to the trough barriers. At a relatively low pressure the nanowires did not aggregate together.

The mechanism for the formation of these nanowires is not completely understood. However, when the pressure applied increases, the transition from the nanowire structure to a hexagonally closely packed nanoparticle 2D array can not be undone.

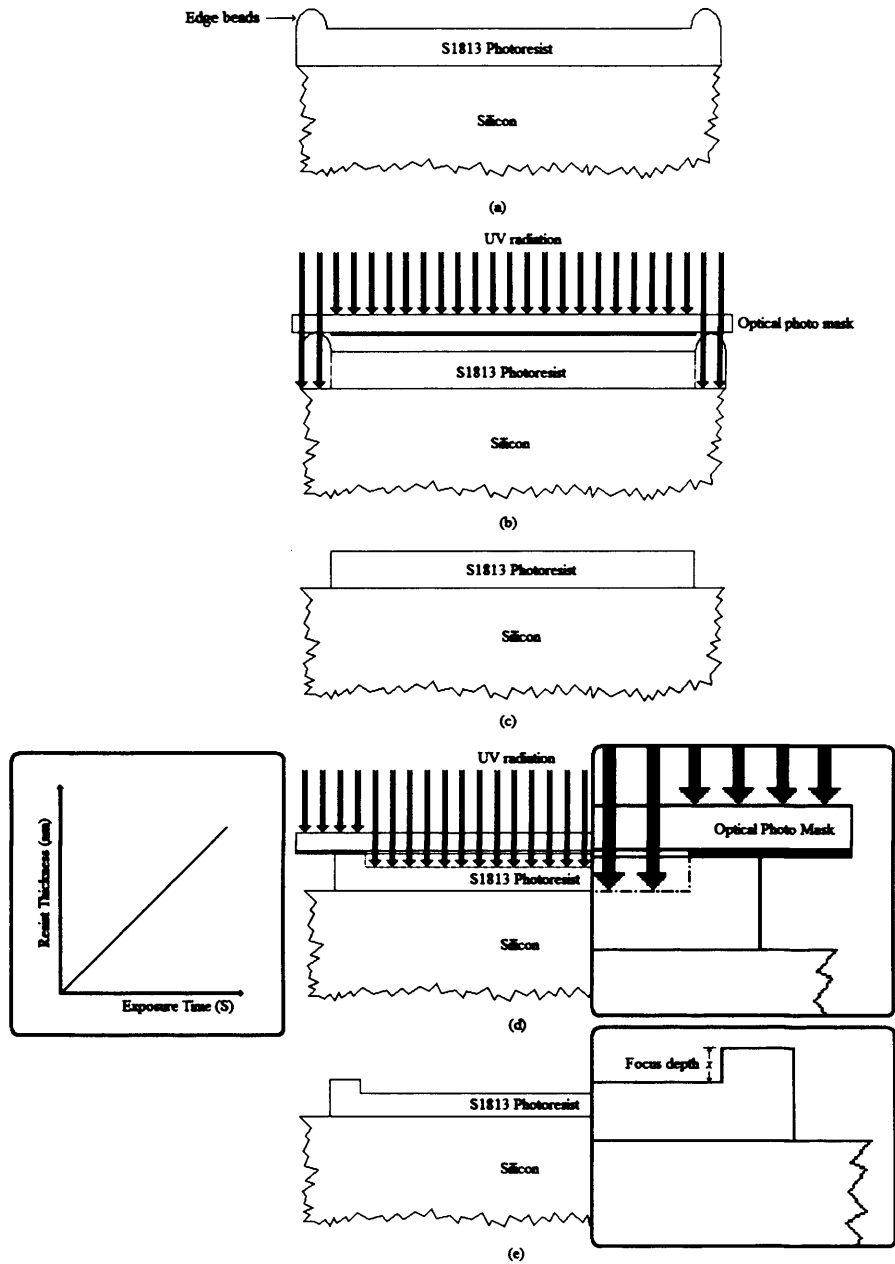
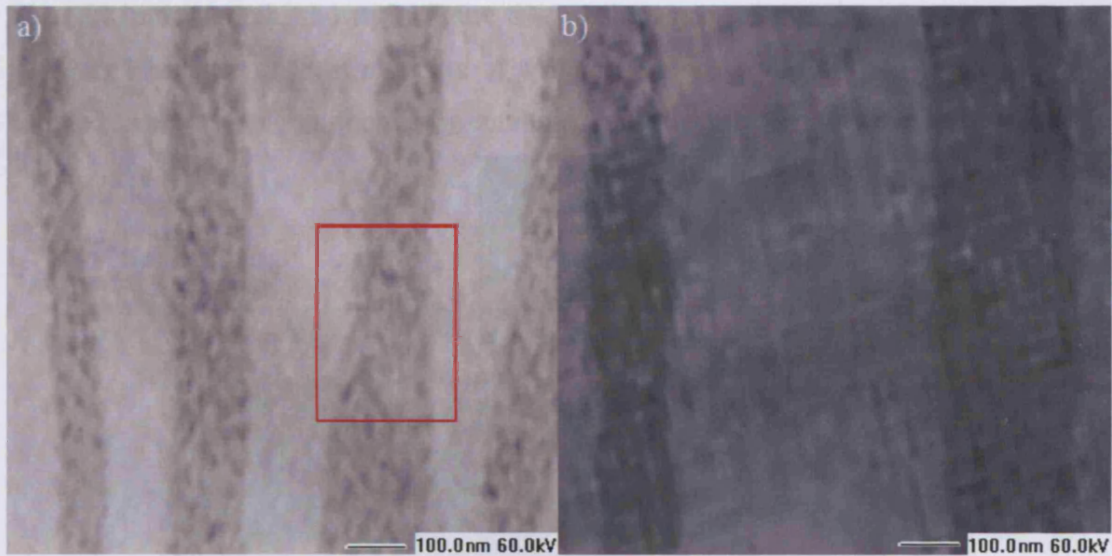


Figure 6 - 14: Schematic of lithographic process to obtain the correct edge bead thickness to focus the plasmonic mask. a) edge beads occurring when spun at a particular speed, b & c) UV exposure to get rid of the edge beads & develop, d) UV exposure as a function of time, inset, close up showing the distance of the UV exposure penetrating the photoresist as a function of time, e) developed photoresist, inset, resultant thickness to focus the plasmonic mask.

Due to the depletion zone that surrounds each nanoparticle, the inter-nanoparticle potential is rather large. Therefore, as each nanoparticle comes into contact with each other, the depletion zone that surrounds the nanoparticle intersects and there is an inter-nanoparticle attraction. However, to keep the hexagonally closely packed nanoparticle 2D array structure from aggregating the long range repulsive interactions (from the alkanethiol monolayer chain lengths are longer than the diameter of the depletion zone) compete with the short range attractions thus a dipole interaction is formed.

The TEM images shown in figure 6 – 15a demonstrate the assembly of the Ag nanoparticle nanowire structures transferred from the water surface inside the PTFE cylinder at a low surface pressure primarily shows a nanowire – like structure with a small space between the lines per sample, the lines are periodic.



*Figure 6 – 15: a) TEM micrograph of self assemblies of Ag nanowire to form a suitable plasmonic mask, b) Developed S1813 photoresist exposed at I-line wavelength produced by surface plasmon.*

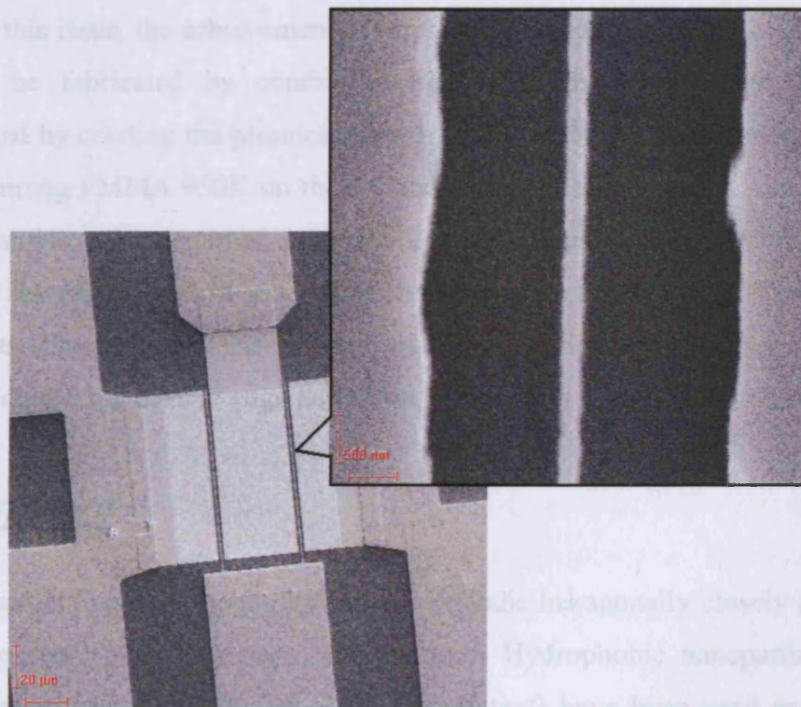
These images show a plasmonic mask for the purpose of fabricating a gate structure for a solid state transistor. The pattern quality of the Ag nanowires is poor, the plasmonic mask shows features of different nanowire widths and oriented at various angles.

It can be clearly seen that the length of the line has two nanowire widths, the transition from approximately 100nm to 180nm, as indicated by the red box.

Figure 6 – 15b shows the developed S1813 photoresist, this experiment was preformed as section 6.3 describes. Evidently the SPR phenomena still occurs because the nanoparticle still positioned in close proximity to each other due to the dipole formed between the repulsive and attraction interactions. Therefore, due to the scaling of the interspatial positioning of the nanoparticles (see insert of figure 6 – 15a) can operate as a 2D grating and the surface roughness still exists.

The TEM images depicted in figure 6 – 15 are not symmetric and the nanoparticles that make up the nanowires have different thicknesses, even though the average size was 30nm. Therefore, the electron beam optics have different foci for the electrons to propagate in two perpendicular planes, therefore, astigmatism was occurring and consequently lead to the aberration of the image.

The SEM micrograph, shown in figure 6 – 16 shows an InP PHEMT solid state device that was fabricated at the University of Manchester by A. Jones. The process that was adopted consists of photolithography combined with electron beam lithography.



*Figure 6 – 16: SEM image of an InP HEMT, Inset shows a 120nm gate structure fabricated using e-beam technology, images courtesy of A. Jones.*



The InP PHEMT has associated with it, large areas for the source and drain contacts, this was accomplished by conventional contact photolithography using the I-line technology. As the gate requires a fine structure, electron beam lithography was employed to complete the device. The e-beam lithography was achieved using PMMA 950K, which was spun at 6000rpm giving a resultant thickness of 300nm. The pattern was written using the Ephly Quantum software. It was found that twenty InP PHEMT devices could be completed in one day. Hence, very low throughput.

It can be seen from figure 6 – 16 that the edge definition in the patterned S1813 photoresist was relatively poor as compared with the gate structure. Here, the gate length was approximately 120nm and was 90 $\mu$ m in width, shown in the insert of figure 6 – 16. Evidently, the edge definition is vastly superior to that of the nano-photolithography technique as discussed above. But importantly, the feature sizes of the nano-photolithography technique are comparable to that of the e-beam lithography, even though improvements in the edge definition are required.

To address this issue, the achievement of improving the edge definition of the plasmonic mask can be fabricated by combining EBL with this technology. This can be accomplished by creating the plasmonic mask via the technique described within section 6.3 and spinning PMMA 950K on the surface of the plasmonic mask. Once the e-beam resist is spun it can be patterned using the Ephly Quantum software. When a pattern is written and the resist is developed, dilute Nitric acid can be used to etch away the silver nanoparticles. Consequently, the e-beam resist can be stripped away. It is envisaged that this could achieve the desired edge definition, however, is beyond the scope of this work.

## **6.8 Summary**

A novel plasmonic photolithography using a periodic hexagonally closely packed silver nanoparticle array mask has been demonstrated. Hydrophobic nanoparticles – Silver nanoparticles capped with oleic acid (as a surfactant) have been used as the building components for LS technique. The silver nanoparticles on a water surface are transferred onto a thermo-responsive polymer surface via the LS technique.



As the temperature increases from 30 - 40°C, the polymer undergoes a phase transition and the polymer film shrinks in all directions. The Silver nanoparticles are pushed closer by the polymer film and the nanoparticle spacing can be tuned by adjusting temperature. Highly ordered high density nanoparticle film can be obtained by heating the film to temperature above the polymer's LCST.

To confirm the existence of surface plasmons propagating at the silver surface, it was found that the SPR was detected at an angle of 62° of the silver film with thicknesses ranging from 30 – 60nm.

Far – field transmission spectra of the hexagonal structures shows strongly enhanced transmission in the UV range, which opens the possibility of lithography using the apertures smaller than the exposing wavelengths. Like previous chapters it was found that the Borosilicate glass was an effective substrate to support the plasmonic mask as its optical transmission was approximately 90% transparent. This provided excellent contrast for the PNIPAM polymer and the silver nanoparticles. As the DEAP photoinitiator cures at lower wavelengths it was effective at the I-line wavelengths, consequently, this has a direct effect on the PNIPAM optical transmission which was approximately 75%. At temperatures of 25°C the optical transparency of the silver nanoparticles was 14% at I-line wavelengths, whereas when the temperature was elevated to 56°C the optical transparency was increased to 7.13%. This was due to the fact that as the temperature increases, the PNIPAM polymer shrinks bringing the silver nanoparticles on its surface closer together to form a periodic 2D grating, therefore, increasing the plasmonic mask opaqueness.

The nanolithography technique utilizes near UV radiation to excite surface plasmons on a metal grating in order to enhance the transmission through sub wavelength periodic apertures with effectively shorter wavelengths compared to the excitation light wavelength. The plasmonic mask consisted of the ordered silver nanoparticle hexagonal arrays with feature sizes of 30 nm with a period of 50 nm, where the resolution of silver nanoparticle plasmonic mask was approximately 12 times smaller than the I-line wavelength ( $\lambda/12$ ). Nanolithography was performed with an optimal I-line exposure time of 8 seconds.

The result of this exposure showed the transfer of the 2D hexagonal array pattern into the photoresist. Here the inter-particle pitch was 46nm and the features of the developed S1813 photoresist had a diameter of 34nm. This was found to be 11 times smaller than the wavelength ( $\lambda/11$ ).

As well as arrays, so called nanowires were experimented with. The nanowire widths varied between approximately 70nm – 10 $\mu$ m and the lengths were tens of microns. These nano structures could be controlled by decreasing the pressure applied to the Ag nanoparticles. When aligning the nanowires, they had a tendency to distort and bend as they were compressed together and even in some instances the nanowires fractured into small chains.

Whilst the suitability of this technique in isolation may not be compatible with high throughput lithography, combining it with e-beam lithography for very high resolution features shows some promise.

## **6.9 References**

- 1) H. Schmid, H. Biebuyck, B. Michel, O. J. F. Martin, 'Light-coupling masks for lenses, sub-wavelength optical lithography', Appl. Phys. Lett. 72, 2379 (1998).
- 2) J. G. Goodberlet, 'Patterning 100nm features using deep-ultraviolet contact photolithography', Appl. Phys. Lett. 76, 667 (2000).
- 3) J. G. Goodberlet, H. Kavak, 'Patterning sub-50nm features with near-field embedded-amplitude masks', Appl. Phys. Lett. 81, 1315 (2002).
- 4) O. J. Martin, N. B. Piller, H. Schmid, H. Biebuyck, B. Michel, 'Energy flow in light-coupling masks for lensless optical lithography', Opt. Express 3, 280 (1998).
- 5) M. M. Alkaisi, R. J. Blaikie, S. J. McNab, R. Cheng, D. R. S. Cumming, 'Sub-diffraction-limited patterning using evanescent near-field optical lithography', Appl. Phys. Lett. 75, 3560 (1999).
- 6) T. W. Ebbesen, H. J. Lezec, H. F. Ghaemi, T. Thio, P. A. Wolff, 'Extraordinary optical transmission through sub-wavelength hole arrays', nature (London) (1998), 391, 667 – 669.

- 7) T. Thio, H. F. Ghaemi, H. J. Lezec, P. A. Wolff, T. W. Ebbesen, 'Surface-plasmon-enhanced transmission through hole arrays in Cr films', *JOSA B* (1999), 16, 1743 – 1748.
- 8) L. Salomon, F. Grillot, A. V. Zayats, F. deFornel, 'Near-field distribution of optical transmission of periodic subwavelength holes in a metal film', *Phys. Rev. Lett.* (2001), 86, 1110 – 1113.
- 9) H. Raether. *Surface Plasmons on Smooth and Rough Surfaces and on Gratings*, Springer, Berlin, (1988), pp 25 – 30.
- 10) V. Santhanam, J. Liu, R. Agarwal, R. P. Andres, 'Self-assembly of uniform monolayer arrays of nanoparticles', *Langmuir* (2003), 19, 7881.
- 11) F. Sbrana, M. T. Parodi, D. Ricci, E. D. Zitti, 'Langmuir films of thiolated gold nanoparticles transferred onto functionalized substrate: 2-D local organization', *Mat. Sci. Eng C* 22 (2002) 187.
- 12) M. J. Serpe, C. D. Jones, L. A. Lyon, 'Layer-by-layer deposition of thermoresponsive microgel thin films', *Langmuir* (2003), 19, 8759.
- 13) J. B. Pendry, 'Negative refraction makes a perfect lens', *Phys. Rev. Lett.* 85 3966, (2000).
- 14) W. Srituravanich, S. Durant, H. Lee, C. Sun, X. Zhang, 'Deep subwavelength nanolithography using localized surface plasmon modes on planar silver mask', *J. Vac. Sci. Technol. B* 23 (6) (2005).
- 15) S. Lewis, R. Wheeler – Jones, V. Haynes, R. M. Perks, 'High density self assembled nanoparticle film with temperature-controllable interparticle spacing for deep sub-wavelength nanolithography using localized surface plasmon modes on planar silver nanoparticle tunable grating', *Micro. Eng.*, 85 (2) pp. 486 – 491 (2008).
- 16) J. Seidel, F. I. Baida, L. Bischoff, B. Guizal, S. Grafström, D. Van. Labeke, L. M. Eng, 'Coupling between surface plasmon modes on metal films', *Phys. Rev. B* 69, 121405 (2004).
- 17) S. W. Chung, G. Markovich, J. R. Heath, 'Fabrication and alignment of wires in two dimensions', *J. Phys. Chem. B* (1998), 102, 6685.

## CHAPTER

# 7

## Conclusion

### Contents

|                      |       |
|----------------------|-------|
| 7.1 Future Work..... | -151- |
| 7.2 References.....  | -153- |

The fabrication of photo masks using a nanocomposite resist and plasmonic nano photolithography have been demonstrated using the techniques described in chapters 2, 3, 4 and 6. Both these techniques adopted very different approaches to achieve essentially the same thing. To produce the photo masks, the nanocomposite resist photo mask used a “top – down” method of producing a pattern on a micron scale, whereas the latter method incorporated nano scale features fabricated from the “bottom – up”.

Producing the photo masks using the nanocomposite resist technology was advantageous for two reasons. The first was that it could be produced with ease and consequently minimized the time taken to fabricate it. Briefly, the nanocomposite resist spun on borosilicate glass and then the pattern had to be written with an electron beam and developed. The route to achieving this was well known. This should be compared with the fabrication of conventional Chrome photo masks, which at geometries of 100nm and below need to be dry etched.

As seen in chapters three and four, the  $\text{Al}_2\text{O}_3$  nanoparticles not only increased the opacity of the PMMA matrix, but impacted on the so called proximity effect. Furthermore, the mechanical stability was improved by the introduction of the  $\text{Al}_2\text{O}_3$  nanoparticles. This prevented the nano structures from toppling over or even collapsing, which was advantageous because the thicker the resist the more metal can be deposited for lift off applications.

In principle, the smallest feature size achievable is around 25nm, comparable with the particulate diameter. However, it was discovered that the  $\text{Al}_2\text{O}_3$  nanoparticles aggregated together as presented in chapters 2 and 3. Here the nanoparticles were shown to be protruding out of the structure side walls. It was found that the size of these aggregations were below 100nm. Therefore, had the potential to directly affect the resultant features following optical exposure.

However, if smaller nanoparticles (say 6nm) were embedded into the PMMA based nanocomposite resist, then the feature sizes could be reduced even further because the multiple scattering produced by the nanoparticles could be increased. Consequently, the overall resist thickness could be decreased.

In this study, the I – line wavelength was used as an example, however, shorter wavelengths like F2 ( $\lambda=157\text{nm}$ ) for example could be utilized to achieve even smaller features into the photoresist. Therefore, this nanocomposite resist was well on target for 2010 as predicted by M. MaCallum [1]. However, this will only be viable if there is a photoresist that has the appropriate acid generators at the F2 wavelengths required to produce a photo acid to expose the inhibitor molecules, so that during the development stage of the photoresist these polymer molecules become soluble.

From the results shown in figure 6 – 13a and b, nanolithography assisted by SPR has been demonstrated using the technique described in chapter 6. The feature sizes patterned in the S1813 photoresist were approximately 11 times smaller than the wavelength which in this case was 365nm and far beyond the diffraction limit. However, the pattern produced by the Langmuir film could be used to pattern a metal (Au for example) on the surface of an LED. This produces a highly directional far – field pattern with strong polarization dependence which alters the spectral shape of the light emission from the LED [2] by coupling a photon (SPR) to the grating structure.



It was found that it may be possible to pattern transmission lines or interconnects via this method in chapter 6 §5.3. Figure 6 – 15 showed a nanowire like structure assembled from the Ag nanoparticles, which were produced by convection currents in the PTFE trough, caused by the thermal entropic interaction in the ethanol solvent (controlling these parameters was very difficult).

The predication of M. MaCallum suggests that the minimum feature sizes would be 157nm in 2010 [1]. Using this technology to produce the next generation microprocessors and discrete transistor devices with ever shrinking gate lengths to meet the demand of progression as defined by Moore's Law is a real possibility as high throughput can be maintained. But this method does not have to restrict its self to computer architecture and discrete transistor technology; it may be applied to the opto-electronics industry by producing a metal contact for a stripe laser device for example.

To contrast both technologies in this study, the production of the nano structures using the nanocomposite resist photo mask was easier to fabricate than that of the plasmonic photo mask. The nanocomposite photo mask technology now brings an opportunity for the e-beam direct writer to be an industry standard piece of equipment instead of a research based equipment, because instead of writing multiple masks-only one mask needs to be written as a master. Therefore, the throughput increases. However, this equipment is very expensive where in 2008, an e-line system is worth more than one million pounds sterling.

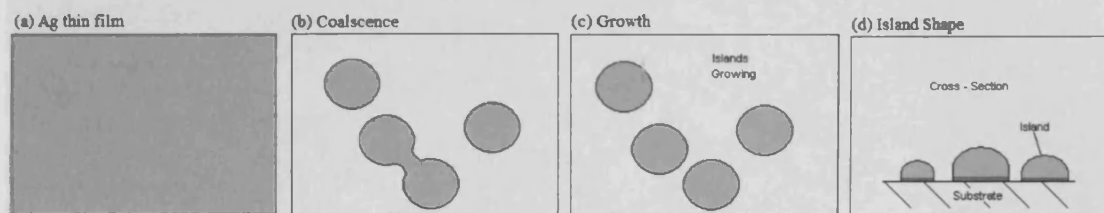
Whilst some interesting results were obtained, the complexity associated with the production of a plasmonic photo mask would suggest that it's application would be restricted to specific geometries and length scale combinations (e.g. large bond pad, small gate length type devices). To put this into context, self assembly was confined to a  $1\mu\text{m}^2$  area as compared with a  $100\times 100\mu\text{m}$  bond pad.

## 7.1 Future Work

Further development of the nanocomposite resist and plasmonic photo mask could be combined to achieve sub 30nm features over a large area. Due to the extremely high level of complexity of the plasmonic photo mask produced in chapter 6, other self assembly

methods of fabricating Ag nano structures such as in figures 6 – 13 and 6 – 15 must be explored.

The preparation of the novel plasmonic mask could be achieved by evaporating approximately 5 to 10nm of Carbon onto a borosilicate glass slide and then sputtering a Silver thin film with a thickness of approximately 80 to 100nm on to the surface of the Carbon. The thin films are then annealed rapidly at a temperature 640°C for 5 minutes. Figure 6 – 1 shows the process of producing the Ag nano structures.

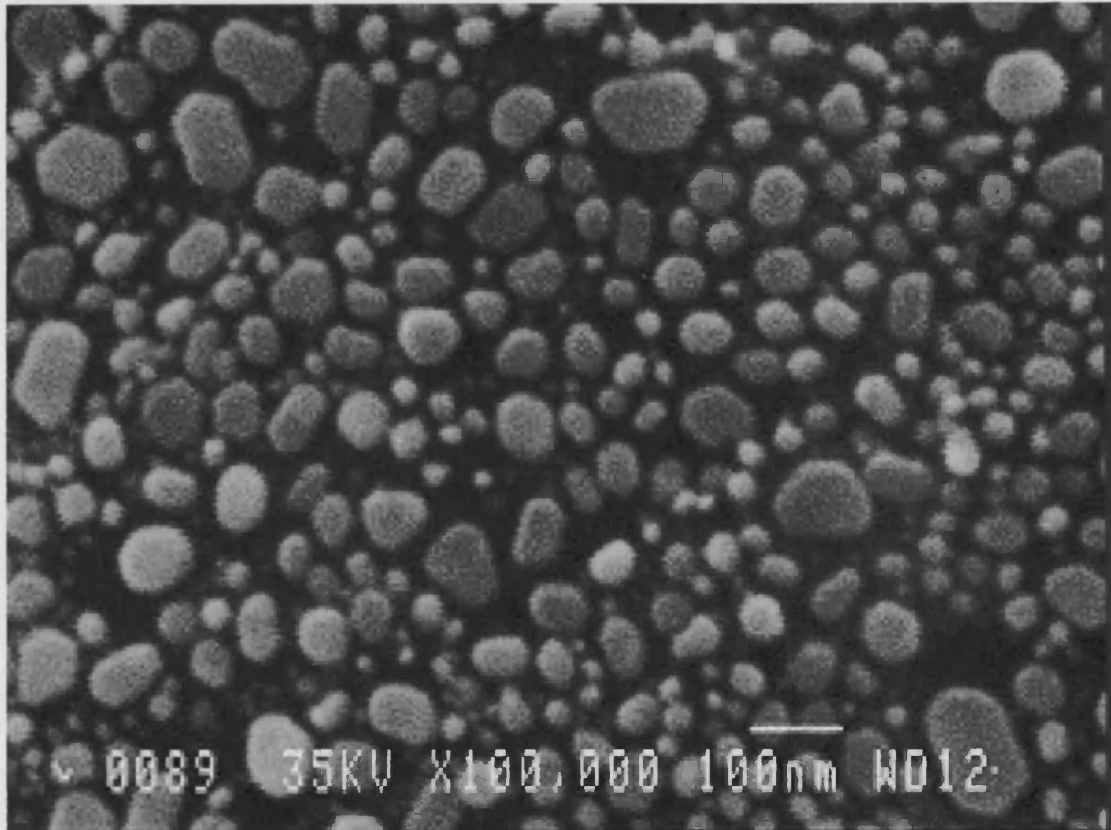


*Figure 7 – 1: The nano island formation process.*

The outcome of this process is shown in figure 6 – 2. Clearly it has some of the features of the 2D hexagonal Ag nanoparticle array, but obviously periodicity and particle diameter variations are an issue. This technique does however have the advantage of targeted application, i.e. via standard lithographic techniques; the Ag film can be deposited in a specific region of the device being fabricated.

Alternatively, once the Ag nano structures have been produced, the next step would be to define a pattern. This could be achieved by spinning the nanocomposite resist on to the surface of the Ag nano structures, filling in the nano gaps between each Ag nano structure. To achieve a pattern consisting of 30nm features, the nanocomposite resist thickness must be approximately 100nm. However, this will have a direct effect on the amount of nanoparticles that can be directly embedded into the PMMA polymer as this will be greatly reduced. Thus, the proximity effect will have an increasing affect and this trend was seen in chapters three and four. However, because the nanocomposite is effectively thinner, the pattern will inevitably be faster to write as the sensitivity will be increased as this was found in the exposure clearing dose trend seen in chapter three. When the pattern is produced in the nanocomposite resist, the Ag and the Carbon must be etched away using a dry etching process, using a gas mixture of  $\text{SF}_6$  and Ar in an

inductively coupled plasma environment. When this is achieved the nanocomposite resist must be removed using Acetone followed by O<sub>2</sub> plasma.



*Figure 7 – 2: A TEM micrograph of Silver on Carbon when the temperature was elevated to 640°C for 5 minutes.*

It was found in chapter 6 that the residual thickness of the features in the S1813 photoresist was 33nm. Clearly this cannot be used for the lift off technique and it would be difficult to obtain the appropriate selectivities necessary for dry etching technique. Therefore, the aspect ratio needs to be improved. As mentioned earlier, the thickness of the Ag nano structures was in the region of 100nm. This will have a direct effect on the optical properties of the plasmonic photo mask. It is expected that the light and dark contrast between the borosilicate glass substrate and the Carbon / Ag nano structures may be increased. Therefore, this may increase the thickness of the developed nano structures in the S1813 photoresist.

However, it was seen in chapter three that, due to the proximity effect, the nano structures fabricated with the unloaded PMMA either toppled over or completely collapsed. It is expected that this may happen to the nano structures produced in the S1813 photoresist. If this proves to be the case, then the method of utilizing the nanocomposite resist technology may be exploited by introducing  $\text{Al}_2\text{O}_3$  nanoparticles into the S1813 photoresist. This may increase the aspect ratio of the nano structures by of the S1813 photoresist as seen in chapter three.

## **7.2 References**

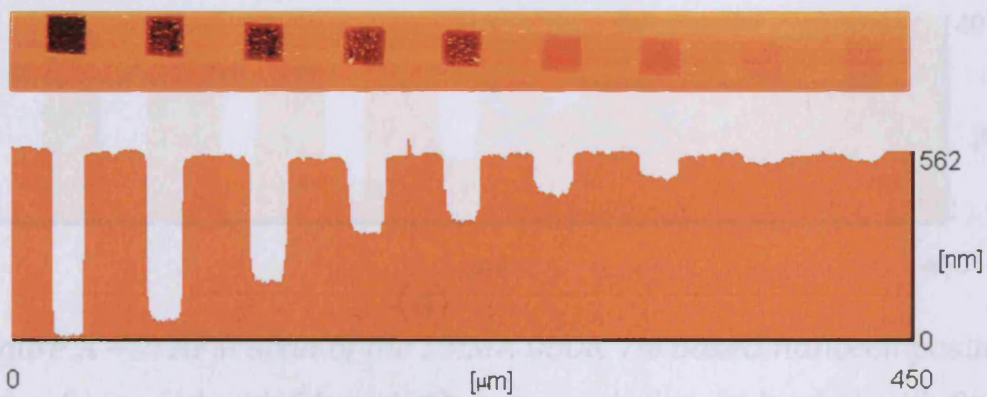
- 1) M. MaCallum, 'Lithography trends: A review and outlook', International SEMATECH, 2000.
- 2) M. D. Harries, H. D. Summers, 'Directional control of light – emitting – diode emission via a subwavelength – apertured metal surface', IEEE Photonics Technol. Lett. Vol 18, no 21, (2006).

## Appendix

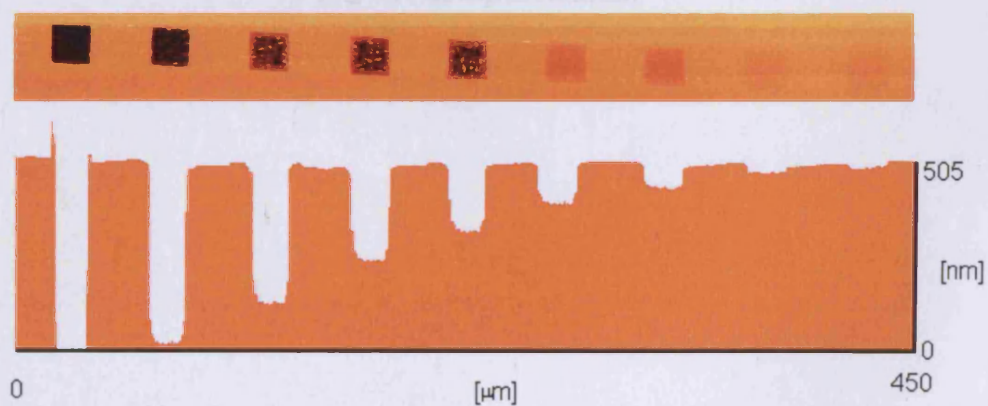
# A

### Clearing Dose of the PMMA 950K 7% based Nanocomposite Resist

Figures A – 1 and 2 depicts a cross section of the PMMA 950K 7% based nanocomposite resist, which was measured using an AFM.



(a)



(b)

Figure A – 1: AFM scan of the PMMA 950K 7% based nanocomposite resist, (a) loaded with 150mg  $\text{Al}_2\text{O}_3$  nanoparticales, (b) loaded with 100mg  $\text{Al}_2\text{O}_3$  nanoparticales.



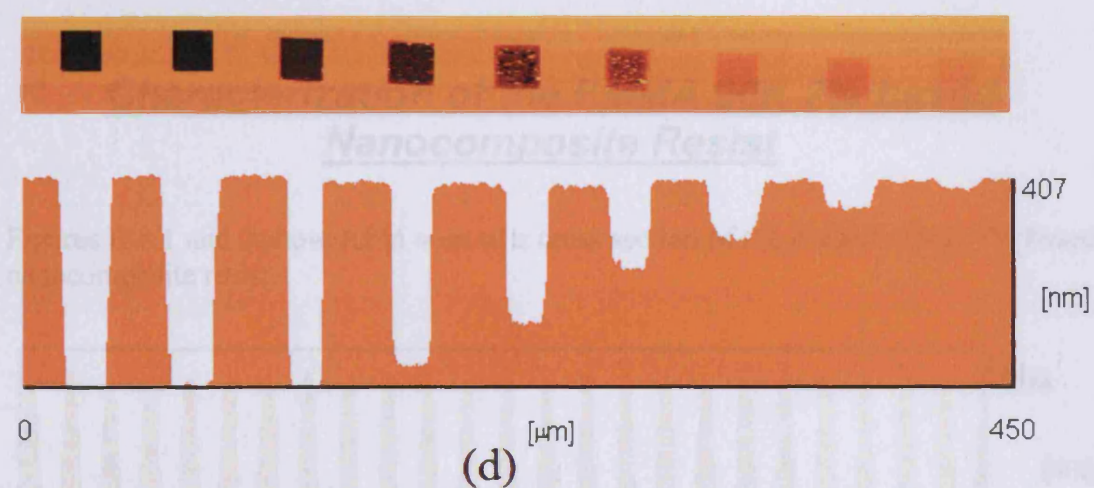
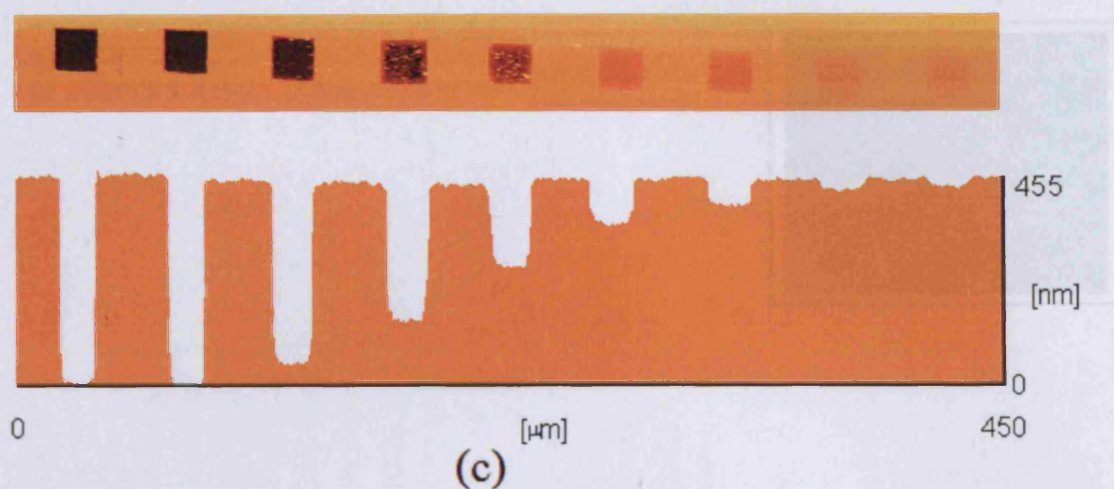


Figure A - 2: AFM scan of the PMMA 950K 7% based nanocomposite resist, (c) loaded with 50mg  $\text{Al}_2\text{O}_3$  nanoparticles, (c) loaded with 0mg  $\text{Al}_2\text{O}_3$  nanoparticles.

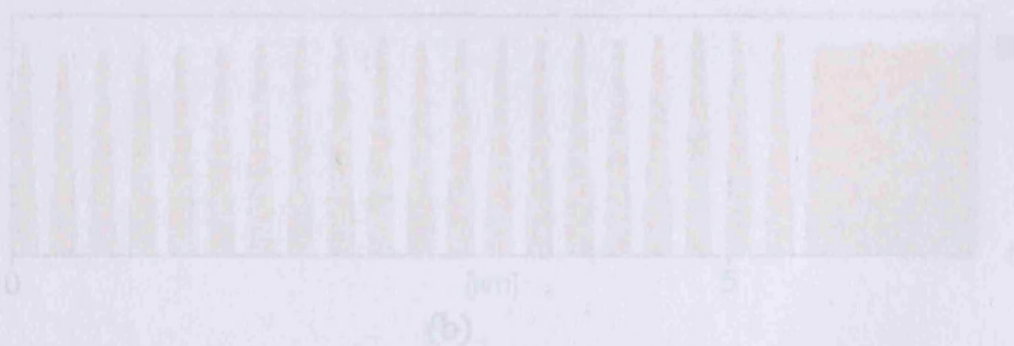


Figure B - 1: AFM scan of the PMMA 96K 7% based nanocomposite resist, (a) loaded with 150mg  $\text{Al}_2\text{O}_3$  nanoparticles, (b) loaded with 100mg  $\text{Al}_2\text{O}_3$  nanoparticles.

## Appendix

# B

### Characterization of the PMMA 96K 7% based Nanocomposite Resist

Figures B – 1 and 2 show AFM scan of a cross section of the PMMA 950K 7% based nanocomposite resist.

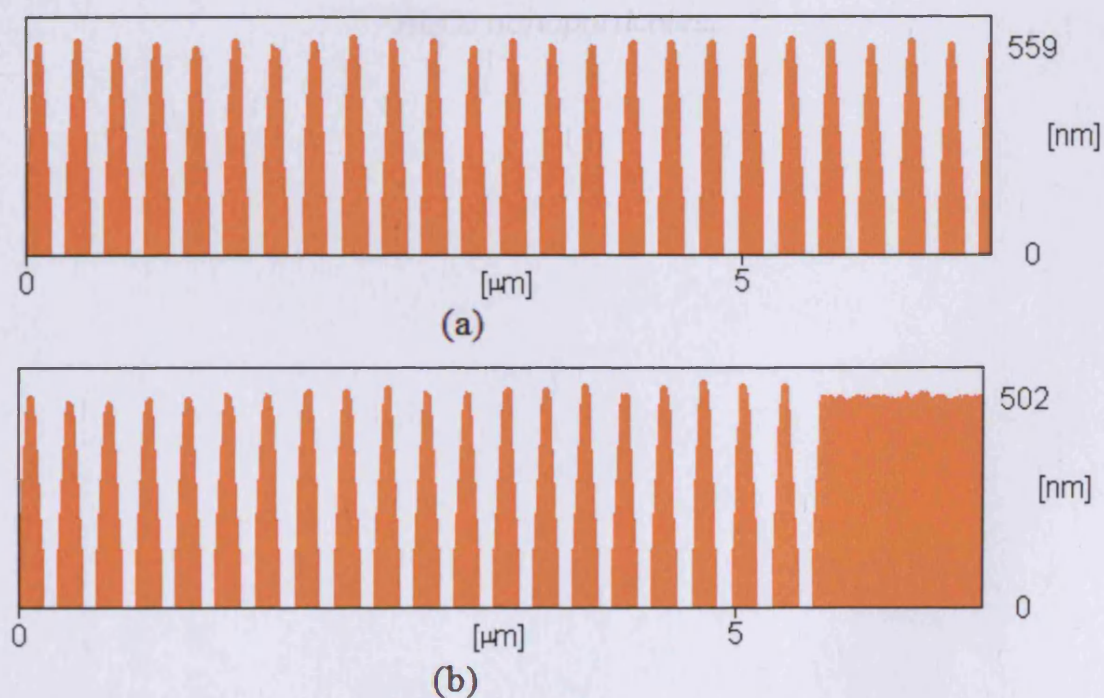
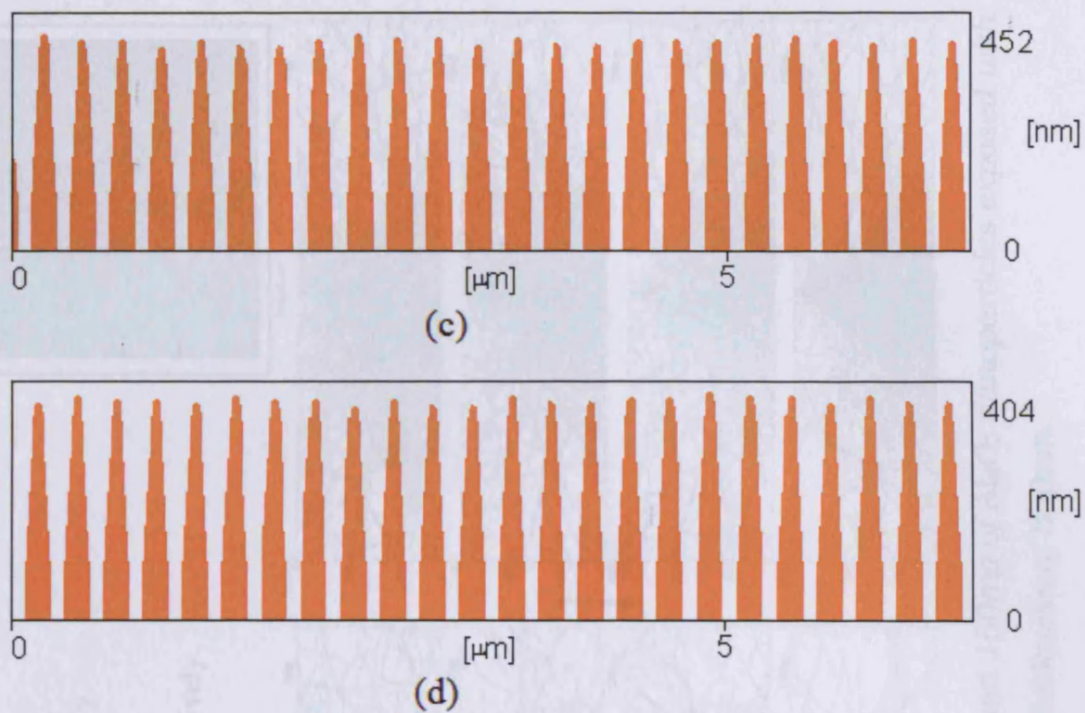


Figure B – 1: AFM scan of the PMMA 96K 7% based nanocomposite resist, (a) loaded with 150mg  $\text{Al}_2\text{O}_3$  nanoparticles, (b) loaded with 100mg  $\text{Al}_2\text{O}_3$  nanoparticles.





*Figure B – 2: AFM scan of the PMMA 96K 7% based nanocomposite resist, (c) loaded with 50mg  $\text{Al}_2\text{O}_3$  nanoparticles, (d) loaded with 0mg  $\text{Al}_2\text{O}_3$  nanoparticles.*

# Appendix

## C

Figures C – 1 and C – 2 shows the point distributions of the nanocomposite resist films with the thickness of 550nm. The accelerating voltages were 25 and 100KeV, respectively. Figures C – 3 to C – 6 shows the point distributions of the nanocomposite resist using accelerating voltages of 50 and 75KeV upon film thicknesses of 400 and 550nm, respectively.

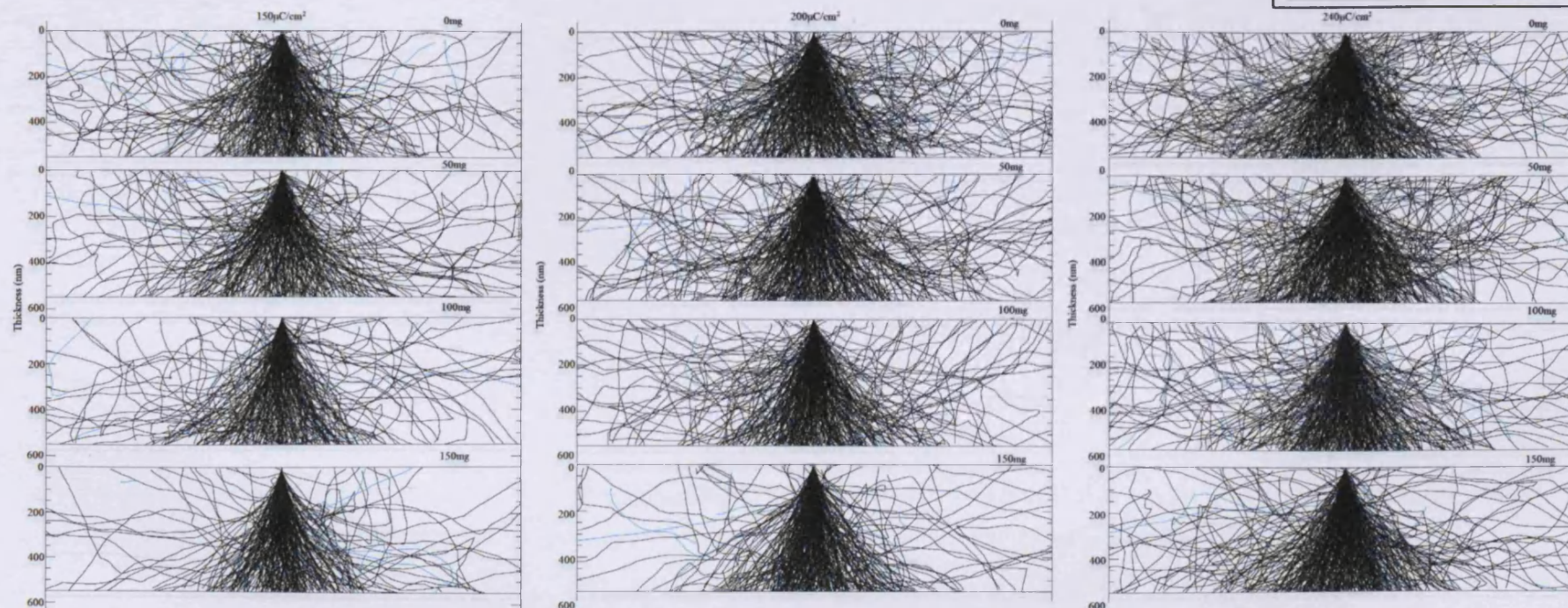


Figure C – 1: Point electron distributions of PMMA loaded with 0, 50, 100 and 150mg of  $\text{Al}_2\text{O}_3$  nanoparticles exposed with dose of 150, 200, 240 $\mu\text{C}/\text{cm}^2$  for 25KeV incident electron beam for a film thickness of 550nm.



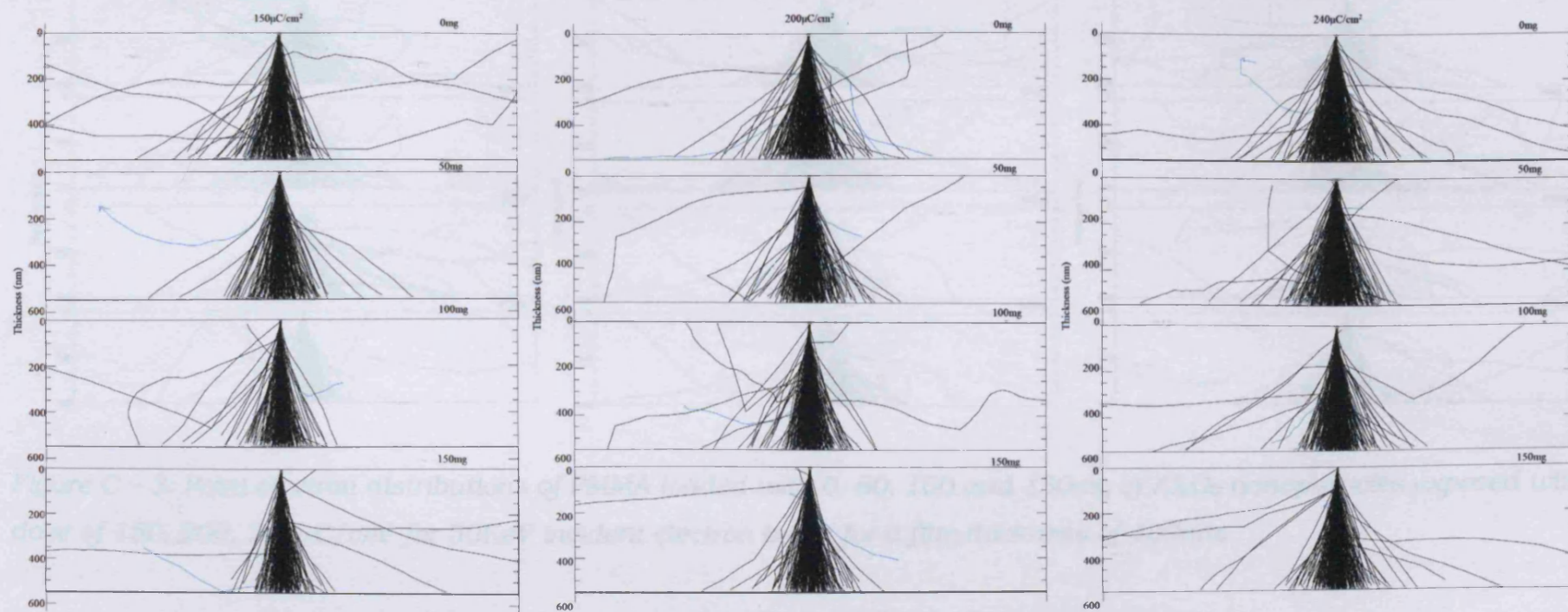


Figure C – 2: Point electron distributions of PMMA loaded with 0, 50, 100 and 150mg of  $\text{Al}_2\text{O}_3$  nanoparticles exposed with dose of 150, 200, 240  $\mu\text{C}/\text{cm}^2$  for 100KeV incident electron beam for a film thickness of 550nm.



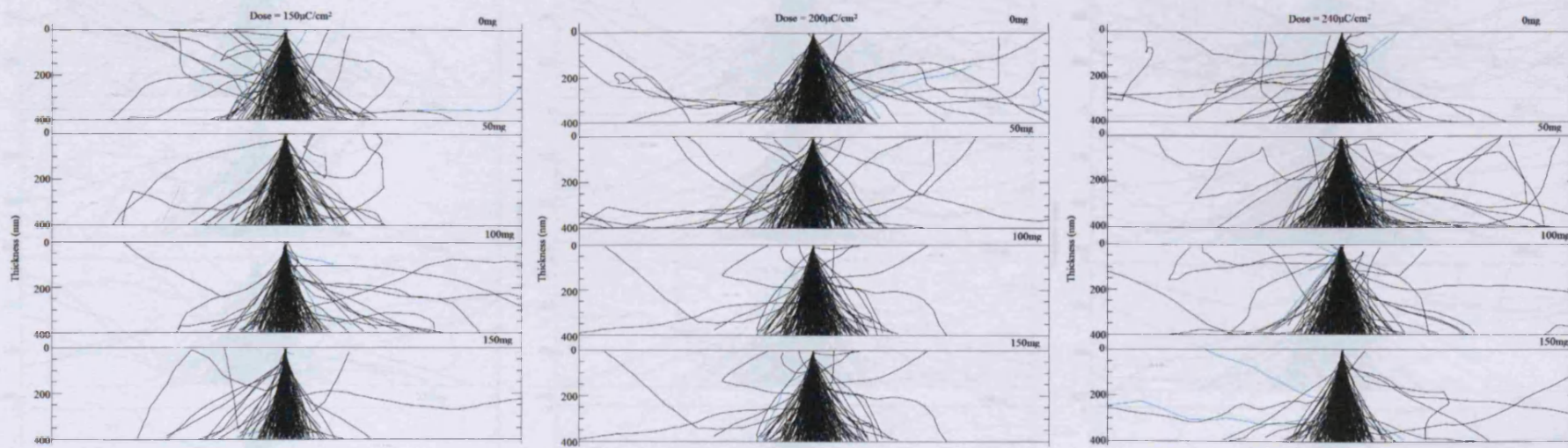


Figure C – 3: Point electron distributions of PMMA loaded with 0, 50, 100 and 150mg of  $\text{Al}_2\text{O}_3$  nanoparticles exposed with dose of 150, 200, 240  $\mu\text{C}/\text{cm}^2$  for 50KeV incident electron beam for a film thickness of 400nm.

Figure C-4: Point electron distributions of PMMA loaded with 0, 50, 100 and 150mg of  $\text{Al}_2\text{O}_3$  nanoparticles exposed with dose of 150, 200, 240  $\mu\text{C}/\text{cm}^2$  for 50KeV incident electron beam for a film thickness of 500nm.

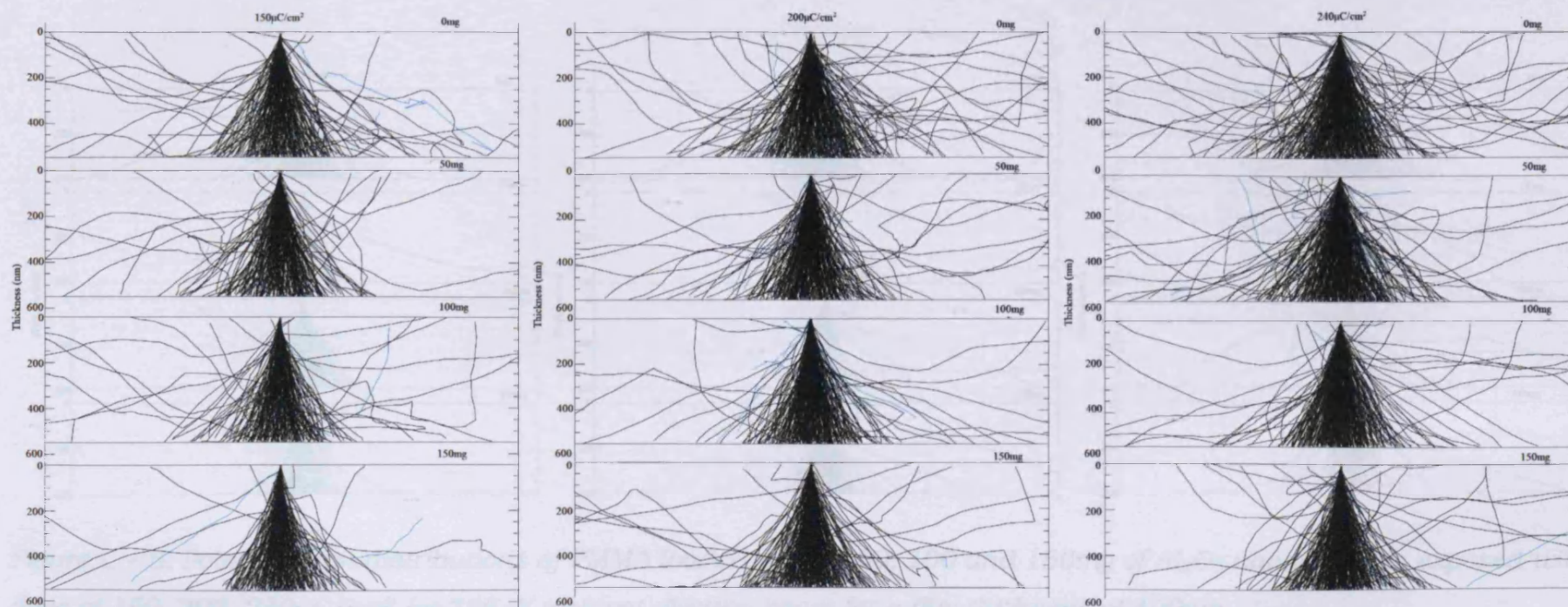


Figure C – 4: Point electron distributions of PMMA loaded with 0, 50, 100 and 150mg of  $\text{Al}_2\text{O}_3$  nanoparticles exposed with dose of 150, 200, 240  $\mu\text{C}/\text{cm}^2$  for 50KeV incident electron beam for a film thickness of 550nm.



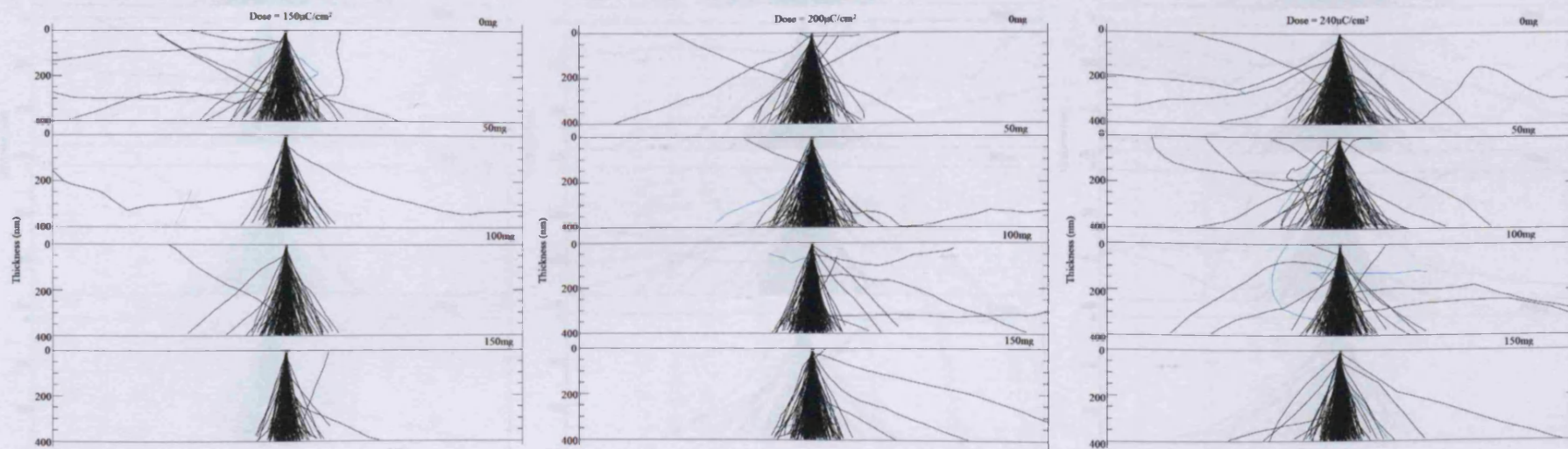


Figure C – 5: Point electron distributions of PMMA loaded with 0, 50, 100 and 150mg of  $\text{Al}_2\text{O}_3$  nanoparticles exposed with dose of 150, 200, 240  $\mu\text{C}/\text{cm}^2$  for 75KeV incident electron beam for a film thickness of 400nm.

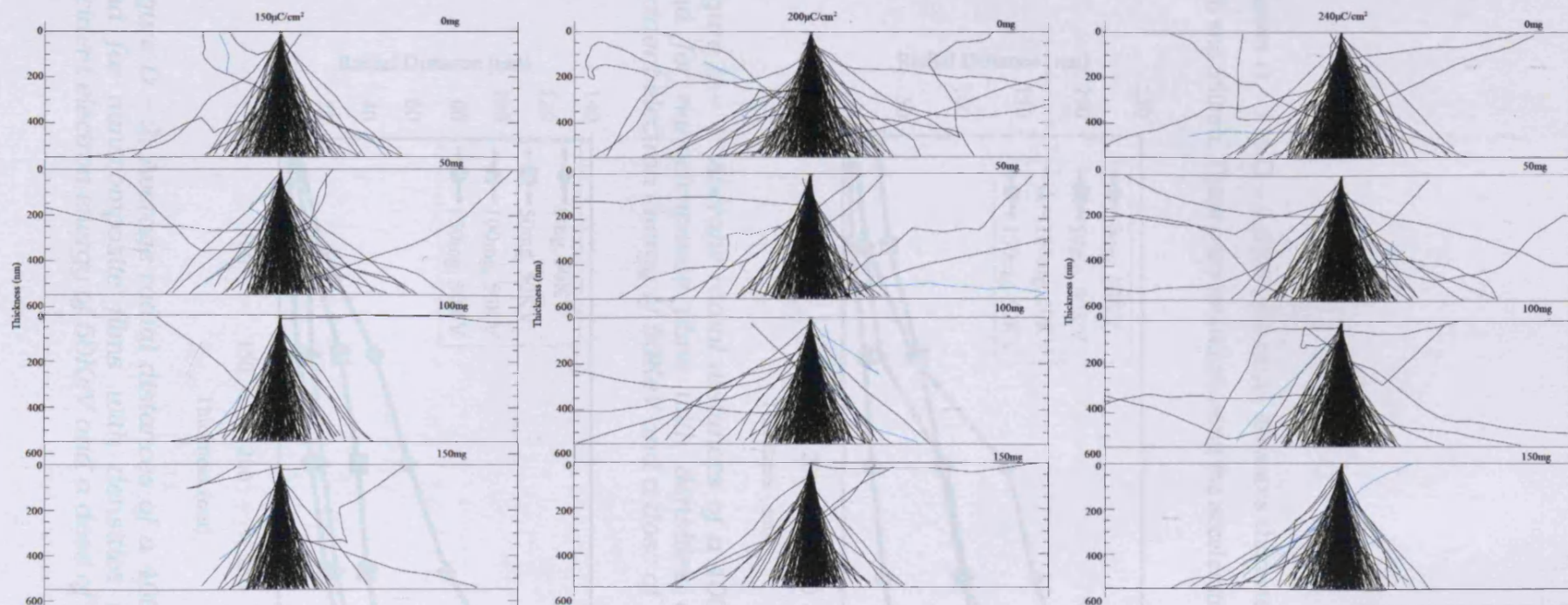


Figure C – 6: Point electron distributions of PMMA loaded with 0, 50, 100 and 150mg of  $\text{Al}_2\text{O}_3$  nanoparticles exposed with dose of 150, 200, 240  $\mu\text{C}/\text{cm}^2$  for 75KeV incident electron beam for a film thickness of 550nm.

## Appendix

# D

Figures D – 1 to D – 6 shows the radial distances characteristics in film thicknesses of 400 and 550nm. These were produced using the accelerating voltages of 50KeV.

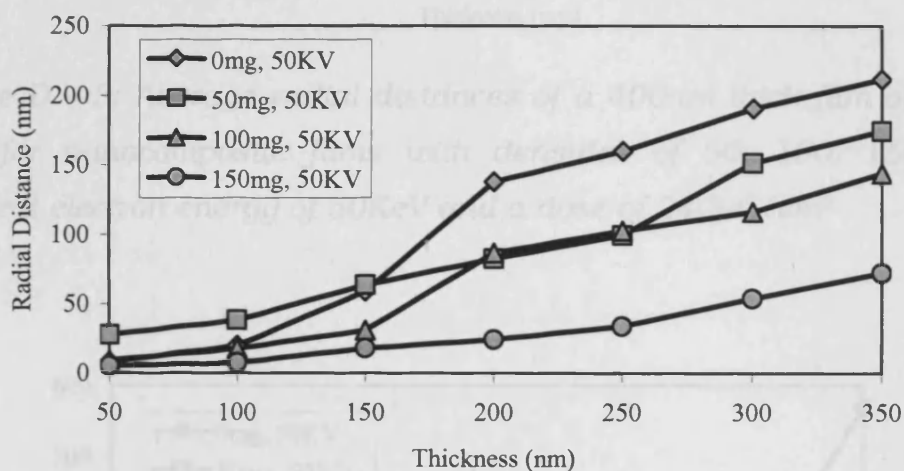


Figure D – 1: Average radial distances of a 400nm thick film of PMMA and for nanocomposite films with densities of 50, 100, 150mg at incident electron energy of 50KeV and a dose of  $150\mu\text{C}/\text{cm}^2$ .

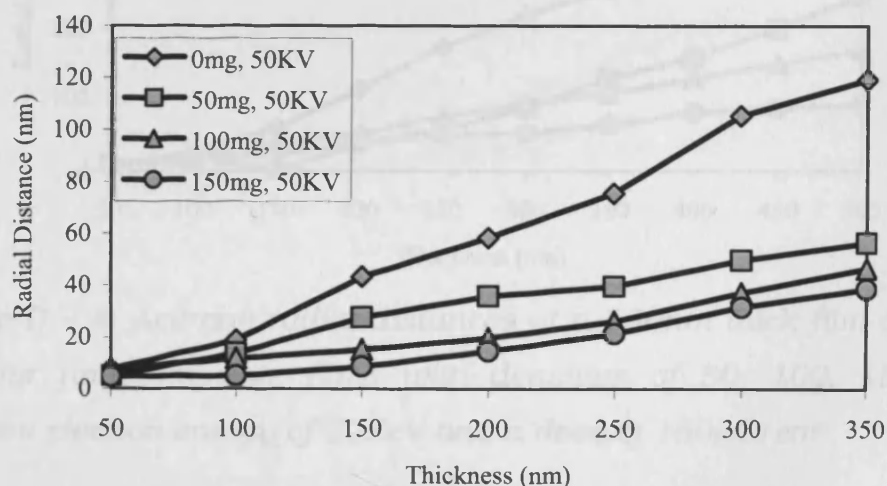


Figure D – 2: Average radial distances of a 400nm thick film of PMMA and for nanocomposite films with densities of 50, 100, 150mg at incident electron energy of 50KeV and a dose of  $200\mu\text{C}/\text{cm}^2$ .



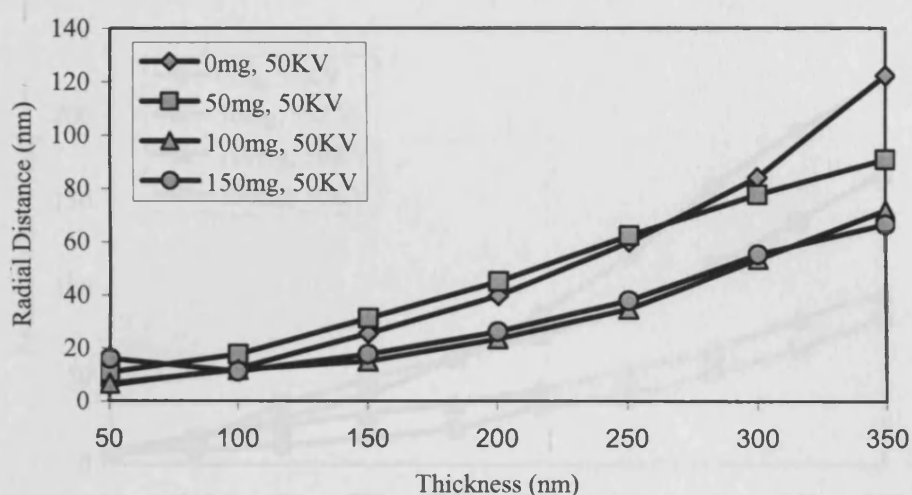


Figure D - 3: Average radial distances of a 400nm thick film of PMMA and for nanocomposite films with densities of 50, 100, 150mg at incident electron energy of 50KeV and a dose of  $240\mu\text{C}/\text{cm}^2$

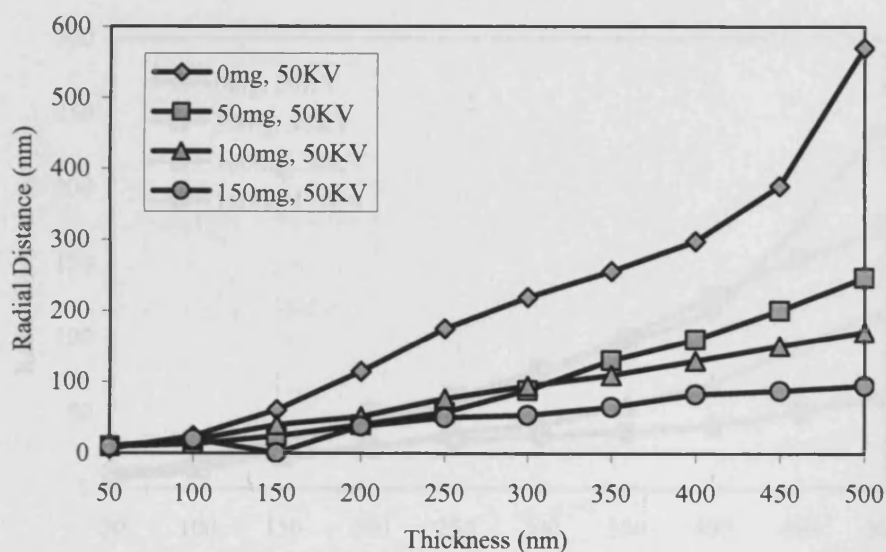


Figure D - 4: Average radial distances of a 550nm thick film of PMMA and for nanocomposite films with densities of 50, 100, 150mg at incident electron energy of 50KeV and a dose of  $150\mu\text{C}/\text{cm}^2$ .

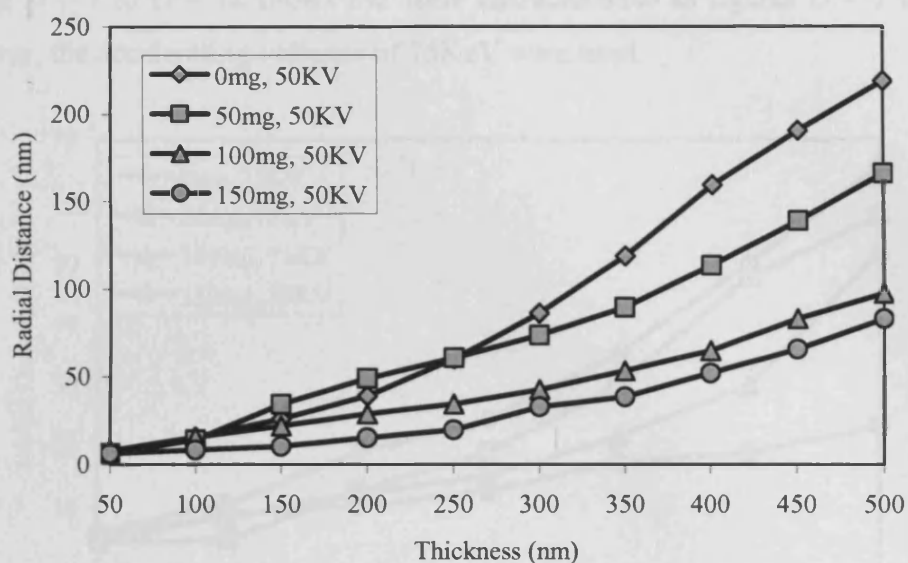


Figure D – 5: Average radial distances of a 550nm thick film of PMMA and for nanocomposite films with densities of 50, 100, 150mg at incident electron energy of 50KeV and a dose of 200µC/cm².

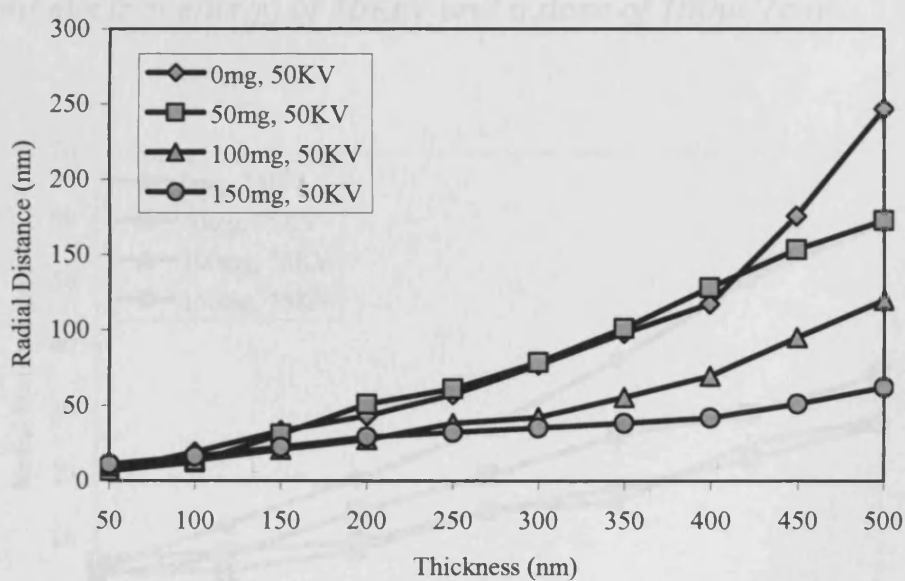


Figure D – 6: Average radial distances of a 550nm thick film of PMMA and for nanocomposite films with densities of 50, 100, 150mg at incident electron energy of 50KeV and a dose of 240µC/cm².

Figures D – 7 to D – 12 shows the same characteristics as figures D – 1 to D – 6. However, the accelerating voltages of 75KeV were used.

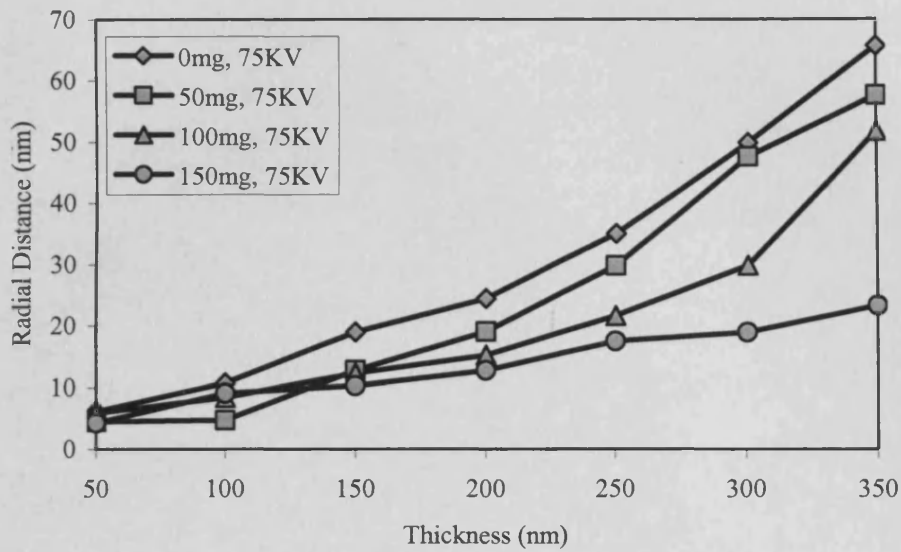


Figure D – 7: Average radial distances of a 400nm thick film of PMMA and for nanocomposite films with densities of 50, 100, 150mg at incident electron energy of 75KeV and a dose of 150µC/cm².

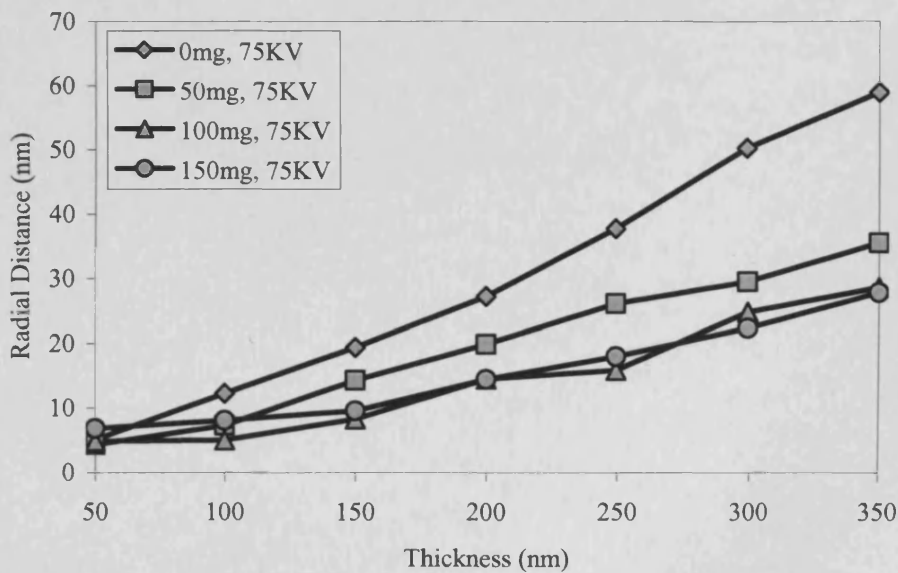


Figure D – 8: Average radial distances of a 400nm thick film of PMMA and for nanocomposite films with densities of 50, 100, 150mg at incident electron energy of 75KeV and a dose of 200µC/cm².

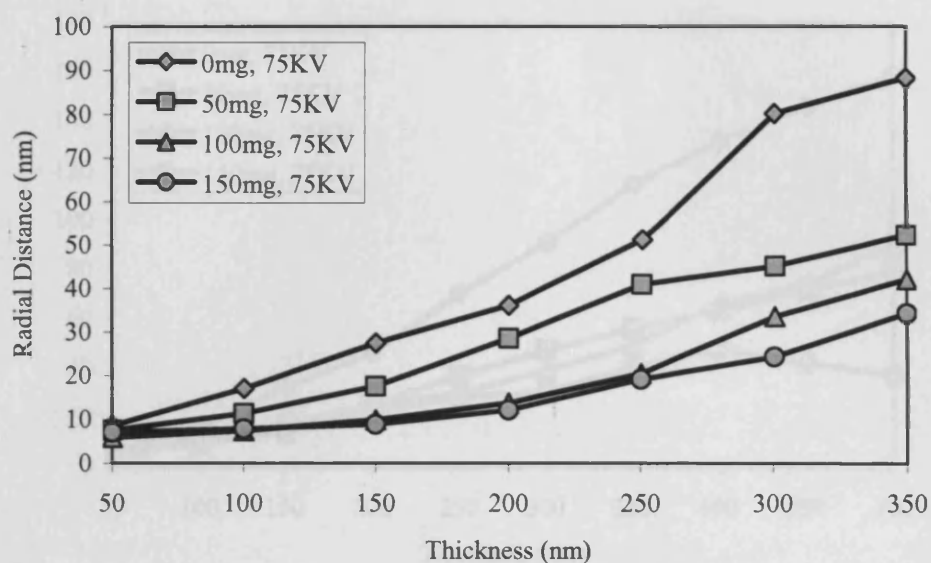


Figure D – 9: Average radial distances of a 400nm thick film of PMMA and for nanocomposite films with densities of 50, 100, 150mg at incident electron energy of 75KeV and a dose of 240μC/cm².

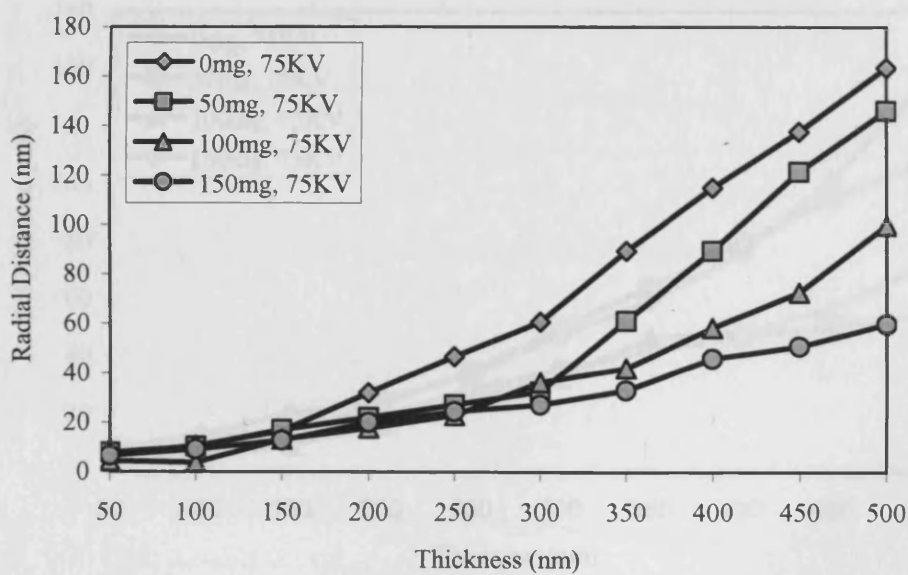


Figure D – 10: Average radial distances of a 550nm thick film of PMMA and for nanocomposite films with densities of 50, 100, 150mg at incident electron energy of 75KeV and a dose of 150μC/cm².

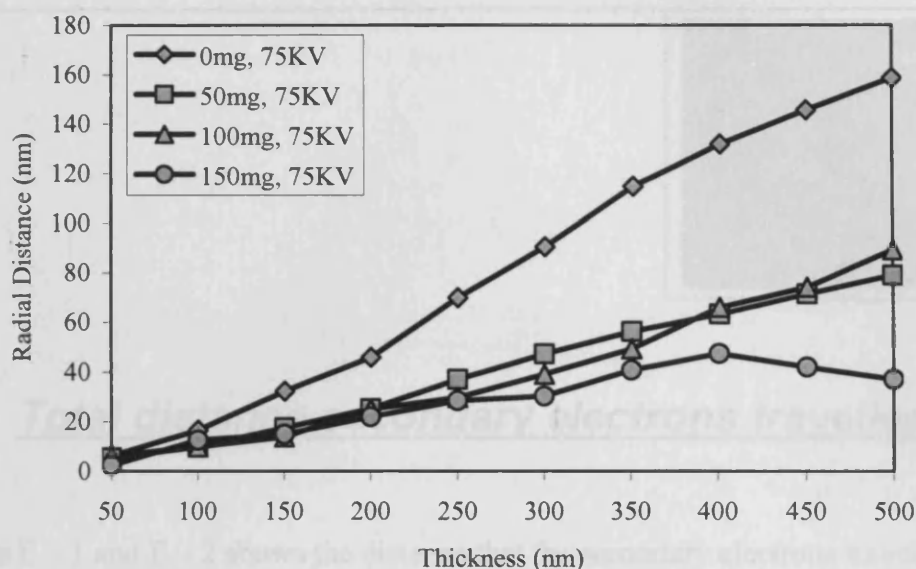


Figure D - 11: Average radial distances of a 550nm thick film of PMMA and for nanocomposite films with densities of 50, 100, 150mg at incident electron energy of 75KeV and a dose of  $200\mu\text{C}/\text{cm}^2$ .

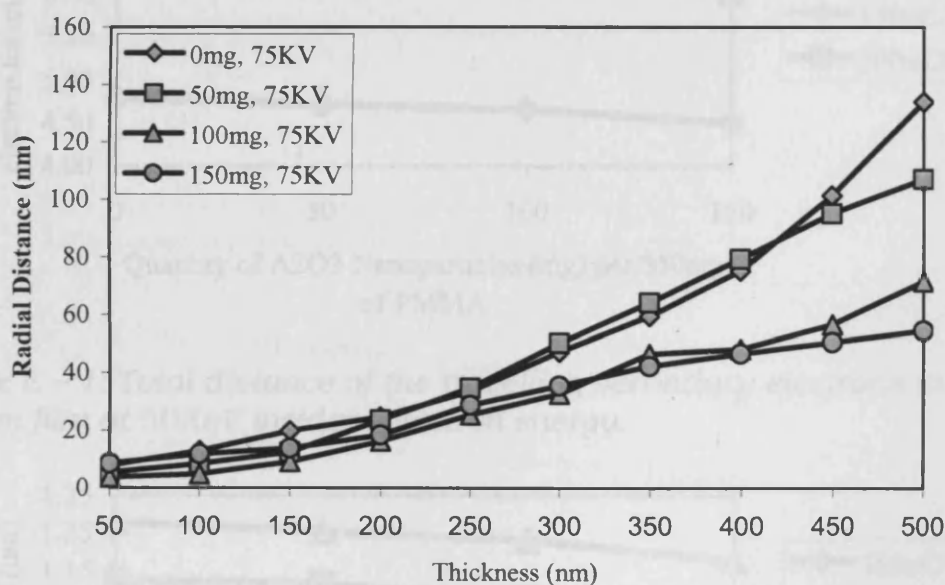


Figure D - 12: Average radial distances of a 550nm thick film of PMMA and for nanocomposite films with densities of 50, 100, 150mg at incident electron energy of 75KeV and a dose of  $240\mu\text{C}/\text{cm}^2$ .



## Appendix

# E

### Total distance secondary electrons travelled

Figures E – 1 and E – 2 shows the distance that the secondary electrons travelled through the nanocomposite resist film of 400 and 550nm respectively, at 50KeV incident electron energy.

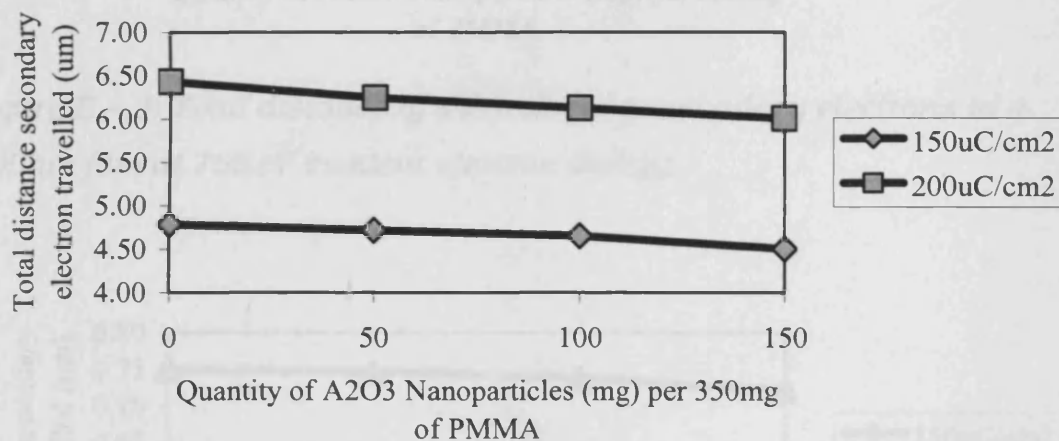


Figure E – 1: Total distance of the travelling secondary electrons in a 400nm film at 50KeV incident electron energy.

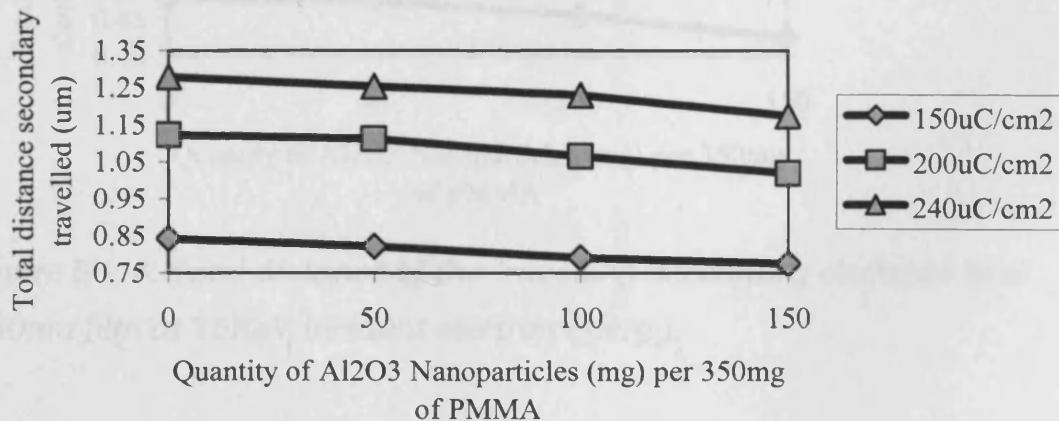


Figure E – 2: Total distance of the travelling secondary electrons in a 550nm film at 50KeV incident electron energy.

Figures E – 3 and E – 4 shows the distance that the secondary electrons travelled through the nanocomposite resist film of 400 and 550nm respectively, at 75KeV incident electron energy.

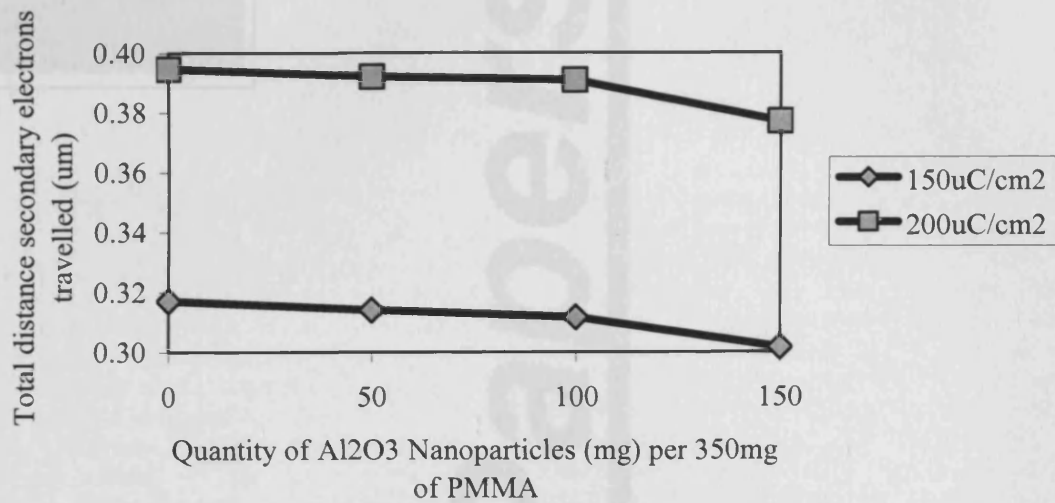


Figure E – 3: Total distance of the travelling secondary electrons in a 400nm film at 75KeV incident electron energy.

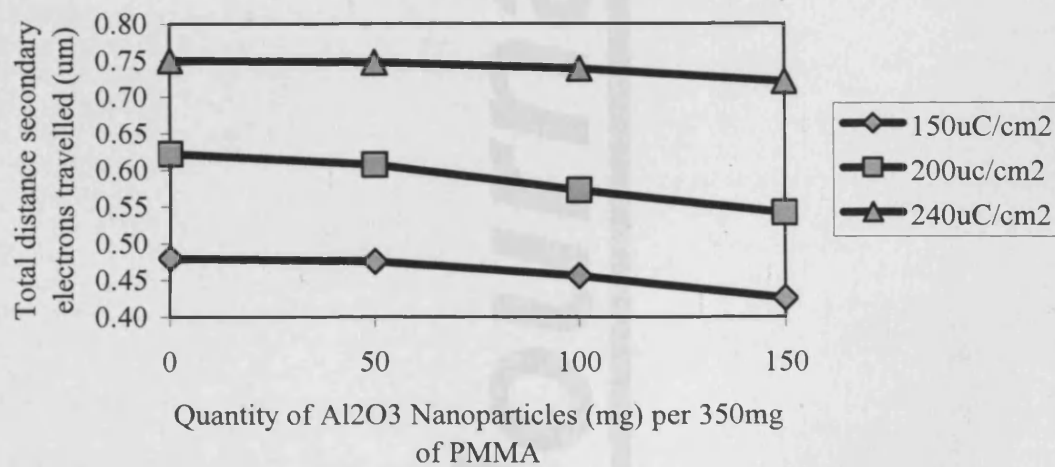


Figure E – 4: Total distance of the travelling secondary electrons in a 550nm film at 75KeV incident electron energy.

## Appendix

# F

# Journal Papers

## Low Cost PMMA based photo-masks for 3D grey scale micro-structuring applications

S. Lewis\*, R. Wheeler - Jones\*, R. Perks\* and V. Haynes\*\*

\*The Institute of Advanced Materials and Energy Systems  
Cardiff School of Engineering

\*\*School of Physics and Astronomy  
Cardiff University, Queens Building, The Parade, Cardiff, U.K. CF24 3AA

### ABSTRACT

The transfer of a three dimensional grey-scale pattern from a polymer composite to a photoresist has been demonstrated. The grey scale structure was fabricated using variable dose electron beam lithography. The optical transparency of the electron beam resist was reduced by the addition of  $\text{Al}_2\text{O}_3$  and  $\text{TiO}_2$  nanoparticles. The reduction in optical transparency of this composite was due to the radiation scattering effects of the poly crystalline nanoparticles. By increasing the nanoparticle density, the overall transparency of the composite is reduced.

**Keywords:** PMMA, nanoparticles, photoresist, 3D grey scale, electron beam lithography.

### 1 INTRODUCTION

Grey-scale lithography is a useful technique for fabricating three dimensional structures in a polymeric thin film [1] and can be achieved by variable dose methods or fixed dose methods [2]. Utilizing structured photoresist as an etch mask for example can enable a three dimensional structure to be transferred to a substrate material such as silicon; anisotropic dry etching is one method. However, fabricating the grey-scale mask in the first instance is technically challenging and time consuming [3]. This is particularly significant in that all etch masks of this type are single use. Transferring the three dimensional grey-scale structure from the electron beam resist to a standard photoresist enables multiple structures to be made from a single mask. Polymethylmethacrylate (PMMA) based electron beam resist is highly transparent at wavelengths associated with the exposure of photoresist. This material alone would not be suitable as a photolithography mask. However, it is possible to modify the optical properties of this polymeric film through the homogeneous dispersal of nanoparticles.

### 2 EXPERIMENTAL

The PMMA composites used in this study were obtained by the homogeneous dispersal of  $\text{Al}_2\text{O}_3$  and  $\text{TiO}_2$  nanoparticles in PMMA. Samples were prepared by adding 10mg through

to 200mg of nano-particles to 1.6g of PMMA. The nano-particles were pre-wetted in 0.5ml of methanol to produce a particle suspension before being mixed with the PMMA. These composites were then spun onto 25mm×25mm borosilicate glass microscope cover slips. The cover slips were sputter coated with a few nm of gold; whilst necessary for electron beam exposure, provided additional adhesion qualities. A spin cycle of 6000rpm for 45 seconds was followed by a soft-bake at 180°C for 3 minutes.

The optical transmission of the composite films at a wavelength of 365nm was obtained using a Jenway spectrophotometer.

The three dimensional structuring of the resist composite was achieved through variable dose exposure using the Raith 50. The exposure dose was modulated from 10 through to 30 $\mu\text{A}/\text{cm}^2$  in increments of 5 $\mu\text{A}/\text{cm}^2$ . The composite resist was developed using MIBK developer and IPA solvent in the ratio 1:3.

These composite photo-masks were used to expose Microposit S1813 positive photoresist (see figure 2–0). This was spun onto silicon substrates at 6000rpm for 45 seconds yielding a photoresist thickness of typically 1.1 $\mu\text{m}$ . The composite masks were then placed in contact with the S1813 and a typical 6 second UV exposure using a Karl Suss mask aligner. The sample was then developed for 40 seconds at room temperature. The developer solution was 2401 developer and water in the ratio 1:10.

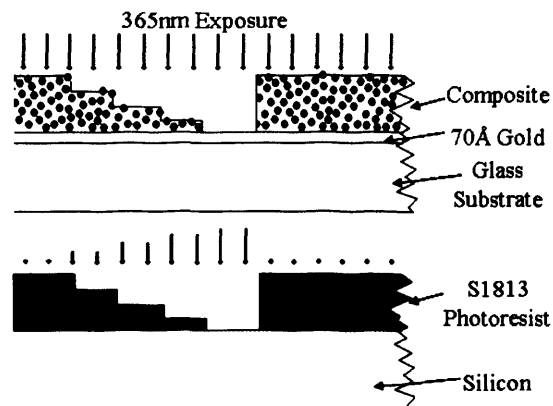


Figure 2–0: A schematic of the contact printing process; the photoresist is show 'as developed'.

### 3 RESULTS

#### 3.1 Optical attenuation and scattering

The optical transmission at 365nm as a function of nanoparticle density for the composite sample is shown in figure 3-0. The optical transmission is inversely proportional to nanoparticle density over the range shown and becomes 90% transparent for PMMA alone. Note: the borosilicate glass substrate alone is at 96%.

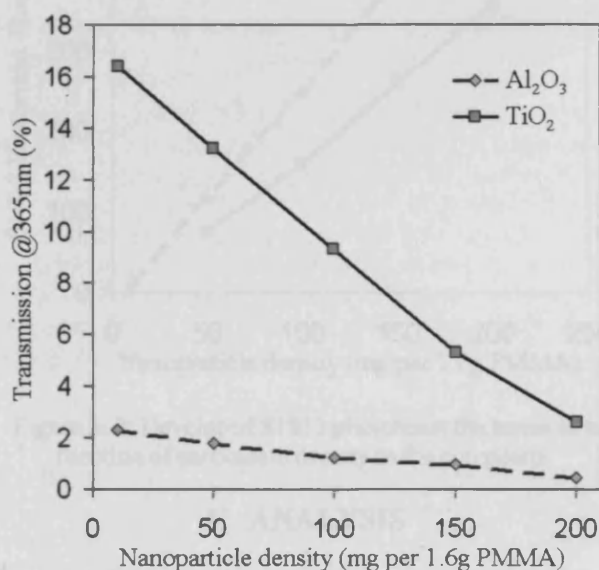


Figure 3-0: Optical transmission as a function of nanoparticle density for both types of composite.

Comparing both the Al<sub>2</sub>O<sub>3</sub> and TiO<sub>2</sub> nanoparticle composites, it is evident that the resultant reduction in transmission is greater with Al<sub>2</sub>O<sub>3</sub> than with TiO<sub>2</sub>. This enhanced opacity through nanoparticle dispersal is a result of particulate scattering rather than by direct absorption [4,5]. In simple terms, the extinction or attenuation of incident light is given by

$$I_t = I_i \exp(-\alpha_{ext} T), \quad (1)$$

where  $I_i$  is the incident intensity,  $T$  is the thickness of the composite resist and  $\alpha_{ext}$  is the extinction coefficient. The standard definition is given by

$$\alpha_{ext} = \psi C_{ext} = \psi C_{abs} + \psi C_{sca}, \quad (2)$$

However, having determined scattering to be the dominant process, the extinction coefficient for an ensemble of randomly sized particles is given by

$$\alpha_{ext} = \sum_j \psi_j C_{sca,j} \quad (3)$$

where  $\psi_j$  is the number of particles of type  $j$  per unit volume with  $C_{sca,j}$  being the scattering cross section. The extinction coefficient  $\alpha_{ext}$  for the Al<sub>2</sub>O<sub>3</sub> and TiO<sub>2</sub> composites studied ranged from  $\sim 4\mu\text{m}^{-1}$  to  $\sim 7\mu\text{m}^{-1}$  and  $\sim 2\mu\text{m}^{-1}$  to  $\sim 5\mu\text{m}^{-1}$  respectively (this assumes a typical 'spun on' PMMA composite thickness of  $0.8\mu\text{m}$ ). The optical transmission of the resultant thin film composite is highly sensitive to thickness variations. Subsequent variable dose electron beam exposure can produce patterns of variable thickness. Micro-structuring a thin film in this way can result in a grey-scale optical mask.

#### 3.2 Grey-scale lithography

The electron beam exposure dose parameters have been characterized and the resultant PMMA thickness following development is shown in figure 3-1. It is clear that as the exposure dose increases the composite resist height decreases; this is reasonably linear over the range shown.

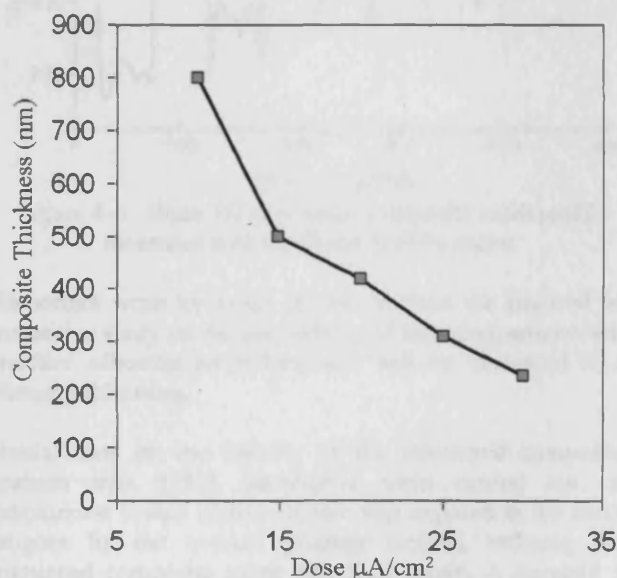


Figure 3-1: Resultant PMMA thickness following development as a function of exposure dose.

In order to test the performance of the composite films during photoresist exposure a number of test samples were prepared consisting of borosilicate glass substrates coated with composites of different nanoparticle density. This experiment is directly analogous to that described above, whereby S1813 photoresist is subjected to a variable dose of UV radiation and the thickness following development is measured. The results obtained are given in figure 3-2



Technical Proceedings of the 2006 Nanotechnology Conference and Trade Show, Vol3, Chapter 2 : Nanoscale Fabrication, pp214 – 217, (May 2006).

following a 6 second exposure in a Karl Suss mask aligner. Again, the variation in S1813 thickness is proportional to nanoparticle density over the range shown.

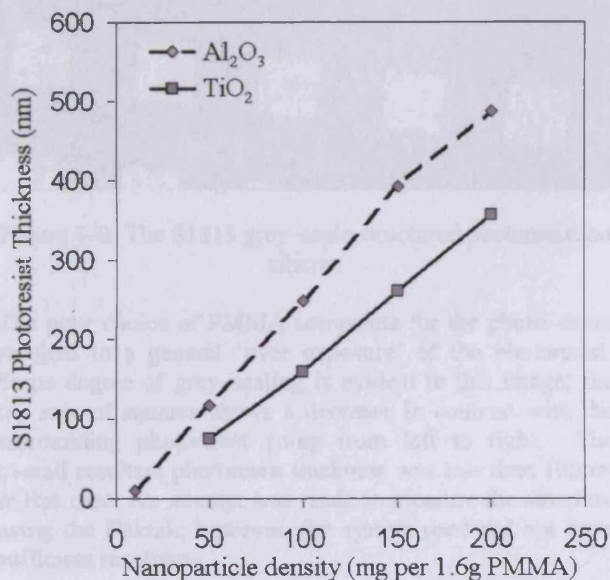


Figure 3-2: Developed S1813 photoresist thickness as a function of particulate density in the composite.

#### 4 ANALYSIS

Feature definition in the exposed composite electron beam resist is next considered. A test pattern was prepared, consisting of a sequence of five 50 $\mu$ m squares, each exposed at a different dose increasing from 10 – 30 $\mu$ A/cm<sup>2</sup> in steps of 5  $\mu$ A/cm<sup>2</sup>. The composite in this case consisted of 10mg of Al<sub>2</sub>O<sub>3</sub> nanoparticles dispersed in 1.6g of PMMA. The particle size averaged 30nm. The 'spun on' thickness of the composite was around 800nm. This particular sample represents a 'worst case'; here a surfactant was not used in the sample preparation. As a result, some particulate clumping was observed in the composite film. The optical microscope image below (figure 4-0) shows the exposed squares. When viewed in color the top row of squares change from red on the left, through green, to blue on the right. This is due to thin film interference effects under white light illumination. The rows of squares below were exposed at doses higher than 30 $\mu$ A/cm<sup>2</sup> resulting in the complete removal of the PMMA composite following development.

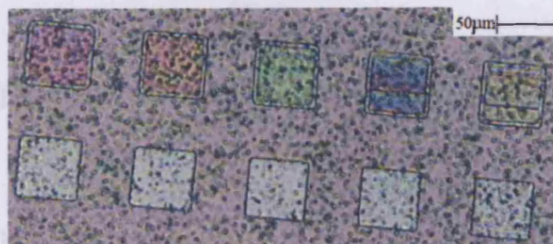


Figure 4-0: PMMA composite following development and variable dose exposure.

The variation in thickness of the resultant thin film across this top row of squares was measured by a Detak stylus profileometer. The trace from this apparatus is shown in Figure 4-1.

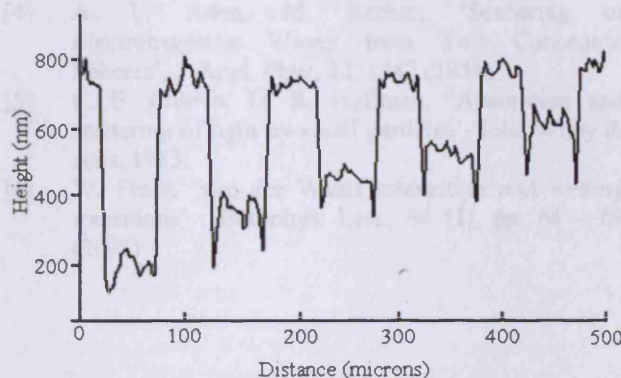


Figure 4-1: 50 $\mu$ m 3D grey scale composite resist profile measured with the Detak profileometer.

Important work by Fenzl [6] has formed the basis of an extensive study on the pre wetting of the nanoparticles and surface adhesion properties; this will be discussed in a future publication.

Initial tests on the transfer of the structured composite pattern into S1813 photoresist were carried out. A photoresist coated silicon sample was exposed in the mask aligner by the contact printing method, utilizing the patterned composite mask described above. A standard 6 second exposure was used followed by a standard development stage. Whilst the mask composite used in this case had the lowest nanoparticle density, the resultant photoresist showed some degree of grey-scale structuring (see figure 4-2 below).





Figure 4-2: The S1813 grey-scale structured photoresist on silicon.

The poor choice of PMMA composite for the photo-mask resulted in a general 'over exposure' of the photoresist. Some degree of grey-scaling is evident in this image; the top row of squares shows a decrease in contrast with the surrounding photoresist going from left to right. The overall resultant photoresist thickness was less than 100nm in this case. An attempt was made to measure the structure using the Dektak; however, the system used did not have sufficient resolution.

## 5 CONCLUSIONS

The fabrication of simple low cost grey scale photo-masks has been demonstrated using the technique described. The optical properties of the PMMA nanoparticle composites were determined by use of a Jenway spectrophotometer. Optical scattering is the dominant attenuation mechanism with nanoparticles of  $\text{Al}_2\text{O}_3$  producing a higher overall attenuation as compared with  $\text{TiO}_2$ . Grey-scale structuring of the composite thin films using a Raith 50 electron beam lithography system has been demonstrated. The transfer of this structure into the photoresist has seen some limited success; however, in retrospect, the higher density nanoparticle composites should have been used in this aspect of the study. The effectiveness of the higher density composites has been demonstrated however. A series of composite masks with increasing nanoparticle density, were used to expose photoresist. The thickness of the developed photoresist films was shown to vary linearly with nanoparticle density over the range described.

## 6 ACKNOWLEDGEMENTS

The authors would like acknowledge the support of Huw Summers of the School of Physics and Astronomy, Cardiff University together with Peter Dunstan of the Multidisciplinary Nanotechnology Centre at Swansea University, Wales, UK. Both are members of the Pan Wales MNT Consortium.

## 7 REFERENCES

- [1] Fuhua Gao, Jun Yao, yangsu Zeng, Shiwei Xie, Yongkang Guo, Zheng Cui, 'One step lithography for fabrication of multifunction diffractive structures with grey - tone mask', *Microelectronic Engineering* 61 - 62, 2002, pg 165 - 171.
- [2] V. Kudryashov, P. D. Prewett, A. G. Michette, 'A new E - beam method for grey scale 3D optical elements', *Microelectronic Engineering* 46, 1999, pg 209 - 212.
- [3] E. Knappek, C. K. Kalus, M. Madore, M. Hintermaier, U. Hofmann, H. Scherer-Winner and R. Schlager, 'Computer aided proximity correction for direct write E-beam lithography' *Microelectronic Engineering*, Volume 13, Issues 1-4, March 1991, Pages 181-184.
- [4] A. L. Aden, M. Kerker, 'Scattering of Electromagnetic Waves from Two Concentric Spheres', *J. Appl. Phys.* 22, 1242 (1951)
- [5] C. F. Bohren, D. R. Huffman, 'Absorption and scattering of light by small particles', John Wiley & sons, 1983.
- [6] W. Fenzl, 'van der Waals interaction and wetting transitions', *Europhys. Lett.*, 64 (1), pp. 64 - 69 (2003)



# High density self assembled nanoparticle film with temperature-controllable interparticle spacing for deep sub-wavelength nanolithography using localized surface plasmon modes on planar silver nanoparticle tunable grating

S. Lewis <sup>a,\*</sup>, R. Wheeler-Jones <sup>a</sup>, V. Haynes <sup>b</sup>, R.M. Perks <sup>a</sup>

<sup>a</sup> *The Institute of Advanced Materials and Energy Systems, Cardiff School of Engineering, UK*

<sup>b</sup> *School of Physics and Astronomy, Cardiff University, Queen's Buildings, The Parade, Cardiff CF24 3AA, UK*

Received 25 April 2007; received in revised form 29 August 2007; accepted 2 September 2007

Available online 26 September 2007

## Abstract

A novel photolithographic technique using a periodic hexagonal close packed silver nanoparticle 2D array photo mask has been demonstrated to transfer a nano-pattern into a photoresist using G–I line proximity photolithography. This method can be made to precisely control the spacing between nanoparticles by using temperature. The high-density nanoparticle thin film is accomplished by self assembly through the Langmuir-Schaefer (LS) technique on a water surface and then transferring the particle monolayer to a temperature sensitive polymer membrane. A 30 nm hexagonal close packed silver nanoparticle 2D array pattern with a 50 nm period has been successfully transferred into S1813 photoresist using I-line exposure wavelength. The resultant feature sizes were 34 nm with a period of 46 nm, due to the surface plasmon resonance where the S1813 photoresist feature is approximately 11 times smaller than I-line exposure wavelength.

© 2007 Elsevier B.V. All rights reserved.

**Keywords:** Nanolithography; Nanoparticle; Self assembly; Silver; Surface plasmon resonance

## 1. Introduction

Photolithography has been a major fabrication method in the integrated circuit (IC) and semiconductor industry over the past several decades. Contact photolithography in the optical near-field has been developed as a technique to enable the fabrication of features of the order of sub-micrometer dimensions. To perform near-field photolithography several methods have been demonstrated which include the probe of a near-field scanning optical micro-

scope, contact imaging through a transmission mask or a binary phase-shift mask [1,2], evanescent near-field lithography with an embedded-amplitude mask [3], light coupling masks [4], plasmon printing [5] and evanescent interferometric methods [6].

Surface plasmon resonance (SPR) has the potential to influence light by enhancing sub-wavelength structures. The scientific community has become interested in the phenomenon of the transmission of opaque metal films when light is enhanced through sub-wavelength hole arrays. [7–11]

The excitation of SPRs on the metal surface dramatically enhances the optical throughput via the sub-wavelength apertures. The surface plasmon dispersion relation,  $\kappa_{sp}$  which incorporates the frequency-dependent SP wave vector, describes the interaction of light and SPR [12], this is shown here

\* Corresponding author. Address: University of Manchester, School of Physics and Astronomy, Sackville Street Building, P.O. Box 88, Manchester M60 1QD, United Kingdom. Tel.: +44 (0) 779 368 3065; fax: +44 (0) 161 306 3922.

E-mail addresses: [Scott.Lewis@Manchester.ac.uk](mailto:Scott.Lewis@Manchester.ac.uk), [slewis@jb.man.ac.uk](mailto:slewis@jb.man.ac.uk) (S. Lewis).



$$\kappa_{sp} = \kappa_0 \sqrt{\frac{\epsilon_d \epsilon_m}{\epsilon_d + \epsilon_m}} \quad (1)$$

where  $\kappa_0$  is the wave vector of light in vacuum,  $\epsilon_m$  and  $\epsilon_d$  are relative dielectric constants of a metal and the surrounding dielectric material. The SPR dispersion curve, shown in Fig. 1a, indicates that smaller features are expected in the lithographic pattern. The wavelength of the excited SPs is shorter than the wavelength of the excitation light at the same frequency. Due to the momentum mismatch between the light waves and the SP waves, light cannot excite SPs in the metal directly. However, by using a rough surface, a grating coupler, or an attenuated total reflection (ATR) coupler, light can be converted into SPs and vice versa. For example, a 2D grating coupler can act as a 2D square array of holes. Light can excite SP waves on the incident side, by selecting a proper periodicity for the hole array and a proper dielectric constant for the medium surrounding the metal substrate, the SP waves can be resonantly coupled through the periodic hole array to the other side of the metal [7,9]. The SP waves on the exit plane are scattered on the hole array and will be converted back into light waves, if the dielectric constant of the dielectric layers match on both sides of the metal layer. The light wavelength that excite the SP resonance mode (when the incident light is normal to the 2D hole array) is given by [9],

$$\lambda_{(i,j)} = \frac{a}{\sqrt{i^2 + j^2}} \sqrt{\frac{\epsilon_d \epsilon_m}{\epsilon_d + \epsilon_m}} \quad (2)$$

where  $\lambda$  is the light wavelength in vacuum,  $a$  is the hole array period,  $i$  and  $j$  are lattice mode indices. The transmission of SP waves through the sub-wavelength plasmonic masks at the I-line wavelength has potential to pattern nanoscale features using conventional near UV light sources. In this paper, we demonstrate a novel UV nanolithography technique utilizing SPR transmitted through sub-wavelength 2D hole array masks.

The configuration of the SPR optical lithography is illustrated in Fig. 1b. A plasmonic mask designed for the UV range is composed of self assembled 30 nm diameter silver nanoparticles hexagonally close packed (hcp) as a 2D array.

## 2. Experimental

To assemble a large-scale monolayer of hydrophobic silver nanoparticles on a water surface [14,15] is a Langmuir–Schaefer (LS) technique [13]. This technique consists of using a colloidal dispersion of silver nanoparticles in an organic liquid, which has a controlled convex curvature on a water surface. A monolayer of silver nanoparticles nucleates at the raised center of the water surface and grows smoothly outward, as the liquid evaporates. By bringing a smooth substrate down (from above) to the nanoparticle film, the monolayer can be transferred to it. By repeating this process, multiple layers of silver nanoparticles can be achieved. In a typical LS process, the formation of a close packed particle film is achieved, when the film is laterally pressurized. The particle array period is determined by the particle diameter and the length of the surfactant molecules [16]. To produce an organized, high-density nanoparticle film where the formation of microscopic holes (at low pressure) and multilayer aggregations (at high pressure) must be avoided. To achieve this, the pressure applied to the monolayer should be precisely controlled. However, when the film is transferred from the water surface to solid substrates, the perfect nanoparticle film could be broken. Therefore, to obtain a large area of closely-packed nanoparticle film on a solid substrate by directly transferring the LS film is not trivial. A thermal sensitive polymer layer was used as a shrinkable substrate in order to further compress the nanoparticle monolayer.

A low critical solution temperature (LCST) transition in the region of 30–40 °C is demonstrated by a polymer called

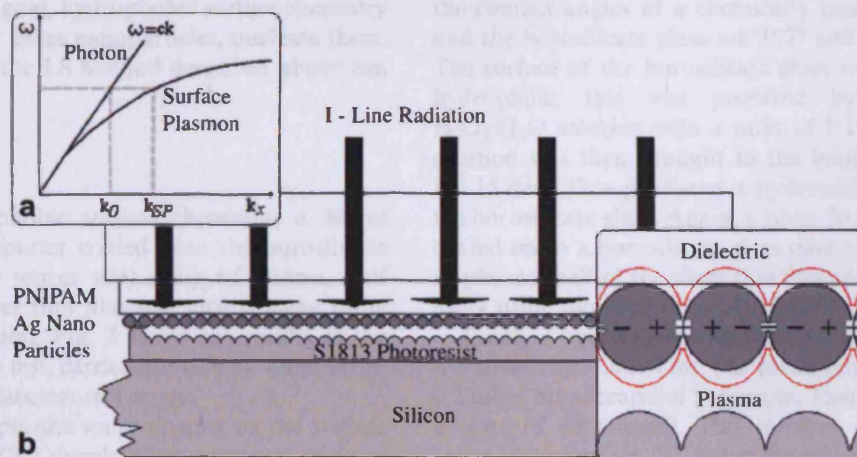


Fig. 1. (a) Schematic drawing of the surface plasmon dispersion curve. At the same frequency, surface plasmons display a shorter modal wavelength compared to that of free space photons, therefore, allowing sub-wavelength lithography; (b) schematic of the nanolithography process using the silver mask. Inset: The charges and the electromagnetic field of surface plasmons propagating on the grating surface in the  $x$  direction.



poly(*N*-isopropylacrylamide) (PNIPAM) [17]. This response is based on the fact that the network polymer chains are fully solvated and the polymer has good compatibility with the solvent. When the temperature increases further than the LCST, the polymer–solvent interaction is disrupted and the polymer–polymer interactions then dominate, resulting in the aggregation of polymer chains.

The PNIPAM thin film is prepared by photopolymerization of PNIPAM monomers, with a small amount of *N,N*-methylenebisacrylamide (bis-AMD) as crosslinker and 2,2'-diethoxyacetophenone (DEAP) as photoinitiator. A typical procedure consisted of 30  $\mu\text{mol}$  of (bis-AMD) and 1.6 mmol of *N*-isopropylacrylamide (NIPAM) being mixed with 2 ml of de-ionised water. Then 0.4  $\mu\text{mol}$  of the photoinitiator 'DEAP' is added into the solution. The resulting solution is dropped onto a borosilicate glass substrate with a pipette and is spread out over the whole surface. To prevent oxidation, it is covered with a thin glass slide. Using attenuated UV light, the samples were polymerized over a 30 min period at room temperature. When the polymer has cured, the top glass (cover slip) is removed and the polymer film can be used as the substrate to 'pick-up' the silver nanoparticle film. The PNIPAM film has a thickness of  $\sim 100 \mu\text{m}$ .

To control nanoparticle spacing this polymer film was an ideal substrate due to its ability to reorder the temperature. Most nanoparticles positioned far away from each other can be brought together as the polymer shrinks at temperatures higher than the transition temperature. The polymer film has about 10% or more shrinkage. Therefore, the interparticle distance can be reduced.

### 3. Results and discussion

In our lithography experiment, the plasmonic mask was prepared as follows: 30 nm diameter hexagonal close packed silver nanoparticle arrays with a period of 50 nm were fabricated by a self assembly technique as described above. To achieve this goal, hydrophobic surface chemistry must be applied to the silver nanoparticles, nucleate them. Once this is achieved, the LS method described above can be used.

#### 3.1. Surface analysis

To test the hydrophobic surface chemistry, a 30 nm thick silver film was sputter coated onto the borosilicate glass microscope slide (cover slip) using r.f plasma, half of the area of the silver thin film was etched away using dilute nitric acid solution. Fig. 2 shows the results of the hydrophobic chemistry test, carried out using a water droplet to measure the surface contact angle.

From the photograph, the water droplet on the surface of the silver thin film (left droplet) has a contact angle of approximately  $60^\circ$ , whereas the contact angle of the borosilicate surface is approximately  $40^\circ$ . Thus, the untreated silver film has a hydrophilic surface state. Fig. 3 shows that

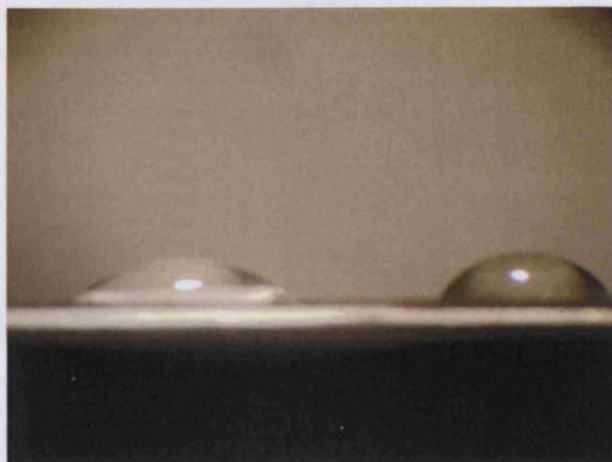


Fig. 2. Contact angle of the untreated silver.



Fig. 3. Contact angle of the hydrophobic silver and hydrophilic borosilicate glass.

the contact angles of a chemically treated silver thin film and the borosilicate glass are  $107^\circ$  and  $11.5^\circ$ , respectively. The surface of the borosilicate glass was first made to be hydrophilic, this was prepared by using  $\text{NH}_4\text{OH}:\text{H}_2\text{O}_2:\text{H}_2\text{O}$  solution with a ratio of 1:1:5. The hydrophilic solution was then brought to the boiling point condition for 15 min. This produced a hydrophilic surface state on the borosilicate glass. Again, a silver 30 nm film was sputter coated on to a borosilicate glass microscope slide using an r.f plasma, half of the silver thin film area was again etched away using dilute nitric acid solution.

Firstly a hydrophobic alkanethiol coating was added to the silver thin film. This was made possible by dissolving 0.2 ml of octadecandiol in hexane. Then this was dissolved in 2 ml of an ethanol. This solution was applied to the entire silver surface. Allowing the ethanol solvent to evaporate, leaving behind an alkanethiol monolayer with the sulphur atoms bound to the silver and the hydrocarbon tails pointing away as shown in Fig. 4.



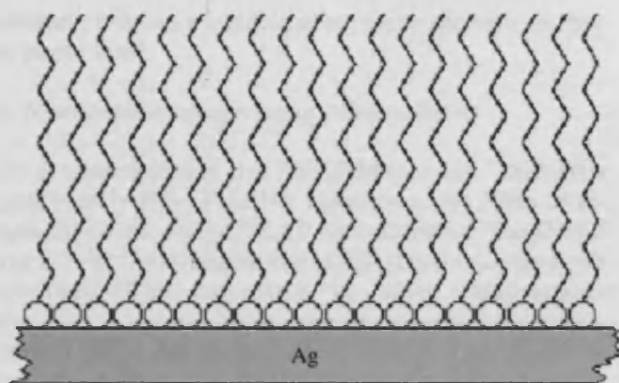


Fig. 4. An alkanethiol monolayer with sulphur atoms bound to the silver surface, creating an hydrophobic silver surface.

From the results shown in Fig. 3, it can be seen that the silver thin film has a hydrophobic surface state, whereas the borosilicate glass has a hydrophilic surface state.

A cylinder of PTFE (5 cm in diameter, with a 2 cm circular hole machined in its center) was used to position the silver nanoparticles close together. Care is taken to ensure that the PTFE cylinder is level. Deionized water is added to the hole in the PTFE cylinder. At this point, the water surface inside the hole assumes a convex meniscus. Control of the water level in the reservoir provides excellent control of the shape of the air–water interface within the hole. For experiments in this paper, the water level in the reservoir was adjusted to produce a water surface with only slight convex upward curvature.

The nanoparticle array is formed by preparing the silver nanoparticles as a colloid suspension using 2 ml of an ethanol solution and 0.2 ml of octadecandiol in hexane, a 0.12 ml portion of oleic acid is then introduced into the solution. A 0.5 ml of the colloid suspension is dropped on the water surface and the ethanol solvent is allowed to evaporate (forming a monolayer of silver nanoparticles at the center) inside a fume cupboard. Care is taken to minimize air currents that might disturb the water surface.

### 3.2. Optical properties of the silver nanoparticle hcp 2D array

To detect the SPR phenomena in the silver nanoparticle hcp 2D array, Silver thin films of various thicknesses were sputter coated on to the surface of borosilicate glass microscope slides (cover slips). Fig. 1b illustrates the set-up of these experiments by having a three layer system; Borosilicate glass ( $\epsilon_0$ ) (for which is the dielectric medium is  $n = 1.536$ ), the silver film ( $\epsilon_1$ ) of thickness  $d$  (the dielectric medium is  $n = -2.3$ ); and a second dielectric, which in our case was air (1) ( $\epsilon_2$ ). A prism was put on the surface of the borosilicate glass and optical contact was made using index matching fluid (Edmund Optics).

Fig. 5 demonstrates the effect of variation of thickness at a constant wavelength  $\lambda$  on the position of the attenuated

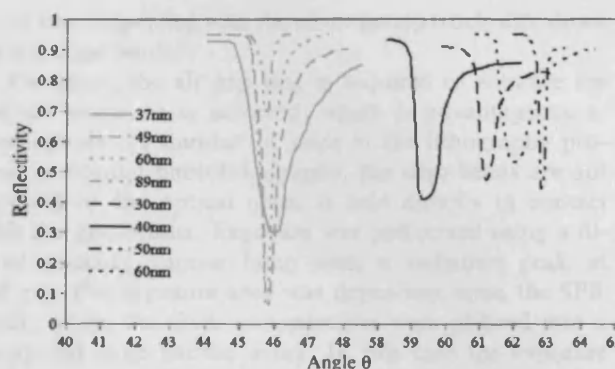


Fig. 5. Reflection of silver films of different thickness. Detection of surface plasmon modes, the data represented in black were performed at the 635 nm wavelength, whereas the data in grey were performed at 546 nm [12].

total reflection (ATR) minimum. The radiation wave, having passed the prism ( $\epsilon_0$ ), is partially reflected at the borosilicate glass/silver film interface. Partially it traverses the silver film (of thickness  $d$ ) as an exponentially decaying wave. At the Silver film/air interface it induces excitations, which radiate light back into the silver film. If the thickness  $d$  increases, the backscattered field disappears. For decreasing thickness  $d$  the back scattered field increases. Since it is in antiphase with the incoming wave, the two interfere destructively thus reducing the reflection. The antiphase radiation field, captured in the metal film, is converted into heat.

Due to experimental error, not all the data have dipped to an angle of 62°, however, surface plasmons have been detected near the desired angle.

For a photolithographic optical mask there must be an opaque contrast between the borosilicate glass and the 30 nm silver nanoparticle thin film. The far-field transmission data are shown in Fig. 6, all the samples used in the nanolithography experiment were obtained using a Jenway spectrophotometer.

The transmittance spectra showed that the borosilicate glass without silver nanoparticles averaged approximately 90% transparency in the near UV-radiation wavelengths.

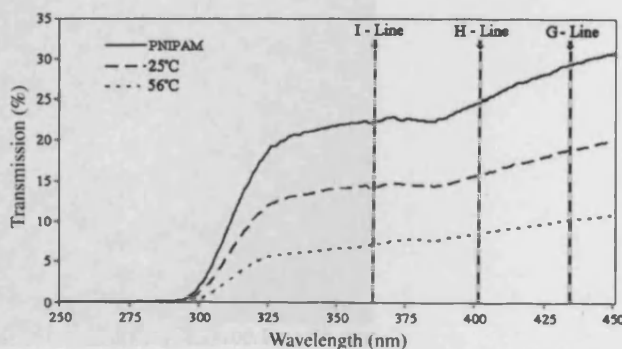


Fig. 6. Transmission spectra of the 30 nm spherical Silver nanoparticle with a spacing period of 20 nm forming a hcp 2D array.

Therefore, this was a suitable substrate to produce an opaque photo mask.

### 3.3. Nano pattern transfer using I-line radiation

It is observed that the PNIPAM polymer attenuates approximately 75% of the UV radiation at the I-line wavelength this is due to the DEAP photoinitiator. The DEAP cures at lower wavelengths but is still effective at the I-line wavelength. The monolayer of silver nanoparticles decreases the optical transmission (producing an opaque contrast) this is due to the SPR. The optical properties of silver nanoparticles are determined by a collective oscillation of free electrons in the nanoparticles. This is mostly described by the term plasma-resonance absorption [18]. The plasma-resonance absorption depends on the nanoparticle material and on nanoparticle structure, size (30 nm diameter) and shape (spherical) [19]. The observed transmission strongly depends on the wavelength and the period of the hcp 2D array, which confirms the role of SPs. The PNIPAM was heated at a temperature of 56 °C for 24 h, the PNIPAM shrank in all directions as the silver nanoparticles on the surface were brought closer together as shown in Fig. 7a. From the data shown, it is evident that the silver mask is more opaque as a function of temperature. It is clear that the silver nanoparticle hcp 2D array does not absorb all of the UV radiation, 7.13% at the I-line wavelength, 8.78% at the H-line wavelength and 10.32% at the G-line wavelength. However, it is evident that from Fig. 7b, the absorption mechanism (SPR at the surface of each silver nanoparticle) was present as the features remain. This will affect the resultant thickness of the exposed photoresist, as the transmission of the UV radiation increases then the developed photoresist thickness will decrease. Therefore, G and H-line wavelengths will result in thinner photoresist thickness.

In the Photo-Nanolithography process, Shipley S1813 photoresist was spun directly on to a silicon substrate at 6000 rpm for the duration of 45 s. This resulted in a uniform thickness of 1.12  $\mu\text{m}$ . As shown in Fig. 1b, the SPR

mask was suspended with the silver nanoparticle side down on the edge beads.

Therefore, the air gap that is required to enhance the surface plasmons is achieved, which is advantageous as this reduces the number of steps in the lithography process. In normal photolithography, the edge beads are not required as the optical mask is held directly in contact with the photoresist. Exposure was performed using a filtered mercury vapour lamp with a radiation peak at 365 nm. The exposure area was dependent upon the SPR mask, where the silver nanoparticles were ordered into a hexagonal close packed array. In this case the exposure area was approximately 3.25  $\mu\text{m}$  in diameter. It was found that it was difficult to achieve a larger area using the method described Section 3.1, as the silver nanoparticles would dislocate and become disordered by the thermal convection currents and Brownian motion produced by the water. The S1813 photoresist was developed after UV exposure using Microposit 2401 developer and was then rinsed in deionized water. The development time was 15 s. After development, the topography of the exposed features was characterized by using a TECNAI TEM, operating at 60 kV.

The TEM image of the self assembled silver nanoparticles is shown in Fig. 7a, which shows the ordered hexagonal arrays, the feature size of 30 nm with a period of 50 nm is uniform. The resolution of silver nanoparticle SPR mask is approximately 12 times smaller than the I-line wavelength ( $\lambda/12$ ). Fig. 7b shows a TEM micrograph of the developed S1813 photoresist, where the thickness was approximately 33 nm (G and H-Line would result in thinner photoresist, see Fig. 6). The developed photoresist features are on average 34 nm in diameter with a smaller period of 46 nm, therefore, the S1813 photoresist features are 11 times smaller ( $\lambda/11$ ). This pattern period is far beyond the diffraction limit of far-field lithography [20]. The optimal exposure time is only 8 s, this is comparable to a typical exposure dose used in conventional lithography with larger features, which implies a strong near-field transmission enhancement due to SPs.

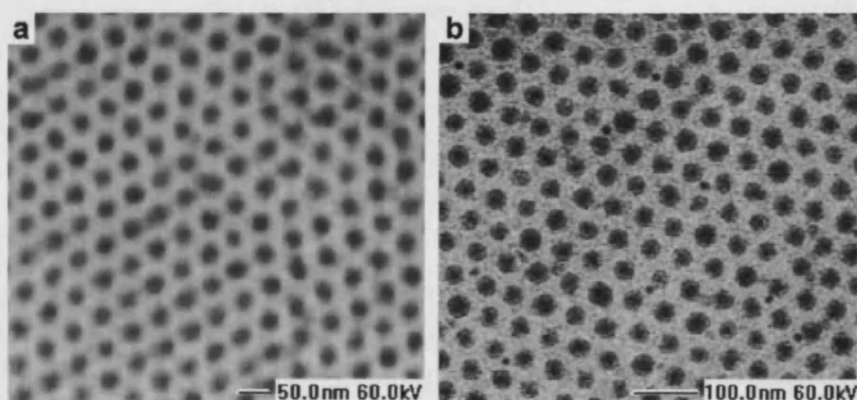


Fig. 7. (a) Silver nanoparticle hcp 2D array positioned by self assembly; (b) developed S1813 photoresist exposed at I-line wavelength enhanced by surface plasmons.

#### 4. Conclusion

A novel plasmon enhanced photolithography using periodic hexagonal close packed silver nanoparticle array mask has been demonstrated. Hydrophobic silver nanoparticles have been used as the building components for LS technique. The silver nanoparticles on a water surface are transferred onto a thermo-sensitive polymer surface. As the temperature increases, the polymer undergoes a phase transition and the polymer film shrinks isotropically. The silver nanoparticles are compacted by the polymer film and the nanoparticle spacing can be tuned by adjusting the temperature. Highly ordered high density nanoparticle film can be obtained by heating the film to temperature above the polymers LCST. The nanolithography technique utilizes near UV radiation to excite surface plasmons on a metal grating in order to enhance the transmission through sub-wavelength periodic apertures with effectively shorter wavelengths compared to the excitation light wavelength. A 34 nm hexagonal nanoparticle 2D array pattern on a 46 nm pitch has been successfully transferred using I-line exposure wavelength. Far-field transmission spectra of the silver hexagonal nano structures show a strongly enhanced transmission in the UV range. This opens the possibility of lithography using apertures smaller than the exposure wavelength. This shows promise in high resolution, high density, and strong transmission optical lithography, which can be used to fabricate periodic structures for potential biosensing and high density patterned magnetic storage devices. The concept of plasmonic lithography applies not only to periodic structure but also to arbitrary shapes [21].

#### Acknowledgement

The authors would like to acknowledge the support of Professor F. Pooley and M. Griffiths of Materials and Min-

erals at the School of Engineering and D.I. Westwood of School of Physics and Astronomy, Cardiff University.

#### References

- [1] H. Schmid, H. Biebuyck, B. Michel, O.J.F. Martin, *Appl. Phys. Lett.* 72 (1998) 2379.
- [2] J.G. Goodberlet, *Appl. Phys. Lett.* 76 (2000) 667.
- [3] J.G. Goodberlet, H. Kavak, *Appl. Phys. Lett.* 81 (2002) 1315.
- [4] O.J.F. Martin, N.B. Piller, H. Schmid, H. Biebuyck, B. Michel, *Opt. Express* 3 (1998) 280.
- [5] P.G. Kik, A.L. Martin, S.A. Maier, H.A. Atwater, *Proc. SPIE* 4810 (2002) 7.
- [6] M.M. Alkaisi, R.J. Blaikie, S.J. McNab, R. Cheng, D.R.S. Cumming, *Appl. Phys. Lett.* 75 (1999) 3560.
- [7] T.W. Ebbesen, H.J. Lezec, H.F. Ghaemi, T. Thio, P.A. Wolff, *Nature (London)* 391 (1998) 667.
- [8] T. Thio, H. F. Ghaemi, H.J. Lezec, P.A. Wolff, T.W. Ebbesen, *JOSA B* 16 (1999) 1743.
- [9] A. Krishnan, T. Thio, T.J. Kim, H.J. Lezec, T.W. Ebbesen, P.A. Wolff, J. Pendry, L. Martin-Moreno, F.J. Garcia-Vidal, *Opt. Commun.* 200 (2001) 1.
- [10] A. Dogariu, A. Nahata, R.A. Linke, L.J. Wang, R. Trebino, *Appl. Phys. B* 74 (2002) S69.
- [11] L. Salomon, F. Grillot, A.V. Zayats, F. deFornel, *Phys. Rev. Lett.* 86 (2001) 1110.
- [12] H. Raether, *Surface Plasmons on Smooth and Rough Surfaces and on Gratings*, Springer, Berlin, 1988, pp. 25–30.
- [13] V. Santhanam, J. Liu, R. Agarwal, R.P. Andres, *Langmuir* 19 (2003) 7881.
- [14] S. Kwan, F. Kim, J. Arkana, P. Yang, *Chem. Commun.* 5 (2001) 447.
- [15] S.W. Chung, G. Markovich, J.R. Heath, *J. Phys. Chem. B* 102 (1998) 6685.
- [16] M.J. Serpe, C.D. Jones, L.A. Lyon, *Langmuir* 19 (2003) 8759.
- [17] A.L. Aden, M. Kerker, *J. Appl. Phys.* 22 (1951) 1242.
- [18] M. Kerker, *The Scattering of Light and Other Electromagnetic Radiation*, Academic Press, New York, 1969 (Chapters 3 and 4).
- [19] J.B. Pendry, *Phys. Rev. Lett.* 85 (2000) 3966.
- [20] W. Srituravanich, S. Durant, H. Lee, C. Sun, X. Zhang, *J. Vac. Sci. Technol. B* 23 (6) (2005) 2636.
- [21] S.-W. Chung, G. Markovich, J.R. Heath, *J. Phys. Chem. B* 102 (35) (1998).

# Synthesis and characterization of a PMMA based nanocomposite resist for next generation nano lithography

S. Lewis <sup>a,\*</sup>, A Jones <sup>b</sup>, V. Haynes <sup>a</sup>, J. Sly <sup>b</sup>, R. M. Perks <sup>c</sup>, L. Piccirillo <sup>a</sup>

<sup>a</sup> School of Physics and Astronomy, Radio Astronomy Technology Group, The University of Manchester, Turning Building, Oxford Rd, Manchester, M13 9PL, UK

<sup>b</sup> School of Electrical and Electronic Engineering, Microelectronics and nanostructures group, The University of Manchester, Sackville St Building, Sackville St, Manchester, M60 1QD, UK

<sup>c</sup> The Institute of Advanced Materials and Energy Systems, Cardiff School of Engineering, Cardiff University, The Parade, Cardiff U.K CF24 3AA.

---

## Abstract

Synthesis and characterization of a novel nanocomposite e-beam resist has been demonstrated. This was created by the incorporation of 150mg, 100mg, 50mg and 0mg of Al<sub>2</sub>O<sub>3</sub> nanoparticles into a PolyMethylMethAcrylate (PMMA) polymer matrix. The molecular weight of the PMMA resist was reduced from PMMA 950K 7% to PMMA 96K 7% which resulted in the thickness of nanocomposite resist decreasing. For the PMMA 950K 7% samples, the clearing doses of these resist were 265, 255, 236 and 200 $\mu$ C/cm<sup>2</sup> respectively and when the same amount of Al<sub>2</sub>O<sub>3</sub> nanoparticles were introduced into the PMMA 96K7% polymer matrix, the resist clearing doses were 200, 172, 160 and 131 $\mu$ C/cm<sup>2</sup> respectively. The high aspect ratio of the PMMA 950K 7% nanocomposite resist ranged from 6.3 to 4.4, for the PMMA 96K 7% samples it ranged from 4 to 2.5. Hence, the aspect ratio was at its greatest when the Al<sub>2</sub>O<sub>3</sub> nanoparticles were introduced.

Keywords: PMMA, Al<sub>2</sub>O<sub>3</sub> Nanoparticles, Nanocomposite, Electron Beam Lithography, High Aspect Ratio

---

## 1.0 Introduction

The trend of Moore's law has been maintained using the current technology of ultra large scale integration which produces circuits with features of sub 100 nm [1]. This has been made possible by sub 100nm lithography, by the design of next generation resists, operating at extreme ultra violet wavelengths. However, it is well known that electron beam lithography can achieve similar dimensions using conventional chain scission resists such as PolyMethylMethAcrylate (PMMA), Polybutene – 1 – Sulfone (PBS) and ZEP520 [2, 3]. Unfortunately, there is a limit to the negative scaling factor, called the proximity effect [4]. Therefore, it is essential to optimize these resists to perform with a higher sensitivity for high throughput and a higher contrast to achieve sub 100nm resolution.

The current trend in new resist materials are nanocomposite resists. These materials can have a large impact on current integrated circuit (IC) fabrication technologies thanks to the properties of maintaining high throughput while increasing the aspect ratio of the resist. Nanoparticles can have an enormous effect on a resist's physical properties. This has been extensively studied using carbon fullerenes and silica nanoparticles [5 – 7].

It is expected that proximity effects can be greatly reduced by nanocomposite resists, with the addition of nanoparticles throughout the PMMA polymer reducing the lateral distance of the electrons travelling through the PMMA polymer. This is due to the fact that the atomic number of the nanoparticle is substantially larger than that of the organic polymer, which also reduces the lateral energy spread of secondary electrons. Hence, the nanoparticles have a larger electron energy stopping power. Reducing the proximity effect provides a means of achieving a higher aspect ratio as the overall resist thickness can be increased [8].

The addition of the nanoparticles will also have a direct effect on the high aspect ratios by increasing the rigidity of the film, as the mechanical properties of the PMMA resist are improved when the density of nanoparticles is increased. The nanoparticles will prevent the nanometer features from collapsing, giving rise to a higher achievable aspect ratio. Subsequently, this can lead to a reduction of line broadening and improve the critical dimension of feature sizes.

Here the focus was on two different polymer resists, PMMA 950K 7% and PMMA 96K 7% that will serve as host matrices for  $\text{Al}_2\text{O}_3$  nanoparticle incorporation. Both of the nanocomposite resists are PMMA based but the molecular weights are vastly different. The reduced molecular weight of PMMA96K as compared to 950K means that the chain size of the molecule is also greatly reduced. Therefore, the electron beam direct write times are greatly reduced as the sensitivity is improved. Thus, a higher throughput can be achieved. The two objectives were to investigate the exposure clearing doses of each nanocomposite resist species and to achieve the highest possible aspect ratio.

## ***2.0 Experimental Details***

### ***2.1 Synthesis***

The PMMA nanocomposites used in this investigation were synthesized by the homogeneous dispersal of 15 – 25nm diameter  $\text{Al}_2\text{O}_3$  (MKnano.com 99.999%) gamma phase nanoparticles in PMMA. Samples were prepared by dissolving the PMMA (Sigma – Aldrich) in the solvent Anisole (Sigma – Aldrich 97%). The PMMA was used 'as is'. The ratio of PMMA was kept at 7% to ensure the thickness of the film was approximately 400nm. This was achieved by dissolving 350mg of PMMA (for each molecular weight of 950K and 96K) in 4.65g of Anisole. The Anisole was filtered under vacuum (assisted by a rotary pump) through a 25nm millipore membrane filter (Fisher Scientific). The PMMA/Anisole samples were shaken using IKA rotary/gyrative shaker for 96 hours, in order for the Anisole to dissolve the PMMA. This produced a PMMA based electron beam resist. This was repeated four times for each molecular weight to obtain eight samples.

The  $\text{Al}_2\text{O}_3$  nanoparticles were filtered through the 25nm membrane filter, to obtain 15 – 25nm  $\text{Al}_2\text{O}_3$  nanoparticles. This was achieved by measuring the nanoparticles by weight to 500mg, which were directly dispersed into 500ml of the deionized water. The deionized water /  $\text{Al}_2\text{O}_3$  nanoparticles were filtered under vacuum. Next, the deionized water /  $\text{Al}_2\text{O}_3$  nanoparticles were put in a desiccator to absorb the deionized water leaving behind the  $\text{Al}_2\text{O}_3$  nanoparticles. The nanoparticles were then weighed to 50, 100, 150mg and directly dispersed into 0.5ml of Methanol (Sigma – Aldrich 99.9%) to produce a nanoparticle suspension before being mixed with the PMMA.



The  $\text{Al}_2\text{O}_3$  nanoparticles that were suspended in Methanol were introduced to the PMMA / Anisole solution and were shaken for 36 hours to achieve a good nanoparticle suspension in the PMMA mix.

These PMMA based nanocomposite resists were then spun onto 24mm×24mm borosilicate glass microscope slide cover slips. The cover slips were sputter coated with a 7nm layer of gold (Au) to obtain additional adhesion qualities necessary to bond the nanocomposite resist to the borosilicate substrate. The nanocomposite was spun using a spin cycle of 4000rpm for 45 seconds which was followed by a soft-bake at 180°C for 3 minutes, as this allows the Anisole and Methanol to evaporate.

The overall thickness of the resist films after spinning was dependent on the density of  $\text{Al}_2\text{O}_3$  nanoparticles incorporated into the polymer matrix.

## ***2.2 Characterization of the e-beam lithography***

Samples were exposed on a converted SEM, JOEL JSM 840A, driven by Elphy quantum software. The samples were exposed with an acceleration voltage of 25kV and beam current of 40pA at a working distance of 7mm. Development was carried out in solutions of MIBK (Methyl IsoButyl Ketone) and IPA (IsoProPanol), in the ratio of 1:3, for 30s followed by a 40s rinse in IPA.

Two test patterns were exposed on each sample. The exposure clearing dose of each resist was determined from a matrix of a hundred 20 $\mu\text{m}$  squares that were exposed with a dose scale in incremental steps of 30 $\mu\text{C}/\text{cm}^2$ . The dose was increased in both directions with the square in the lower left having a dose of 30 $\mu\text{C}/\text{cm}^2$ , and that of the upper right having a dose of 600 $\mu\text{C}/\text{cm}^2$ . The size of the squares allowed for accurate AFM measurements of the remaining resist thickness for each dose, and hence the clearing dose could be determined of each resist.

To investigate the aspect ratio of developed features a series of 90 nm lines with spacings of 180 nm and a length of 20  $\mu\text{m}$  were exposed with a dose of 300 $\mu\text{C}/\text{cm}^2$ . SEM images and AFM measurements were used to determine the aspect ratio achieved in each resist.

## ***3.0 Results and Discussion***

### ***3.1 Clearing doses of the nanocomposite resist***

As shown in the inset of figure 1, it was found that by decreasing the molecular weight of the PMMA polymer from 950K7% to 96K7%, the overall resist thickness was decreased. The molecule chain sizes of 950K7% and 96K7% were approximately 5108 and 520 respectively. Therefore, the clearing dose required for the exposure of the PMMA 96K7% would be lower than that of the PMMA 950K7% samples because the PMMA 96K7% has fewer molecule chains to be cleaved by the incident electron beam.

Comparing just PMMA 950K7% with PMMA 96K7% the thicknesses were 407nm and 228nm respectively. However, when 50mg, 100mg and 150mg of  $\text{Al}_2\text{O}_3$  nanoparticles were introduced into the PMMA 950K7% polymer matrix, the overall resist thicknesses were increased to 455nm, 505nm and 562nm. The overall resist thicknesses were 276nm, 331nm and 364nm, when 50mg, 100mg and 150mg of  $\text{Al}_2\text{O}_3$  nanoparticles were introduced into the PMMA 96K7% polymer matrix.

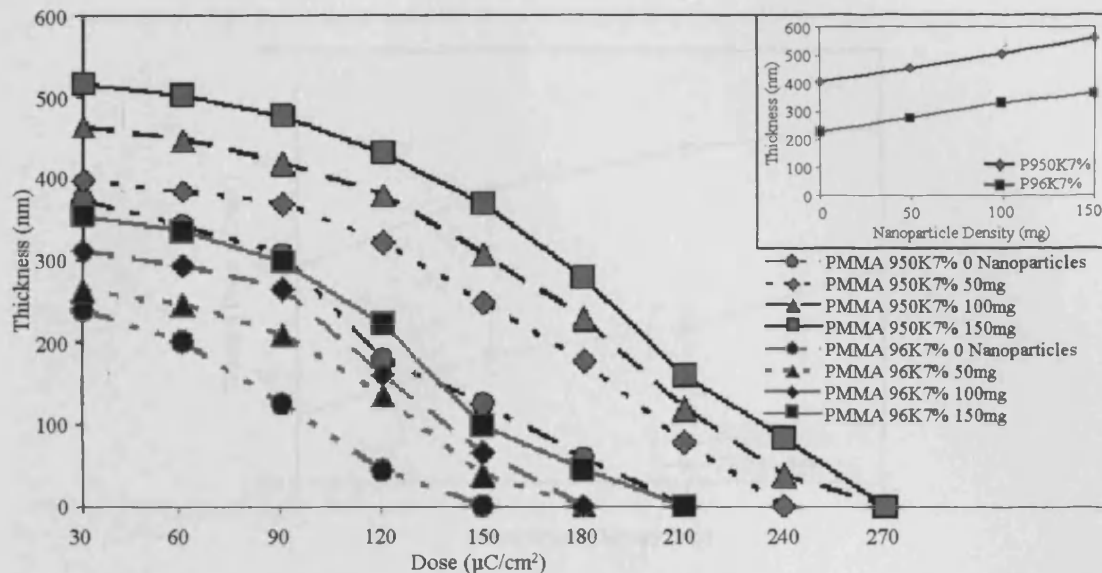


Figure 1: Exposure doses of nanocomposite resist, Inset: Overall thickness's of the nanocomposite resist.

It was clear that the overall resist thickness was increased by the introduction of  $\text{Al}_2\text{O}_3$  nanoparticles into the PMMA polymer matrix. Figure 1 indicates that the exposure clearing doses of both the PMMA 950K7% and PMMA 96K7% resists decreased as the density of  $\text{Al}_2\text{O}_3$  nanoparticles embedded into the PMMA was increased. The combination of the increased resist thickness and the  $\text{Al}_2\text{O}_3$  nanoparticles resulted in higher exposure doses being required in order for the chain scission process to occur throughout the nanocomposite resist.

As seen in figure 1, the exposure clearing doses of the PMMA 950K7% loaded with 0mg, 50mg, 100mg and 150mg of  $\text{Al}_2\text{O}_3$  nanoparticles were in the range of  $180 - 210 \mu\text{C}/\text{cm}^2$ ,  $210 - 240 \mu\text{C}/\text{cm}^2$ ,  $240 - 270 \mu\text{C}/\text{cm}^2$  and  $240 - 270 \mu\text{C}/\text{cm}^2$  respectively, as determined from the dose scale. It should be noted that this exposure matrix method only gives a dosage range (e.g  $240 - 270 \mu\text{C}/\text{cm}^2$ ) within which complete resist exposure occurs. However, an estimate of the exact clearance dose can be obtained by extrapolation from the data set up to – but not including – the final point (where the resist thickness is zero). This gives clearance doses of  $200 \mu\text{C}/\text{cm}^2$ ,  $236 \mu\text{C}/\text{cm}^2$ ,  $255 \mu\text{C}/\text{cm}^2$  and  $265 \mu\text{C}/\text{cm}^2$  for PMMA 950K 7% loaded with 0mg, 50mg, 100mg and 150mg respectively. Similarly, clearance doses of  $131 \mu\text{C}/\text{cm}^2$ ,  $160 \mu\text{C}/\text{cm}^2$ ,  $172 \mu\text{C}/\text{cm}^2$  and  $200 \mu\text{C}/\text{cm}^2$  are obtained for PMMA 96K 7% loaded with 0mg, 50mg, 100, 150mg respectively.

Figure 2 shows the electron beam clearing dose trend that was taken from the data shown in figure 1. In both PMMA 950K7% and PMMA 96K7% based nanocomposite resists, it was found that as the density of  $\text{Al}_2\text{O}_3$  nanoparticles increases, the clearing dose needed to be increased. This was because the  $\text{Al}_2\text{O}_3$  nanoparticles increased the overall resist thickness and therefore the electrons must be transmitted at a higher exposure dose to overcome the increased resist thickness and the  $\text{Al}_2\text{O}_3$  nanoparticles as the nanoparticles act as electron scattering centers and consequently decrease the electron momentum [9, 10].

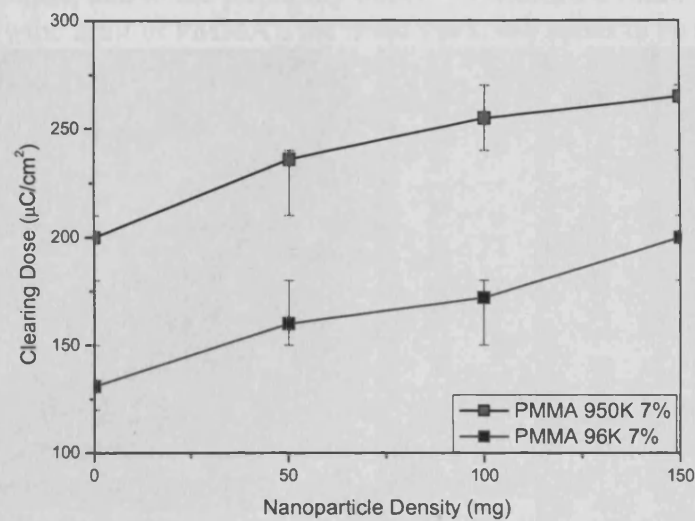


Figure 2: Electron exposure clearing doses of the PMMA 950K7% and PMMA 96K7% based nanocomposite resists.

### 3.2 Characterization of the nanocomposite resists

Figures 3 and 4 show SEM images of all the samples based on PMMA 950K7% and PMMA 96K7%. The features shown in figure 4 have been over exposed by a greater percentage than those in figure 3 because the overall resist thickness was reduced for PMMA 96K7%.

Figure 3a shows features in the PMMA 950K7% sample loaded with 150mg of nanoparticles. These features consisted of lines and spaces (trenches). The lines had a width of 185nm and the spacing between each of the lines were 91nm. Consequently this gave a high aspect ratio of approximately 6.2, (as the resist thickness was 562nm). The SEM images of the PMMA 950K 7% samples loaded with 100mg and 50mg of  $\text{Al}_2\text{O}_3$  nanoparticles are shown in figures 3b and c. The widths of the lines were 185nm and 180nm with spacings of 92 and 90nm respectively. This gives aspect ratios of 5.5 and 5.05. The SEM image in figure 3d shows the unloaded PMMA 950K 7% resist. The high aspect ratio is 4.4, as the width of the lines was 185nm with spacings of 91nm.

Figure 4a shows the feature sizes in the PMMA 96K 7% sample loaded with 150mg of nanoparticles. The width of each line was 180nm and the spacing between each line was 91nm, consequently this gave an aspect ratio of 4.

The SEM images in figure 4b and c depicts the sample of PMMA 96K 7% loaded with 100mg and 50mg of  $\text{Al}_2\text{O}_3$  nanoparticles. The widths of each line were 180nm and 188nm with spacings of 90nm and 92nm respectively. From this, the high aspect ratios were determined to be 3.6 and 3. The unloaded PMMA 96K 7% e-beam resist is shown in figure 4d. The high aspect ratio was 2.5 (as each line was 187nm with spacings of 90nm).

Figure 5 shows the relationship between the  $\text{Al}_2\text{O}_3$  nanoparticle density and the high aspect ratio. The PMMA 950K samples have the greater aspect ratio because the size of the PMMA chains were considerably larger than those in the PMMA 96K, producing a thicker resist. As a reference, the smallest spaces possible within standard PMMA are approximately 100nm for a resist thickness of approximately 400nm, i.e. an aspect ratio is 4:1. At this thickness, if the spaces were smaller than 100nm, the

resist would collapse, due to the proximity effect. To achieve a 10nm structure (which is approximately the limit of PMMA), the resist thickness needs to be about 40nm.

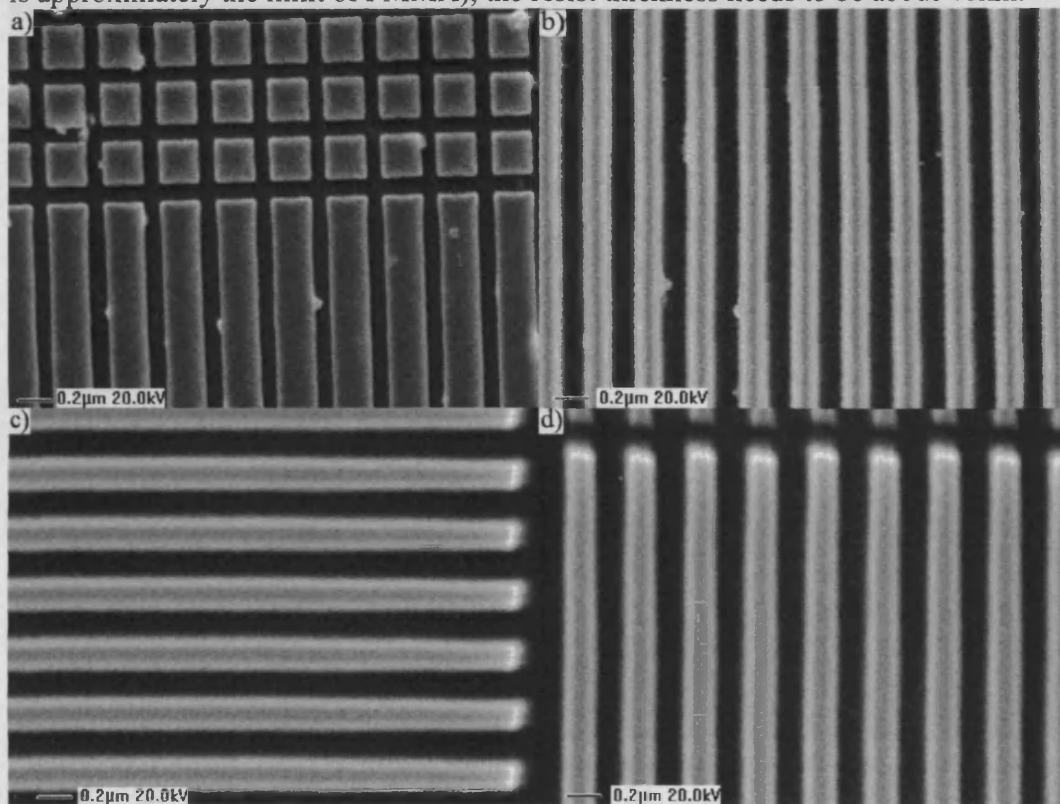


Figure 3: PMMA 950K7% nanocomposite resist exposed at  $300\mu\text{C}/\text{cm}^2$ , a) loaded with 150mg of  $\text{Al}_2\text{O}_3$  nanoparticles, b) loaded with 100mg of  $\text{Al}_2\text{O}_3$  nanoparticles, c) loaded with 50mg of  $\text{Al}_2\text{O}_3$  nanoparticles, d) Unloaded PMMA 950K7%.

However, we have produced 90nm trenches in a thicker resist because the  $\text{Al}_2\text{O}_3$  nanoparticles have contributed to reducing the proximity effect. This is due to the primary and secondary electrons penetrating the PMMA polymer, which have diverging scattering trajectories from the incident primary electron beam. These diverging electrons are blocked, or their energy is considerably reduced, by the  $\text{Al}_2\text{O}_3$  nanoparticles, which have a large electron energy stopping powers and therefore reduce the energy of the electrons [9, 10], thus affecting the distance travelled through the PMMA polymer. Also the mechanical properties of the PMMA have been improved by providing an internal structure (much like the mechanical properties of a skeleton for a human body) that bonds the PMMA resist together.

From the SEM images in figures 3a & b and 4a, b & c it can be seen that the resultant features are degraded due to  $\text{Al}_2\text{O}_3$  nanoparticles that have aggregated together. This has occurred because each nanoparticle is surrounded by a depletion zone; the depletion of Anisole molecules from this region, due to an effective internanoparticle/nanoparticle attraction. The Anisole molecule is formed around a conjugated ring and does not have hydroxyl groups attached to it. Therefore, the Anisole can not suspend the nanoparticles because the  $\text{Al}_2\text{O}_3$  nanoparticles are hydrophilic due to the hydroxyl groups at their surface. Hence, there is no mechanism for hydrogen bonding to occur. The osmotic pressure of the PMMA/Anisole becomes unbalanced and pushes the nanoparticles towards one another.

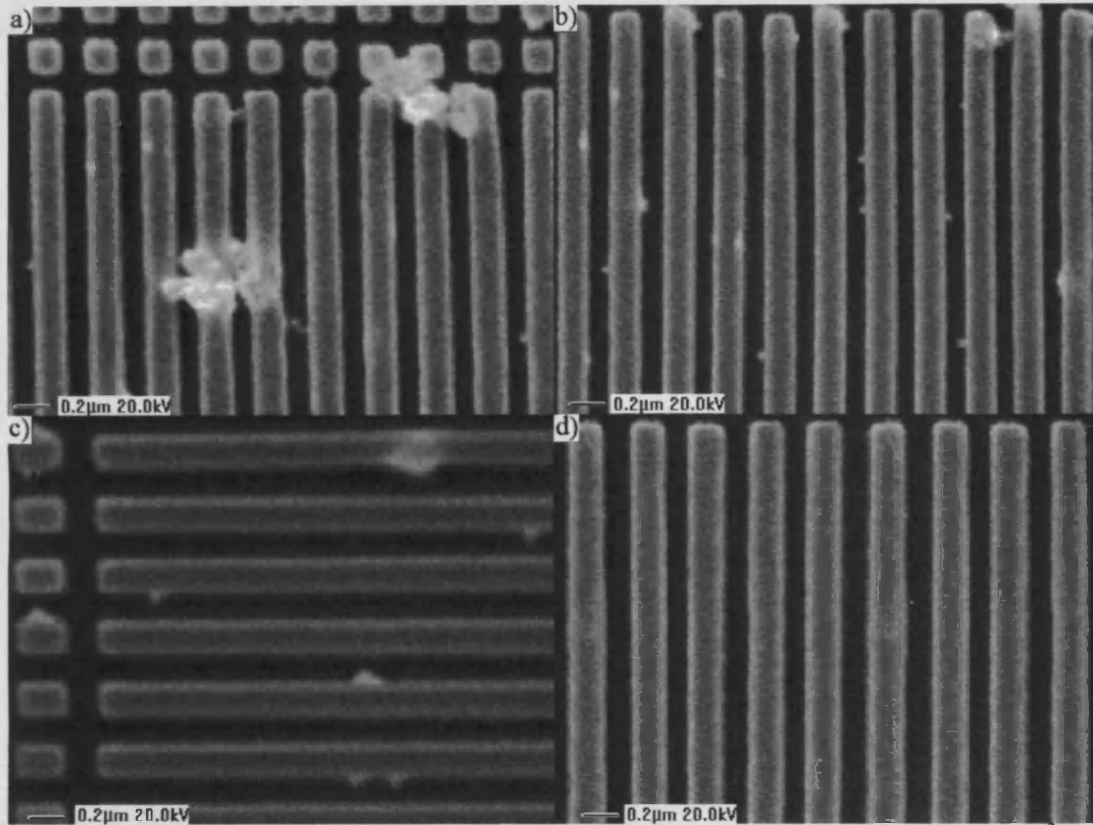


Figure 4: PMMA 96K7% based nanocomposite resist exposed at  $300\mu\text{C}/\text{cm}^2$ , a) loaded with 150mg of  $\text{Al}_2\text{O}_3$  nanoparticles, b) loaded with 100mg of  $\text{Al}_2\text{O}_3$  nanoparticles, c) loaded with 50mg of  $\text{Al}_2\text{O}_3$  nanoparticles, d) Unloaded PMMA 96K7%.

This allows the depletion zone around each  $\text{Al}_2\text{O}_3$  nanoparticle to intersect and the  $\text{Al}_2\text{O}_3$  nanoparticles are attracted to one another and aggregate. By using Methanol to suspend the  $\text{Al}_2\text{O}_3$  nanoparticles, the nanoparticle aggregations are greatly reduced. The Methanol molecules have hydroxyl groups attached to them and are attracted to the hydroxyl groups at the surface of the  $\text{Al}_2\text{O}_3$  nanoparticles via their dipoles.

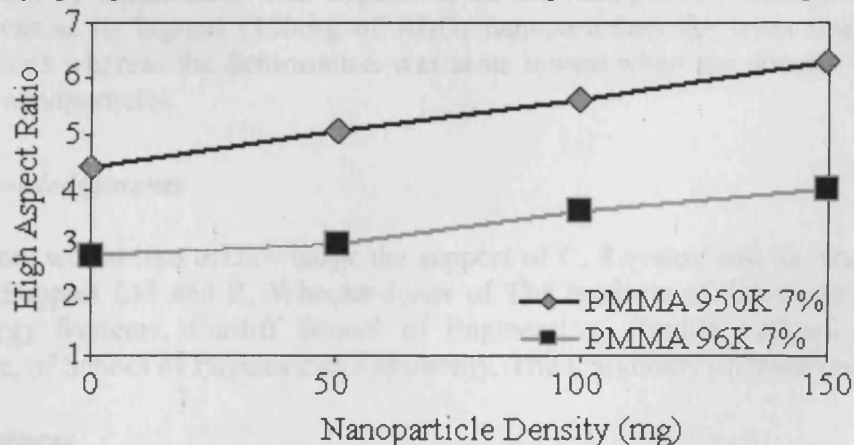


Figure 5: High aspect ratios of the PMMA 950K and 96K based nanocomposite resists.

Therefore, as the Methanol surrounds the  $\text{Al}_2\text{O}_3$  nanoparticles a physical barrier, with a thickness greater than that of the depletion zone (which surrounds the oxide



nanoparticle) is formed. The depletion region of the  $\text{Al}_2\text{O}_3$  nanoparticles can never intersect. Hence, the oxide nanoparticle attraction is greatly reduced and the oxide nanoparticle suspension is stable. However, as the quantity of Anisole is greater than that of Methanol, it has contributed to the intersection of depletion zones, causing the nanoparticle attraction. This attraction is irreversible.

The overall shape of the feature (resist line) was affected by the  $\text{Al}_2\text{O}_3$  nanoparticles. It can be seen from the SEM images that in both the samples of PMMA 950K7% and PMMA 96K7% the attributes of the features are improved when nanoparticle aggregations are reduced by reducing the density of the  $\text{Al}_2\text{O}_3$  nanoparticles. However, the aspect ratio is also reduced. Figures 4a, b and c shows that the nanoparticle aggregations are worse than that in PMMA 96K7% than in PMMA 950K 7%, because the overall thickness is reduced.

#### **4.0 Summary**

A novel electron beam resist has been demonstrated that incorporates  $\text{Al}_2\text{O}_3$  nanoparticles, with a diameter of 15 – 25nm into the PMMA polymer matrix. By introducing these additives the structural properties of the resist were improved and consequently the aspect ratio of the resultant features was increased. In an attempt to decrease e-beam direct writing times, the molecular weight of the PMMA was reduced from 950K to 96K. It was found that this reduced the overall thickness of the resist and hence a reduced aspect ratio was produced.

It was clear that introducing  $\text{Al}_2\text{O}_3$  nanoparticles into the PMMA caused an increase in the overall thickness of the film, which gave rise to the highest aspect ratio when the largest density of nanoparticles was incorporated. This led to larger clearing doses. Due to the interaction of the incident electron beam with the  $\text{Al}_2\text{O}_3$  nanoparticles, the under-cutting action of the proximity effect was reduced. The aspect ratio of the PMMA 950K 7% was higher for all nanoparticle concentrations as the  $\text{Al}_2\text{O}_3$  nanoparticles prevented the lines from collapsing by providing mechanical structure for the PMMA, allowing the polymer to bond together.

The density of nanoparticles had an impact on the shape of the lines. It was found that the nanoparticle aggregations pierced the resist surface causing the lines to deform. The amount of deformation was dependent on the nanoparticle density. When the density was at its highest (150mg of  $\text{Al}_2\text{O}_3$  nanoparticles) the lines had the most deformations whereas the deformation was at its lowest when the density was 50mg of  $\text{Al}_2\text{O}_3$  nanoparticles.

#### **5.0 Acknowledgements**

The authors would like acknowledge the support of C. Royston and the team at E M Systems Support Ltd and R. Wheeler-Jones of The Institute of Advanced Materials and Energy Systems, Cardiff School of Engineering, Cardiff University and D. Jeanmaire, of School of Physics and Astronomy, The University of Manchester.

#### **6.0 References**

- [1] G. E. Moore, 'Cramming more components onto integrated circuits', Electronics, vol 38, No 8, Apr (1965).
- [2] R. L. Dean, H. Y. Lem, C. A. Sauer, H. Chang, 'PBS resist profile studies for sub – micron mask lithography', Proc. SPIE, vol. 2322, 102 (1994).

- [3] Zeonrex electron chemicals, 'ZEP520, high resolution positive electron beam resist', Technical report, ZEP520. Ver 1. 02, March (2001).
- [4] T. Ishii, H. Nozawa, T. Tamamura, 'A nano – composite resist system: a new approach to nanometer pattern fabrication', Microelectronic Engineering, vol 35, no 1 pp 113 – 116 (1997).
- [5] T. Ishii, T. Tamamura, K. Shigehara, 'Fullerene – derivative nanocomposite resist for nanometer pattern fabrication', Jpn. J. Appl. Phys. 39 pp L1068 – L1070 (2000).
- [6] T. Ishii, H. Nozawa, T. Tamamura, 'C60 incorporated nanocomposite resist system', J. Photopolymer. Sci. Technol, vol 10, no 4 pp 651 – 656 (1997).
- [7] T. Ishii, Y. Murate, K. Shigehara, 'Contrast enhancement of ZEP520 resist by fullerene – derivate incorporation', Jpn. J. Appl. Phys 40 pp L478 – L480 (2001).
- [8] K. E. Gonsalves, L. Merhari, H. Wu, Y. Hu, 'Organic – Inorganic nanocomposite: unique resists for nanolithography', Advanced Materials, vol 13, no 10 (2001).
- [9] Y. Hu, H. wu, K. Gonsalves. L. Merhari, 'Nanocomposite resist for electron beam nanolithography', Microelectronic Engineering 56 pp 289 – 294 (2001).
- [10] L. Merhari, K. E. Gonsalves, Y. Hu, W. He, W. S. Huang, M. Angelopoulos, 'Nanocomposite resist systems for next generation lithography', Microelectronic Eng. 63 pp391 – 403 (2002).

